UNIVERSITY OF SOUTHAMPTON

Faculty of Engineering, Science and Mathematics
School of Engineering Sciences
Aerodynamics and Flight Mechanics Research Group

DYNAMICS AND STABILITY OF FLOW PAST A CIRCULAR CYLINDER IN GROUND EFFECT

By

Takafumi NISHINO

Thesis for the degree of Doctor of Philosophy

October 2007

UNIVERSITY OF SOUTHAMPTON

ABSTRACT

FACULTY OF ENGINEERING, SCIENCE AND MATHEMATICS
SCHOOL OF ENGINEERING SCIENCES
AERODYNAMICS AND FLIGHT MECHANICS RESEARCH GROUP

Doctor of Philosophy

DYNAMICS AND STABILITY OF FLOW PAST A CIRCULAR CYLINDER IN GROUND EFFECT

by Takafumi Nishino

A combined experimental, computational and theoretical study is presented on the dynamics and stability characteristics of turbulent flow past a circular cylinder placed near and parallel to a moving ground. The study consists of four main parts: (i) wind tunnel experiment, (ii) numerical simulation, (iii) linear stability analysis, and (iv) proper orthogonal decomposition (POD) analysis. The main focus of the study is on the cessation of large-scale, von Kármán-type vortex shedding in 'ground effect,' i.e., the cessation observed when the cylinder comes close to the ground.

The experiments, performed at upper-subcritical Reynolds numbers of 0.4 and 1.0×10^5, show that the cessation of von Kármán-type vortex shedding and an attendant critical drag reduction of the cylinder (equipped with end-plates) occurs at the gap-to-diameter ratio h/d of around 0.35, at which point the flow through the gap between the cylinder and the ground is still not blocked at all due to the ground moving at the same speed as the free stream. It is subsequently shown that detached-eddy simulations (DES) can correctly reproduce these critical phenomena, whereas unsteady RANS simulations predict them at much smaller h/d of between 0.1 and 0.2, despite the fact that the unsteady RANS simulations are 'overly dissipative' compared with the DES. The linear stability analysis of analytical wake profiles then provides a possible explanation for the above experimental and computational results; that is, the cessation of the von Kármán-type vortex shedding in ground effect may also be largely explained by the change of inviscid instability characteristics in the near wake region from 'absolutely unstable' to 'convectively unstable,' in analogy with the case for a cylinder equipped with a backward splitter plate in a free stream. Finally, the near wake structure of the cylinder in ground effect is further investigated with the POD analysis. The results show that about 60% of the total kinetic energy in the near wake region (in the time-averaged sense) is contained only in the first three POD modes even when the energetically dominant, von Kármán-type vortex shedding becomes intermittent at $h/d = 0.4$. It is also shown that both shedding and non-shedding states at this gap ratio can roughly be reproduced from the combination of these three POD modes.

Acknowledgements

The research presented in this thesis was carried out during my three-year stay in the Aerodynamics and Flight Mechanics Research Group at the University of Southampton. I would like to thank my supervisors, Dr. Graham Roberts and Prof. Xin Zhang, for their support throughout the research. I would also like to thank Prof. Neil Sandham and Dr. Richard Sandberg for their comments and advice on the research, especially those regarding the linear stability analysis. My thanks also go to Mr. Mike Tudor-Pole and Dr. Martijn van den Berg for their assistance in performing the wind tunnel tests, and Mr. James Chitty for his help in preparing the models for the tests. I also want to thank my colleagues and friends, especially Hiroshi Narita and Yuichi Kuya, for many fruitful talks and discussions. Finally, I would like to thank my parents for their continuous support throughout my three-year study in Southampton.

Takafumi Nishino
University of Southampton, UK
August 2007

This thesis was submitted to the Office of the School of Engineering Sciences on 22 August 2007 for the degree of Doctor of Philosophy, and was accepted on 19 October 2007 after the award of the degree being recommended by the examiners: Prof. Peter W. Bearman (Imperial College London) and Dr. T. Glyn Thomas (University of Southampton).

Contents

List of Figures

List of Tables

Nomenclature

A_f	area of each face of control-volume	$[\mathrm{m}^2]$
$\boldsymbol{A}_f$	area vector of each face of control-volume ($\equiv A_f \boldsymbol{n}_f$)	$[\mathrm{m}^2]$
a_i	time-dependent modal coefficient for the i-th mode	$[-]$
a_i^k	discrete modal coefficient at time instant $t = t_k$	$[-]$
B	wake width	$[\mathrm{m}]$
b_1, b_2	half-widths of model wake profile	$[\mathrm{m}]$
C	two-time covariance matrix	
C_{b1}, C_{b2}	model coefficients in S-A model	$[-]$
C_D	drag coefficient ($\equiv D/\frac{1}{2}\rho U_\infty^2 ld$)	$[-]$
C_D'	fluctuation of drag coefficient	$[-]$
C_{Df}	friction drag coefficient	$[-]$
C_{Dp}	pressure drag coefficient	$[-]$
C_{des}	model coefficient in S-A-based DES	$[-]$
C_f	friction coefficient ($\equiv \lvert\tau_{\mathrm{w}}\rvert/\frac{1}{2}\rho U_\infty^2$)	$[-]$
C_L	lift coefficient ($\equiv L/\frac{1}{2}\rho U_\infty^2 ld$)	$[-]$
C_L'	fluctuation of lift coefficient	$[-]$
C_p	pressure coefficient ($\equiv \{p - p_\infty\}/\frac{1}{2}\rho U_\infty^2$)	$[-]$
C_{pb}	base pressure coefficient	$[-]$
C_{pq}	element of two-time covariance matrix C	
C_{s}	model coefficient in Smagorinsky model	$[-]$
$C_{v1}, C_{w1}, C_{w2}, C_{w3}$	model coefficients in S-A model	$[-]$
$C_{\epsilon 1}, C_{\epsilon 2}, C_\mu$	model coefficients in LS k-ϵ model	$[-]$
CFL	CFL number ($\equiv \Delta t \cdot U_i/\Delta x_i$)	$[-]$
c	complex wave velocity	$[\mathrm{m/s}]$
c_i	imaginary part of complex wave velocity c	$[\mathrm{m/s}]$
c_r	real part of complex wave velocity c	$[\mathrm{m/s}]$
D	drag force	$[\mathrm{N}]$
$\underline{\underline{D}}^{\mathrm{2D}}$	two-dimensional velocity gradient tensor	$[1/\mathrm{s}]$
d	diameter of cylinder	$[\mathrm{m}]$
E	model quantity in LS k-ϵ model	$[-]$
F_1, F_2	model functions for analytical wake profile	$[-]$
$F(\phi^n)_{\mathrm{P}}$	sum of all time-independent terms for ϕ_{P}^n	

f	frequency	[Hz]
f_{v1}, f_w	damping functions in S-A model	[−]
f_μ, f_1, f_2	damping functions in LS k-ϵ model	[−]
g	model quantity in S-A model	[−]
H	gap between wake centreline and ground	[m]
h	gap between cylinder and ground	[m]
K	average height of excrescences	[m]
k	turbulent kinetic energy per unit mass ($\equiv \overline{u_i' u_i'}/2$)	[m^2/s^2]
k	complex wave number	[rad/m]
k_i	imaginary part of complex wave number k	[rad/m]
k_r	real part of complex wave number k	[rad/m]
k^+, k^-	k^+ and k^- branches (cf. Huerre 2000)	
L	lift force	[N]
L_f	vortex formation length	[m]
L_r	recirculation length	[m]
L_s	length scale in Smagorinsky model	[m]
L_x, L_y	correlation length / integral length scale	[m]
l	length of cylinder	[m]
M	number of modes	[−]
N	number of samples/snapshots	[−]
N	shape factor of analytical wake model	[−]
N_1, N_2	shape factors of analytical wake model	[−]
n	distance from (or direction normal to) wall	[m]
$\tilde{n}$	length scale in S-A-based DES	[m]
$\boldsymbol{n}_f$	unit vector normal to each face of control-volume	[−]
P	mean/filtered pressure ($= \overline{p}$)	[Pa]
P'	pressure correction in SIMPLE algorithm	[Pa]
p	pressure	[Pa]
$\overline{p}$	mean/filtered pressure ($= P$)	[Pa]
$\widehat{p}$	long-time-averaged pressure	[Pa]
$\widetilde{p}$	periodic component of pressure	[Pa]
p'	stochastic/perturbation component of pressure	[Pa]
p_∞	freestream pressure	[Pa]
R_1, R_2	model functions for analytical wake profile	[−]
Re	Reynolds number ($\equiv U_\infty d/\nu$)	[−]
Re_T	(modified) turbulent Reynolds number	[−]
r	model quantity in S-A model	[−]
S	distance between two cylinders	[m]
$\tilde{S}$	deformation parameter in S-A model	[1/s]

S_{ij}	mean strain-rate tensor	[1/s]
S_{P}^{ϕ}	apparent source of ϕ at each control volume	
St	Strouhal number ($\equiv fd/U_{\infty}$)	[−]
$\overline{s}_{ij}$	filtered strain-rate tensor	[1/s]
t	time	[s]
t_k, t_n	time instants	[s]
t_{n-i}	previous time instant ($\equiv t_n - i\Delta t$)	[s]
$\vec{U}$	mean velocity vector (non-dimensionalized)	[−]
U_{c}	velocity at the centre of model wake profile	[m/s]
$\widetilde{U}_{\mathrm{c}}$	minimum velocity of local wake profile	[m/s]
U_{g}	velocity at $y = -\infty$ of model wake profile	[m/s]
$\widetilde{U}_{\mathrm{g}}$	local maximum velocity on the near-ground side of wake	[m/s]
U_i	mean/filtered velocity ($= \overline{u_i}$)	[m/s]
U_{∞}	freestream velocity	[m/s]
$\widetilde{U}_{\infty}$	local maximum velocity on the far-ground side of wake	[m/s]
$\boldsymbol{U}$	mean/filtered velocity vector	[m/s]
$\boldsymbol{U}_f$	velocity vector at each face of control-volume	[m/s]
u, v, w	Cartesian (x, y, z) components of velocity ($= u_1, u_2, u_3$)	[m/s]
$\vec{u}$	velocity vector (non-dimensionalized)	[−]
u'	fluctuation of streamwise velocity [or $(\overline{u'^2})^{\frac{1}{2}}$ in some cases]	[m/s]
$\vec{u'}$	fluctuating part of velocity vector (non-dimensionalized)	[−]
u_i	velocity	[m/s]
$\overline{u_i}$	mean/filtered velocity ($= U_i$)	[m/s]
$\widehat{u}_i$	long-time-averaged velocity	[m/s]
$\widetilde{u}_i$	periodic component of velocity	[m/s]
u_i'	stochastic/perturbation component of velocity	[m/s]
u_{τ}	friction velocity ($\equiv \sqrt{\lvert\tau_{\mathrm{w}}\rvert/\rho}$)	[m/s]
$\boldsymbol{u}$	velocity vector	[m/s]
V_{cv}	volume of control-volume	[m^3]
$\mathcal{V}$	domain of control-volume	
x, y, z	Cartesian coordinates ($= x_1, x_2, x_3$)	[m]
x_i, x_i'	Cartesian coordinates	[m]
y_{e}	distance from the bottom edge of end plate to cylinder	[m]
y^+	scaled wall distance ($\equiv u_{\tau} n/\nu$)	[−]

Greek letters

α	angle of attack	[degrees]
Γ_f^{ϕ}	apparent diffusivity of ϕ at each face of control-volume	

$\Delta_{\max}$	maximum value of Δx_i	[m]
Δt	time step size	[s]
$\Delta x, \Delta y, \Delta z$	size of control-volume ($= \Delta x_1, \Delta x_2, \Delta x_3$)	[m]
Δx_i	size of control-volume in the i-th direction	[m]
δ_B	boundary layer thickness	[m]
δ_{ij}	Kronecker delta	[−]
$(\nabla\phi)_f$	gradient of ϕ at each face of control-volume	
ϵ	dissipation rate of k	[m^2/s^3]
$\tilde{\epsilon}$	modified dissipation rate of k	[m^2/s^3]
ϵ_0	dissipation rate of k on wall	[m^2/s^3]
θ	angle	[degrees]
θ_{sep}	separation angle	[degrees]
θ^+_{sep}	separation angle for upper/open side of cylinder	[degrees]
θ^-_{sep}	separation angle for lower/gap side of cylinder	[degrees]
κ	von Kármán constant	[−]
λ_{ci}	swirl strength	[1/s]
λ_i	eigenvalue	
μ	dynamic viscosity	[kg/m s]
ν	kinematic viscosity	[m^2/s]
$\tilde{\nu}$	modified kinematic eddy viscosity	[m^2/s]
ν_T	kinematic eddy viscosity	[m^2/s]
ν_T^{s}	subgrid-scale kinematic eddy viscosity	[m^2/s]
ρ	density	[kg/m^3]
$\sigma_k, \sigma_\epsilon$	model coefficients in LS k-ϵ model	[−]
σ_x	standard deviation	
$\sigma_{\tilde{\nu}}$	model coefficient in S-A models	[−]
τ_{ij}	Reynolds stress	[N/m^2]
τ_{ij}^{s}	subgrid-scale Reynolds stress	[N/m^2]
τ_{w}	wall shear stress	[N/m^2]
ϕ	general variable / eigenfunction	
ϕ_f	value of ϕ at each face of control-volume	
$\vec{\phi}_i$	spatial basis function vector	[−]
$\phi_{x,\,i}$	streamwise component of spatial basis function	[−]
χ	ratio of $\tilde{\nu}$ to ν	[−]
ψ'	perturbation stream function	[m^2/s]
ω	complex frequency	[rad/s]
ω_i	non-dimensional vorticity ($\equiv \{\partial u_k/\partial x_j - \partial u_j/\partial x_k\} d/U_\infty$)	[−]
ω_i	imaginary part of complex frequency ω	[rad/s]
ω_i^0	ω_i value at branch point of dispersion relation	[rad/s]

ω_r	real part of complex frequency ω	[rad/s]
ω_r^0	ω_r value at branch point of dispersion relation	[rad/s]
Ω	rotation parameter	[1/s]
Ω_{ij}	mean rotation-rate tensor	[1/s]

Subscripts

c	critical value
i, j, k	Cartesian tensor indices* ($i = 1$, 2 and 3, *etc.*) 1: streamwise (x) direction 2: lateral (y) direction 3: spanwise (z) direction *Einstein summation convention is applied
P	value at centre of each control-volume

Superscripts

k	value at time instant $t = t_k$
n	value at time instant $t = t_n$

Glossary

2D	Two-dimensional
3D	Three-dimensional
AMG	Algebraic multigrid method
CCD	Charge coupled device
CFD	Computational fluid dynamics
CFL	Courant-Friedrichs-Levy
DES	Detached-eddy simulation
DNS	Direct numerical simulation
Exp.	Experiments
FST	Free-stream turbulence
FVM	Finite volume method
LES	Large-eddy simulation
LES-NWM	LES with near-wall modelling
LES-NWR	LES with near-wall resolution
LS k-ϵ	Low Reynolds number k-ϵ model of Launder and Sharma
LSE	Linear stochastic estimation
PIV	Particle image velocimetry
POD	Proper orthogonal decomposition
RANS	Reynolds-averaged Navier-Stokes
S-A	Spalart-Allmaras model
SAS	Scale-adaptive simulation
SFV	Surface flow visualisation
SIMPLE	Semi-implicit method for pressure-linked equations
SST	Shear-stress-transport model
TLA	Trip-less approach
TrSL	Transition-in-shear-layers (or subcritical) flow regime
TrSL2	Intermediate-subcritical flow regime
TrSL3	Upper-subcritical flow regime
URANS	Unsteady Reynolds-averaged Navier-Stokes
VIV	Vortex-induced vibration
WFV	Wake flow visualisation
YAG	Yttrium aluminium garnet

Chapter 1

Introduction

1.1 Introduction

All solid objects in our daily lives are exposed to air, water, and other kinds of fluids, and most of them are *bluff bodies* (or non-streamlined bodies) in terms of fluid mechanics. Flow past bluff bodies contains a variety of fluid-dynamic phenomena, such as *separation*, *vortex shedding*, and the transition to *turbulence*, all of which are of fundamental interest as well as of great importance in many practical applications. In particular, the vortex shedding from bluff bodies has been the subject of a number of studies as it may significantly affect various fluid-mechanical properties of practical importance, such as flow-induced forces, vibrations and noise, and the efficiencies of heat and mass transfer.

To study the complex physics of bluff body flows systematically, it is natural to focus on bodies of simple two-dimensional shapes such as circular and square cylinders. Although the instantaneous flow structures observed there are still three-dimensional and rather complicated except for very low Reynolds number (Re) cases, the flow behind two-dimensional bluff bodies, or the (nominally) two-dimensional *wake*, is one of the most basic or 'canonical' flows in fluid mechanics. In fact, the flow past cylinders has been investigated by many researchers so far (as will be reviewed later in Section 1.4.2) since this flow configuration is of direct relevance to many practical applications, e.g., tall buildings, bridge towers, struts, aerial and submarine cables, pipelines, cooling towers, and heat exchanger tubes.

When given a circular cylinder with its axis perpendicular to fluid flow, von Kármán-type (asymmetric, alternating) vortex shedding may or may not occur behind the cylinder. As will be described later in Section 1.4.2, the characteristics of the flow (and hence also of the force acting on the cylinder) are mainly governed by the Reynolds number; the von Kármán-type vortex shedding occurs when the Reynolds number exceeds a critical value of about 50 for a circular cylinder in a free stream, for example. There are, however, many situations where this type of vortex shedding may cease even at much higher Reynolds numbers, and one of the simplest (but its mechanisms are still unclear) is when a cylinder is located near a plane boundary or 'ground' — the focus of the present study is on this flow configuration.

Earlier studies have shown that the characteristics of the flow in this case are governed not only by the Reynolds number but also by the gap ratio h/d, where h is the gap distance between the cylinder and the ground and d is the diameter of the cylinder. For example,

Bearman and Zdravkovich (1978) have reported that the von Kármán-type vortex shedding was suppressed when h/d was less than about 0.3 for a circular cylinder placed near a fixed plane ground. However the effect of h/d, or the *ground effect*, is in general very complicated and still far from being fully understood, mainly because it can be significantly affected by the state of the *boundary layer* on the ground (e.g., Hiwada *et al.* 1986; Lei *et al.* 1999; see Section 1.4.3 for more details).

The main idea underlying the present study (especially for the experimental part of the study in Chapter 2) is to place a cylinder near a ground running at the same speed as the free stream, so that substantially no boundary layer develops on the ground. The concept of such a *moving ground* has been widely used in the field of vehicle aerodynamics, especially of high-performance racing cars, to properly consider the influence of the ground in the frame of reference of moving vehicles (Bearman 1980; Zhang *et al.* 2006). This, however, has rarely been applied to the study of flow past cylinders. By using a moving ground in a series of wind tunnel tests, some fundamental aspects of the ground effect (that are otherwise obscured by the influence of the boundary layer) are experimentally observed in this study.

The cessation of the large-scale, von Kármán-type vortex shedding in this flow configuration is of special interest in the respect that it may be observed not only in laminar (or low Reynolds number) but also in turbulent (or high Reynolds number) cases, depending on the single geometric parameter h/d. This flow may therefore serve as a simple but challenging test case for numerical simulation. In fact, the flow past a circular cylinder at high Reynolds numbers of about 10^4 or above is still a challenging subject in today's computational fluid dynamics (CFD) even if the cylinder is outside the ground effect, since the direct numerical simulations (DNS) of the Navier-Stokes equations for such flows are currently not feasible due to the huge computational costs required (Spalart 2000). However, as will be reviewed later in Section 1.4.5, recent studies have shown that the unsteady motion of the vortex shedding behind a cylinder can be reasonably predicted, with acceptable computational costs, by using some novel techniques such as unsteady Reynolds-averaged Navier-Stokes (URANS) simulations and detached-eddy simulations (DES). It is therefore of great interest to see if these numerical simulations can correctly predict the cessation of the large-scale vortex shedding in ground effect, which is also investigated in this study.

The use of the moving ground in this study also gives us a very interesting and essential question, i.e., the cause of the cessation of the vortex shedding in ground effect. Basically the flow through the gap between the cylinder and the moving ground is not blocked but slightly accelerated when the vortex shedding ceases (see Chapter 2 for more details), and hence the cessation of the vortex shedding in this case cannot be explained by the blockage of the gap flow. In general, the formation of von Kármán-type vortices behind a cylinder is considered to be due to *wake instability* somehow caused by a communication between the two shear layers separated from the cylinder. This can be confirmed, for example, by the cessation of the shedding behind a cylinder equipped with a backward splitter plate of sufficient length, which was first experimentally observed by Roshko (1955). Recent studies have shown that the vortex shedding is explained by *absolute instability* in the near wake, which allows local disturbances to propagate both upstream and downstream and thus produces a resonance

between the travelling *instability waves* (Huerre and Monkewitz 1990; Oertel 1990). From this point of view, it can be concluded that the splitter plate mentioned above suppresses the vortex shedding as the plate restricts the propagation of disturbances in the near wake region. Of interest here is that a similar explanation might also be applicable to the cessation of the vortex shedding in ground effect, i.e., the existence of the nearby ground does not block the gap flow but does somehow restrict the propagation of disturbances in the near wake region and thus prevents the resulting von Kármán-type vortex shedding. This issue is also examined, based on linear stability theory, in this study.

While the mechanisms of the wake instability are still not totally understood and many investigations are still ongoing on such essential issues, another interest in the field of bluff body aerodynamics in recent years is the development of control or suppression systems of vortex shedding. In particular, the von Kármán-type vortex shedding from a circular cylinder has been attracting the attention of many researchers as a simple but challenging test case for active feedback flow control. One of the biggest issues in the development of such feedback flow control systems is to reduce the huge amount of information concerning the flow field to be dealt with in real time, and a possible solution to this issue is to use 'low-dimensional' or 'reduced-order' techniques based on, e.g., the proper orthogonal decomposition (POD) method (Holmes *et al.* 1996). Recent studies have shown that the vortex shedding from a cylinder could be adequately controlled based on rather limited information about energetically dominant flow structures obtained by the POD, but only in the laminar regime so far (see Section 1.4.7 for more details). Against this background, the POD analysis is also performed in this study on the experimental and computational data obtained in the turbulent regime. Although the development of practical flow control systems is outside the scope of the present study, the POD analysis of the turbulent near wake of the cylinder in ground effect, especially in the intermediate gap regime where the vortex shedding becomes intermittent, might provide an illustration of the capability of the POD-based low-dimensional techniques to capture the onset/cessation of the turbulent vortex shedding.

The flow past a cylinder near a moving ground investigated in this study contains many fundamental aspects of general bluff body flows. It is the author's hope that this combined experimental, computational and theoretical study will contribute to a better understanding of the complex physics of bluff body flows as well as to a further development of various practical applications in this field.

1.2 Objectives of the study

The main objectives of the present study are summarised as follows:

1. To observe experimentally the fundamental aspects of the flow past a circular cylinder in ground effect, where a moving ground is used instead of a fixed ground in order to avoid the confusing effects of the boundary layer developing on the ground.

2. To examine the capability of DES and URANS simulations to predict correctly the flow past a circular cylinder in ground effect, by comparing with the experimental results.

3. To discuss the mechanisms of the cessation of the von Kármán-type vortex shedding in ground effect from the viewpoint of linear stability theory.

4. To investigate further the near wake structure of the cylinder in ground effect by using the POD method, and to demonstrate the capability of the POD-based low-dimensional techniques to capture the onset/cessation of the turbulent vortex shedding.

1.3 Outline of the thesis

This thesis is composed of six main chapters. In the remainder of this introductory chapter, an extensive review is given on earlier studies on the flow past cylinders, including those in ground effect. Also some basic concepts and recent progress of numerical simulations, linear stability analysis, and POD analysis are summarised in this chapter with a major focus on their applications to the flow past cylinders.

In Chapter 2, the results of wind tunnel experiments are presented. A distinctive, critical drag reduction of a circular cylinder in ground effect is observed due to the use of a moving ground, and this is found to be directly related to the cessation of von Kármán-type vortex shedding in the near wake region of the cylinder.

In Chapter 3, the results of numerical simulations are presented. It is shown that DES capture the cessation of the vortex shedding and the attendant drag reduction of the cylinder in a physically reasonable h/d range, whereas URANS simulations predict them in a much smaller h/d range. The reason of this 'delayed' cessation of vortex shedding in the URANS solutions is also discussed in this chapter.

In Chapter 4, the mechanisms of the cessation of von Kármán-type vortex shedding in ground effect are further investigated using a linear stability analysis. An analytical model of general two-dimensional wakes in ground effect is proposed, and its fundamental stability characteristics are examined in detail. The results are then compared with the experiments and numerical simulations to show that the cessation of the vortex shedding in ground effect may indeed be explained by changes in the stability characteristics of the near wake.

In Chapter 5, the POD is applied to the results of the experiments and numerical simulations to investigate further the near wake structure of the cylinder in ground effect. It is shown that the von Kármán-type vortex shedding is still energetically dominant even in the fully turbulent wake and hence can be roughly reproduced by the combination of only a small number of POD modes, suggesting the promise of POD-basis low-dimensional techniques for the control of turbulent vortex shedding.

In Chapter 6, a concluding summary of the entire study is presented, followed by some recommendations for future work in this research field.

1.4 Literature review

1.4.1 Overview

In general, the configuration or type of flow past cylinders can be classified by the following: the *shape* of cylinders, the *number* and *arrangement* of cylinders, and the type of *surrounding* in which the cylinders are placed. Figure 1.1 illustrates some examples of the flow around cylinders.

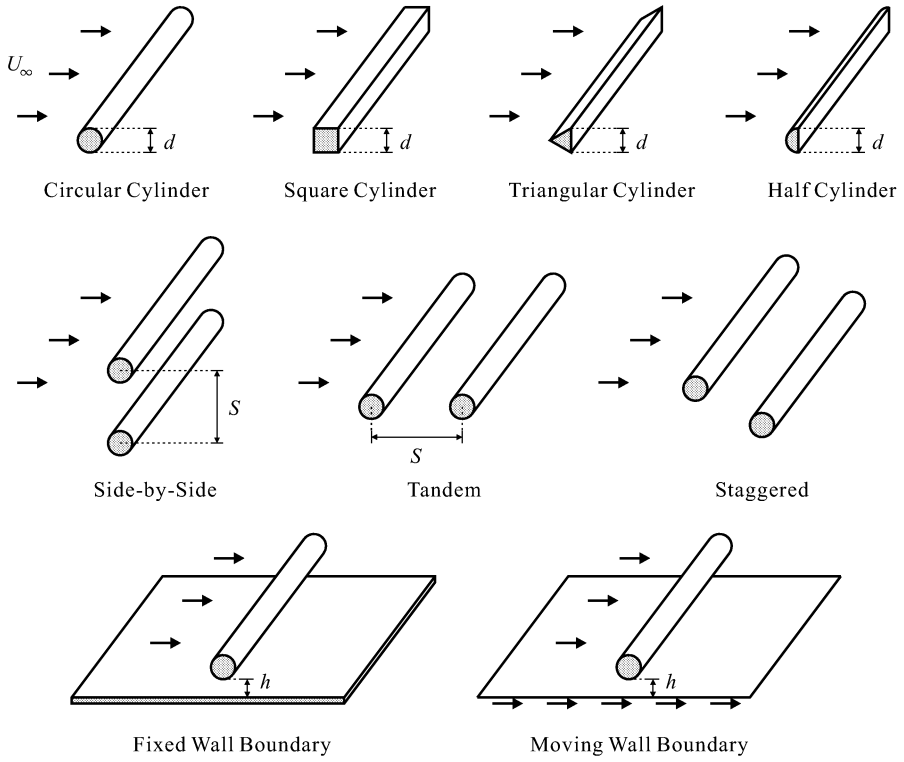

Figure 1.1: Examples of flow past cylinders.

For the shape of cylinders, a number of studies have been performed so far on *circular* cylinders (as will be reviewed in Sections 1.4.2 and 1.4.3), whereas cylinders of different cross-sectional shapes, such as *square*, *triangular* and *half-circular*, have also been widely studied (as will be reviewed in Section 1.4.4). As concerns the number and arrangement of cylinders, though outside the scope of the present study, flows around two cylinders arranged in *side-by-side*, *tandem*, and *staggered* arrangements have often been studied as the basic components of general multi-cylinder flows; a review on this topic (but only for circular cylinders) has been given by Zdravkovich (2003).

In terms of the surrounding of cylinders, most investigations may be classified as either *unbounded* or *wall-bounded* cases. In the latter category, several studies have focused on a cylinder placed near and parallel to a *fixed* wall boundary or ground, whereas only a few have been reported so far on a cylinder placed near a *moving* ground (as will be reviewed in Sections 1.4.3 and 1.4.4). In addition to these, differences in the *incoming-flow profile* also

give a variation of the flow configuration. *Uniform cross-flow* is the most fundamental and well-studied incoming-flow condition, whereas *uniform shear* and/or *oblique flows* have also been examined by many researchers; reviews on these topics (but only for circular cylinders) have been given by Zdravkovich (1997, 2003).

Apart from the differences in the flow configuration described above, the global state or pattern of the flow past cylinders generally depends on a variety of *influencing parameters* (Zdravkovich, 1997). For a long circular cylinder placed in a free stream (i.e., uniform cross-flow), for example, the most dominant influencing parameter, or the *governing parameter*, is the Reynolds number Re ($\equiv U_\infty d/\nu$, where U_∞, d and ν are the free-stream velocity, cylinder diameter and the kinematic viscosity of fluid, respectively). The state of flow past a circular cylinder may be classified by Re into four fundamental regimes: subcritical, critical, supercritical and postcritical regimes, the details of which will be described in the next section. In most practical cases, however, other influencing parameters may also have major effects on the flow pattern. Those parameters include the level of *free-stream turbulence* (FST), the *surface roughness* of the cylinder, and the *aspect ratio* of the cylinder. In addition to these, for the wall-bounded cases, the *gap-to-diameter ratio* (or the '*gap ratio*' for short) h/d also has a significant influence on the flow pattern.

The flow around cylinders may be investigated by several different approaches, i.e., *experimental*, *computational*, and *theoretical* approaches. In the following, earlier experimental works will be reviewed first for each type of flow configuration, and then some of the other approaches (numerical simulation, linear stability analysis, POD analysis) will be reviewed with a focus on their applications to the flow past cylinders.

1.4.2 Circular cylinders in a free stream

A single circular cylinder placed in a free stream is one of the most fundamental subjects in bluff body aerodynamics. In the following, the fundamental effects of the Reynolds number on this flow are reviewed first with some historical perspective, and then further details are described for the 'upper-subcritical' Reynolds number regime, in which the present study is performed. Finally, the effects of other influencing factors, such as the level of free-stream turbulence and the aspect ratio of a cylinder, are also reviewed.

Flow regimes based on the Reynolds number (with historical perspective)

Since the early twentieth century the flow past a circular cylinder has been studied by many researchers. It was already well known in the early years that, due to the principle of *flow similarity* first studied in 1883 by Osborne Reynolds (see, e.g., von Kármán 1954, p.73), the characteristics of the flow past a cylinder and also of the flow-induced forces on a cylinder might be expressed as functions of the Reynolds number, Re, of the flow. In particular, the influence of the Reynolds number on the drag acting on a cylinder had attracted the interest of many researchers in the early years.

One of the most significant results on this issue was first published by Wieselsberger in 1922 (see Schlichting 1979, p.17), who performed mean drag measurements on cylinders of various diameters thereby covering a wide Reynolds number range of $4 < \mathrm{Re} < 8 \times 10^5$.

The drag (or, to be precise, the drag coefficient C_D) was found to suddenly decrease at the Reynolds number of about 2 to 5×10^5, i.e., the 'critical' Reynolds number Re_c. According to Zdravkovich (1997, p.6), Wieselsberger had already suggested in 1914 that a similar 'drag crisis' found on spheres was related to the transition to turbulence near the separation line. Then Taylor, who observed a drastic change in pressure distribution around a cylinder near the critical Reynolds number, suggested in 1916 that the drag crisis of the cylinder was also related to the transition to turbulence. The pressure distribution on a cylinder around Re_c was then further investigated by Flachsbart in 1932 (see Schlichting 1979, p.21) to describe the mechanism of the critical drag reduction.

Following these experimental results in the early years, it had become widely accepted that the flow past a circular cylinder could be classified into three fundamental regimes, i.e., 'subcritical' ($\mathrm{Re} < \mathrm{Re}_c$), 'critical' ($\mathrm{Re} \simeq \mathrm{Re}_c$), and 'supercritical' ($\mathrm{Re} > \mathrm{Re}_c$) regimes. The main features of these three flow regimes may be summarised as follows:

- Subcritical ($\mathrm{Re} < \mathrm{Re}_c$): The boundary layer on the cylinder remains laminar and the transition to turbulence occurs after the flow separation. At higher Reynolds numbers of about 2×10^4 to 2×10^5, for example, a sudden burst to turbulence occurs in the separated free shear layers, which then roll up to form turbulent von Kármán-type vortices. It follows that a wide turbulent wake is formed behind the cylinder and the mean drag coefficient C_D shows a higher value of about 1.2.

- Critical ($\mathrm{Re} \simeq \mathrm{Re}_c$): The transition to turbulence occurs just after the separation and the separated flow reattaches subsequently, i.e., *separation-reattachment bubbles* are formed on the cylinder. This leads to a narrowing of the wake, an increase in the base pressure C_{pb}, and consequently a significant drop of C_D to about 0.3.

- Supercritical ($\mathrm{Re} > \mathrm{Re}_c$): The von Kármán-type vortex shedding ceases as the location of the transition to turbulence moves further upstream and the separation bubbles are irregularly fragmented along the span of the cylinder. The width of the wake gently increases and thus C_D gently recovers as the Reynolds number increases.

These critical phenomena, however, had not been clarified in detail in the early studies, and therefore the supercritical regime had generally been considered to begin just after the critical drop of C_D, at which the von Kármán-type vortex shedding had also been considered to cease. Later, Bearman (1969) found that the von Kármán-type vortex shedding could still continue, after the critical drop of C_D, up to the Reynolds number of at least 5.5×10^5 (note that the critical drop of C_D occurs with the formation of the separation bubbles, whereas the cessation of the vortex shedding occurs due to the fragmentation of the separation bubbles), and proposed that the cessation of the vortex shedding should be taken as a criterion of the upper-end of the critical regime.

In addition to the above three fundamental regimes, Roshko (1961) discovered the fourth regime at $\mathrm{Re} > 3.5 \times 10^6$, which was referred to as 'transcritical' at that time and is now generally known as 'postcritical' regime. The main features of the postcritical regime may be summarised as follows:

- Postcritical ($\mathrm{Re} > 3.5 \times 10^6$): The transition to turbulence occurs before the separation all along the cylinder span and the separation bubbles totally disappear. The regular vortex shedding reappears and the wake becomes wider than that in the critical and supercritical regimes (but still narrower than that in the subcritical regime). It follows that C_D shows an intermediate value of about 0.7.

Roshko (1961) noted in his article that '*it seems unlikely that there will be any further transitions, since the point of boundary-layer transition can now only move smoothly forward on the cylinder*' as Re increases. In a theoretical sense, there might be an ultimate state of flow for $\mathrm{Re} \to \infty$, where all flow regions around the cylinder are turbulent. However, it is hardly possible to verify this state because the effects of compressibility cannot be avoided at such high Reynolds numbers.

More recently, Roshko (1993) and Williamson (1996) proposed more detailed definitions of the Re-based flow regimes, with thorough reviews on the flow physics especially for lower Reynolds number regimes. Another comprehensive classification of the flow was presented by Zdravkovich (1997), who classified the flow into five regimes, i.e., fully laminar (L), transition-in-wake (TrW), transition-in-shear-layers (TrSL), transition-in-boundary-layers (TrBL) and fully turbulent (T) regimes, as shown in Fig. 1.2 [reproduced from Zdravkovich (1997)]. Note that, in this classification, the TrSL regime is subdivided into three regimes: 'lower' (TrSL1),

STATE		REGIME		*Re* RANGES
L	LAMINAR	1	NO-SEPARATION	0 to 4–5
		2	CLOSED WAKE	4–5 to 30–48
		3	PERIODIC WAKE	30–48 to 180–200
Tr W	TRANSITION IN WAKE	1	FAR-WAKE	180–200 to 220–250
		2	NEAR-WAKE	220–250 to 350–400
Tr SL	TRANSITION IN SHEAR LAYERS	1	LOWER	350–400 to 1k–2k
		2	INTERMEDIATE	1k–2k to 20k–40k
		3	UPPER	20k–40k to 100k–200k
Tr BL	TRANSITION IN BOUNDARY LAYERS	0	PRECRITICAL	100k–200k to 300k–340k
		1	SINGLE BUBBLE	300k–340k to 380k–400k
		2	TWO-BUBBLE	380k–400k to 500k–1M
		3	SUPERCRITICAL	500k–1M to 3.5M–6M
		4	POSTCRITICAL	3.5M–6M to (?)
T	FULLY TURBULENT	1	INVARIABLE	(?) to ∞
		2	ULTIMATE	

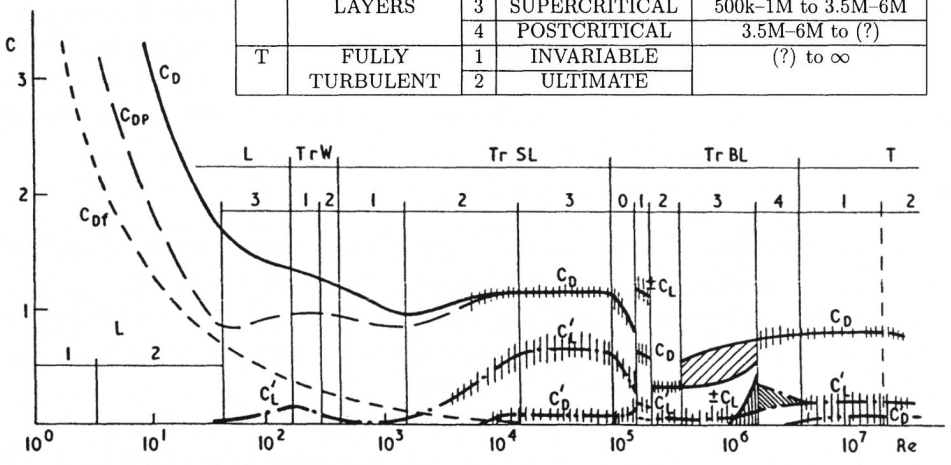

Figure 1.2: Reynolds number effects on the drag and lift coefficients of a circular cylinder in a free stream [reproduced from Zdravkovich (1997)]. C_{Df} and C_{Dp} are the friction and pressure drag coefficients, respectively.

'intermediate' (TrSL2) and 'upper' (TrSL3) sub-regimes, all of which are contained in the subcritical regime described on Page 7. Meanwhile, the TrBL regime is subdivided into five regimes: 'precritical' (TrBL0), 'single bubble' (TrBL1), 'two-bubble' (TrBL2), 'supercritical' (TrBL3) and 'postcritical' (TrBL4) sub-regimes, where the TrBL0 to TrBL2 regimes correspond to the critical regime described on Page 7.

Upper-subcritical regime (TrSL3)

Among the flow regimes listed above, the upper-subcritical or TrSL3 regime ($2 \sim 4 \times 10^4 < \mathrm{Re} < 1 \sim 2 \times 10^5$) is one of the most intensively studied regimes because of its practical importance in many engineering applications. Also of interest is that the flow pattern is less sensitive to the Reynolds number and hence the fluid-dynamic properties such as C_D and C_{pb} are almost constant in this Reynolds number regime, which is advantageous for researchers who want to reveal the effects of other influencing factors on the flow physics.

This quasi-invariable nature observed in the TrSL3 regime is mainly due to the less sensitivity of the transition point, and also of the first *vortex formation length*, to the Reynolds number. In the intermediate-subcritical or TrSL2 regime ($1 \sim 2 \times 10^3 < \mathrm{Re} < 2 \sim 4 \times 10^4$), the transition point moves upstream and the vortex formation length L_f decreases as the Reynolds number increases (Bloor 1964; Kourta *et al.* 1987). The decrease in L_f leads to a decrease in C_{pb} — since '*the growing vortices draw in fluid from the base region and it is this continual entrainment process that sustains the low base pressure*' as suggested by Bearman and Trueman (1972) — and hence to an increase in C_D in this flow regime. In the TrSL3 regime, however, the transition to turbulence is reduced to a sudden burst occurring in the free shear layers close to the cylinder (i.e., before the formation of the first vortex), and the vortex formation region does not move any closer to the cylinder.

As concerns the vortex formation length L_f, several different definitions have been used to date. Bloor (1964) detected the end of the formation region by the disappearance of low-frequency fluctuations in the wake. In contrast, Bearman (1965) proposed, in his investigation on the wake of a half elliptic cylinder, that the position in the wake at which the velocity-fluctuation peak occurred could be regarded as the position of the first fully-formed vortex; similar ideas have also been proposed for a circular cylinder by Gerrard (1965) and Griffin and Votaw (1972). Meanwhile, Roshko (1993) discussed the relation between C_{pb} and the mean *recirculation length*, L_r, which is simply defined by the distance from the centre of the cylinder to the position where the mean streamwise velocity becomes zero and might be used as an alternative to the formation length L_f. Recent experiments have shown that L_r in the TrSL3 regime is about $1.2d$ (Cantwell and Coles 1983; Braza *et al.* 2006)

Although the vortex formation length is less sensitive to the Reynolds number and is constant along the cylinder span in the mean sense, the instantaneous size and shape of the vortex formation region varies along the cylinder span and also from cycle to cycle of the vortex shedding in the TrSL3 regime (Toebes 1969; Shimizu and Kawamura 1972; Szepessy and Bearman 1992). For example, Shimizu and Kawamura (1972) reported that the spanwise correlation length of the streamwise velocity in the near wake region ($2d$ downstream) decreased from more than $10d$ in the TrSL2 regime to about $4d$ in the TrSL3 regime.

Due to the random or turbulent characteristics in the near wake region, the flow-induced force on a circular cylinder also irregularly fluctuates in the TrSL3 regime. Drescher (see Zdravkovich 1997, p135) reported a simultaneous measurement of instantaneous pressures at eleven points around a circular cylinder at $\mathrm{Re} = 1.13 \times 10^5$ and thus showed the mechanisms of C_D and C_L variations during a cycle of the vortex shedding. Basically, C_D fluctuates at double the vortex shedding frequency whilst C_L fluctuates at the same frequency as the vortex shedding. Due to the irregularity of the vortex formation, however, the fluctuations of C_D and C_L are significantly modulated (Humphreys 1960). The Strouhal number St of the vortex shedding is about 0.2 and the root-mean-square values of the force fluctuations, C'_D and C'_L, are about 0.05 and 0.5, respectively, in the TrSL3 regime.

Whilst the variations of C_D and C_L almost entirely come from the change in the pressure distribution, the skin friction distribution around a cylinder is also of interest for the study of the characteristics of the flow, especially of the flow separation points. Achenbach (1968) measured skin friction distributions around a circular cylinder at several different Reynolds numbers; at $\mathrm{Re} = 1.0 \times 10^5$ (TrSL3 regime) the mean separation angle θ_{sep} was found to be 78°, which was much smaller than that of 147° at $\mathrm{Re} = 8.5 \times 10^5$ (critical or TrBL2 regime) and also of 115° at $\mathrm{Re} = 3.6 \times 10^6$ (postcritical or TrBL4 regime). As concerns the fluctuation of the separation points, Dwyer and McCroskey (1973) reported time-resolved skin friction distribution on a circular cylinder at $\mathrm{Re} = 1.06 \times 10^5$.

For the unsteady characteristics of the turbulent near wake of a cylinder, an extensive investigation was carried out by Cantwell and Coles (1983), who measured instantaneous velocity fields behind a cylinder at $\mathrm{Re} = 1.4 \times 10^5$ using a flying-hot-wire technique. They showed a sequence of phase-averaged pictures of the flow and thus examined the topology of the statistically periodic vortex shedding behind the cylinder. In recent years, the complex three-dimensional near wake structures have been investigated in more detail by means of particle image velocimetry (PIV) techniques. Most of the earlier studies with PIV have been performed at Reynolds numbers lower than those for the TrSL3 regime, e.g., at Re of about 500 by Wu *et al.* (1996) and also of 1×10^4 by Chyu and Rockwell (1996). However, owing to the improvement of both spatial and temporal resolutions of PIV systems in recent years, the wake structures at high Reynolds numbers have also begun to be investigated, for example at $\mathrm{Re} = 1.4 \times 10^5$ by Djeridi *et al.* (2003) and Braza *et al.* (2006).

Effects of free-stream turbulence (FST)

In general, the characteristics of flow past a circular cylinder cannot be determined solely by the Reynolds number; one of the other important parameters is the level of free-stream turbulence (FST). In fact, most of the earlier experiments have been performed in wind or water tunnels with relatively low levels of FST, and nevertheless substantial discrepancies often exist among the results due to the differences in FST. It should also be noted that the level of FST has a significant role in many practical applications, where relatively high levels of FST are often encountered.

The level of FST can be statistically quantified by the *intensity* and *length scale* of turbulence in a free stream. The intensity of turbulence is usually defined as the ratio of the

root-mean-square (r.m.s.) value of the streamwise velocity fluctuations, $(\overline{u'^2})^{\frac{1}{2}}$ or u' for short, to the mean free-stream velocity U_∞, whereas the length scale may be defined by the longitudinal or streamwise integral length scale L_x, which is defined as

$$L_x = \int_{x_0}^{\infty} \overline{u'(x_0)u'(x)} \,/\, \left(\overline{u'(x_0)^2}\,\overline{u'(x)^2}\right)^{\frac{1}{2}} dx\,, \tag{1.1}$$

where $u'(x_0)$ and $u'(x)$ are the fluctuations of streamwise velocities at two points separated by a distance $(x - x_0)$ in the streamwise direction. A further discussion on the definitions of the intensity and length scale of FST can be found in Bearman and Morel (1983).

A remarkable effect of FST can be seen on the critical Reynolds number Re_c. Fage and Warsap (see Zdravkovich 1997, p.446) measured drag on a circular cylinder placed behind a rope netting with various distances thereby producing various levels of FST; the critical Reynolds number decreased as the intensity of FST increased. This is because the FST has an effect of promoting the transition to turbulence especially in the free sheer layers.

As concerns the scale of FST, Surry (1972) measured the mean C_D and C_p distributions on a circular cylinder with two different L_x/d of 0.36 and 4.3 coupled with a high intensity of $u'/U_\infty = 0.1$. The Reynolds number was about 4×10^4, which lies in the TrSL3 regime (if the FST is sufficiently low). The large-scale FST had no appreciable effect on the force characteristics of the cylinder, whereas the small-scale FST made the force characteristics similar to those for the precritical (TrBL0) regime. This implies that the scale of FST needs to be small enough in order to affect the flow in the TrSL3 regime, since the laminar part of the free shear layers to be affected by the FST is very short in the TrSL3 regime.

Since the flow past a circular cylinder is affected by both the intensity and scale of FST, many researchers have attempted to analyse their experimental results in terms of the two parameters combined. Among them, Bearman (1968) showed that the critical Reynolds number Re_c could be expressed as a function of a turbulence parameter $(u'/U_\infty)/(L_y/d)^{\frac{1}{5}}$, where L_y is the lateral integral scale of the streamwise components of FST. This type of parameter is often referred to as the Taylor number, since a similar parameter was first proposed by Taylor in 1936 (see Bearman and Morel 1983). The Taylor number, however, was originally derived through physical arguments on the problems of 'attached' boundary-layer transition, and therefore Bearman and Morel (1983) noted that the drag reduction of cylinders, which is triggered by the early transition in the 'separated' free shear layers, could not be meaningfully analysed with the Taylor number.

Effects of cylinder aspect ratio and spanwise-end condition

Two other common influencing factors for the flow past a circular cylinder are the aspect ratio of the cylinder l/d, where l is the cylinder length, and the spanwise-end condition of the cylinder. Considering a closed test section in a wind or water tunnel, the spanwise-end conditions may be categorised into the following three groups: (i) free-ends, (ii) closed-ends, and (iii) ends equipped with end-plates.

For the case of free-ends, i.e., when a cylinder of finite length is isolated in a flow rather than connected to walls/plates, the aspect ratio of the cylinder significantly affects the flow characteristics since strong swirling flows are induced around the free-ends. Wieselsberger

(see Zdravkovich *et al.* 1989; see also Goldstein 1965, p.439) measured mean drag on circular cylinders of various l/d; the drag coefficient decreased as l/d decreased below 40. This drag reduction can be explained by the inflow from the outside of the free-ends into the near wake region, increasing the base pressure of the cylinder. A strong 'disturbing' effect of free-ends on the two-dimensionality of the flow has been observed by Fox *et al.* (1993), who measured a spanwise pressure distribution on a long cantilevered circular cylinder and showed that the disturbing effect could extend to a distance of $20d$ from the free-end.

Also for the case of closed-ends, i.e., when a cylinder is directly connected to the walls of a test section, the flow characteristics could be affected by the aspect ratio of the cylinder. This is because the so-called *horseshoe-vortices* (Baker 1979, 1980) are formed around the closed-ends, which may significantly disturb the two-dimensionality of the flow if the aspect ratio of the cylinder is not large enough. In general, using end-plates of an appropriate size is an effective way to minimise the end effects of cylinders of small aspect ratios. Stansby (1974) investigated the effects of rectangular end-plates of different size on the spanwise distribution of C_{pb} on circular cylinders of $l/d = 8$ and 16, and concluded that rectangular end-plates of suitable size could ensure nearly two-dimensional flows around the cylinders. More details on the end-plates recommended by Stansby will be described later in Chapter 2.

Effects of other influencing parameters

In addition to Re, FST, l/d and the spanwise-end condition described above, there are still many influencing parameters for the flow past a circular cylinder. These parameters include the surface roughness and vibration of the cylinder. The type of the incoming flow, e.g., shear flows and oblique flows, may also be considered as one of those parameters.

The surface roughness of a cylinder may be quantified by the *relative roughness* K/d, where K is the average height of excrescences, and also by the *texture* of the roughness. The texture here means the shape and distribution pattern of the excrescences. An extensive investigation of the effects of the surface roughness was first reported by Fage and Warsap (see Zdravkovich 2003, p.751), who showed that the critical Reynolds number Re_c decreases as K/d increases (see also Guven *et al.* 1980). The shift of the critical regime toward lower Re due to the surface roughness was also confirmed through the measurements of C_p and C_f distributions by Achenbach (1971). Another important effect of the surface roughness is to narrow down the range of the critical and supercritical regimes as the roughness disturbs the formation of the separation bubbles (Buresti 1981).

The effects of the vibration of cylinders on the flow are in general very complicated as the vibration may be induced by the unsteady flow field itself, i.e., the movements of fluid and cylinders interact with each other. Such *flow-induced* or *vortex-induced vibration* (VIV) has been the subject of a number of studies and has been reviewed by many authors, e.g., Williamson and Govardhan (2004). Since VIV is outside the scope of the present study, further descriptions on this topic are not provided here.

Although most of the earlier studies have been conducted in a free stream or a uniform cross-flow, there have been several investigations with other types of incoming flows, such as shear flows and oblique flows. The effects of shear flows on a circular cylinder are reviewed

by Zdravkovich (1997), and those of oblique flows are also reviewed by Zdravkovich (2003). These topics are outside the scope of the present study and are thus not described here. It should be noted, however, that a cylinder placed in a shear flow is of some relevance to that submerged in a thick boundary layer formed on a fixed nearby ground, which is reviewed in the next subsection.

1.4.3 Circular cylinders in ground effect

The characteristics of flow past a circular cylinder placed near and parallel to a ground are largely determined by the Reynolds number and also the 'gap ratio,' i.e., the ratio of the gap distance between the cylinder and the ground, h, to the cylinder diameter d. However, the details of the effects of h/d, or the 'ground effect,' are still far from being fully understood because of other influencing factors, in particular the confusing effects of the boundary layer usually developing on the ground.

Below is a review of earlier experimental studies, most of which were carried out with a ground fixed relative to a cylinder and thus were subject to the influence of the boundary layer on the ground. Some fundamental effects of the gap ratio on the flow are summarised first, and then rather controversial results on the influence of the boundary layer developing on a fixed ground are reviewed. A summary of these studies is given later in Table 1.1.

Fundamental effects of the gap ratio

One of the earliest experiments on this topic was reported by Taneda (1965), who visualised the flow behind a circular cylinder towed through stagnant water close to a stationary ground (i.e., the water and ground moving together relative to the cylinder and hence substantially no boundary layer formed on the ground) at a very low Reynolds number of 170. The regular von Kármán-type vortex shedding occurred at $h/d = 0.6$, whereas only a weak single row of vortices was generated at $h/d = 0.1$. More details of the cessation of the regular vortex shedding behind a towed cylinder were later visualised by Zdravkovich (1985a) and Lin *et al.* (2005), but only at low Reynolds numbers of 3550 and 780, respectively.

Meanwhile, in the upper-subcritical (TrSL3) flow regime, Roshko *et al.* (1975) measured C_D and C_L of a cylinder placed near a fixed ground ($\mathrm{Re} = 2.0 \times 10^4$) and showed that C_D rapidly decreased and C_L increased as the gap ratio h/d was reduced to less than about 0.6 (as will be presented later in Figs. 2.6 and 2.8). The thickness of the boundary layer δ_B formed on the ground was $0.5d$ at the position of the cylinder in their study. Further investigations in the TrSL3 regime were conducted by Bearman and Zdravkovich (1978), who measured mean C_p distributions on a cylinder placed near a fixed ground ($\mathrm{Re} = 4.8 \times 10^4$, $\delta_B/d = 0.8$) and thus explained the variations of C_D and C_L in ground effect. It was demonstrated that the lower C_D for the smaller h/d cases was due to a higher base pressure, whereas the positive C_L was caused by a downward shift of the front stagnation point on the cylinder.

Bearman and Zdravkovich (1978) also measured velocity fluctuations in the near wake of the cylinder to study the variation of the vortex shedding frequency in ground effect. The Strouhal number St was found to be almost constant at 0.2 for all h/d down to 0.3, and the spectral peak disappeared for h/d of less than 0.3. This threshold gap ratio is often referred

to as the *critical gap ratio* $(h/d)_c$ for the cessation of the von Kármán-type vortex shedding in ground effect. It should be noted, however, that the disappearance of the spectral peak of the local velocity fluctuations in the near wake region does not necessarily coincide with the global cessation of the vortex shedding. Price *et al.* (2002) recently reported, for lower Reynolds numbers of 1200 to 1400, that the cessation of the vortex shedding was observed at $h/d \leq 0.375$ in their flow visualisation tests, but their hot-film anemometer indicated a reasonably strong periodicity even at $h/d = 0.125$.

Similar measurements of St and $(h/d)_c$ have also been carried out at higher and lower Reynolds numbers (Buresti and Lanciotti 1979; Angrilli *et al.* 1982; Grass *et al.* 1984). In particular, Buresti and Lanciotti (1979) measured the shedding frequency for two different types of cylinders, i.e., with smooth and roughened surfaces, placed near a fixed ground at higher Reynolds numbers of 8.5×10^4 to 3×10^5 ($\delta_B/d = 0.1$). For the smooth cylinder in the subcritical regime ($\mathrm{Re} \leq 1.9 \times 10^5$ in this case), the critical gap ratio $(h/d)_c$ was found to be 0.4, and St was about 0.2 for $h/d \geq 0.4$. The same results were also obtained for the roughened cylinder in the subcritical regime ($\mathrm{Re} \leq 1.4 \times 10^5$ in this case due to the roughened surface). However, for the roughened cylinder in the postcritical regime ($\mathrm{Re} \geq 2.4 \times 10^5$ due to the roughened surface), $(h/d)_c$ was found to be 0.3, i.e., slightly smaller than that in the subcritical regime, and St scattered within the range of 0.22 to 0.25.

Controversial results on the influence of the boundary layer

Although the fundamental effects of h/d were successfully observed by the above authors, the influence of the boundary layer developing on the ground is rather complicated and is still unclear despite several extensive investigations reported so far.

Zdravkovich (1985b) observed in his force measurements ($4.8 \times 10^4 \leq \mathrm{Re} \leq 3.0 \times 10^5$, $0.52 \leq \delta_B/d \leq 0.97$) that the rapid decrease in C_D occurred as the gap was reduced to less than the thickness of the boundary layer δ_B on the ground, and thus concluded that the variation of C_D was dominated by h/δ_B rather than by the conventional gap ratio h/d. He also noted that C_L could be significantly affected by the state of the boundary layer, though it was insensitive to the thickness of the boundary layer. When the cylinder was immersed in a rod-generated boundary layer, C_L showed an increase as h/d decreased to less than about 0.5, similar to the results by Roshko *et al.* (1975) reviewed above. For the cylinder immersed in a mesh-wire-generated boundary layer, however, negative C_L (i.e., downforce) of about -0.1 to -0.2 was obtained but only when h/d was around 0.5. Zdravkovich (1985b) argued that the difference in the C_L behaviour came from the difference in the mean velocity profile in the two different types of boundary layers. Such negative C_L values were also observed by Lei *et al.* (1999) at lower Reynolds numbers of 1.3 to 1.45×10^4. They noted, however, that the negative C_L might be attributed to the presence of their tripping device itself, which effectively changed the pressure distribution around the cylinder.

Meanwhile, Hiwada *et al.* (1986) measured the mean forces at $\mathrm{Re} = 2 \times 10^4$ with a wide δ_B/d range of $0.23 \leq \delta_B/d \leq 2.82$, where C_D decreased as h/d decreased and also as h/δ_B decreased. For the case of the smallest δ_B/d of 0.23, however, the decrease in drag started around $h/d = 0.5$, where the cylinder was still outside the thin boundary layer, suggesting

that the drag reduction could be caused not only by the direct interference of the boundary layer. Hiwada *et al.* (1986) also reported that the variations of C_L were quite similar to those by Roshko *et al.* (1975) and no negative C_L values were observed for all δ_B/d investigated. They also measured the vortex shedding frequency, and found the critical gap ratio $(h/d)_c$ to be 0.3 for all δ_B/d investigated. On this point, however, Lei *et al.* (1999) later observed that $(h/d)_c$ slightly decreased from 0.3 to 0.2 as δ_B/d increased from 0.14 to 0.48. Buresti and Lanciotti (1992) have also reported that $(h/d)_c$ slightly decreased from 0.4 to 0.3 as δ_B/d increased from 0.1 to 1.1 in their experiments.

More recently, Zdravkovich (2003) reported the drag behaviour for a cylinder placed near a moving ground (i.e., substantially no boundary layer on the ground) at a higher Reynolds number of 2.5×10^5. In contrast to all the investigations reviewed above, the decrease in C_D due to the decrease in h/d did not occur in his measurements. It has not been clear, however, whether this was attributed to the nonexistence of the boundary layer on the ground, or the higher Reynolds number that seems to be within the critical flow regime rather than within the subcritical flow regime, or any other influencing factors.

1.4.4 Non-circular cylinders in ground effect

The characteristics of flow past non-circular cylinders largely depend on their cross-sectional shapes, in addition to the governing/influencing parameters for circular cylinders reviewed in the previous subsections. In particular, the existence and location of sharp edges often have a significant influence on whether and where flow separation occurs, and thus on the wake characteristics as well as on the drag and lift forces acting on the cylinder.

Square cylinders in ground effect

Among non-circular cylinders of various cross-sectional shapes, square cylinders are one of the most widely studied. In general, the characteristics of flow past a square cylinder are significantly affected by the angle of attack (or incidence) α, but are not significantly affected by the Reynolds number since the flow separation points are fixed at the sharp edges of the cylinder. The effects of α on C_D, C_L, C_p and St have been investigated, but mostly in a free stream, by Vickery (1966), Lee (1975), and Obasaju (1983), among others.

As concerns the ground effect, a square cylinder with $\alpha = 0^\circ$ (i.e., two faces are normal and the other two are parallel to the incoming flow) has been the subject of several studies, e.g., at $\mathrm{Re} = 1.36 \times 10^4$ by Durao *et al.* (1991), at $\mathrm{Re} = 2.2 \times 10^4$ by Bosch *et al.* (1996), and at $\mathrm{Re} = 1.89 \times 10^4$ by Martinuzzi *et al.* (2003). A remarkable feature of their results was that there was little influence of δ_B/d on the critical gap ratio $(h/d)_c$, which was found to be about 0.3 to 0.4 for various boundary-layer thicknesses $0.13 < \delta_B/d < 1.5$. There was, however, an ambiguity in exactly identifying $(h/d)_c$ since the vortex shedding was found to be intermittent for gap ratios slightly larger than $(h/d)_c$ (Bosch *et al.* 1996; Martinuzzi *et al.* 2003). Martinuzzi *et al.* (2003) suggested that this intermittency of the vortex shedding, observed at $0.3 < h/d < 0.6$ in their study with $\delta_B/d = 0.5$, was due to the intermittency of the reattachment of the separated shear layer (from the bottom leading edge) on the bottom surface of the cylinder.

Martinuzzi *et al.* (2003) have also reported the mean and fluctuating forces on the square cylinder ($\mathrm{Re} = 1.89 \times 10^4$, $\delta_B/d = 0.5$), where three different h/d regimes were identified. For $h/d > 0.9$, the force coefficients were almost insensitive to the gap ratio. As h/d decreased from 0.9 to 0.4, the mean C_D monotonously decreased from 2.2 to 1.5 and also the mean C_L from -0.2 to -0.7. The fluctuations of C_D and C_L also decreased as h/d decreased in this h/d regime. Below $h/d = 0.4$, however, the mean C_L increased from -0.7 to about zero as the cylinder came close to the ground, whereas C_D continued to decrease to about 1.2. The fluctuations of C_D and C_L were found to be small in this h/d regime.

Other types of cylinders in ground effect

Everitt (1982) reported that the critical gap ratio $(h/d)_c$ for a flat plate placed normal to the incoming flow, which might be considered as an extreme case of rectangular cylinders with $\alpha = 0°$, was 0.55 for several different δ_B/d of 0.72 to 2.53. The Reynolds number based on the plate height d was 3.5×10^4. Meanwhile, Kamemoto *et al.* (1984) found $(h/d)_c$ for a normal flat plate and also for a triangular cylinder (with one edge turned upstream and one face turned downstream, cf. Fig. 1.1) to be 0.6 and 0.37, respectively ($\mathrm{Re} = 2.7 \times 10^4$, $\delta_B/d = 0.375$). Kamemoto *et al.* (1984) also reported that the mean C_D decreased as h/d decreased to less than about 1.0 for the normal flat plate, and less than about 0.7 for the triangular cylinder, respectively.

Kumarasamy and Barlow (1995) focused on a half-circular cylinder, with the flat surface turned downstream (cf. Fig. 1.1), placed near a fixed ground ($\delta_B/d = 0.1$). The Reynolds number was 4.67×10^5, which lies within the critical flow regime for a full-circular cylinder but the laminar separation bubbles are not formed in this case because of the truncated geometry of the cylinder. They reported that the critical gap ratio $(h/d)_c$ was 0.33, that is, the vortex shedding ceased when the cylinder was still outside the boundary layer on the ground. The effects of h/d on the pressure distribution around the cylinder were similar to those reported by Bearman and Zdravkovich (1978) for a circular cylinder; the base pressure increased and hence the drag decreased as h/d decreased.

More recently, Zhang *et al.* (2005) performed experiments on a half cylinder placed near a moving ground. The Reynolds number was $6.8 \times 10^4 \leq \mathrm{Re} \leq 1.7 \times 10^5$, in which range no appreciable effect of Re was found on the results. They found the critical gap ratio $(h/d)_c$ to be between 0.525 and 0.55. A noteworthy finding was that the mean C_D showed a sudden drop at the critical gap ratio, i.e., C_D was almost constant at 1.5 for $h/d > 0.55$ and at 1.0 for $h/d < 0.525$, in contrast to the gradual decrease in C_D usually observed near a fixed ground (for all types of cylinders as reviewed above). Zhang *et al.* (2005) also showed by using PIV measurements that the mean recirculation length L_r behind the cylinder was significantly elongated as h/d decreased from 0.55 to 0.525, corresponding to the cessation of the vortex shedding and also to the increase in the base pressure. This direct relationship between the critical drag reduction and the cessation of the vortex shedding is of great importance for understanding the fundamental aspects of bluff body flows in ground effect, and is also of particular interest in the present study, where not a half-circular but a full-circular cylinder is placed near a moving ground.

Table 1.1: Summary of earlier experiments on the flow past a circular cylinder near a plane boundary.

Authors	Re	h/d	δ_B/d	l/d	Key measurements
Taneda (1965)	170	0.1 - 0.6	0 (towed cylinder)	n.a.	WFV
Roshko *et al.* (1975)	2.0×10^4	0 - 6.0	0.5	n.a.	C_D, C_L
Bearman and Zdravkovich (1978)	2.5×10^4 - 4.8×10^4	0 - 3.5	0.8	32 (CE)	C_p, St, SFV
Buresti and Lanciotti (1979)	8.5×10^4 - 3.0×10^5	0 - 2.5	0.1	6.6 (CE)	St
Angrilli *et al.* (1982)	2860 - 7640	0.5 - 6.0	< 0.25	9.0 (OW)	St
Grass *et al.* (1984)	2000 - 4000	0 - 2.0	0.28 - 6.0	20 (CE)	St, WFV
Zdravkovich (1985a)	3550	0.1 - 1.6	0 (towed cylinder)	11.8 (OW)	WFV
Zdravkovich (1985b)	4.8×10^4 - 3.0×10^5	0 - 2.0	0.52 - 0.97	13.5, 25 (EP)	C_D, C_L
Hiwada *et al.* (1986)	2.0×10^4	0 - 4.0	0.23 - 2.82	20 (CE)	C_D, C_L, St, SFV, WFV
Taniguchi and Miyakoshi (1990)	9.4×10^4	0 - 3.0	0.34 - 1.05	14 (CE)	C_D, C_L, St
Buresti and Lanciotti (1992)	8.6×10^4 - 2.8×10^5	0 - 1.5	0.1 - 1.1	6.6 (CE)	C_D, C_L, St
Lei *et al.* (1999)	1.3×10^4 - 1.45×10^4	0 - 3.0	0.14 - 2.89	26 (EP)	C_D, C_L, C_p, St
Price *et al.* (2002)	1200 - 4960	0 - 2.0	0.45	16.25 (CE)	St, WFV, PIV
Zdravkovich (2003)	2.5×10^5	0.02 - 0.5	0 (moving ground)	21	C_D, C_L
Lin *et al.* (2005)	780	0 - 4.0	0 (towed cylinder), 0.86 - 1.41	33.1 (FE)	St, WFV, PIV
Present study	4.0×10^4 - 1.0×10^5	0.05 - 2.0	0 (moving ground)	8.33 (EP, FE)	C_D, C_L, SFV, PIV

(CE: closed-ends, EP: end-plates, FE: free-ends, OW: open water channel, SFV: surface flow visualisation, WFV: wake flow visualisation)

1.4.5 Numerical simulations (CFD)

With the rapid progress of computer technology in recent years, computational or numerical simulation is becoming a powerful tool for investigating the physics of various complex flows in fluid mechanics. The flow past cylinders at high Reynolds numbers of about 10^4 or above, however, is still a challenging subject in today's computational fluid dynamics (CFD) since the direct numerical simulations (DNS) of the Navier-Stokes equations for such high Reynolds number flows are currently not feasible due to the huge computational costs required (Spalart 2000).

As reviewed in the previous sections, flow past cylinders generally accompanies massive flow separation, vortex shedding, and the transition to turbulence. For the case of a circular cylinder, a further difficulty arises from the fact that the flow separation points are not fixed or determined by the geometry but depend on the flow pattern, especially on the location of the transition to turbulence. This is the key reason why the critical drag reduction of a circular cylinder, reported first by Wieselsberger in 1922 (cf. Section 1.4.2), still cannot be reproduced with sufficient accuracy in the numerical simulations of today, including unsteady Reynolds-averaged Navier-Stokes (URANS) simulations, large-eddy simulations (LES), and detached-eddy simulations (DES).

In the following, some basic concepts and recent progress of URANS, LES, and DES are reviewed with a major focus on their applications to the flow past cylinders. Further details of the procedure of these simulations are described later in Chapter 3.

Unsteady RANS simulations

The concept of URANS is based on the triple decomposition of time-dependent variables (Hussain and Reynolds 1970), where each instantaneous variable such as velocity and pressure is decomposed into *long-time-averaged*, *periodic*, and *turbulent* (or *stochastic/random*) components. The sum of the first two is often referred to as a *coherent* (or *phase-averaged*) component, for which the Reynolds-averaged Navier-Stokes (RANS) equations are derived and solved with using some turbulence closure models. In fact, the operation of the URANS of today largely relies on turbulence models and techniques for traditional (steady) RANS simulations, which have been well established compared with those for LES. A review of the models for RANS/URANS has been given by Wilcox (1998). It should be noted, however, that most of those turbulence models are basically adjusted to reproduce the spreading rate of mixing layers in *steady* RANS simulations, i.e., the Reynolds stresses predicted by the models implicitly contain contributions not only from the turbulent or random motions but also from the coherent motions of the flow (Spalart, 2000), and thus the models are in general 'overly dissipative' (Menter *et al.*, 2003) when used in URANS simulations.

As concerns the applications of URANS to the flow past cylinders, one of the first systematic investigations was conducted by Franke and Rodi (1991). They showed, for the flow past a square cylinder (in a free stream, $\mathrm{Re} = 2.2 \times 10^4$), that URANS could predict the periodic motion of the von Kármán-type vortex shedding behind the cylinder. The results were considerably sensitive to the turbulence model used, but the time-averaged results of

URANS basically agreed better with experiment than the results of steady RANS using the same turbulence models. Within the scope of URANS approaches, Franke and Rodi (1991) concluded that the Reynolds-stress model by Launder *et al.* (1975) yielded the best results, compared with eddy-viscosity-based models such as the standard k-ϵ model by Launder and Spalding (1974).

An encouraging result of the k-ϵ model, however, was later reported by Kato and Launder (1993), who proposed an *ad hoc* modification of the model to avoid the excessive production of turbulence in the stagnation region of a square cylinder in a free stream. This modification was also used by Bosch and Rodi (1996) for a square cylinder placed near a fixed ground ($\mathrm{Re} = 2.2 \times 10^4$). The original k-ϵ model incorrectly predicted the cessation of the vortex shedding at $h/d = 0.5$, at which point the vortex shedding was still observed experimentally (Bosch *et al.* 1996), whereas the Kato-Launder modification yielded reasonable predictions at all gap ratios investigated. Meanwhile, Iaccarino *et al.* (2003) recently applied the v^2-f model by Durbin (1995) to a square cylinder in a free stream ($\mathrm{Re} = 2.2 \times 10^4$); the results were reasonable and comparable to those by the Kato-Launder k-ϵ model.

As for a circular cylinder, less successful results have been obtained from RANS/URANS despite a number of attempts so far. A special difficulty for a circular cylinder arises from the fact that the flow separation points are not fixed but depend significantly on the location of the transition to turbulence, which can hardly be predicted by common RANS/URANS approaches. Some plausible results have been obtained, but only when the location of the transition, or 'trip,' was given *a priori* (Celik and Shaffer 1995). An alternative way to cope with this problem was proposed by Shur *et al.* (1996), who introduced the *trip-less approach*, where the inflow boundary conditions are given in a special manner and no transition information is given *a priori* (see Chapter 3 for more details). They applied this approach to the subcritical flow past a circular cylinder at $\mathrm{Re} = 1.4 \times 10^5$ with using the Spalart-Allmaras (S-A) model (Spalart and Allmaras 1992) and also the Shear-Stress-Transport (SST) k-ω model (Menter 1994). The S-A model coupled with the trip-less approach yielded reasonable results, although the quantitative agreement with experiment was not perfect.

More recent studies have shown that URANS, when coupled with sophisticated models to roughly predict the transition to turbulence, could capture the qualitative trends of not only the subcritical but also the critical and supercritical flows past a circular cylinder (Saghafian *et al.* 2003; Holloway *et al.* 2004; Langtry *et al.* 2004), although it still predicts flows that are too smooth or organised. In general, URANS cannot sufficiently capture the three-dimensional flow structures of wide-ranging spatial/time scales even if the computation is performed in a three-dimensional domain (Shur *et al.* 2005).

Large-eddy simulations

Such three-dimensional flow structures of wide-ranging scales may be analysed using LES, in which 'large-scale' eddies (or motions) are directly solved whereas small 'subgrid-scale' eddies are filtered and modelled. The oldest and best known subgrid-scale model is the one proposed by Smagorinsky (1963), where the concept of eddy viscosity was used in order to model the subgrid-scale Reynolds stress (see Chapter 3 for more details). A disadvantage of

the Smagorinsky model, however, was the need and difficulty of the modification of the eddy viscosity in near-wall regions. Later, Germano *et al.* (1991) proposed the dynamic subgrid-scale model (or 'procedure' in a proper sense), where the model parameters are not constant but are calculated locally and at each time step by using a coarse 'test filter.' This method was then modified by Lilly (1992) and is now widely used; further descriptions of the models and procedures for LES can be found in, e.g., Ferziger (1996) and Pope (2000).

For wall-bounded flows, Pope (2000) classified LES into two categories: LES with *near-wall resolution* (LES-NWR or 'pure' LES) and LES with *near-wall modelling* (LES-NWM). In general, the former requires huge computational costs and is thus still infeasible for high Reynolds number flows, whereas the latter requires (and is sensitive to) near-wall models or treatments. The influence of the near-wall models/treatments in LES-NWM, however, has not been examined enough compared with that in RANS/URANS.

The applications of LES to flow past cylinders have been reported by several authors. Rodi *et al.* (1997) summarised the results of '*Workshop on LES of Flow Past Bluff Bodies*' held in Germany in June 1995, where the flow past a square cylinder (in a free stream, Re $= 2.2 \times 10^4$) was selected as one of two test cases investigated by several research groups in the world. Breuer (1998, 2000) reported similar LES assessments but for the flow past a circular cylinder (Re $= 3.9 \times 10^3$ and 1.4×10^5, respectively). Ma *et al.* (2000) also reported their results for a circular cylinder at Re $= 3.9 \times 10^3$. More recently, Catalano *et al.* (2003) simulated the flow past a circular cylinder at Re $= 5 \times 10^5$, 1×10^6, and 2×10^6. On the whole, the results of LES agreed better with experiments than URANS, especially in the near wake region of the square/circular cylinder. However, as noted above, an essential problem in the use of LES is that a very fine filter is required at near-wall regions to resolve the 'large-scale' eddies that contain the bulk of turbulent kinetic energy (i.e., LES-NWR), which is infeasible in the cases of high Reynolds number flows discussed here. Inevitably given a 'coarse' filter (i.e., LES-NWM), the influence of the subgrid-scale model increases more and more (and also the grid dependence of the results increases) as the Reynolds number becomes higher, and the details of such influences are still unclear.

Detached-eddy simulations

The detached-eddy simulation (DES), the basic principles of which were given by Spalart *et al.* (1997) and then the first results were reported by Shur *et al.* (1999), is one of the novel attempts to combine URANS and LES to obtain realistic results for practical high Reynolds number flows at acceptable computational costs. In this approach, the wall boundary layers (or *attached eddies*) are analysed with URANS techniques whereas the separated regions (or *detached eddies*) are solved based on the concept of LES. The main feature of DES is that a single turbulence model serves as a statistical model (URANS mode) in near-wall regions and also serves as a subgrid-scale model (LES mode) in far-wall regions, so that no explicit boundary exists between the URANS and LES zones (such an approach is often referred to as 'non-zonal' coupling of URANS and LES; see Chapter 3 for more details).

Travin *et al.* (2000) applied DES to flow past a circular cylinder for both the subcritical (laminar-separation) and postcritical (turbulent-separation) cases. The former was simulated

using the trip-less approach by Shur *et al.* (1996) at Re $= 5 \times 10^4$ and 1.4×10^5, whereas the latter was simulated using a fully-turbulent condition at Re $= 1.4 \times 10^5$ and 3×10^6. The results were comparable to LES in terms of predicting the major properties of the flow (e.g., force coefficients, base pressure and separation angle) and also of capturing the three-dimensional wake structures. However, also similar to LES, the quantitative agreement with experiment was not perfect, especially at higher Reynolds numbers.

Due to the simple 'mode-switching' concept employed, however, the original DES has an issue concerning the physical interpretation of the 'grey area,' where the operation mode is switched between URANS and LES; the justification of this switch relies on the disparity in the scales between the attached- and detached-eddies (Spalart 2001). In practice, the switch between the URANS and LES modes can take place inside the boundary layers when using excessively fine computational grids (since the mode-switching point is determined based on the local grid spacing; see Chapter 3 for more details), and this often causes a premature or grid-induced separation (Menter *et al.* 2003). It follows that the grid spacing in the original DES must be carefully decided so that the boundary layers are analysed in the URANS mode rather than in the LES mode. To achieve this may not be easy when dealing with general industrial flows of complex geometry, as pointed out by Menter *et al.* (2003), who alternatively proposed a so-called scale-adaptive simulation (SAS) model to remedy the problem of the explicit grid dependency in DES. Nevertheless, a certain degree of grid convergence can still be achieved in an 'appropriate' resolution range in the original DES, at least when the flow configuration is relatively simple, as will be demonstrated in the present study.

1.4.6 Linear stability analysis

The origin of the stability analysis of flows goes back to Reynolds and Rayleigh in the late nineteenth century, but the interest in the stability of bluff body wakes has been dramatically increasing in the last two decades with the concept of *absolute versus convective instability* being fully applied to this field of study (Oertel 1990). Recent studies have shown that the von Kármán-type vortex shedding behind cylindrical bluff bodies may be explained as a result of absolute instability in the near wake region, which allows local disturbances in the flow to propagate both upstream and downstream and hence produces a resonance between the travelling instability waves; comprehensive reviews on this topic have been given by, for example, Huerre and Monkewitz (1990) and Huerre (2000).

Among a variety of techniques developed in the field of flow stability analysis, the *local* (i.e., parallel or nearly parallel flow assumed) *linear stability analysis* based on Rayleigh's and Orr-Sommerfeld type equations is one of the most popular and well developed techniques, the details of which have been documented by Drazin and Reid (1981) and Criminale *et al.* (2003); see also Chapter 4 for more details. This type of stability analysis has been successful in revealing the basic stability characteristics of many types of parallel (or nearly parallel) shear flows, such as wall boundary layers, mixing layers, jets, and wakes.

As concerns the wakes of two-dimensional bluff bodies, the local linear stability analysis has been performed by several researchers so far. Betchov and Criminale (1966) reported first the results of *spatio-temporal* stability analysis of a simple analytical wake profile. Koch

(1985) investigated a multi-parameter family of model wake profiles, including asymmetric ones, using the concept of absolute versus convective instability. Monkewitz (1988) further investigated the local absolute and convective instability of model wake profiles and its link to the global dynamics of the wake, i.e., the onset and cessation of the von Kármán-type vortex shedding, by comparing the results with experiments. Meanwhile, Hannemann and Oertel (1989) applied the analysis to wake profiles directly obtained from the Navier-Stokes equations and then compared the results between the stability analysis and the numerical simulations. A similar investigation was also performed by Hammond and Redekopp (1997) on asymmetric wake profiles numerically obtained. More recently, Castro (2005) reported a comparison between the Navier-Stokes computations and linear stability analysis on a flat-plate wake but with a symmetry plane imposed on the wake centreline and also with a slip boundary placed parallel to the free stream.

The crucial part of this type of analysis is the link between the local linear stability characteristics and the global mode selection of the flows. Monkewitz and Nguyen (1987) proposed the *initial resonance criterion* for the wakes of two-dimensional bluff bodies; that is, the global mode (i.e., the overall frequency and associated spatial structures) of the wake is determined by the local resonance at the first streamwise station of local absolute instability. This scenario was recently found to be the case not only in the framework of linear stability theory but also in the theory of *steep nonlinear global modes*, which was first identified in a model problem using the one-dimensional complex Ginzburg-Landau equation by Pier *et al.* (1998) and was then confirmed in the context of real wake flows governed by the Navier-Stokes equations by Pier and Huerre (2001). According to these authors, the upstream edge or *front* of the region of local linear absolute instability acts as a *wavemaker* to generate nonlinear waves travelling downstream and imposes its local frequency on the global oscillation of the downstream flow. This shows that the results of local linear stability analysis may indeed give some useful insights into the physics of the real (nonlinear) von Kármán-type vortex shedding.

1.4.7 POD analysis

The proper orthogonal decomposition (POD) method — which was first introduced in the field of fluid mechanics by Lumley (1967) as an unbiased technique to study the so-called *coherent structures* in turbulent flows — has attracted the attention of many researchers during the last two decades in the context of active feedback flow control. One of the biggest challenges in the development of feedback flow control systems is to reduce the complexity of the system, or to reduce the huge amount of information about the flow to be controlled, and the POD can be used for this purpose, i.e., to extract only the (energetically) dominant flow structures as spatial basis functions, or *modes*, and to build a 'low-dimensional' or 'reduced-order' model of the flow to be controlled (Holmes *et al.* 1996).

The concept of POD is to decompose multi-dimensional data into a linear combination of a finite number of orthogonal basis functions. In the context of fluid dynamics, the POD is usually used to decompose an unsteady flow field into the so-called spatial basis functions (or POD modes) and time-dependent modal coefficients. The basis functions obtained by

the POD are 'optimal' (compared with other linear representations such as a Fourier series) in the sense that the projection of the original data onto the basis functions is maximised (Berkooz *et al.* 1993; Holmes *et al.* 1996), and this is the reason why the POD is a logical and efficient way to build a low-dimensional basis that captures energetically dominant flow structures. The original (or traditional) POD method introduced by Lumley (1967), however, was computationally expensive and was not applicable to two- or three-dimensional flow field data of high spatial resolution. Later, Sirovich (1987) proposed the *snapshot POD* method, which provides POD modes equivalent to those by the traditional POD method but with less computational costs required (see Chapter 5 for more details).

The wake of cylindrical bluff bodies is a typical example of unsteady flows to which the POD analysis and also the POD-based low-dimensional feedback control techniques may be applied. Deane *et al.* (1991) performed the POD of the near wake of a circular cylinder (Re = 100 to 200); the laminar von Kármán-type vortex shedding was well represented by the combination of the first two POD modes. Ma *et al.* (2000) also performed it but at a higher Reynolds number of 3900, and showed that, even for the turbulent wake, the majority of the fluctuating energy was captured in less than 10 to 20 modes as the von Kármán-type vortex shedding was still energetically dominant compared to the background turbulence. Also van Oudheusden *et al.* (2005) recently reported for the turbulent near wake of a square cylinder ($\mathrm{Re} = 1.0 \times 10^4$) that about 75 percent of the fluctuating energy was captured in the first two POD modes, with which the large-scale vortex shedding motion was well reproduced. On the other hand, several advanced studies on the POD-based feedback control have already been reported for a circular cylinder in a free stream (Gillies 1998; Cohen *et al.* 2003; Bergmann *et al.* 2005), and also for a square cylinder placed in a channel (Galletti *et al.* 2004). These studies have demonstrated the promise of the POD-based low-dimensional techniques for the feedback control of the wakes of bluff bodis, but only in the laminar flow regime so far. The possibility of the application of these techniques to the control of turbulent vortex shedding, which is of more importance in practical engineering problems, has not been investigated in detail.

Chapter 2

Experimental Study of Flow Past a Circular Cylinder in Ground Effect

2.1 Introduction

The flow past a circular cylinder in ground effect has been the subject of a number of studies; the details of the ground effect, however, are still far from being fully understood because of the existence of several influencing factors, as reviewed in Section 1.4.3. The objective of the experimental study described in this chapter is to elucidate the mechanisms of the ground effect in more detail by wind tunnel tests using: (i) a moving ground, on which substantially no boundary layer develops to interfere with the cylinder (and hence the rather 'confusing' effects of the state/thickness of the boundary layer are avoided), and (ii) a pair of end-plates, with and without which the influence of the spanwise-end condition of the cylinder in ground effect is explicitly examined.

The purposes of this chapter are to show experimental results and to discuss the fundamental physics of the flow, in particular the direct relationship between the cessation of the von Kármán-type vortex shedding from the cylinder and the drag reduction of the cylinder in ground effect. In the following, the details of the experiments will be described in Section 2.2, and then the results will be presented in Section 2.3. A further discussion of the results will be given in Section 2.4, and finally a concluding summary will be given in Section 2.5. Note that the experimental data presented in this chapter are later compared with numerical simulations and linear stability analysis in Chapters 3 and 4, respectively, and then further examined using the POD analysis in Chapter 5.

2.2 Experimental details

Mean drag and lift measurements, surface oil flow visualisation, and particle image velocity (PIV) measurements were performed for a circular cylinder of an aspect ratio of 8.33, placed near and parallel to a moving ground, at two upper-subcritical Reynolds numbers of 0.4 and 1.0×10^5 (based on the cylinder diameter d and the free-stream velocity U_∞). Details of the experiments are described below.

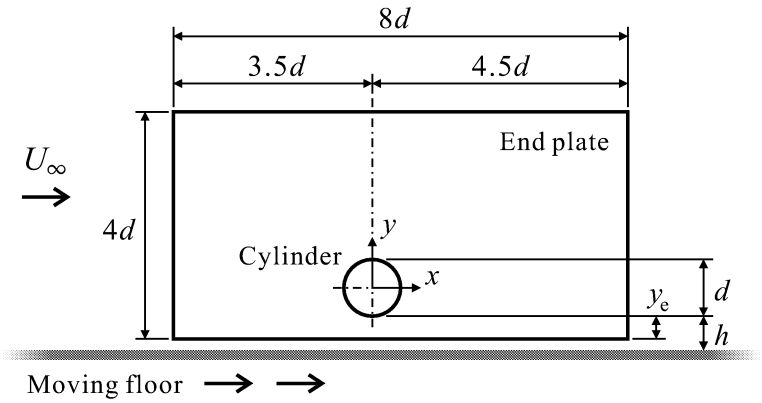

Figure 2.1: Schematic of circular cylinder model and end-plates.

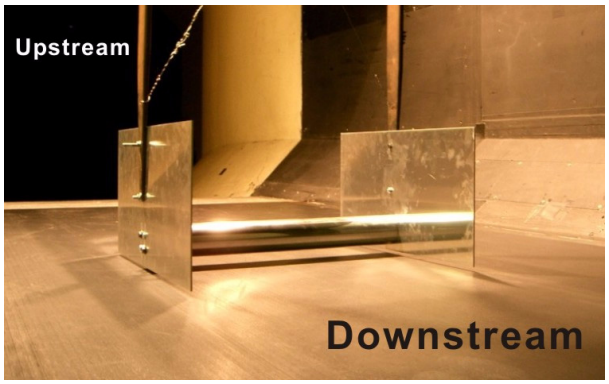

Figure 2.2: Model installation in the wind tunnel.

2.2.1 Wind tunnel, cylinder, and end-plates

The experiments were performed in the 2.1×1.5 m ($7' \times 5'$) wind tunnel at the University of Southampton. The tunnel is of conventional closed circuit design, and the working section of 2.1 m wide $\times$ 1.5 m high $\times$ 4.4 m long is equipped with a large moving belt rig (1.5 m wide $\times$ 3.2 m long) and also a three-component overhead balance to measure the time-averaged forces. The moving belt travels at the same speed as the free stream and works in conjunction with a boundary layer suction system, which ensures uniform airflow in the near-floor region. The intensity of the free-stream turbulence (FST) is less than 0.3%. A further description of the wind tunnel facility is given by Burgin *et al.* (1986).

Figure 2.1 describes a standard layout of the cylinder model and end-plates used in this study, and Fig. 2.2 is a photograph of the model installed in the wind tunnel. The cylinder was placed above the moving floor with the axis lying parallel to the floor and perpendicular to the free stream. The cylinder model used is 6 cm in diameter and 50 cm in length: the aspect ratio $l/d = 8.33$. The model is made of aluminium alloy, and the surface is smooth; the relative roughness K/d, where K is the estimated height of excrescences, is less than 0.01%. Aluminium end-plates 3 mm thick (or Perspex end-plates 6.5 mm thick in the case

of PIV measurements) were attached to both ends of the cylinder for the majority of the experiments. The size of the end-plates, described in Figs. 2.1 and also 2.3, basically follows recommendations by Stansby (1974), who optimised the distance from the leading edge of the plates to a cylinder placed in a free stream to provide an essentially two-dimensional flow around the cylinder. An additional factor to be considered here, however, is the gap between the end-plates and the moving floor since the plates are not allowed to contact the moving floor. In this study, the distance from the bottom edge of the plates to the cylinder, denoted by y_e in Fig. 2.1, was set at three different levels of 0, $0.2d$ and $0.4d$ to examine the effects of the end-plate position, i.e., four different end conditions in total (three with end-plates and one without end-plates) were investigated in this study.

The model was mounted on two steel struts, which were connected to the overhead balance of the wind tunnel. Two thin steel wires crossed between the struts to prevent the vibration of the model. The total blockage of the test section caused by the cylinder model, end-plates, and struts was less than 3%, and hence no corrections for the blockage effects were made for the experimental results.

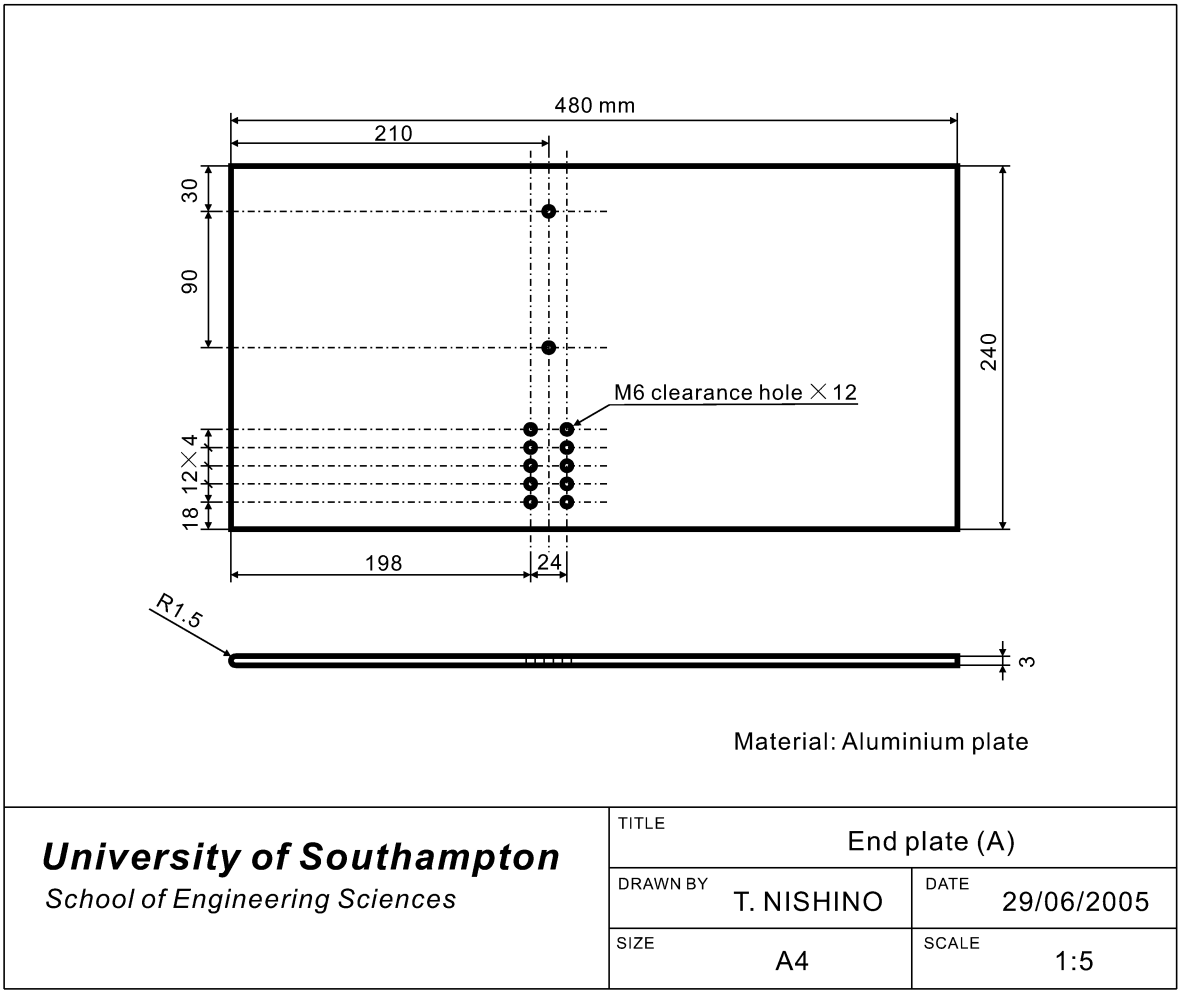

Figure 2.3: Drawing of aluminium end-plates.

Table 2.1: Experimental conditions.

	h/d	0.05	0.1	0.15	0.2	0.25	0.3	0.35	0.4	0.45	0.5	0.6	0.8	1.0	1.5	2.0
Force	($y_e/d = 0$)	○	○	○	○	○	○	○	○	○	○	○	○	○	○	○
	($y_e/d = 0.2$)					○	○	○	○	○	○	○	○	○		
	($y_e/d = 0.4$)									○	○	○	○	○	○	○
	(no end-plates)	○	○	○	○	○	○	○	○	○	○	○	○	○	○	○
Oil flow	($y_e/d = 0$)				△		△		△		△			△		
	(no end-plates)				△									△		
PIV	($y_e/d = 0$)				▽		▽		▽			▽				
	(no end-plates)				▽							▽				

(○: Re = 0.4 and 1.0×10^5, △: Re = 1.0×10^5, ▽: Re = 0.4×10^5)

2.2.2 Force measurements

The time-averaged drag and lift measurements were performed as follows. First, the forces acting on the 'total' package, consisting of the cylinder model, end-plates, struts, and wires, were measured for each experimental condition (Reynolds numbers of 0.4 and 1.0×10^5, gap ratio h/d of 0.05 to 2.0, and the four cylinder-end conditions; see Table 2.1 for details). Second, the forces acting on the 'tare' package, consisting only of the end-plates, struts, and wires, were measured for each condition. The drag and lift coefficients of the cylinder, C_D and C_L, were then calculated from the two sets of measurements, taking into account the changes in air density due to slight variations of the free-stream temperature and pressure during the tests.

The wind tunnel was started up and shut down for each gap ratio and end condition due to the need to change these conditions (i.e., model configuration) manually, whereas the two wind (and also the floor) speeds U_∞ of 10 and 25 m/s, which approximately correspond to the Reynolds numbers of 0.4 and 1.0×10^5, respectively, were consecutively tested without shutting down the tunnel. Five consecutive measurements of the time-averaged drag and lift forces, where each single measurement takes about 20 seconds to obtain the time-averaged value, were conducted for each condition. The five time-averaged data were further averaged to obtain the final results. In addition, a repeatability test was also carried out (but only for one representative model configuration) to roughly estimate the uncertainties stemming from the whole experimental process, as will be described below.

Uncertainties in force measurements

Two different levels of random uncertainties (or precision errors) were estimated for the time-averaged C_D and C_L measurements, basically following the theory of uncertainty analysis by Moffat (1982) and Taylor (1982).

First of all, the standard deviation σ_x of the five consecutive measurements of the time-averaged drag and lift forces was calculated, for each experimental condition, to estimate the *first order uncertainty* (Moffat 1982) of the measurements, i.e., the uncertainty coming only from the unsteadiness of the system. For the lower Reynolds number cases ($U_\infty = 10$ m/s), the first order uncertainties ($2\sigma_x/\sqrt{5}$) were found to be 0.028 N for the drag and 0.019 N for the lift at the maximum, which correspond to the uncertainties in C_D and C_L of ± 0.016 and ± 0.011, respectively, with 95% confidence. For the higher Reynolds number cases ($U_\infty = 25$

m/s), the uncertainties were found to be 0.082 N for the drag and 0.033 N for the lift at the maximum, corresponding to the uncertainties in C_D and C_L of ± 0.0075 and ± 0.0030, respectively, with 95% confidence.

Second, the standard deviation σ_x of three independent final results of C_D and C_L, which were obtained from the repeatability test only for one typical model configuration ($h/d = 0.6$ with $y_e/d = 0$), were calculated to estimate the other uncertainties stemming from the whole experimental process, including the installation process of the model. For the lower Reynolds number case, the uncertainties ($2\sigma_x$, not $2\sigma_x/\sqrt{3}$) in C_D and C_L were estimated to be ± 0.0089 and ± 0.0241, respectively. For the higher Reynolds number case, they were estimated to be ± 0.0040 and ± 0.0097, respectively.

Finally, the sum of the uncertainties estimated from this repeatability test *plus* the first order uncertainties (estimated for each experimental condition) was calculated as an estimation of 'total' random uncertainties for each experimental condition, which will be plotted later in Figs. 2.7 and 2.9. The fixed or bias errors, i.e., the uncertainties coming from the nature of the experimental apparatus and thus cannot be detected from the repeatability test described above, were assumed to be negligible in this study.

For the uncertainties in the gap ratio h/d, an accuracy of ± 0.002 was obtained for the smallest h/d of 0.05, and ± 0.01 for the other cases. As for the Reynolds number, it was found to vary from 0.37 to 0.41 $\times 10^5$ for $U_\infty = 10$ m/s and from 0.92 to 1.01 $\times 10^5$ for $U_\infty = 25$ m/s due to changes in the free-stream temperature and pressure during the tests. The uncertainties in the measurements of the wind speed U_∞ were found to be negligible, in terms of the influence on the Reynolds number, compared with the changes in the free-stream temperature and pressure. Note that since the influence of the Reynolds number is not significant in this upper-subcritical flow regime (as reviewed in Section 1.4.2 and will also be shown in this study), the notations of Re = 0.4 and 1.0×10^5 are used as synonyms of the two wind speed conditions of $U_\infty = 10$ m/s and 25 m/s, respectively, for the sake of convenience.

2.2.3 Surface oil flow visualisation

For the surface oil-flow visualisation (and also for the PIV measurements) the cylinder model was painted matt black to obtain clear images of the flow pattern. A mixture of liquid paraffin and fine powder *Invisible Blue T70* was applied to the model surface, and then the tunnel was run for about 30 minutes to evaporate the paraffin, making the surface flow pattern visible and available to be photographed. Both the upper (open-side) and bottom (gap-side) surfaces of the cylinder were directly photographed, after demounting the cylinder model with special care not to disturb the flow pattern obtained, to estimate the flow separation angles. The oil flow tests were conducted for several h/d with and without end-plates, but only at the higher Reynolds number of 1.0×10^5 (cf. Table 2.1).

2.2.4 PIV measurements

The PIV measurements were performed using a Dantec FlowMap 2D-PIV system (PIV2100); the experimental setup for the PIV measurements is described in Fig. 2.4. A double-pulse

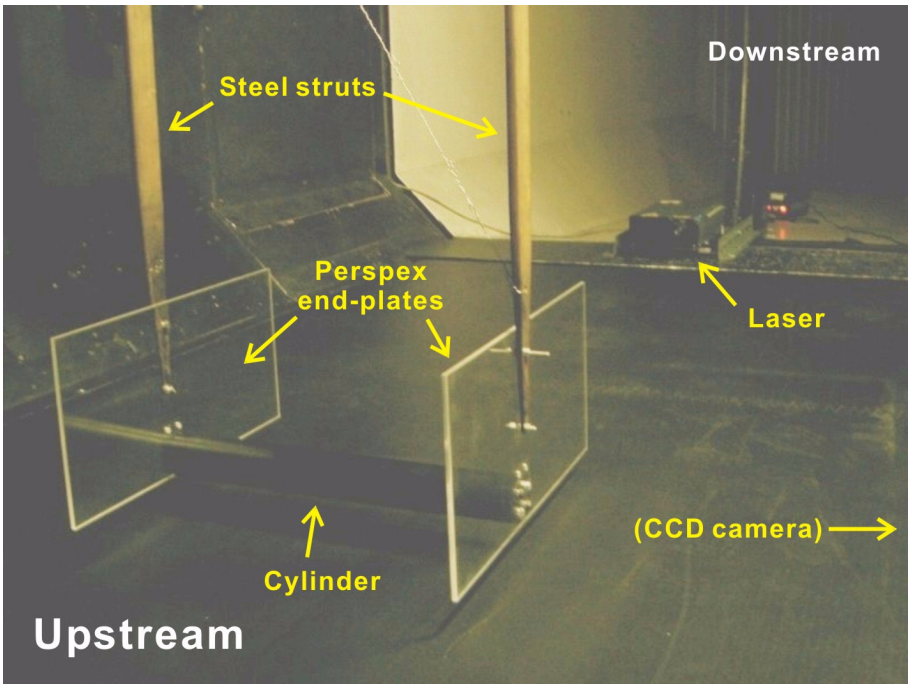

Figure 2.4: Experimental setup for PIV measurements.

Nd:YAG laser (120 mJ/pulse) was located approximately 1.5 m ($25d$) downstream of the centre of the cylinder to create a laser sheet of about 1 mm thick, illuminating the mid-span plane behind the cylinder. Smoke particles of about 1 μm in size were used as tracer particles to be illuminated by the laser sheet. The illuminated particle images were captured using a Dantec HiSense CCD camera (1280×1024 pixels, 8 bits/pixel), which was synchronised with the laser to implement the so-called 'double-frame/single-exposure' recording (Raffel *et al.* 1998). The time delay between the two laser pulses was set at 50 μs, and 400 pairs of images were continuously recorded for each experimental condition with a sampling rate of 2 Hz, which was unfortunately not high enough to resolve the time evolution of vortex shedding behind the cylinder in this study.

Each pair of images recorded was then analysed using a cross-correlation technique with an interrogation area of 32×32 pixels with 50% overlapping in both horizontal and vertical directions. The resulting vectors were validated by the *correlation-peak-height*, *velocity-range*, and *moving-average* validations (Jensen 2004); the rejected vectors were replaced with interpolated values from the surrounding valid vectors. The 400 instantaneous velocity field data obtained were then averaged, for each condition, to yield time-averaged flow field data. An example of the convergence of the time-averaging is shown in Fig. 2.5; the convergence is not perfect but reasonably acceptable, considering the complexity of the turbulent vortex shedding in this near wake region.

The PIV measurements were carried out for several h/d with and without end-plates, but only at the lower Reynolds number of 0.4×10^5 (cf. Table 2.1) due to technical difficulties at the higher Reynolds number. For the majority of the measurements, only the near wake

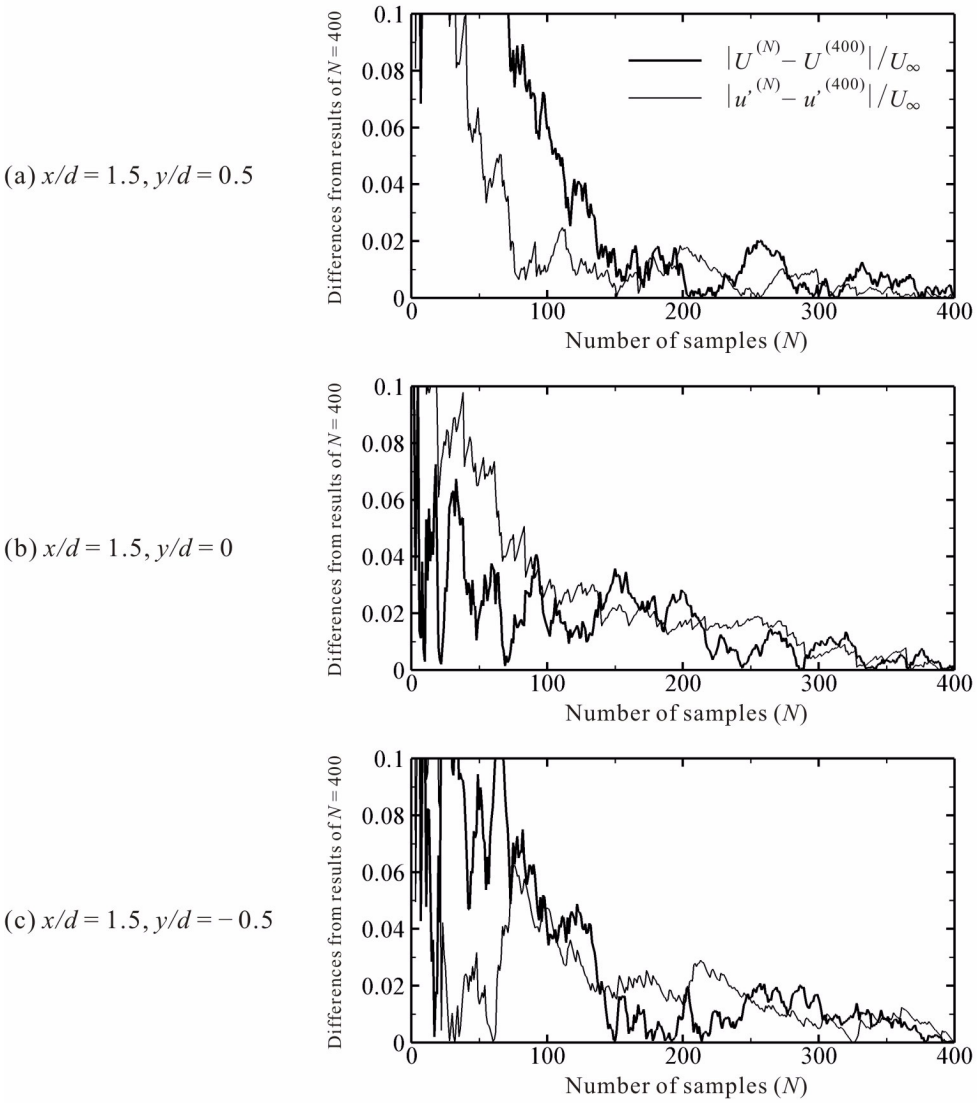

Figure 2.5: Convergence of the mean and r.m.s. values of local streamwise velocities ($h/d = 0.6$, $y_e/d = 0$, Re $= 0.4 \times 10^5$); u' is the r.m.s. of streamwise velocity fluctuation, i.e., $(\overline{u'^2})^{\frac{1}{2}}$.

region of $0.2 < x/d < 2.7$ was captured within a single camera view. The downstream region of $2.5 < x/d < 5$, however, was additionally measured for a few cases in order to detect the length of an elongated recirculation region behind the cylinder.

2.3 Experimental results

2.3.1 Drag and lift coefficients

The variations of the time-averaged drag coefficient of the cylinder in ground effect are shown in Fig. 2.6 for the four different cylinder-end conditions investigated. The results of some of the earlier studies reviewed in Section 1.4.3 are also included in this figure for the purpose of comparison. Note that, for the present results, only those for the higher Reynolds number of 1.0×10^5 are shown here since no substantial differences were observed between the two

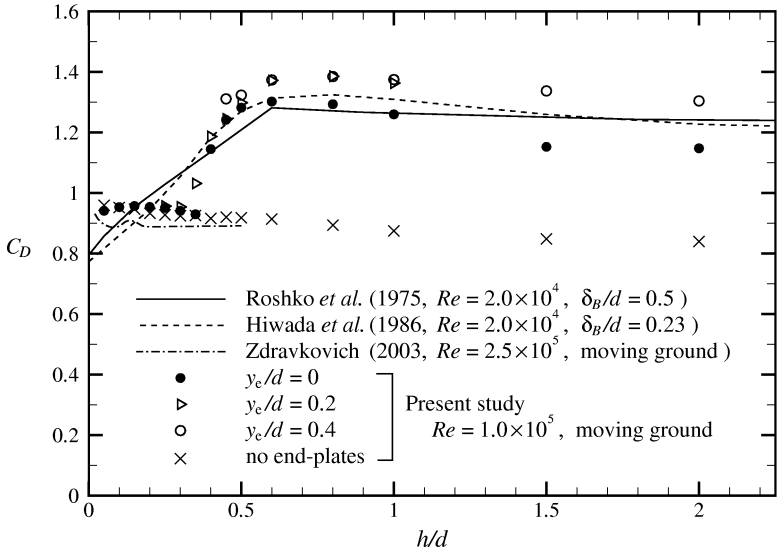

Figure 2.6: Mean drag coefficient of a circular cylinder in ground effect.

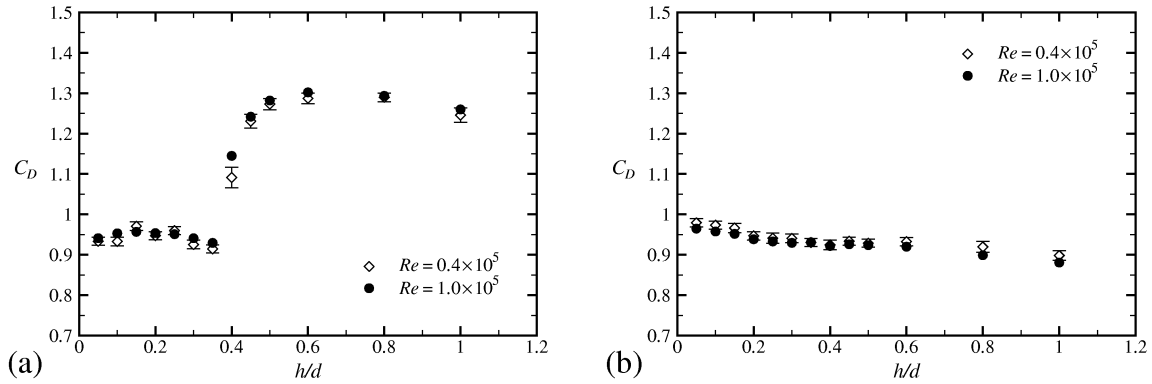

Figure 2.7: Effects of the Reynolds number on the mean drag behaviour: (a) with end-plates at $y_e/d = 0$, (b) without end-plates.

Reynolds numbers tested. The effects of the Reynolds number are shown in Fig. 2.7, where the estimated total random uncertainties (cf. Section 2.2.2) are also indicated by error bars but only for the lower Reynolds number; the uncertainties for the higher Reynolds number were too small to be plotted on the figure.

As can be seen from Fig. 2.6, for all three cases in which the end-plates were attached to the cylinder ($y_e/d = 0$, 0.2, and 0.4), a rapid reduction in C_D occurred as h/d decreased to less than about 0.5; this is similar to that observed by Roshko *et al.* (1975) and Hiwada *et al.* (1986), who used a fixed ground rather than a moving ground. Unlike their results, however, the drag reduction observed in the present study suddenly stopped around $h/d = 0.35$ and then C_D remained almost constant at slightly less than 1 as the cylinder came close to the ground. As will be shown later, the critical change in C_D around $h/d = 0.35$ seems to coincide with the cessation of the large-scale von Kármán-type vortex shedding in the near wake region of the cylinder.

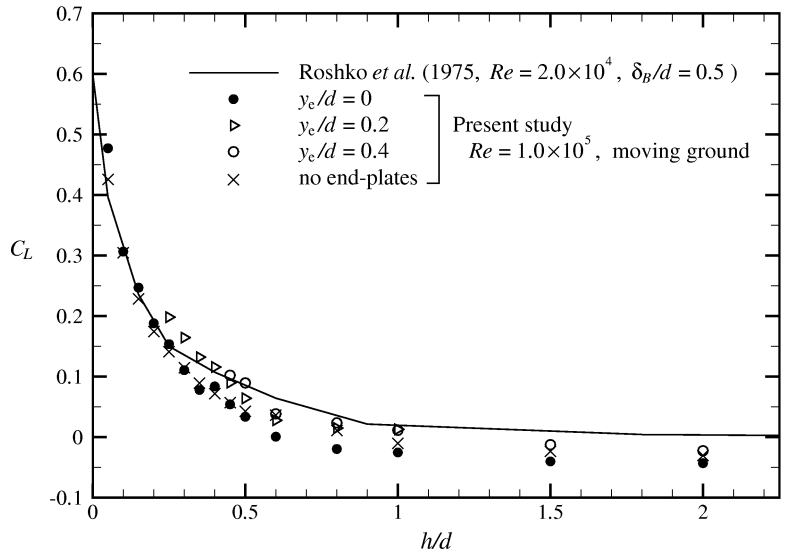

Figure 2.8: Mean lift coefficient of a circular cylinder in ground effect.

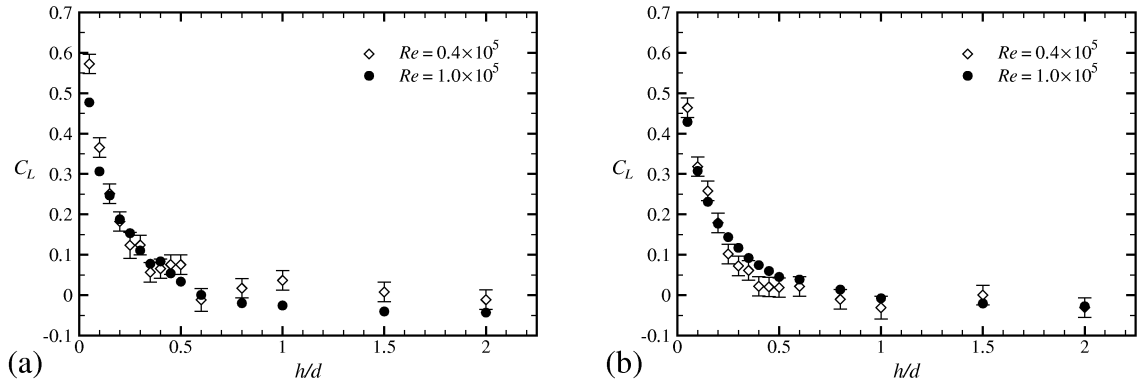

Figure 2.9: Effects of the Reynolds number on the mean lift behaviour: (a) with end-plates at $y_e/d = 0$, (b) without end-plates.

As concerns the influence of the position of the end-plates, there is a certain difference between $y_e/d = 0$ and 0.2 especially at larger gap ratios, but little difference between $y_e/d = 0.2$ and 0.4. This may be interpreted such that the effectiveness of the end-plates is reduced as the distance from the bottom edge of the plates to the cylinder, y_e, is decreased close to zero. At the largest gap ratio of $h/d = 2$, the drag coefficient of the cylinder with end-plates at $y_e/d = 0.4$ was found to be 1.3, which is comparable to that for a long circular cylinder in a free stream (i.e., outside the ground effect) in the upper-subcritical (TrSL3) flow regime (cf. Fig. 1.2), suggesting the full effectiveness of the end-plates in this case.

Meanwhile, the drag behaviour of the cylinder without end-plates is totally different from that for the cylinder with end-plates; the drag gradually decreased, with no critical change, as the gap ratio increased (cf. Fig. 2.6). At the largest gap ratio of $h/d = 2$, the drag coefficient of the cylinder without end-plates was found to be 0.85, which is consistent with that for a short circular cylinder of similar aspect ratio in a free stream (cf. Zdravkovich *et al.* 1989). Of

greater interest here, however, is that no substantial influence of the cylinder-end condition can be seen at smaller gap ratios of $h/d < 0.35$, where C_D showed an almost constant value of 0.95 for the cylinder with end-plates ($y_e/d = 0$ and 0.2) and also for the cylinder without end-plates. It should also be noted that this almost constant drag behaviour looks similar to that recently reported by Zdravkovich (2003); the details of his experiments, however, have not been clarified enough, as reviewed in Section 1.4.3.

Figure 2.8 shows the variations of the time-averaged lift coefficient of the cylinder in ground effect, at the higher Reynolds number of 1.0×10^5, for the four different cylinder-end conditions. The results for a fixed ground by Roshko *et al.* (1975) are also shown here for the purpose of comparison. It can be seen that both the ground condition (moving or fixed) and the cylinder-end condition (with or without end-plates) have only minor effects on the lift behaviour in ground effect. At the lower Reynolds number of 0.4×10^5, however, a little more scattered variations of C_L were observed in this study, as shown in Fig. 2.9. Note that here the estimated total random uncertainties (cf. Section 2.2.2) are also indicated by error bars but only for $\mathrm{Re} = 0.4 \times 10^5$; those for $\mathrm{Re} = 1.0 \times 10^5$ were too small to be plotted on the figure. It is difficult to judge if these slightly different variations of C_L are attributed to some essential physics of the ground effect or to some unknown errors due to the current measurement system/procedure itself. Nevertheless, it may be concluded that, basically, C_L increased as h/d decreased to less than about 0.5 for all cases investigated.

2.3.2 Surface oil flow pattern

Figures 2.10 and 2.11 show, respectively, the oil flow patterns on the upper (open-side) and bottom (gap-side) surfaces of the cylinder for six different configurations (four cases for the cylinder with end-plates at $y_e/d = 0$ and the other two cases for the cylinder without end-plates). Note that only half of the cylinder span is shown here since the oil flow patterns appeared to be symmetric in the spanwise direction for all cases tested. The airflow direction is from downside to upside in Fig. 2.10, and is from upside to downside in Fig. 2.11.

As is obvious from the orderly oil-flow patterns in the upstream region, for all cases, the airflow remains laminar and almost two dimensional before the separation, i.e., the flow is subcritical. The separation line on the upper surface of the cylinder is straight when with end-plates at $y_e/d = 0$ [Figs. 2.10(a) to (d)], and is slightly curved near the ends when without end-plates [Figs. 2.10(e) and (f)]. A similar pattern of this slightly-curved separation near the free-ends has been reported for a circular cylinder of finite length in a free stream (i.e., outside the ground effect) by Zdravkovich *et al.* (1989). On the bottom surface of the cylinder in ground effect, however, the separation line remains straight even without end-plates [Figs. 2.11(e) and (f)]. An enlarged photo of the straight separation line on the bottom surface of the cylinder (without end-plates, $h/d = 0.2$) is also presented in Fig. 2.12.

It can also be seen from the oil flow patterns that the position of flow separation moves upstream on the upper side and downstream on the bottom side as the cylinder comes close to the ground; this qualitatively agrees with an observation by Bearman and Zdravkovich (1978) for a circular cylinder near a fixed ground. Figure 2.13 summarises the magnitude of the separation angle θ_{sep} [the angle from the front ($x/d = -0.5$, $y/d = 0$) to the separation

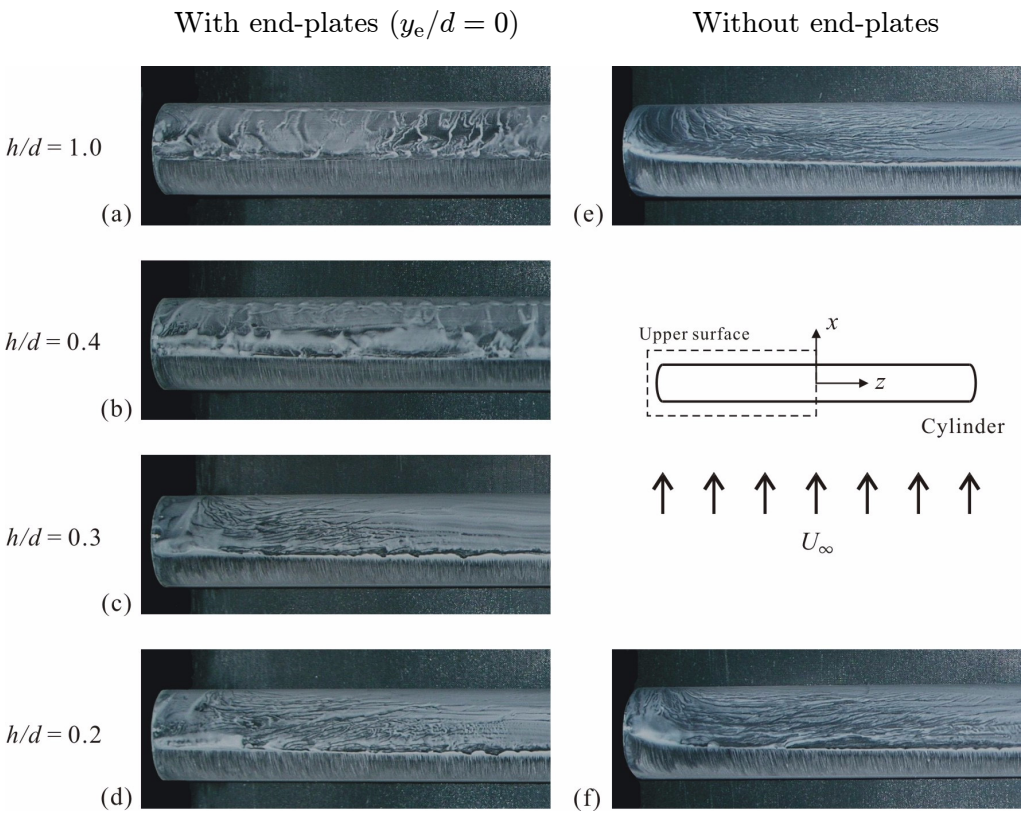

Figure 2.10: Oil flow patterns on the upper surface of the cylinder: (a-d) with end-plates, and (e, f) without end-plates, for $h/d =$ (a, e) 1.0, (b) 0.4, (c) 0.3, (d, f) 0.2; Re $= 1.0 \times 10^5$.

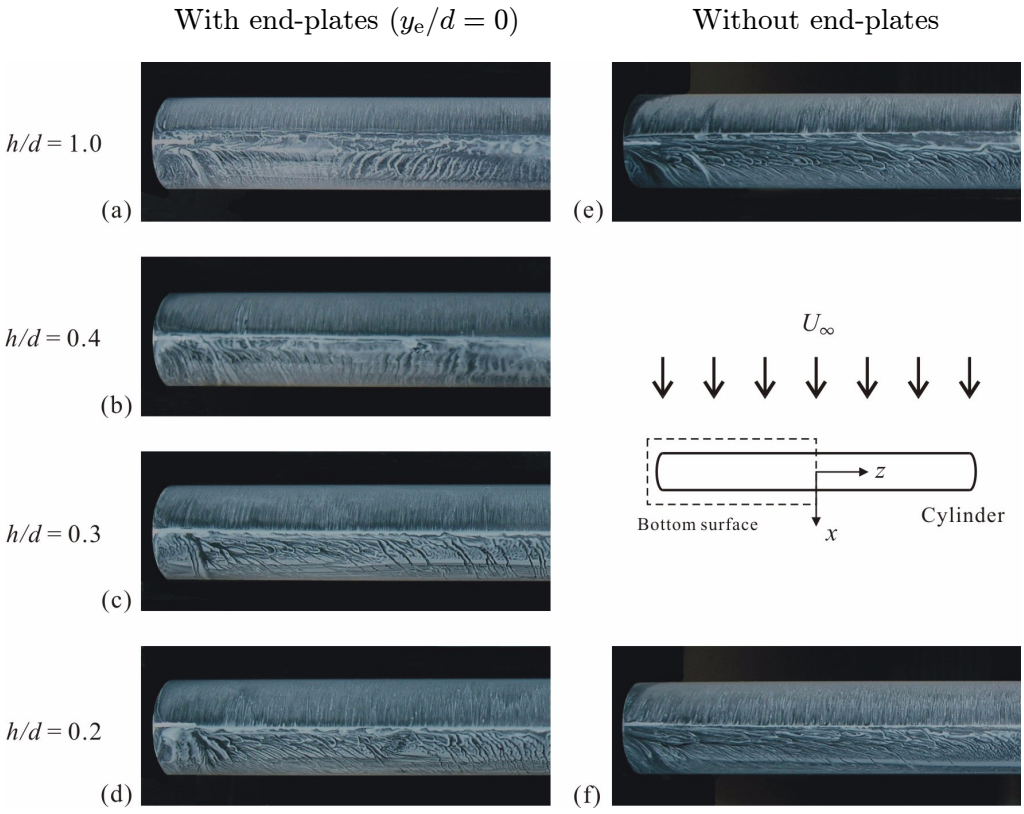

Figure 2.11: Oil flow patterns on the bottom surface of the cylinder: (a-d) with end-plates, and (e, f) without end-plates, for $h/d =$ (a, e) 1.0, (b) 0.4, (c) 0.3, (d, f) 0.2; Re $= 1.0 \times 10^5$.

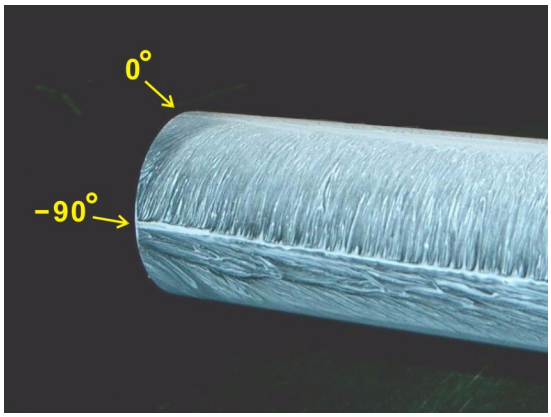

Figure 2.12: Straight separation line on the bottom surface of the cylinder without end-plates ($h/d = 0.2$, $\mathrm{Re} = 1.0 \times 10^5$).

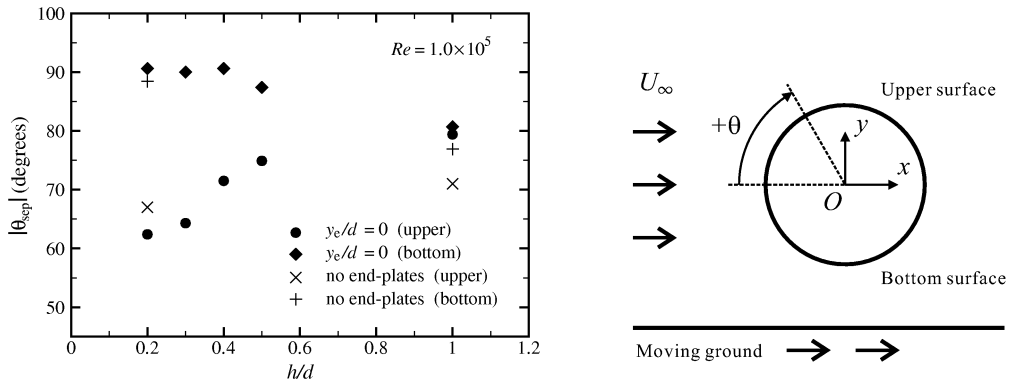

Figure 2.13: Time-averaged separation angle (estimated from surface oil flow patterns) vs. gap ratio for the cylinder with end-plates ($y_e/d = 0$) and without end plates.

point estimated from the oil flow patterns at the mid-span of the cylinder] for all gap ratios investigated. As has been suggested by Bearman and Zdravkovich (1978), the lift variation of a circular cylinder in ground effect (cf. Fig. 2.8) can be largely explained by this angular shift of the flow field around the cylinder, i.e., the lift increases as the front stagnation point shifts downward when the cylinder comes close to the ground.

Although the flow after the separation is basically time-dependent and thus cannot be exactly captured by this oil flow visualisation, an interesting trend can be seen in the oil flow patterns also behind the separation lines. That is, a relatively clear or organised flow pattern appears when without end-plates [Figs. 2.10(e), (f) and 2.11(e), (f)], suggesting the existence of a quasi-steady (i.e., not fully unsteady) flow even after the separation. Of interest is that a similar pattern can also be seen on the cylinder with end-plates but only when $h/d \leq 0.3$ [Figs. 2.10(c), (d) and 2.11(c), (d)]; such an organised pattern cannot be recognised on the cylinder with end-plates when $h/d \geq 0.4$ [Figs. 2.10(a), (b) and 2.11(a), (b)]. This difference in the near wake structure can be more clearly observed by the PIV measurements, as will be described in the next section.

2.3.3 Near wake structure (with end-plates)

Figure 2.14 shows the time-averaged, mid-span ($z/d = 0$) flow field data, obtained from 400 samples of PIV data for each case, behind the cylinder with end-plates at $y_e/d = 0$. The time-averaged velocity vectors, streamwise velocity contours, and spanwise vorticity contours are depicted in Figs. 2.14(a-d), (e-h), and (i-l), respectively, for four different h/d of 0.6, 0.4,

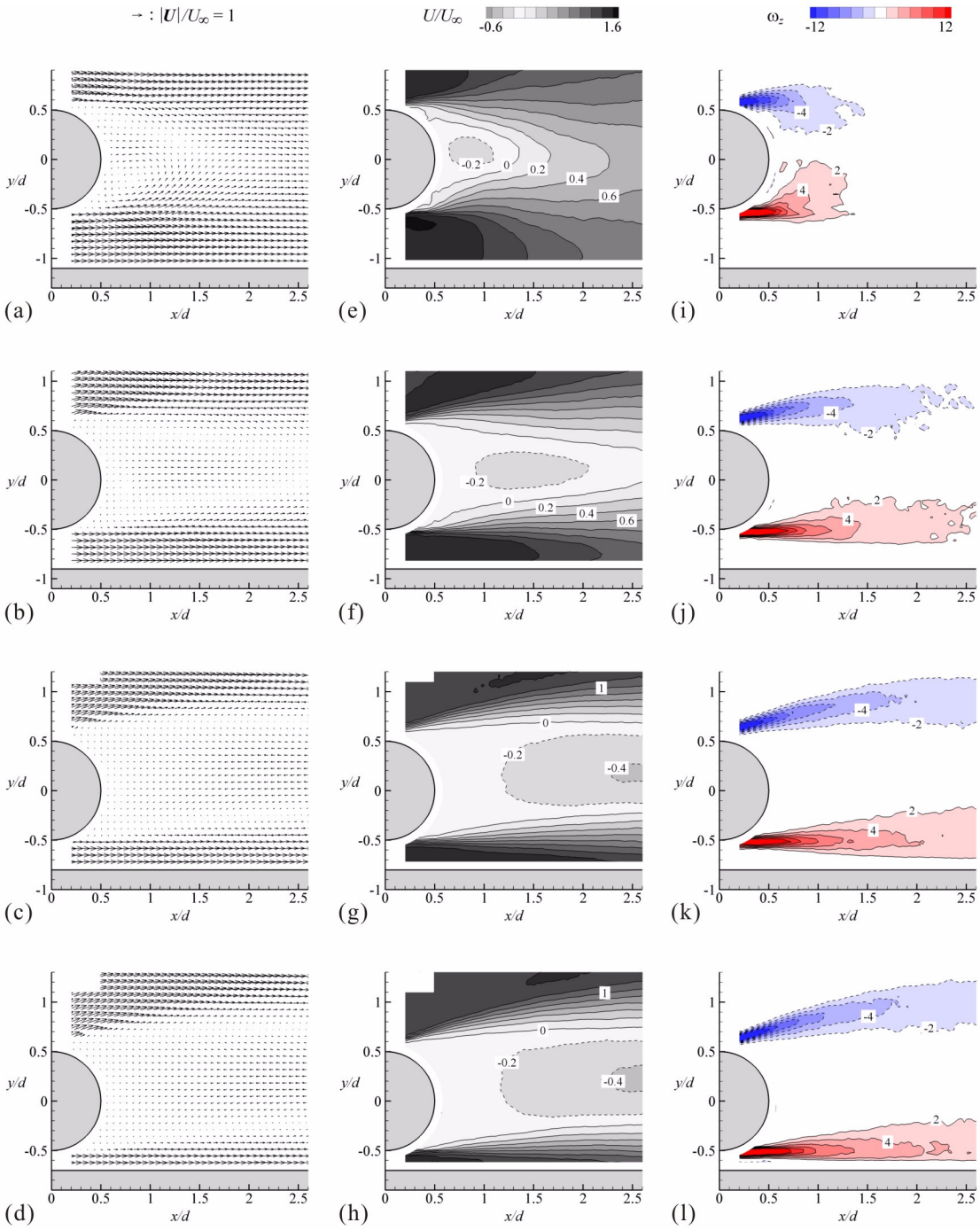

Figure 2.14: Time-averaged flow fields behind the cylinder with end-plates ($y_e/d = 0$): (a-d) velocity vectors, (e-h) contours of streamwise velocity, and (i-l) contours of spanwise vorticity; at four different gap ratios: (a, e, i) $h/d = 0.6$, (b, f, j) $h/d = 0.4$, (c, g, k) $h/d = 0.3$, and (d, h, l) $h/d = 0.2$; Re $= 0.4 \times 10^5$.

0.3, and 0.2. Note that the velocity is nondimensionalised by the free-stream velocity U_∞, and the vorticity is also nondimensionalised by U_∞ and the cylinder diameter d as

$$\omega_z \quad = \quad (\partial v/\partial x - \partial u/\partial y)\, d/U_\infty \,. \tag{2.1}$$

Also note that the PIV data close to the cylinder and ground surfaces have been discarded as they were disturbed by the reflection of light from the surfaces. It can be seen from the figures that the recirculation region behind the cylinder is significantly elongated as the gap ratio h/d is reduced from 0.6 to 0.3 and 0.2; see also Fig. 2.15 for the whole picture of the elongated recirculation bubble. The elongated recirculation length L_r at $h/d = 0.2$ is about $5d$ compared to $1.35d$ at $h/d = 0.6$. Also of particular interest is that the flow through the gap between the cylinder and the ground is not blocked or choked but slightly accelerated even at the smallest gap ratio of $h/d = 0.2$.

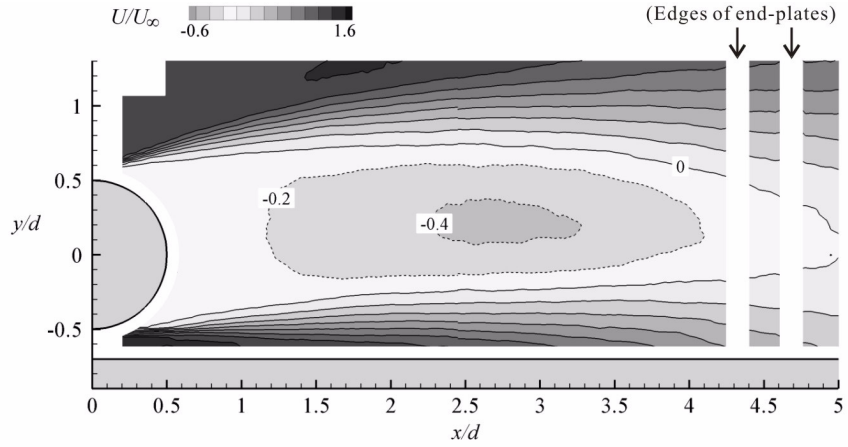

Figure 2.15: Elongated recirculation bubble behind the cylinder in ground effect ($h/d = 0.2$, with end-plates at $y_e/d = 0$, Re $= 0.4 \times 10^5$).

More details of the near wake structure of the cylinder can be seen from instantaneous PIV data. Figures 2.16(a) and (b) show typical instantaneous velocity fields at $h/d = 0.6$ and 0.2, respectively, and the corresponding instantaneous vorticity contours are plotted in Figs. 2.16(c) and (d), respectively. In addition, Figs. 2.16(e) and (f) show the corresponding instantaneous contours of the (two-dimensional) *swirl strength*, λ_{ci}, that is the imaginary part of the complex eigenvalue of the local velocity gradient tensor (cf. Adrian *et al.* 2000). Note that the local velocity gradient tensor $\underline{\underline{D}}^{2D}$ is defined as

$$\underline{\underline{D}}^{2D} \quad = \quad \begin{bmatrix} \frac{\partial u}{\partial x} & \frac{\partial u}{\partial y} \\ \frac{\partial v}{\partial x} & \frac{\partial v}{\partial y} \end{bmatrix} \,. \tag{2.2}$$

Also note that the diamond symbols plotted in Figs. 2.16(e) and (f) indicate the position of *vortex cores*, which were automatically identified by the position of the peaks of the swirl strength that were above an arbitrary threshold of 0.8 s^{-1}. It can be seen from these figures that, at $h/d = 0.6$ [Figs. 2.16(a), (c), and (e)], large-scale von Kármán-type (alternating) vortices are generated just behind the cylinder, which is a common feature of the wake of

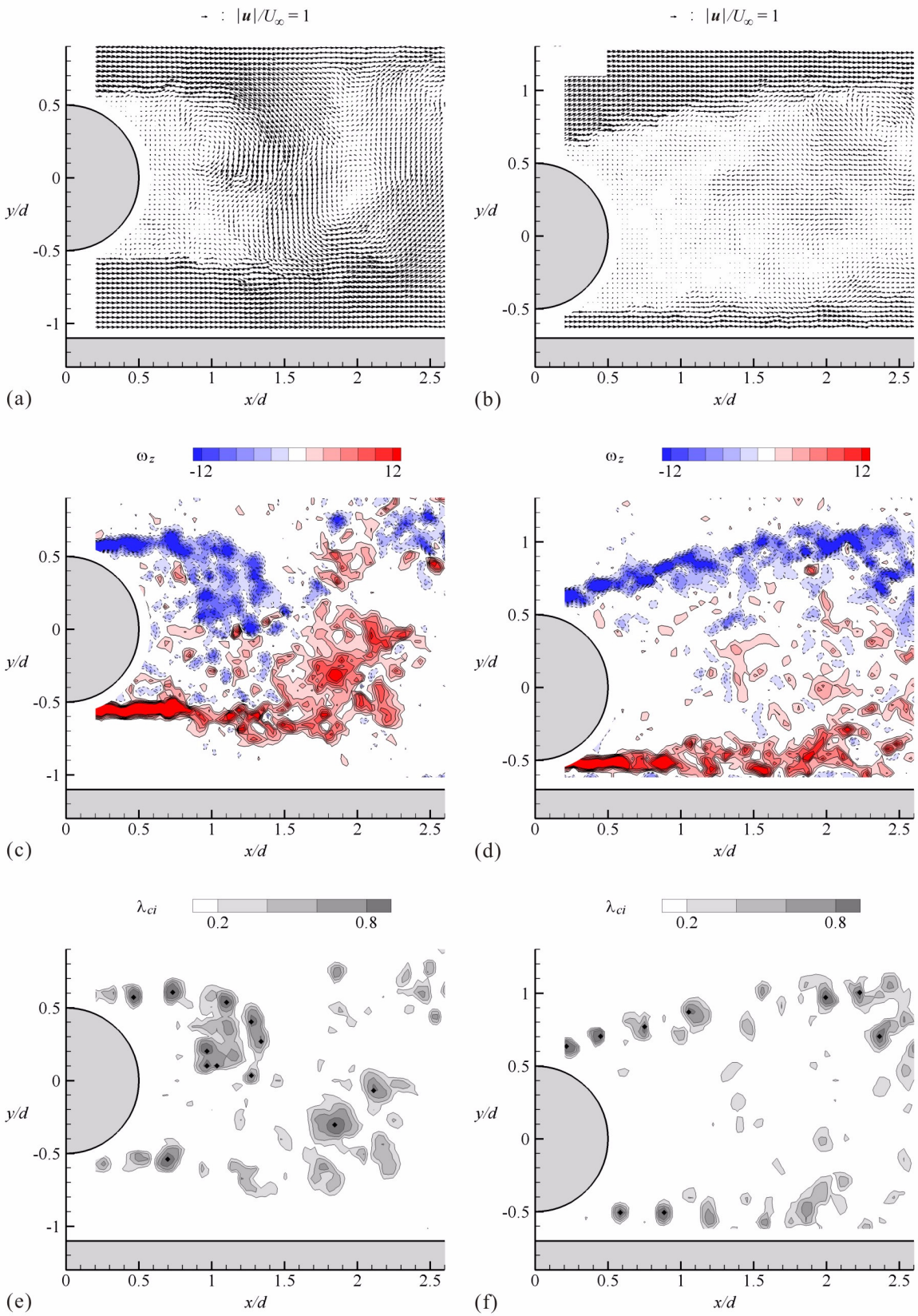

Figure 2.16: Typical instantaneous flow fields behind the cylinder with end-plates ($y_e/d = 0$): (a, b) velocity vectors, (c, d) contours of spanwise vorticity, and (e, f) contours of swirl strength; at two different gap ratios: (a, c, e) $h/d = 0.6$, and (b, d, f) $h/d = 0.2$; Re $= 0.4 \times 10^5$.

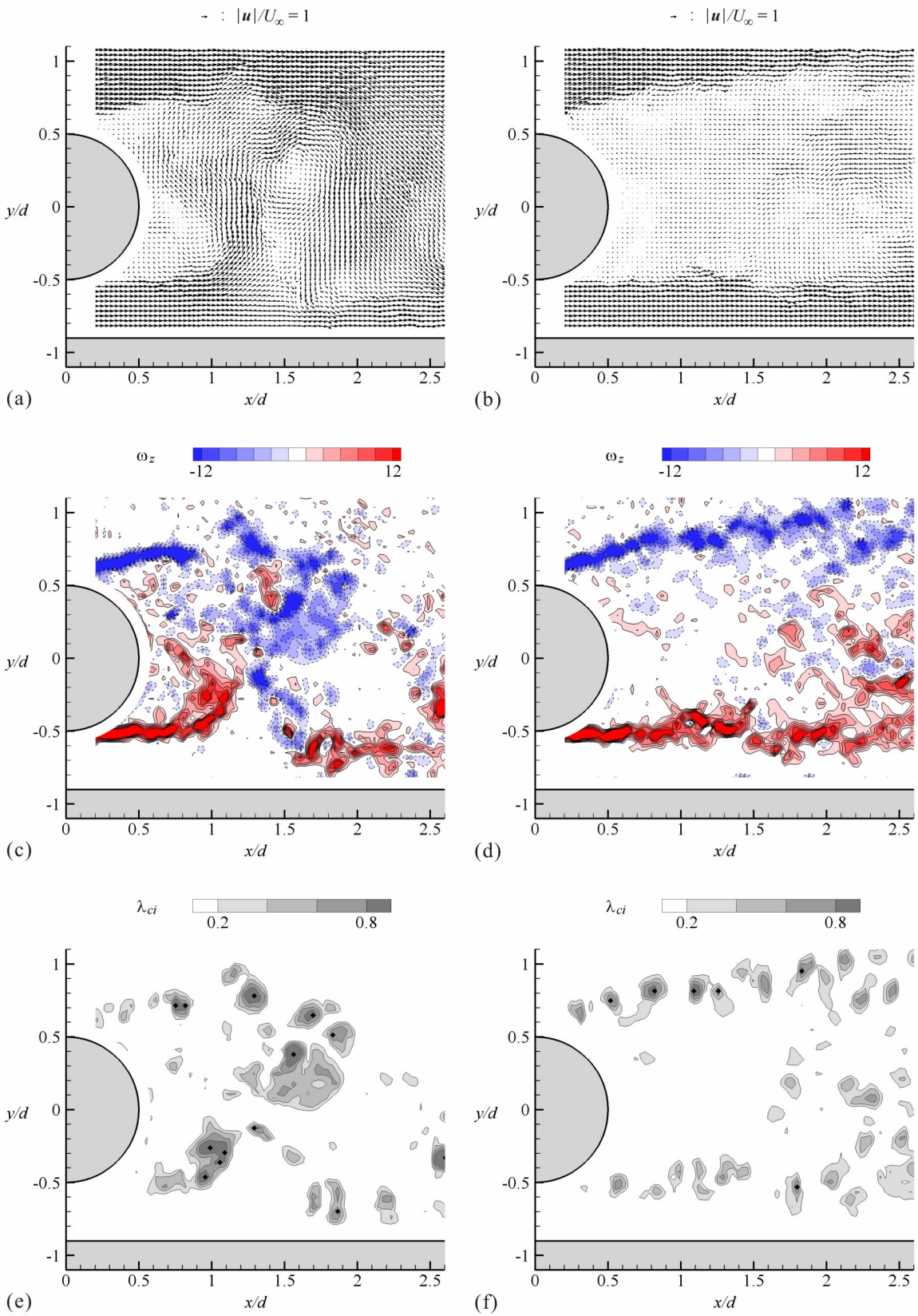

Figure 2.17: Two typical instantaneous flow fields behind the cylinder with end-plates ($y_e/d = 0$) at $h/d = 0.4$: (a, b) velocity vectors, (c, d) contours of spanwise vorticity, and (e, f) contours of swirl strength; $\mathrm{Re} = 0.4 \times 10^5$; showing the intermittency of the von Kármán-type vortex shedding.

a circular cylinder in a free stream (i.e., outside the ground effect) in the upper-subcritical (TrSL3) flow regime (cf. Section 1.4.2). At $h/d = 0.2$ [Figs. 2.16(b), (d), and (f)], however, such large-scale vortices are not generated and instead a so-called 'dead-fluid' zone is created behind the cylinder, bounded by two nearly parallel shear layers each producing only small-scale vortices (due to the shear layer instability) in the near wake region. A similar dead-fluid zone bounded by two nearly parallel shear layers was also continuously observed at $h/d = 0.3$ (not presented here).

Of further interest is that, at an 'intermediate' gap ratio of $h/d = 0.4$, the von Kármán-type vortex shedding was found to be intermittent in the near wake region. Two typical instantaneous flow fields at this gap ratio are shown in Fig. 2.17. As can be seen from the figures, at a certain moment when the large-scale vortices are formed behind the cylinder [Figs. 2.17(a), (c), and (e)] the near wake structure looks similar to that observed at the larger gap ratio [Figs. 2.16(a), (c), and (e)], whereas at another moment when the vortex shedding is suppressed [Figs. 2.17(b), (d), and (f)] the wake structure looks similar to that observed at the smaller gap ratio [Figs. 2.16(b), (d), and (f)].

Although the time evolution of the near wake structure was not able to be captured in this study due to the low sampling rate of the PIV recording, a statistical observation of this intermittency of the vortex shedding can be made by plotting the position of vortex cores. Figure 2.18 shows the plots of vortex cores, which were extracted from 100 instantaneous

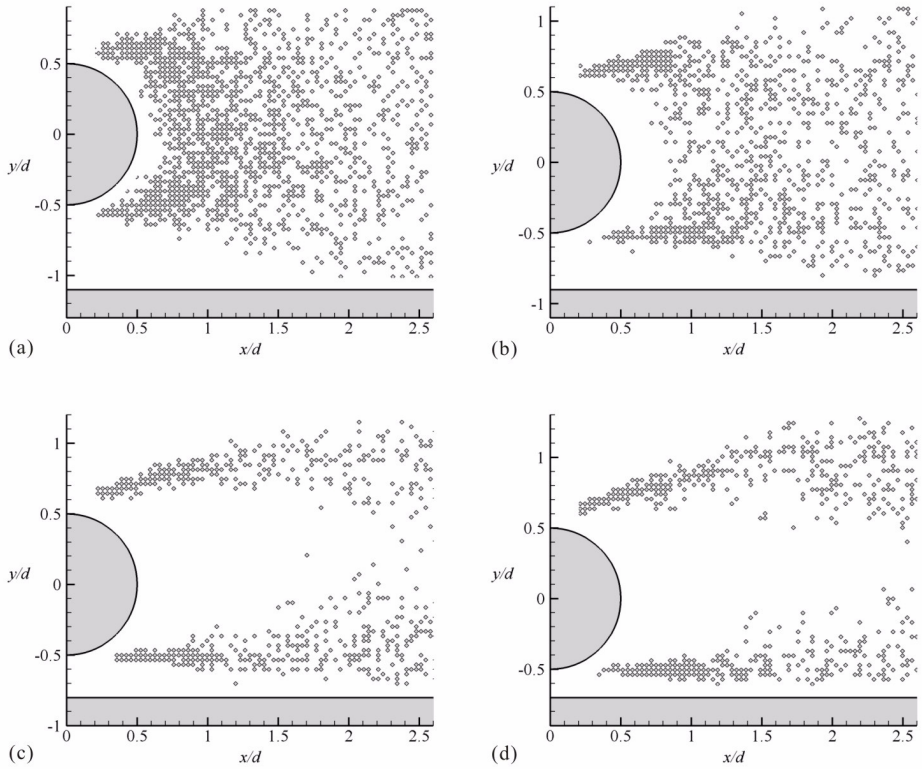

Figure 2.18: Plots of vortex cores (extracted from 100 instantaneous PIV data for each case) behind the cylinder with end-plates ($y_e/d = 0$): (a) $h/d = 0.6$, (b) $h/d = 0.4$, (c) $h/d = 0.3$, and (d) $h/d = 0.2$; $\mathrm{Re} = 0.4 \times 10^5$.

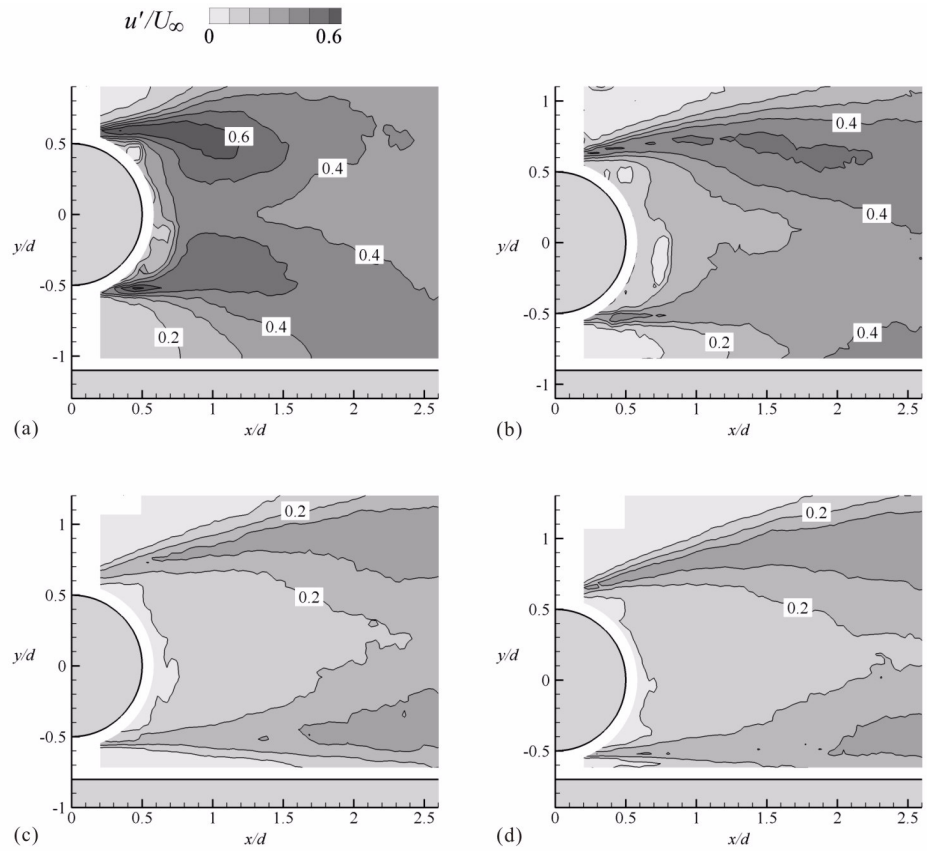

Figure 2.19: Contours of the r.m.s. of streamwise velocity fluctuation behind the cylinder with end-plates at $y_e/d = 0$: (a) $h/d = 0.6$, (b) $h/d = 0.4$, (c) $h/d = 0.3$, and (d) $h/d = 0.2$; $\mathrm{Re} = 0.4 \times 10^5$.

PIV data and then superimposed onto one figure for each case, for four different gap ratios of 0.6, 0.4, 0.3, and 0.2. These plots clearly show that the von Kármán-type vortex shedding is totally suppressed and a dead-fluid zone is formed behind the cylinder at $h/d = 0.2$ and 0.3, and also show that the number of the vortex cores captured behind the cylinder at $h/d = 0.4$ is less than that at $h/d = 0.6$, i.e., the von Kármán-type vortex shedding is intermittent at $h/d = 0.4$.

The cessation of the von Kármán-type vortex shedding at smaller gap ratios may also be presented in a more traditional manner, i.e., based on the statistics of velocity fluctuation. Figure 2.19 shows the contours of the r.m.s. values of streamwise velocity fluctuation, $(\overline{u'^2})^{\frac{1}{2}}$, for the four different gap ratios of 0.6, 0.4, 0.3, and 0.2. At $h/d = 0.6$, a pair of clear peaks in the velocity fluctuation can be seen just behind the cylinder, which looks similar to that observed behind a cylinder in a free stream (e.g., Braza *et al.* 2006). The vortex formation length L_f, which is usually defined as the distance from the centre of the cylinder to the peak of streamwise velocity fluctuation (cf. Section 1.4.2), is about $1.1d$ at this gap ratio; this is also similar to that for a cylinder in a free stream. As h/d is reduced to 0.3 and 0.2, however, the fluctuations become weak and the peaks move downstream, indicating the cessation of the vortex shedding in the near wake region.

2.3.4 Near wake structure (without end-plates)

Figure 2.20 shows the time-averaged, mid-span ($z/d = 0$) flow field data for the cylinder without end-plates. The time-averaged velocity vectors, streamwise velocity contours, and spanwise vorticity contours are described in Figs. 2.20(a, b), (c, d), and (e, f), respectively, for two different h/d of 0.6 and 0.2. Then Fig. 2.21 shows the plots of vortex cores for the two gap ratios, again extracted from 100 instantaneous PIV data for each case, and Fig. 2.22 shows the contours of the r.m.s. of streamwise velocity fluctuation. Note that here the data in the upper region of the cylinder as well as in the vicinity of the cylinder and ground surfaces have been discarded since they were disturbed by the reflection of light.

As can be seen from these figures, when without end-plates there are only minor differences in the near wake structure between the two gap ratios. The recirculation region is elongated and a dead-fluid zone is formed behind the cylinder even at $h/d = 0.6$ [Figs. 2.20(a), (c), (e), and Fig. 2.21(a), respectively], i.e., von Kármán-type vortices were not generated even at $h/d = 0.6$ when without end-plates. In fact, instantaneous mid-span flow fields for the two cases ($h/d = 0.6$ and 0.2, without end-plates) were found to be similar to those for the cylinder with end-plates with $h/d = 0.2$ [Fig. 2.16(b), (d), (f)], i.e., two nearly parallel shear layers were regularly observed in the near wake region.

Figure 2.23 shows a comparison of the time-averaged streamwise velocity profiles for the cases with and without end-plates at $h/d = 0.6$ and 0.2. Note that the profiles at $x/d = 1.0$, 1.5, 2.0, and 2.5 on the mid-span plane are plotted in these figures. The effects of the end-

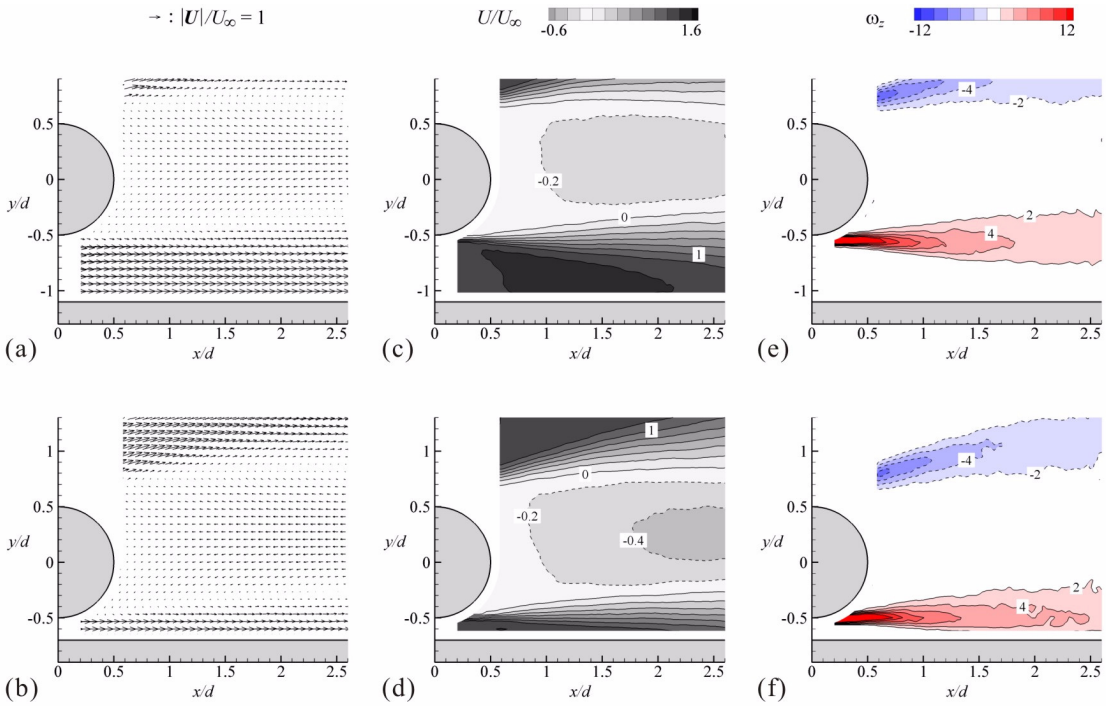

Figure 2.20: Time-averaged flow fields behind the cylinder without end-plates: (a, b) velocity vectors, (c, d) contours of streamwise velocity, and (e, f) contours of spanwise vorticity; at two different gap ratios: (a, c, e) $h/d = 0.6$, and (b, d, f) $h/d = 0.2$; Re $= 0.4 \times 10^5$.

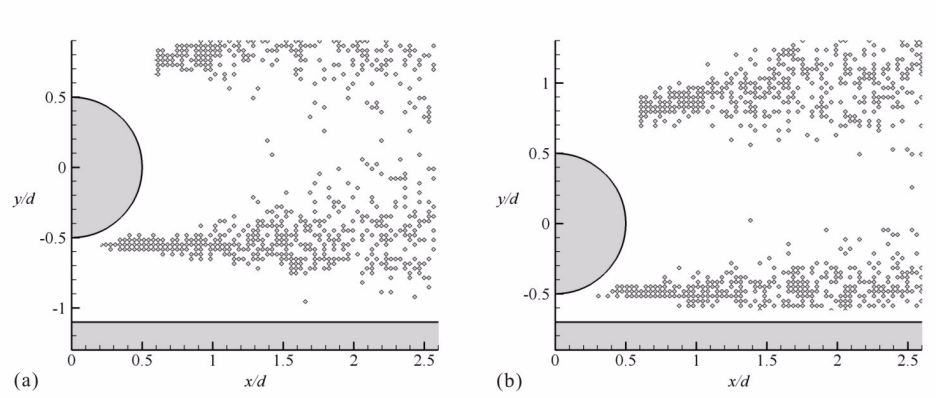

Figure 2.21: Plots of vortex cores (extracted from 100 instantaneous PIV data for each case) behind the cylinder without end-plates: (a) $h/d = 0.6$, (b) $h/d = 0.2$; $\mathrm{Re} = 0.4 \times 10^5$.

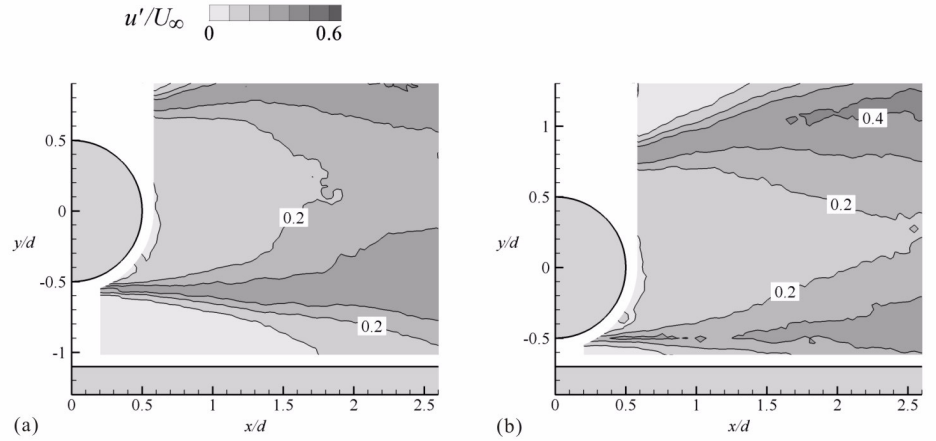

Figure 2.22: Contours of the r.m.s. of streamwise velocity fluctuation behind the cylinder without end-plates: (a) $h/d = 0.6$, (b) $h/d = 0.2$; $\mathrm{Re} = 0.4 \times 10^5$.

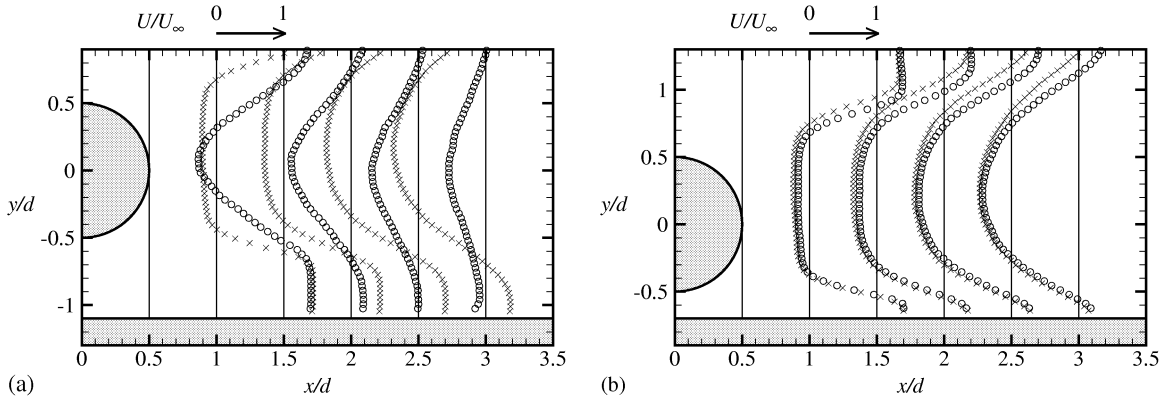

Figure 2.23: Mean streamwise velocity profiles: (a) $h/d = 0.6$, (b) $h/d = 0.2$; $\mathrm{Re} = 0.4 \times 10^5$. Circles ($\circ$) show the results for the cylinder with end-plates ($y_e/d = 0$), and cross marks ($\times$) show the results for the cylinder without end-plates.

plates are significant at $h/d = 0.6$ since the von Kármán-type vortex shedding occurs if the plates are used at this gap ratio, whereas no substantial effect can be seen at $h/d = 0.2$ as the vortex shedding does not occur for both cases at this gap ratio.

2.4 Discussion of results

In the following, further discussions will be made on: (i) the relation between the cessation of the von Kármán-type vortex shedding and the drag reduction of the cylinder in ground effect; (ii) the cause of the cessation of the vortex shedding in ground effect; and (iii) the intermittency of the vortex shedding in ground effect.

Link between the drag reduction and the cessation of vortex shedding

As concerns the first point of the discussion, it can be concluded that the drag reduction of the cylinder in ground effect observed in this study (when with end-plates) is directly related to the cessation of the von Kármán-type vortex shedding. It can be confirmed from Figs. 2.6 and 2.18 that, for the cylinder with end-plates, the gap regime in which the von Kármán-type vortex shedding is continuously observed [cf. Fig. 2.18(a)] corresponds to the regime of higher C_D ($h/d > 0.5$), whereas the regime in which the vortex shedding is totally suppressed [cf. Figs. 2.18(c) and (d)] corresponds to the regime of lower C_D ($h/d < 0.35$).

This direct relationship is relatively straightforward to understand since in general the von Kármán-type vortices behind a cylindrical bluff body continuously draw in fluid from the base region of the body during their growth and thereby sustain a low base pressure and therefore a high drag force acting on the body, for example as demonstrated by Bearman and Trueman (1972) for a cylinder in a free stream. The critical drag reduction observed in the present study may also be reasonably explained by this mechanism, i.e., the drag decreased because the base pressure increased due to the cessation of the vortex shedding. Although the base pressure of the cylinder was not measured in this study due to technical difficulties, the increase in the base pressure was clearly observed in numerical simulations, which will be presented later in Chapter 3.

It should also be noted that the intermediate value of the time-averaged C_D observed in the intermediate gap regime ($0.35 < h/d < 0.5$ when with end-plates, cf. Fig. 2.6) can also be explained by the above mechanism since it is in this regime that the von Kármán-type vortex shedding was found to become intermittent. In addition, the results for the cylinder without end-plates are also consistent with the above explanation, i.e., lower C_D was observed even in the larger gap regime of $h/d > 0.5$ as the von Kármán-type vortices were not generated when without end-plates.

This direct relationship between the drag reduction and the cessation of the von Kármán-type vortex shedding observed in this study is because of the use of the moving ground. The results obtained in this study, however, are also of great importance for understanding the physics of the ground effect with a fixed ground. That is to say, the continuous decrease in C_D usually observed for a cylinder placed near a fixed ground (cf. Sections 1.4.3 and 1.4.4) can now be explained by the combination of the effects of: (i) the cessation of the vortex

shedding; and (ii) the direct interference of the boundary layer formed on the ground. For example, the continuous drag reduction observed by Hiwada *et al.* (1986) at $h/d < 0.5$ with $\delta_B/d = 0.23$ (cf. Fig. 2.6) might be divided into two regimes: $0.3 < h/d < 0.5$, where the drag reduction is mainly due to the cessation of the vortex shedding, and $h/d < 0.3$, where it is mainly due to the direct interference of the boundary layer [note that Hiwada *et al.* (1986) found the critical gap ratio (for the cessation of the vortex shedding) to be 0.3 in their study]. This explanation is also consistent with the observation by Zdravkovich (1985b) that the decrease in C_D occurred when $h/d < \delta_B/d$; this is because he performed his experiments with $0.52 \leq \delta_B/d \leq 0.97$, i.e., the boundary layer was thicker than the critical gap ratio in his study (cf. Section 1.4.3).

Cause of the cessation of vortex shedding

Another important conclusion confirmed by using the moving ground in this study is that the von Kármán-type vortex shedding from the cylinder (with end-plates) did cease at $h/d < 0.3$ to 0.4 despite the use of the moving ground [note that the flow through the gap between the cylinder and the ground was not choked but accelerated even at $h/d = 0.2$, cf. Figs. 2.15 and 2.23(b)]. This leads to the second point of the discussion, i.e., the cause of the cessation of the von Kármán-type vortex shedding in ground effect.

First of all, it should be noted that a very thin boundary layer still locally existed on the moving ground in this study since the ground was running at the same speed as the free stream rather than as the locally accelerated flow through the gap between the cylinder and the ground. Therefore it might still be possible to argue that the very thin boundary layer generated vorticity of opposite sign and thus interfered with the separated shear layer from the bottom side of the cylinder, just as in the cases with a thick boundary layer formed on a fixed ground (Grass *et al.* 1984; Taniguchi and Miyakoshi 1990). Judging from the mean spanwise vorticity contours [Figs. 2.14(k) and (l)], however, the vorticity of the shear layer from the bottom side of the cylinder appears to be as strong as that from the upper side of the cylinder. Hence, there should be another explanation to the cessation of the shedding in ground effect.

In general (i.e., for general two-dimensional bluff bodies in a free stream), the formation of the von Kármán-type vortices is due to the wake instability caused by the communication between the two shear layers. As reviewed in Section 1.4.6, recent studies have shown that this wake instability can be explained by the existence of an absolutely unstable region in the near wake, which allows local disturbances to propagate both upstream and downstream and thus to produce a resonance between the travelling instability waves. From this viewpoint, the cessation of vortex shedding behind a cylinder with a backward splitter plate (Roshko 1955), for example, can be explained as that the plate prevents the resonance and hence the resulting vortex shedding when the plate changes the state of the near wake from being absolutely unstable to being convectively unstable. Of interest here is that a similar explanation might also be applicable to the cessation of the vortex shedding in ground effect observed in this study, i.e., the existence of the ground somehow restricts the propagation of disturbances in the near wake region and thus prevents the resulting von Kármán-type vortex shedding. This

issue will be further investigated using a linear stability analysis in Chapter 4.

For the cylinder without end-plates, however, an additional influence from the free-ends (or the effect of the aspect ratio l/d of the cylinder) also needs to be considered, since the von Kármán-type vortex shedding did not occur not only in the smaller gap regime but also in the larger gap regime. Concerning this point, Zdravkovich *et al.* (1989) has reported for a short circular cylinder ($2 \leq l/d \leq 8$) in a free stream that the dominant frequency of velocity fluctuation in the near wake region was different from that for a long circular cylinder, and hence he suggested the existence of a different type of vortex shedding behind a short cylinder (compared to the von Kármán-type vortex shedding behind a long cylinder). Although the PIV measurements in the present study were conducted only at the mid-span of the cylinder, it is inferred that the von Kármán-type vortex shedding behind the cylinder without end-plates was suppressed not only due to the influence of the nearby ground but also due to the influence of the tip vortices generated from the two free-ends of the cylinder. In other words, the results for the cylinder without end-plates show the combined effect of small h/d and l/d, both of which tend to discourage the formation of the von Kármán-type vortices.

Cause of the intermittency of vortex shedding

The third and final point of the discussion here is the intermittency of the von Kármán-type vortex shedding (behind the cylinder with end-plates) in the intermediate gap regime, which may also be of some relevance to the mechanisms of the cessation of the shedding discussed above. A similar intermittency of vortex shedding in an intermediate gap regime has been observed by Martinuzzi *et al.* (2003) for a square cylinder placed near a fixed ground. They suggested, however, that the intermittency of the shedding behind the square cylinder was due to the intermittency of the reattachment of the separated shear layer (from the bottom leading edge) on the bottom surface, which is not the case for a circular cylinder in ground effect. Bearman and Zdravkovich (1978) also suggested, based on the measurements of local velocity fluctuation in the near wake region, the intermittency of the vortex shedding for a circular cylinder placed near a fixed ground; but the mechanism of this intermittency is still unexplained.

A possible clue to the mechanism of the shedding intermittency can be found in the recent experiments by Zhang *et al.* (2005) for a half cylinder placed near a moving ground (with the flat surface of the cylinder facing downstream, cf. Fig. 1.1), where the vortex shedding was suddenly suppressed and the drag coefficient of the cylinder was suddenly dropped from about 1.5 to 1 as the gap ratio h/d was reduced from 0.55 to 0.525, as reviewed in Section 1.4.4. They reported that the flow separation from the bottom side of the half cylinder was fixed at the cylinder edge (i.e., the separation angle $\theta_{\text{sep}} = 90^\circ$) when $h/d \leq 0.525$, whereas that measured on the circular cylinder in the present study at $h/d = 0.4$ (at which the intermittency of the shedding occurs) was slightly greater than 90° (cf. Fig. 2.13) and presumably was not fixed but fluctuated in time due to the smooth geometry. Considering the other similarities between the two experiments, it is inferred that the fluctuation or unsteadiness of the flow separation point should be of some importance to the intermittency of the vortex shedding from a circular cylinder in the intermediate gap regime.

2.5 Conclusions

In this chapter, the characteristics of flow past a circular cylinder placed near and parallel to a moving ground were experimentally investigated at two upper-subcritical Reynolds numbers of 0.4 and 1.0×10^5. The experiments were performed using a moving ground running at the same speed as the free stream in order to avoid the confusing effects of the boundary layer formed on the ground and thereby to reveal the essence of the ground effect. The influence of the spanwise-end condition of the cylinder (the aspect ratio $l/d = 8.33$) was also examined by conducting the experiments with and without end-plates.

For the cylinder with end-plates, on which the surface oil flow patterns were observed to be essentially two-dimensional, significant effects of the gap ratio were observed on the near wake structure and also on the time-averaged drag coefficient. The flow characteristics may be classified into three gap regimes: large-gap ($h/d > 0.5$), intermediate-gap ($0.35 < h/d < 0.5$), and small-gap ($h/d < 0.35$) regimes. In the large-gap regime, large-scale von Kármán-type vortices were generated just behind the cylinder, resulting in higher drag coefficients of about 1.3 as the vortices continuously entrained air from the base region of the cylinder. In the intermediate-gap regime, the vortex shedding became intermittent, and hence the time-averaged drag coefficient rapidly decreased as h/d was reduced from 0.5 to 0.35. In the small-gap regime, the shedding totally ceased and instead a dead-fluid zone was created, bounded by two nearly parallel shear layers each producing only small-scale vortices. Of particular interest here was that there was little influence of h/d on the drag coefficient of the cylinder in the small-gap regime: C_D was almost constant at a lower value of slightly less than 1 for $h/d < 0.35$, unlike with that usually observed near a fixed ground.

For the cylinder without end-plates, on the other hand, no such significant effects of h/d were observed either on the near wake structure or on the drag coefficient. The von Kármán-type vortices were not generated in the near wake region, resulting in a nearly constant, lower drag coefficient of 0.85 to 0.95 for a wide h/d range from 2.0 to 0.05. A dead-fluid zone was continuously formed and thus a large recirculation region was created behind the cylinder at both larger and smaller gap ratios of 0.6 and 0.2.

Discussions were also given to the essential cause of the cessation of the von Kármán-type vortex shedding (for the cylinder with end-plates) in ground effect. A very thin boundary layer still locally existed on the moving ground and hence it might still be possible to argue that this thin boundary layer generated vorticity of opposite sign to interfere with the separated shear layer from the bottom side of the cylinder (just as in the cases with a thick boundary layer formed on a fixed ground). A more probable explanation to the cessation of the shedding observed in this study, however, is that the ground restricts the propagation of disturbances and thus prevents a resonance between the travelling instability waves in the near wake region, similar to the mechanism for the cessation of vortex shedding behind a cylinder equipped with a backward splitter plate. This issue will be further investigated using a linear stability analysis in Chapter 4.

Finally, the following point should be noted once again. It is true that these interesting results obtained in this experimental study is largely due to the use of the moving ground.

However, these results are of great importance also for understanding the fundamental physics of the ground effect with a fixed ground. That is to say, the effects of a fixed ground on the flow past a nearby cylinder may now be described by the combination of two main factors: (i) fundamental influence of the ground itself, which was revealed in the present study; and (ii) additional influence of the interference of the boundary layer formed on the ground. It should be fair to say that this experimental study 'indirectly' resolved, at least to some degree, the controversy concerning the continuous drag reduction of a circular cylinder placed near a fixed ground (cf. Section 1.4.3), which can now be explained by the combined effects of the cessation of the vortex shedding and the direct interference of the boundary layer.

Chapter 3

Numerical Study of Flow Past a Circular Cylinder in Ground Effect

3.1 Introduction

The von Kármán-type vortex shedding from a circular cylinder at high Reynolds numbers of about 10^4 or above is still a challenging subject in today's computational fluid dynamics (CFD) since the direct numerical simulations (DNS) of the Navier-Stokes equations for such flows are currently not feasible due to the huge computational costs required. Recent studies have shown, however, that some novel techniques such as unsteady RANS (URANS) and detached-eddy simulations (DES) could predict, to some extent, the unsteady motion of the vortex shedding with acceptable computational costs, as reviewed in Section 1.4.5.

The main objective of the numerical study described in this chapter, where the flow past a circular cylinder placed near a moving ground is simulated, is twofold. The first goal is to examine whether, and how accurately, URANS and DES can reproduce the cessation of the von Kármán-type vortex shedding and also the critical drag reduction of the cylinder in ground effect, both of which were observed in the experiments described in the previous chapter. The flow configuration studied here may be considered, from the viewpoint of CFD researchers, as one of the simplest (but still challenging) test cases that contain the problem of large-scale vortex shedding and its cessation or suppression, and hence the results of the present validation may serve as a primary criterion for the applicability of URANS and DES to such vortical flows often encountered in engineering applications. The second objective, on the other hand, is to investigate the predicted flow fields in more detail, and thus to provide further insight into the physical mechanisms of the flow as well as into the reason why the DES and URANS can/cannot correctly capture the cessation of the von Kármán-type vortex shedding in ground effect.

In the following, the details of the computation will be described in Section 3.2, and then some results of preliminary computations will be presented in Section 3.3. The main results and discussion will be given in Section 3.4, and finally a concluding summary will be given in Section 3.5. The DES in this study, which is based on the Spalart-Allmaras one-equation model (S-A model; Spalart and Allmaras 1992), is performed in a three-dimensional domain

with periodicity imposed in the spanwise direction, basically following the DES for a circular cylinder in a free stream by Travin *et al.* (2000). Meanwhile, the URANS simulations are carried out in both two- and three-dimensional domains, where the S-A model and also a classical, low-Reynolds-number k-ϵ model of Launder and Sharma (LS k-ϵ model; Launder and Sharma 1974) are employed. In addition to these, large-eddy simulations (LES) based on the constant Smagorinsky model (Smagorinsky 1963) are also performed, but only for the purpose of comparison in Section 3.3.

The Reynolds number of the flow is limited to the upper-subcritical regime ($0.4 \times 10^5 \leq \mathrm{Re} \leq 1.0 \times 10^5$) in line with the experimental study in the previous chapter. The influence of the Reynolds number in the numerical simulations will be presented in Section 3.3, but the main discussion in Section 3.4 will be developed on the results for a single Reynolds number of 0.4×10^5 to focus on the issues relevant to the ground effect rather than to the Reynolds number effect.

3.2 Computational details

3.2.1 Overview

Figure 3.1 summarises the computational domain and boundary conditions employed in this study; the ground effect was simulated by changing the gap ratio h/d from 1.0 to 0.1. The computations were conducted using a commercial CFD package, FLUENT6 (Fluent Inc. 2005), in which a finite volume method was used to discretise the governing/model equations for incompressible turbulent flows to be numerically solved. The equations were spatially discretised with second-order accuracy on multi-block structured grids (cf. Fig. 3.2), temporally discretised using a second-order fully-implicit scheme, and then iteratively solved. Further details of the computation are described in the following subsections.

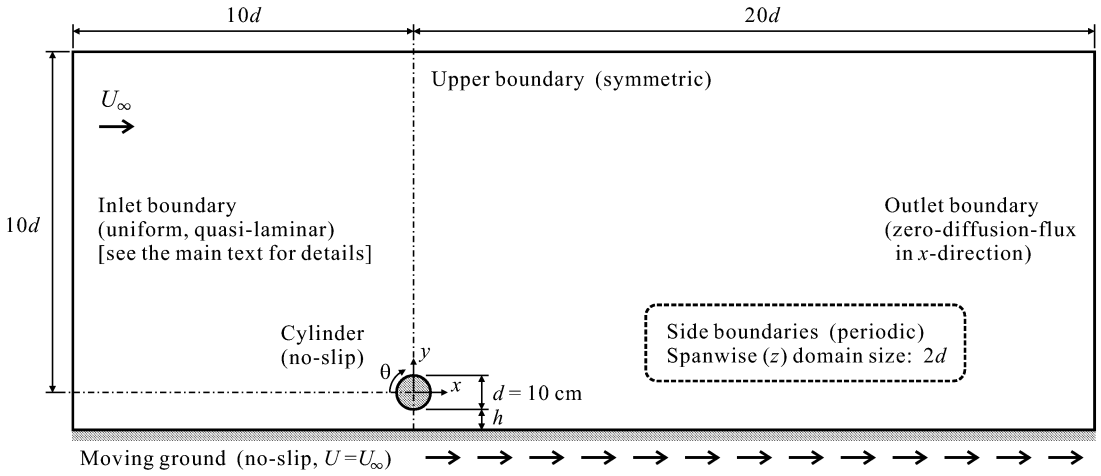

Figure 3.1: Computational domain and boundary conditions.

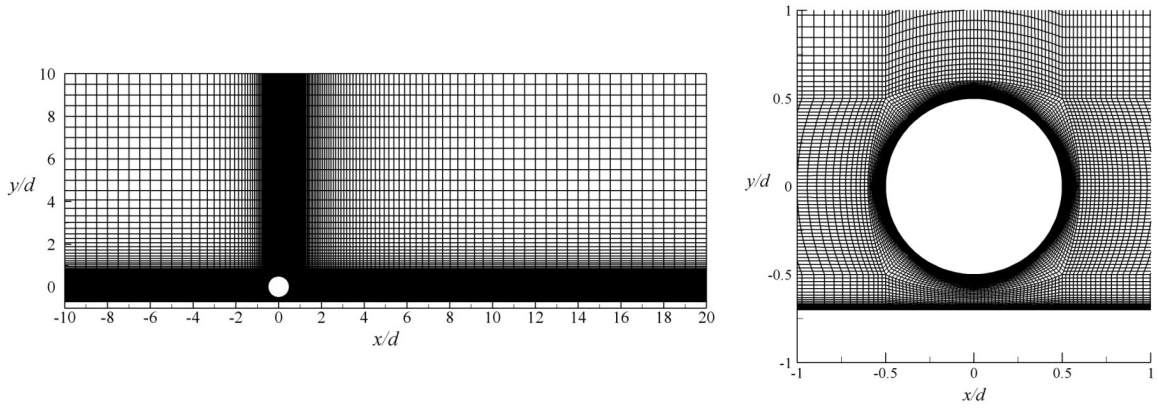

Figure 3.2: Example of computational grids ($h/d = 0.2$).

3.2.2 Governing equations and turbulence models

In general the motion of incompressible Newtonian fluids is expressed, regardless of whether the state of the flow is laminar or turbulent, by the following continuity and momentum (or Navier-Stokes) equations:

$$\frac{\partial u_i}{\partial x_i} \;=\; 0\,, \tag{3.1}$$

$$\frac{\partial u_i}{\partial t} + u_j \frac{\partial u_i}{\partial x_j} \;=\; -\frac{1}{\rho}\frac{\partial p}{\partial x_i} + \nu \frac{\partial^2 u_i}{\partial x_j \partial x_j}\,, \tag{3.2}$$

where x_i ($i = 1, 2$ for two-dimensional, or $1, 2, 3$ for three-dimensional systems) denote the Cartesian coordinates, u_i are the Cartesian components of instantaneous velocity of fluid, p is instantaneous static pressure, ρ and ν are the density and kinematic viscosity of fluid, respectively, and $\nu = \mu/\rho$, where μ is the dynamic viscosity. The physical properties (i.e., ρ, ν, and μ) are assumed to be constant in the present study.

For the cases where the state of the flow is turbulent, however, to numerically solve the above equations directly (i.e., direct numerical simulation) requires enormous computational costs due to a wide range of spatial/time scales of the flow. Hence the following turbulence models/approaches were employed in this study.

Unsteady RANS equations

As noted in Section 1.4.5, the concept of URANS is based on the triple decomposition of time-dependent variables (Hussain and Reynolds 1970). For the flow system considered here, the instantaneous velocity $u_i(t)$ and pressure $p(t)$ are to be decomposed as follows:

$$u_i(t) \;=\; \widehat{u}_i + \widetilde{u}_i(t) + u_i'(t)\,, \qquad p(t) \;=\; \widehat{p} + \widetilde{p}(t) + p'(t)\,, \tag{3.3}$$

where $\widehat{u}_i$, $\widetilde{u}_i(t)$ and $u_i'(t)$ denote the long-time-averaged, periodic and turbulent (stochastic) components of the velocity, respectively, and the same applies to $\widehat{p}$, $\widetilde{p}(t)$ and $p'(t)$. The first two components of each variable can be described as

$$\widehat{u}_i + \widetilde{u}_i(t) \;=\; U_i(t)\,, \qquad \widehat{p} + \widetilde{p}(t) \;=\; P(t)\,, \tag{3.4}$$

where $U_i(t)$ and $P(t)$ are the coherent components of the velocity and pressure, respectively. They can also be expressed by $\overline{u_i(t)}$ and $\overline{p(t)}$ with the overlines here denoting the process of ensemble-averaging, rather than time-averaging. Substituting the above relations into Eqs. (3.1) and (3.2) and taking ensemble-averages, we obtain the governing equations of $U_i(t)$ to be solved in URANS computations:

$$\frac{\partial U_i}{\partial x_i} \;=\; 0\,, \tag{3.5}$$

$$\frac{\partial U_i}{\partial t} + U_j\frac{\partial U_i}{\partial x_j} \;=\; -\frac{1}{\rho}\frac{\partial P}{\partial x_i} + \frac{\partial}{\partial x_j}\left(\nu\frac{\partial U_i}{\partial x_j} - \overline{u_i'u_j'}\right)\,. \tag{3.6}$$

Equation (3.6) is referred to as the unsteady Reynolds-averaged Navier-Stokes (URANS) equations, which contain unknown correlation terms $\overline{u_i'u_j'}$ to be modelled below. Note that $-\rho\overline{u_i'u_j'} = -\rho(\overline{u_iu_j} - U_iU_j) = \tau_{ij}$ are called the Reynolds stresses since they act as apparent stresses on the mean (i.e., ensemble-averaged) flow field.

Launder-Sharma k-ϵ model

The low Reynolds number k-ϵ model of Launder and Sharma (LS k-ϵ model; Launder and Sharma 1974) belongs to the family of linear eddy-viscosity models, in which the Reynolds stresses are modelled based on the Boussinesq eddy-viscosity concept as

$$-\overline{u_i'u_j'} \;=\; 2\nu_T S_{ij} - \frac{2}{3}k\delta_{ij}\,, \tag{3.7}$$

where ν_T is the kinematic eddy viscosity, and S_{ij} denotes the mean strain-rate tensor:

$$S_{ij} \;=\; \frac{1}{2}\left(\frac{\partial U_i}{\partial x_j} + \frac{\partial U_j}{\partial x_i}\right)\,. \tag{3.8}$$

In order to obtain the value of ν_T, in the LS k-ϵ model, the following two model transport equations are solved for the turbulent kinetic energy k and a quantity $\tilde{\epsilon}$:

$$\frac{\partial k}{\partial t} + U_j\frac{\partial k}{\partial x_j} \;=\; \frac{\partial}{\partial x_j}\left\{\left(\nu + \frac{\nu_T}{\sigma_k}\right)\frac{\partial k}{\partial x_j}\right\} + 2\nu_T S_{ij}S_{ij} - (\tilde{\epsilon} + \epsilon_0)\,, \tag{3.9}$$

$$\frac{\partial \tilde{\epsilon}}{\partial t} + U_j\frac{\partial \tilde{\epsilon}}{\partial x_j} \;=\; \frac{\partial}{\partial x_j}\left\{\left(\nu + \frac{\nu_T}{\sigma_\epsilon}\right)\frac{\partial \tilde{\epsilon}}{\partial x_j}\right\} + \frac{\tilde{\epsilon}}{k}\left(2C_{\epsilon1}f_1\nu_T S_{ij}S_{ij} - C_{\epsilon2}f_2\tilde{\epsilon}\right) + E\,, \tag{3.10}$$

where $\tilde{\epsilon}$ is related to ϵ, or the dissipation rate of k, by

$$\epsilon \;=\; \tilde{\epsilon} + \epsilon_0\,. \tag{3.11}$$

The kinematic eddy viscosity ν_T is then estimated as

$$\nu_T \;=\; C_\mu f_\mu \frac{k^2}{\tilde{\epsilon}}\,, \tag{3.12}$$

with the following model constants and damping functions:

$$C_\mu \;=\; 0.09\,, \qquad C_{\epsilon1} \;=\; 1.44\,, \qquad C_{\epsilon2} \;=\; 1.92\,, \qquad \sigma_k \;=\; 1.0\,, \qquad \sigma_\epsilon \;=\; 1.3\,, \tag{3.13}$$

$$\epsilon_0 \;=\; 2\nu\left(\frac{\partial\sqrt{k}}{\partial x_j}\right)^2\,, \qquad E \;=\; 2\nu\nu_T\left(\frac{\partial^2 U_i}{\partial x_j\partial x_k}\right)^2\,, \tag{3.14}$$

$$f_\mu \;=\; e^{-3.4/(1+\mathrm{Re}_T/50)^2}\,, \qquad f_1 \;=\; 1.0\,, \qquad f_2 \;=\; 1-0.3\,e^{-\mathrm{Re}_T^2}\,, \tag{3.15}$$

where Re_T is the (modified) turbulent Reynolds number locally defined as

$$\mathrm{Re}_T \;=\; \frac{k^2}{\tilde{\epsilon}\nu}\,. \tag{3.16}$$

Further details of the model equations, constants and damping functions can be found in the original paper by Launder and Sharma (1974) and also in some technical books, e.g., by Wilcox (1998).

Spalart-Allmaras model

The Spalart-Allmaras model (S-A model; Spalart and Allmaras 1992) is another type of eddy-viscosity-based RANS model. In the S-A model, the Reynolds stresses are estimated based on the eddy-viscosity concept, but not taking into account the contribution from k, as

$$-\overline{u_i' u_j'} \;=\; 2\nu_T S_{ij}\,, \tag{3.17}$$

since neither k nor ϵ is calculated in this model. Alternatively, the following single model transport equation is solved for $\tilde{\nu}$, which corresponds to a modified form of the kinematic eddy-viscosity ν_T:

$$\frac{\partial\tilde{\nu}}{\partial t} + U_j\frac{\partial\tilde{\nu}}{\partial x_j} \;=\; \frac{1}{\sigma_{\tilde{\nu}}}\left[\frac{\partial}{\partial x_j}\left\{(\nu+\tilde{\nu})\,\frac{\partial\tilde{\nu}}{\partial x_j}\right\} + C_{b2}\left(\frac{\partial\tilde{\nu}}{\partial x_j}\right)^2\right] + C_{b1}\tilde{S}\tilde{\nu} - C_{w1}f_w\left(\frac{\tilde{\nu}}{n}\right)^2, \tag{3.18}$$

where

$$\tilde{S} \;=\; \sqrt{2\Omega_{ij}\Omega_{ij}} + \frac{\tilde{\nu}}{\kappa^2 n^2}\left(1-\frac{\chi}{1+\chi f_{v1}}\right)\,, \qquad f_w \;=\; g\left(\frac{1+C_{w3}^6}{g^6+C_{w3}^6}\right)^{1/6}\,,$$
$$f_{v1} \;=\; \frac{\chi^3}{\chi^3+C_{v1}^3}\,, \qquad \chi \;=\; \frac{\tilde{\nu}}{\nu}\,, \qquad g \;=\; r + C_{w2}\left(r^6-r\right)\,, \qquad r \;=\; \frac{\tilde{\nu}}{\tilde{S}\kappa^2 n^2}\,, \tag{3.19}$$

and

$$\sigma_{\tilde{\nu}} \;=\; \frac{2}{3}\,, \qquad C_{b1} \;=\; 0.1335\,, \qquad C_{b2} \;=\; 0.622\,, \qquad C_{v1} \;=\; 7.1\,,$$
$$C_{w1} \;=\; \frac{C_{b1}}{\kappa^2} + \frac{1+C_{b2}}{\sigma_{\tilde{\nu}}}\,, \qquad C_{w2} \;=\; 0.3\,, \qquad C_{w3} \;=\; 2.0\,, \qquad \kappa \;=\; 0.4187\,. \tag{3.20}$$

Here n is the distance from the nearest wall boundary, and κ is the von Kármán constant. The physical meaning and derivation of each term/coefficient can be found in the original paper by Spalart and Allmaras (1992). The kinematic eddy-viscosity ν_T is then calculated from $\tilde{\nu}$ as

$$\nu_T \;=\; f_{v1}\tilde{\nu}\,. \tag{3.21}$$

Note that, as can be seen from the definition given above, f_{v1} serves as a damping function for ν_T in near-wall regions. That is, the S-A model is also a low Reynolds number model, which is basically designed to be used with a fine computational grid that can resolve the viscous sublayer on a wall.

Large-eddy simulation

Although performed only for comparison in this study, the fundamentals of LES are also given here as they are closely related to DES described later. As noted in Section 1.4.5, the concept of LES is to directly simulate the motion of large-scale eddies, which are generally much more energetic and therefore influential on the global behaviour of the flow than the small-scale eddies that are to be modelled. The large-scale motion of the flow can be defined by the process of 'filtering' (Leonard 1974). It follows that a filtered flow field is solved in LES in contrast to an ensemble-averaged flow field being solved in URANS.

For LES several types of filtering methods have been proposed so far. When the LES is performed with the finite volume method, however, the process of spatial discretisation itself, details of which will be described later, implicitly serves as a so-called box-filter:

$$\overline{u}_i(x_1, x_2, x_3, t) \;=\; \frac{1}{V_{\mathrm{cv}}(x_1, x_2, x_3)} \iiint_{\mathcal{V}} u_i(x'_1, x'_2, x'_3, t)\, \mathrm{d}x'_1 \mathrm{d}x'_2 \mathrm{d}x'_3 \;, \quad x'_1, x'_2, x'_3 \in \mathcal{V} \;, \tag{3.22}$$

where the overline denotes the process of filtering, rather than ensemble-averaging or time-averaging. V_{cv} is the volume of a control-volume (or a cell), and $\mathcal{V}$ is the domain of the control-volume. It should be noted that the size of the box-filter is hence identical to that of each control-volume in this case.

Filtering the continuity and the Navier-Stokes equations [Eqs. (3.1) and (3.2)], respectively, yields the following governing equations to be solved in LES:

$$\frac{\partial \overline{u}_i}{\partial x_i} \;=\; 0 \;, \tag{3.23}$$

$$\frac{\partial \overline{u}_i}{\partial t} + \frac{\partial \overline{u_i u_j}}{\partial x_j} \;=\; -\frac{1}{\rho}\frac{\partial \overline{p}}{\partial x_i} + \nu \frac{\partial^2 \overline{u}_i}{\partial x_j \partial x_j} \;. \tag{3.24}$$

The filtered Navier-Stokes equation [Eq. (3.24)] contains unknown terms $\overline{u_i u_j}$ produced by the filtering of the non-linear convection terms in the original Navier-Stokes equation (note that the filtered products $\overline{u_i u_j}$ are not identical to the products of filtered variables $\overline{u}_i\, \overline{u}_j$). Introducing the subgrid-scale Reynolds stress τ^{s}_{ij} as

$$\tau^{\mathrm{s}}_{ij} \;=\; -\rho \left(\overline{u_i u_j} - \overline{u}_i\, \overline{u}_j \right) \;, \tag{3.25}$$

which is analogous to the Reynolds stress τ_{ij} in the RANS approach [cf. Eq. (3.6)], and then using the notations U_i and P for the filtered (or resolved) velocity $\overline{u}_i$ and pressure $\overline{p}$, respectively, we can rewrite Eqs. (3.23) and (3.24) as

$$\frac{\partial U_i}{\partial x_i} \;=\; 0 \;, \tag{3.26}$$

$$\frac{\partial U_i}{\partial t} + U_j \frac{\partial U_i}{\partial x_j} \;=\; -\frac{1}{\rho}\frac{\partial P}{\partial x_i} + \frac{\partial}{\partial x_j}\left(\nu \frac{\partial U_i}{\partial x_j} + \frac{\tau^{\mathrm{s}}_{ij}}{\rho} \right) \;. \tag{3.27}$$

The above equations are in the same form as the governing equations for URANS [Eqs. (3.5) and (3.6)] except for the difference of τ^{s}_{ij} and τ_{ij}. Hence the governing equations for URANS and LES can be solved using the same numerical schemes (note that this is an important factor that makes DES feasible, although the spatial discretisation methods employed in the present study are different between URANS and LES/DES as will be described later).

One of the most basic and famous models to calculate the subgrid-scale Reynolds stress τ_{ij}^{s} is the Smagorinsky model (Smagorinsky 1963), which was employed in this study. The model is based on the Boussinesq eddy-viscosity concept as

$$\tau_{ij}^{\mathrm{s}} \;=\; 2\nu_T^{\mathrm{s}}\overline{s}_{ij}\,, \qquad \overline{s}_{ij} \;=\; \frac{1}{2}\left(\frac{\partial U_i}{\partial x_j}+\frac{\partial U_j}{\partial x_i}\right)\,, \tag{3.28}$$

where

$$\nu_T^{\mathrm{s}} \;=\; L_{\mathrm{s}}^2\overline{s}\,, \qquad \overline{s} \;=\; \sqrt{2\overline{s}_{ij}\overline{s}_{ij}}\,, \tag{3.29}$$

and

$$L_{\mathrm{s}} \;=\; \min\left[\,\kappa n\,,\; C_{\mathrm{s}}V_{\mathrm{cv}}^{\frac{1}{3}}\right]\,, \qquad C_{\mathrm{s}} \;=\; (\text{constant};\ 0.1 \text{ in the present study})\,. \tag{3.30}$$

Here κ is the von Kármán constant [cf. Eq. (3.20)] and n is the distance from the nearest wall. Note that the scale of the spatial filter (or the grid scale $V_{\mathrm{cv}}^{\frac{1}{3}}$) required to perform 'LES-NWR' or 'pure LES' (cf. Section 1.4.5) is much smaller than that used in this study (described later), and this is the main reason why the LES described above is used only for the purpose of comparison in this study. A number of studies have been reported on 'LES-NWM' and also on the dynamic Smagorinsky model, but the details are not provided here; see Ferziger (1996) and Pope (2000) for more details on those topics.

Detached-eddy simulation

In the detached-eddy simulation (DES; Shur *et al.* 1999), a single turbulence model serves as a statistical model for calculating τ_{ij} in near-wall regions (URANS mode) and also serves as a subgrid-scale model for calculating τ_{ij}^{s} in far-wall regions (LES mode). A slightly modified version of the S-A model was used by Shur *et al.* (1999) as the single turbulence model in their DES; the same model was also used in the present study.

As noted before, the S-A model is a turbulence model originally designed to close and solve the RANS equations [Eq. (3.6)], i.e., the model contributes to calculate the Reynolds stress τ_{ij}. Hence, in principle, applying the S-A model to the filtered Navier-Stokes equations [Eq. (3.27)] is physically incorrect. However, under the condition of local equilibrium (where the production of turbulence quantities is balanced by their dissipation or destruction), the S-A model leads to the relation $\tilde{\nu} \sim n^2\tilde{S}$, which has a similar form to the Smagorinsky model [Eq. (3.29)] for LES. It is this analogy that makes feasible the use of the (modified) S-A model not only as a statistical model in the URANS mode but also as a subgrid-scale model in the LES mode.

Specifically, the S-A model is used as the single turbulence model in DES after replacing the wall-distance n with a new length scale $\tilde{n}$ defined as

$$\tilde{n} \;=\; \min\left[\,n\,,\; C_{\mathrm{des}}\Delta_{\max}\,\right]\,, \qquad C_{\mathrm{des}} = 0.65\,, \qquad \Delta_{\max} = \max\left[\Delta x_1, \Delta x_2, \Delta x_3\right] \tag{3.31}$$

where Δ_i is the size of each control-volume (or grid spacing) in the i-th direction. It follows that the model works as a statistical model to calculate τ_{ij} when $n < C_{\mathrm{des}}\Delta_{\max}$ (URANS mode), and as a subgrid-scale model to calculate τ_{ij}^{s} when $n > C_{\mathrm{des}}\Delta_{\max}$ (LES mode). That

is, the solution of DES represents the ensemble-averaged flow field where $n < C_{\mathrm{des}}\Delta_{\max}$, and the filtered flow field where $n > C_{\mathrm{des}}\Delta_{\max}$.

A big advantage of DES is that a grid highly stretched in the streamwise and spanwise directions can be used in near-wall regions since the flow is solved there in the URANS mode. This significantly reduces the computational cost of DES compared with that of (pure) LES, without impairing the capability to capture large-scale eddy structures in far-wall regions. The simple formulation of DES described by Eq. (3.31), however, raises an issue concerning the physical interpretation of the 'grey area' ($n \sim 0.65\Delta_{\max}$), where the operation mode is switched between URANS and LES (i.e., the physical meaning of the solution is switched between the ensemble-averaged flow field and the filtered flow field). The justification of this switch solely relies on the disparity in the scales between the attached- and detached-eddies (Spalart 2001). In practice, the switch between the URANS and LES modes can take place inside the boundary layers when using excessively fine computational grids, and this often causes a premature or grid-induced separation (Menter *et al.* 2003). It follows that the grid spacing for DES must be carefully decided so that the boundary layers are analysed in the URANS mode rather than in the LES mode.

3.2.3 Computational grids

Two- and three-dimensional multi-block structured grids were created, the former of which were only for URANS and the latter of which were for both URANS and DES. The same three-dimensional grids were also used for LES for the purpose of comparison with URANS and DES, although recognising that the grids were not suitable for LES . The multi-block grid topology shown in Fig. 3.2, which basically follows that used for a circular cylinder in a free stream by Menter *et al.* (2003), was employed because of its applicability to the current flow configuration (i.e., with a nearby ground). For the main part of the study (i.e., to study the ground effect), fourteen different grids (seven for two-dimensional and the other seven for three-dimensional cases, for $h/d = 0.1$, 0.2, 0.3, 0.4, 0.5, 0.6, and 1.0, respectively) were created but keeping the same grid topology; details are described below.

For the two-dimensional (x-y) grids, 200 grid points were equidistantly located around the cylinder, whereas 180 points were non-equidistantly distributed on the ground. The distance from the solid (i.e., the cylinder and ground) surfaces to the nearest grid points is $0.0002d$, which ensures a sufficient spatial resolution of $y^+ \leq 1.2$ for the cases of $\mathrm{Re} = 1.0 \times 10^5$ and $y^+ \leq 0.6$ for $\mathrm{Re} = 0.4 \times 10^5$ (y^+ is the dimensionless distance defined as $y^+ = u_\tau n/\nu$, and u_τ is the friction velocity). The number of the grid points for the two-dimensional grids ranges from 27,200 (for $h/d = 0.1$) to 35,300 (for $h/d = 1.0$).

The three-dimensional grids were then created by simply extending the two-dimensional grids in the spanwise (z) direction. The spanwise length of the domain was set at $2d$ with periodic boundary conditions imposed on the ends, following the DES by Travin *et al.* (2000), and 40 grid points were equidistantly located in that direction, i.e., the total number of the grid points for the three-dimensional grids ranges from 1.1 to 1.4 million (depending on h/d), and the spanwise grid spacing $\Delta z = 0.05d$. It should be noted that this spanwise grid spacing was selected considering the thickness of the boundary layer on the cylinder surface (about

$0.03d$ at the maximum) since Δz is the largest grid spacing (i.e., larger than Δx and Δy) around the cylinder and hence in the DES directly affects the switching between the URANS and LES modes in that region [cf. Eq. (3.31)]. Specifically, for the region around the cylinder, a thin URANS layer of $0.65\Delta z$ ($= 0.0325d$) thickness was formed, in which 30 grid points were allocated in the direction normal to the cylinder surface.

In addition to these fourteen grids for the main part of the study (i.e., the study on the ground effect), another five grids of different spatial resolutions (in the x-y plane and also in the z direction) were also created (but only for $h/d = 1.0$) to examine the grid dependency of the simulations. Although a problem of explicit grid dependency in DES has been pointed out by Menter *et al.* (2003) and other researchers, a certain degree of grid convergence was achieved in this study due to the rather simple geometry of the flow simulated; details will be described later in Section 3.3, where the grid dependency of URANS, DES, and LES will be compared with each other.

3.2.4 Discretisation methods

For the spatial discretisation, FLUENT6 employs the finite volume method with the collocated grid system (Rhie and Chow 1983). In this method, the governing and model transport equations are spatially discretised, after being integrated over each control-volume defined by the grid, into the following form of equations:

$$\sum_{\text{faces}} \phi_f \boldsymbol{U}_f \cdot \boldsymbol{A}_f \;=\; \sum_{\text{faces}} \Gamma_f^{\phi} \left(\nabla\phi\right)_f \cdot \boldsymbol{A}_f + S_{\text{P}}^{\phi} V_{\text{cv}} \,, \tag{3.32}$$

where ϕ denotes the variables to be solved in URANS, DES and LES (U_i, k, $\tilde{\epsilon}$ and $\tilde{\nu}$), and f indicates each interface of the control-volume of interest. $\boldsymbol{U}_f$ is the velocity vector at face f. $\boldsymbol{A}_f = A_f \boldsymbol{n}_f$ is the area vector, where A_f is the area of face f and $\boldsymbol{n}_f$ is the unit vector normal to face f. Γ_f^{ϕ} and $(\nabla\phi)_f$ are the 'apparent' diffusivity and gradient of each variable ϕ at face f, respectively, and S_{P}^{ϕ} is the 'apparent' source of ϕ at the control-volume of interest. Note that S_{P}^{ϕ} here includes the time-dependent term, and hence the equations need to be further discretised temporally. Also note that the pressure term is also included in S_{P}^{ϕ} for $\phi = U_i$. Hence in this study the SIMPLE algorithm (Patankar 1980) was used to solve both the velocity and pressure fields implicitly; details will be described later.

For URANS computations in this study, the values of ϕ_f in the convection term [i.e., the left hand side of Eq. (3.32)] were interpolated by using a second-order upwind scheme. For DES and LES, however, a second-order central-difference scheme was used rather than the upwind scheme, in order to reduce the influence of numerical diffusion (see, e.g., Ferziger and Peric 2002). Meanwhile, Γ_f^{ϕ} and $(\nabla\phi)_f$ in the (apparent) diffusion term [i.e., the first term of the right hand side of Eq. (3.32)] were interpolated using the second-order central-difference scheme (for URANS, DES and LES). The volume flux $\boldsymbol{U}_f \cdot \boldsymbol{n}_f$ was calculated not by linear interpolation but by the method of momentum-weighted averaging so as to avoid the problem of oscillatory or 'checker-boarding' pressure field on the collocated grid system (cf. Rhie and Chow 1983). Further details of the above schemes can also be found in the FLUENT6 guide (Fluent Inc. 2005).

For the temporal discretisation, a second-order (or three-time-level) fully-implicit scheme was employed in this study as follows:

$$\frac{3\phi_{\mathrm{P}}^{n} - 4\phi_{\mathrm{P}}^{n-1} + \phi_{\mathrm{P}}^{n-2}}{2\Delta t} \;=\; F(\phi^{n})_{\mathrm{P}} \;, \tag{3.33}$$

where the superscripts n, $n-1$ and $n-2$ represent time t_n, t_{n-1} and t_{n-2}, respectively, and $t_{n-i} \equiv t_n - i\Delta t$, where Δt is a short 'time step' to be given later. The subscript P denotes the control-volume of interest, and $F(\phi^n)_{\mathrm{P}}$ is the sum of all the time-independent terms of the spatially-discretised equation for ϕ_{P}^n. Note that $F(\phi^n)_{\mathrm{P}}$ contains unknown values of ϕ at the own and neighbour control-volumes at 'new' time $t = t_n$, so that several iterations are required to solve the flow field for each time point, as will be described below.

3.2.5 Solution algorithm

The discretised transport equations for ϕ, which are a series of nonlinear algebraic equations, were linearised and solved in this study by using the 'segregated' solver in FLUENT6 (Fluent Inc. 2005), in which the equations for each variable are sequentially (i.e., segregated from one another) solved by using the Gauss-Seidel method coupled with an algebraic multigrid (AMG) method. Since the momentum equations contain the pressure term, for which there are no independent equations to be solved, the SIMPLE algorithm (Patankar 1980) was used in the solution process to derive equations for the pressure correction P' from the combination of the continuity and the momentum equations. Hence the whole solution process can be summarised as follows:

1. Give initial conditions for all variables.
2. Calculate and update the coefficients of all the algebraic equations for $t = t_n$ based on the values of ϕ^n, ϕ^{n-1} and ϕ^{n-2}.
3. Solve the algebraic equations for U_i^n.
4. Solve the algebraic equations for P'^n.
5. Correct the values of P^n based on P'^n and the current values of P^n.
6. Correct the values of U_i^n based on P'^n and the current values of U_i^n.
7. Solve the algebraic equations for k^n, $\tilde{\epsilon}^n$ and $\tilde{\nu}^n$ (as appropriate).
8. If the solution is judged to be...
   (a) not converged, return to Step 2.
   (b) converged, set the time forward (i.e., $n = n + 1$) and then return to Step 2.

For most computations in this study, 20 to 30 iterations were found to be enough for the solution at each time instant to be converged (judging from the magnitude of residuals as well as from several test computations in which more iterations were carried out to directly check the influence of the iteration errors). The dimensionless time step $\Delta t \cdot U_\infty / d$ was set at 0.021, which ensured sufficiently small CFL numbers of less than 2 for most part of the computational domain (the CFL number is locally defined by $\Delta t \cdot U_i / \Delta x_i$). A smaller $\Delta t \cdot U_\infty / d$ of 0.0042 was preliminarily tested for comparison, and the difference between the two cases were found to be very small, as will be shown later in Section 3.3.

The above iteration process was first continued until the flow field had sufficiently developed, i.e., the influence of initial conditions (a uniform flow was given for most cases) had become negligible, and then was further continued to obtain the long-time-averaged data of the flow field. At least 100 dimensionless time units ($t \cdot U_\infty/d$), which corresponded to about 20 to 30 vortex-shedding cycles, were taken at this stage so as to obtain reliable statistical information.

3.2.6 Boundary conditions

At the inlet boundary of the domain (see Fig. 3.1), a steady uniform flow of low turbulence level was given so as to simulate the subcritical flow ($\mathrm{Re} = 4.0 \times 10^4$) around the cylinder. Specifically, the turbulence level corresponding to the turbulent viscosity ratio of unity was given for the DES and S-A URANS simulations, and also the turbulence intensity of 0.3% was additionally given for the LS k-ϵ URANS simulations. For the DES and S-A URANS, however, the so-called *trip-less approach* (TLA) was additionally used, following Travin *et al.* (2000), in order to obtain more 'plausible' results for the upper-subcritical flow (i.e., the transition to turbulence taking place just after the flow separation from the cylinder, cf. Section 1.4.2). Specifically, the turbulent viscosity ratio at the inlet was reduced from unity to 10^{-9} after the flow field had sufficiently developed under the original boundary conditions. This modification provides a 'self-sustaining' eddy-viscosity field behind the flow separation from the cylinder. That is, the (almost) zero eddy viscosity values from the inlet propagates to the region before the separation (i.e., laminar boundary layer) but the non-zero values behind the separation are sustained as they diffuse into the separated shear layers and cause a rapid production of themselves; thus the sudden increase in the eddy viscosity after the flow separation can be imitated without giving any information on the transition point *a priori*. After the change of the inlet turbulent viscosity ratio from 1 to 10^{-9}, the computation was further continued until the flow field had developed again, and thereafter the time-averaged data of the flow were collected. For the LES, a totally laminar flow (i.e., no perturbation) was given at the inlet, for comparison with the DES coupled with the TLA.

At the outlet boundary, a condition of zero-diffusion-flux in the streamwise (x) direction (which assumes no velocity gradient in that direction and is referred to as the 'outflow' boundary condition in FLUENT6) was applied. Note that the distance from the cylinder to the outlet boundary was sufficiently long for the outlet boundary condition to have negligible influence on the near wake region of the cylinder flow. As concerns the upper boundary of the domain (cf. Fig. 3.1), a symmetry (or slip) condition was imposed also because the distance from the cylinder to the upper boundary was large enough. For the side boundaries, periodic conditions were imposed as mentioned before. As for the cylinder and ground surfaces, no-slip conditions ($U = V = W = 0$ for the cylinder, whereas $U = U_\infty$ and $V = W = 0$ for the moving ground) were employed.

3.3 Results of preliminary computations (at $h/d = 1.0$)

In this section, some important results of preliminary computations are presented. First, the influence of spatial and time resolution on the results is shown in Section 3.3.1 for URANS, DES and LES. Then, with using the standard grids (i.e., the grids to be used in the main part of the study in Section 3.4), the influence of the Reynolds number on the results is given in Section 3.3.2 to show the 'incapability' of the simulations to reproduce the correct Reynolds number effect. The influence of the use of TLA (cf. Section 3.2.6) is also presented in this section.

Computational conditions for this preliminary section are summarised in Table 3.1. Six different types of simulations are performed here, namely, '2D k-ϵ', '2D S-A without TLA', '2D S-A', '3D S-A', 'DES', and 'LES'. Note that these notations are consistent with those used in the main part of the study in Section 3.4, where, however, only '2D k-ϵ', '2D S-A', '3D S-A', and 'DES' will be presented to discuss the issues relevant to the ground effect.

Table 3.1: Summary of the conditions for the preliminary computations.

Case	Type	Model	TLA*	h/d	Re
2D k-ϵ	2D, URANS	LS k-ϵ	No	1.0	0.4, 1.0×10^5
2D S-A without TLA	2D, URANS	S-A	No	1.0	0.4, 0.5, 0.6, 0.7, 0.8, 0.9, 1.0×10^5
2D S-A	2D, URANS	S-A	Yes	1.0	0.4, 0.5, 0.6, 0.7, 0.8, 0.9, 1.0×10^5
3D S-A	3D, URANS	S-A	Yes	1.0	0.4, 1.0×10^5
DES	3D, DES	(Modified) S-A	Yes	1.0	0.4, 1.0×10^5
LES	3D, LES	Smagorinsky	No	1.0	0.4, 1.0×10^5

*TLA: Trip-less approach (cf. Section 3.2.6)

3.3.1 Influence of spatial and time resolution

Tables 3.2 to 3.6 summarise the major results of preliminary computations on the influence of spatial and time resolution ($h/d = 1.0$, Re $= 0.4 \times 10^5$). Note that 'Baseline' in the tables indicates the case employing the spatial and time resolution that was eventually adopted in the main part of the study in Section 3.4.

Tables 3.2 and 3.3 show the results for the 2D URANS simulations. Cases A1, A2 (= Baseline), and A3 compare the influence of spatial resolution in the x and y directions. In Case A1 the number of grid points in each (x and y) direction was reduced by 40 percent from the baseline, whereas in Case A3 that was increased by 40 percent from the baseline. It can be seen that, for both 2D k-ϵ (Table 3.2) and 2D S-A (Table 3.3), the differences between Cases A2 and A3 are very small, suggesting a sufficient degree of grid convergence in 2D URANS simulations in this study. Meanwhile, Cases C1 (= Baseline) and C2 compare the influence of time resolution on the results. Note that in Case C2 the time step size is reduced to one-fifth of that used in the baseline case. It is obvious that, for both 2D k-ϵ and 2D S-A, the differences between Cases C1 and C2 are very small.

Table 3.4 summarises the influence of spatial and time resolution in 3D S-A simulations. Again Cases A1, A2 (= Baseline), and A3 compare the influence of spatial resolution in the x and y directions, and Cases C1 (= Baseline) and C2 compare the influence of time resolution on the results. Similar to the results for the 2D S-A mentioned above, a good convergence can be seen between Cases A2 and A3, and also between Cases C1 and C2. In addition to

Table 3.2: Influence of spatial and time resolution (2D k-ϵ, $h/d = 1.0$, Re $= 0.4 \times 10^5$).

2D k-ϵ	Grid (x, y)	Grid (z)	$\Delta t U_\infty / d$	C_D	St	θ^+_{sep} (°)	θ^-_{sep} (°)	L_r
Baseline	35300	1	0.021	0.74	0.292	107.1	108.9	1.34
Different resolutions in (x, y)								
A1	12708	1	0.021	0.76	0.285	105.9	110.1	1.25
A2 (= Baseline)	35300	1	0.021	0.74	0.292	107.1	108.9	1.34
A3	69188	1	0.021	0.74	0.298	107.0	109.0	1.33
Different resolutions in time								
C1 (= Baseline)	35300	1	0.021	0.74	0.292	107.1	108.9	1.34
C2	35300	1	0.0042	0.75	0.294	107.1	108.9	1.29

Table 3.3: Influence of spatial and time resolution (2D S-A, $h/d = 1.0$, Re $= 0.4 \times 10^5$).

2D S-A	Grid (x, y)	Grid (z)	$\Delta t U_\infty / d$	C_D	St	θ^+_{sep} (°)	θ^-_{sep} (°)	L_r
Baseline	35300	1	0.021	1.50	0.237	89.1	93.6	0.79
Different resolutions in (x, y)								
A1	12708	1	0.021	1.46	0.241	87.9	93.6	0.79
A2 (= Baseline)	35300	1	0.021	1.50	0.237	89.1	93.6	0.79
A3	69188	1	0.021	1.50	0.236	89.6	93.6	0.78
Different resolutions in time								
C1 (= Baseline)	35300	1	0.021	1.50	0.237	89.1	93.6	0.79
C2	35300	1	0.0042	1.50	0.238	89.1	93.6	0.79

Table 3.4: Influence of spatial and time resolution (3D S-A, $h/d = 1.0$, Re $= 0.4 \times 10^5$).

3D S-A	Grid (x, y)	Grid (z)	$\Delta t U_\infty / d$	C_D	St	θ^+_{sep} (°)	θ^-_{sep} (°)	L_r
Baseline	35300	40	0.021	1.46	0.215	87.3	92.7	0.85
Different resolutions in (x, y)								
A1	12708	40	0.021	1.39	0.211	86.1	90.9	0.92
A2 (= Baseline)	35300	40	0.021	1.46	0.215	87.3	92.7	0.85
A3	69188	40	0.021	1.46	0.215	87.8	93.5	0.82
Different resolutions in z								
B1	35300	10	0.021	1.45	0.209	87.3	92.7	0.86
B2	35300	20	0.021	1.46	0.214	87.3	92.7	0.85
B3 (= Baseline)	35300	40	0.021	1.46	0.215	87.3	92.7	0.85
B4	35300	80	0.021	1.46	0.214	87.3	92.7	0.85
Different resolutions in time								
C1 (= Baseline)	35300	40	0.021	1.46	0.215	87.3	92.7	0.85
C2	35300	40	0.0042	1.46	0.214	87.3	92.7	0.83

Table 3.5: Influence of spatial and time resolution (DES, $h/d = 1.0$, Re $= 0.4 \times 10^5$).

DES	Grid (x, y)	Grid (z)	$\Delta t U_\infty / d$	C_D	St	θ^+_{sep} (°)	θ^-_{sep} (°)	L_r
Baseline	35300	40	0.021	1.33	0.210	79.2	85.5	1.35
Different resolutions in (x, y)								
A1	12708	40	0.021	1.03	0.242	86.1	87.9	1.44
A2 (= Baseline)	35300	40	0.021	1.33	0.210	79.2	85.5	1.35
A3	69188	40	0.021	1.41	0.200	81.4	87.0	1.21
Different resolutions in z								
B1	35300	10	0.021	1.40	0.205	84.6	90.0	1.01
B2	35300	20	0.021	1.34	0.211	80.1	86.4	1.29
B3 (= Baseline)	35300	40	0.021	1.33	0.210	79.2	85.5	1.35
B4	35300	80	0.021	1.47	0.201	81.9	87.3	1.11
Different resolutions in time								
C1 (= Baseline)	35300	40	0.021	1.33	0.210	79.2	85.5	1.35
C2	35300	40	0.0042	1.32	0.212	80.1	84.6	1.36

Table 3.6: Influence of spatial and time resolution (LES, $h/d = 1.0$, Re $= 0.4 \times 10^5$).

LES	Grid (x, y)	Grid (z)	$\Delta t U_\infty / d$	C_D	St	θ^+_{sep} (°)	θ^-_{sep} (°)	L_r
Baseline	35300	40	0.021	1.58	0.209	91.8	99.0	0.92
Different resolutions in (x, y)								
A1	12708	40	0.021	1.26	0.248	90.6	93.9	1.29
A2 (= Baseline)	35300	40	0.021	1.58	0.209	91.8	99.0	0.92
A3	69188	40	0.021	1.70	0.208	92.3	99.3	0.84
Different resolutions in z								
B1	35300	10	0.021	1.24	0.226	93.6	99.0	1.34
B2	35300	20	0.021	1.39	0.216	90.0	95.4	1.25
B3 (= Baseline)	35300	40	0.021	1.58	0.209	91.8	99.0	0.92
B4	35300	80	0.021	1.68	0.205	91.8	97.2	0.89

these, Cases B1, B2, B3 (= Baseline), and B4 compare the influence of spatial resolution in the spanwise (z) direction. Of interest is that, in the 3D S-A URANS, the number of grid points in the spanwise direction has no significant influence on the mean flow characteristics. This is basically because the three-dimensional vortical structures behind the cylinder are captured only roughly in 3D S-A URANS even with a good spanwise resolution. Figure 3.3 shows a comparison of instantaneous wake structures predicted in Cases B1 and B3. Both cases predicted not only spanwise vortices but also streamwise 'rib' vortices; the structures of these vortices, however, are still much coarser (or much more organised) than those predicted by the DES shown later in Fig. 3.4 (more detailed discussion on the flow will be given later in the main part of the study in Section 3.4).

Table 3.5 summarises the influence of spatial and time resolution in DES. It can be seen that the differences between Cases A2 and A3 are smaller than those between Cases A1 and A2, suggesting a certain degree of grid convergence in the x and y directions, although not as good as that for the URANS shown above. Meanwhile, the differences between Cases C1 and C2 are very small, i.e., the time resolution of $\Delta t U_\infty / d = 0.021$ is sufficient for the DES as well as for the URANS.

Of major concern here is the influence of the spanwise resolution in the DES. Note that Δz ($2d$ divided by the number of grid points in the z direction) is the largest grid spacing (i.e., larger than Δx and Δy) around the cylinder and thus directly affects the switching between the URANS and LES modes in that region (cf. Section 3.2.3). Compared with the boundary layer thickness around the cylinder (about $0.03d$ at the maximum), the thickness of the URANS region around the cylinder is slightly larger in Case B3 ($0.0325d$), much larger in Cases B1 and B2 ($0.13d$ and $0.065d$, respectively), and smaller in Case B4 ($0.01625d$). It is therefore unsurprising that some discrepancies from Case B3 (= baseline) are observed not only in Case B1, where the spanwise resolution is simply too coarse to properly capture the three-dimensional vortical structures behind the cylinder (cf. Fig. 3.4), but also in Case B4, where the switch between the URANS and LES modes undesirably takes place inside the boundary layer due to the too fine spanwise resolution. Of interest, however, is that only small differences can be seen in the results between Cases B2 and B3. This shows that, even though the mode switching in DES depends on the resolution of the grids, a certain degree of grid convergence could be achieved in an 'appropriate' resolution range.

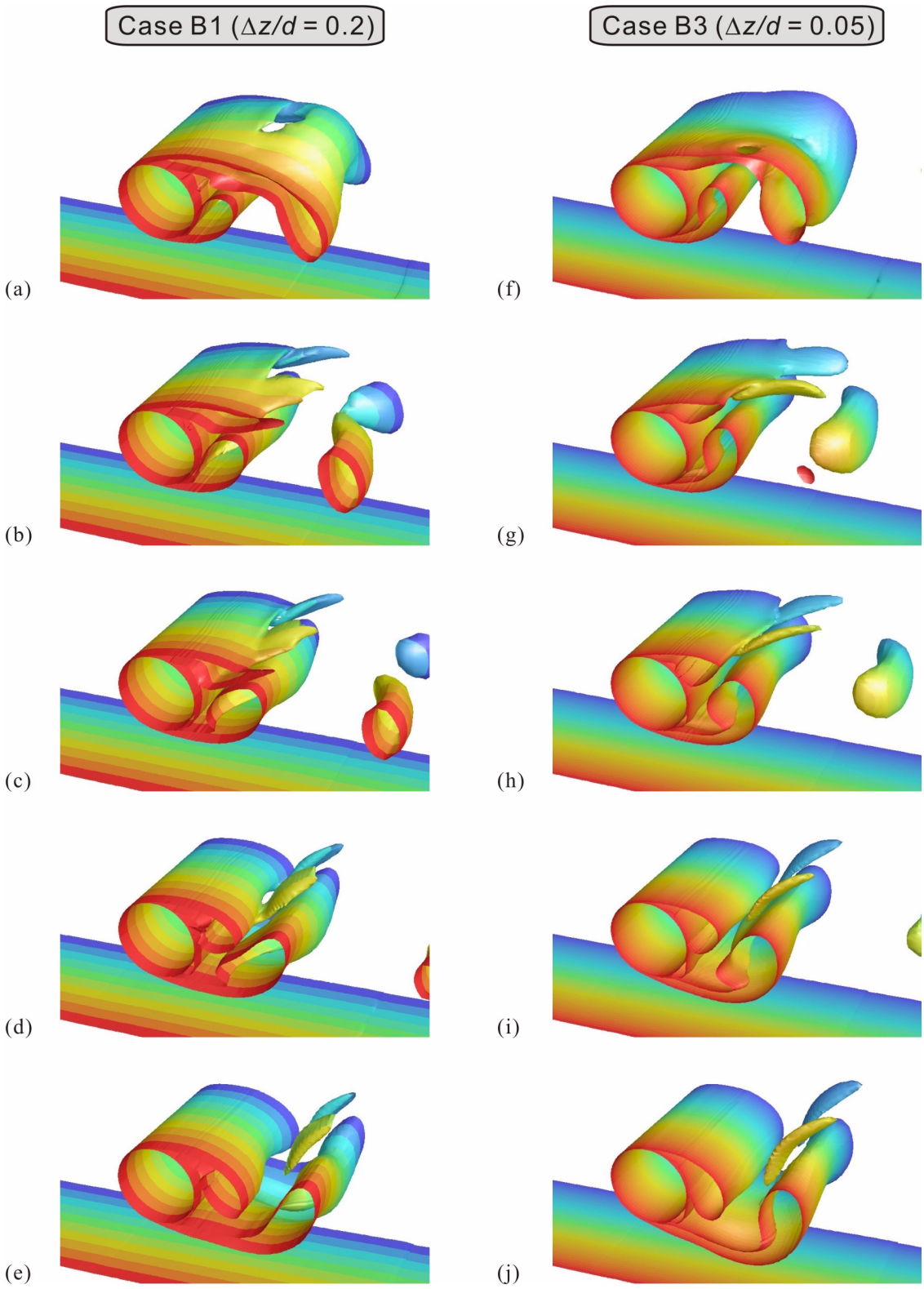

Figure 3.3: Influence of the spanwise resolution on the near wake structure predicted by the 3D S-A URANS (isosurfaces of the magnitude of instantaneous vorticity, $h/d = 1.0$, Re $= 0.4 \times 10^5$): (a-e) Case B1, and (f-j) Case B3. Note that the figures roughly correspond to a half cycle of the von Kármán-type vortex shedding; C_L increases from the local minimum value at (a) and (f) to the local maximum value at (e) and (j).

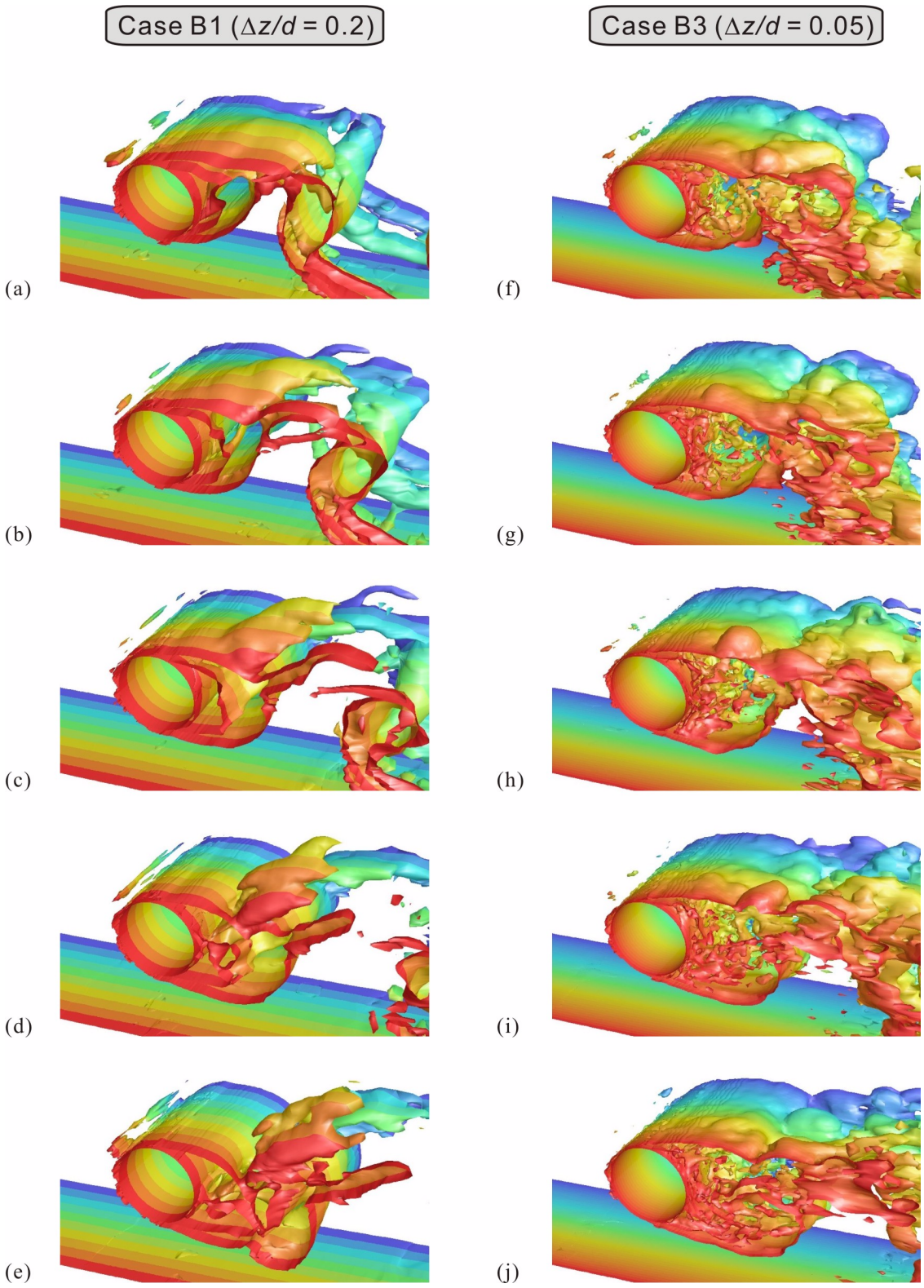

Figure 3.4: Influence of the spanwise resolution on the near wake structure predicted by the DES (isosurfaces of the magnitude of instantaneous vorticity, $h/d = 1.0$, $\mathrm{Re} = 0.4 \times 10^5$): (a-e) Case B1, and (f-j) Case B3. Note that the figures roughly correspond to a half cycle of the von Kármán-type vortex shedding; C_L increases from the local minimum value at (a) and (f) to the local maximum value at (e) and (j).

Finally, the preliminary results of the LES are summarised in Table 3.5. Compared with the results of the DES, the grid dependency in the LES seems to be more significant. This is basically because the grids are still too coarse for the LES especially in the near-wall region, similar to most of the earlier studies that applied LES to circular/square cylinders in a free stream (cf. Section 1.4.5). Although some more sophisticated near-wall treatments have been proposed and they were not tested in the present study, this kind of grid dependency is often a major problem in the application of LES to high Reynolds number flows.

In conclusion, good grid convergence was obtained in both 2D and 3D URANS simulations, whereas that in the DES was not perfect but clearly better than the LES performed on the same set of grids. Also the baseline time resolution $\Delta t U_\infty/d = 0.021$ was found to be sufficient in both URANS and DES.

3.3.2 Influence of the Reynolds number

Table 3.7 summarises the major results of preliminary computations on the influence of the Reynolds number ($h/d = 1.0$). Note that the spatial and time resolution employed here is that used as 'Baseline' in the previous section.

The Reynolds number range examined here ($0.4 \times 10^5 \leq \mathrm{Re} \leq 1.0 \times 10^5$) corresponds to the upper-subcritical or TrSL3 regime (cf. Fig. 1.2). Hence, as is obvious from the literature review given in Section 1.4.2 and also from the experimental results presented in Chapter 2 (for example see Fig. 2.6), the physically correct behaviour of the flow to be expected here is that the flow characteristics are *not* sensitive to the Reynolds number. This, however, is a formidable task for today's CFD to achieve, as reviewed in Section 1.4.5, and the results summarised in Table 3.7 show how difficult it is to be achieved, i.e., significant influence of the Reynolds number can be seen in both 2D and 3D S-A URANS and also in the DES. A common tendency for these three cases is that the characteristics of the subcritical flow are (to varying degrees) reasonably predicted at Re $= 0.4 \times 10^5$ whereas the results at Re $= 1.0 \times 10^5$ incorrectly show typical characteristics of the postcritical flow rather than of the subcritical flow (e.g., larger separation angles, higher shedding frequency, smaller amplitude of lift fluctuation, and lower drag coefficient). The only case that predicted less sensitivity to the Reynolds number is the 2D k-ϵ, which, however, incorrectly shows the characteristics of the postcritical flow mentioned above rather than of the subcritical flow at both higher and lower Reynolds numbers.

Figure 3.5 shows the drag coefficient of the cylinder ($h/d = 1.0$) predicted at different Reynolds numbers. The experimental results shown in Chapter 2 are also plotted here for the purpose of comparison. The figure clearly shows the incapability of the computations to predict the correct Reynolds number effect in this flow regime. At Re $= 1.0 \times 10^5$ all cases tested here predicted lower C_D values of about 0.7 compared with the experimental value of about 1.25. Of interest is that the advantageous effect of the TLA (to obtain 'plausible' upper-subcritical flows, cf. Section 3.2.6), which can be seen from the difference between '2D S-A' and '2D S-A without TLA', also diminishes as the Reynolds number increases. At Re $= 0.4 \times 10^5$ the TLA did make the separation angles smaller and thus the drag coefficient higher, but at Re $= 1.0 \times 10^5$ the TLA did not make any substantial differences (cf. Table

Table 3.7: Influence of the Reynolds number ($h/d = 1.0$).

Case	Re	C_D	C_L	C'_L	St	θ^+_{sep} (°)	θ^-_{sep} (°)	L_r
2D k-ϵ	0.4×10^5	0.74	0.05	0.24	0.292	107.1	108.9	1.34
	1.0×10^5	0.68	0.05	0.21	0.303	110.7	112.5	1.34
2D S-A without TLA	0.4×10^5	1.05	0.06	0.80	0.251	92.7	95.4	0.94
	1.0×10^5	0.67	0.05	0.19	0.263	97.2	99.9	1.54
2D S-A	0.4×10^5	1.50	0.12	1.21	0.237	89.1	93.6	0.79
	1.0×10^5	0.67	0.05	0.20	0.266	97.2	99.9	1.51
3D S-A	0.4×10^5	1.46	0.08	1.13	0.215	87.3	92.7	0.85
	1.0×10^5	0.68	0.05	0.21	0.266	97.2	99.9	1.51
DES	0.4×10^5	1.33	0.05	0.58	0.210	79.2	85.5	1.35
	1.0×10^5	0.70	0.04	0.10	0.305	96.3	99.0	1.62

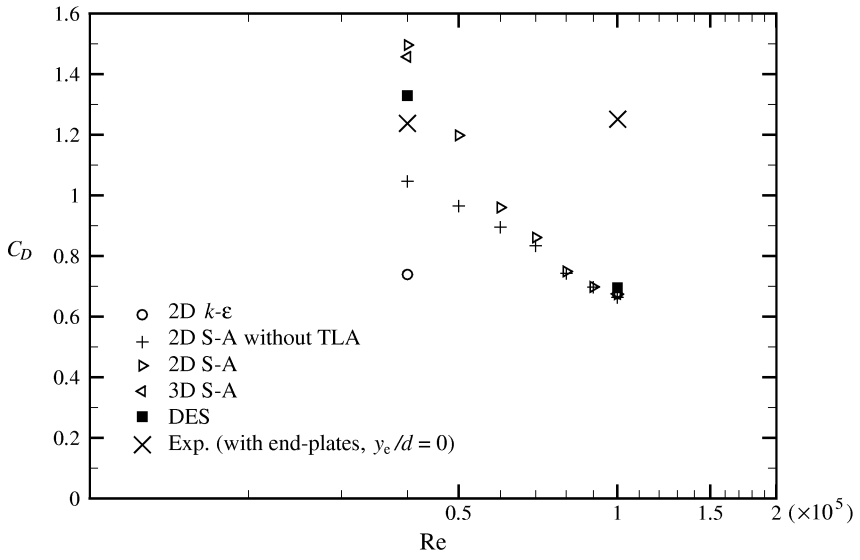

Figure 3.5: Influence of the Reynolds number on the drag coefficient ($h/d = 1.0$).

3.7), showing the limit of the usefulness of the TLA in this Reynolds number range. This is basically because, even with the TLA, the turbulent viscosity calculated in the boundary layer gradually increases as the Reynolds number increases, leading to the delay of the flow separation from the cylinder surface and thus the decrease in C_D.

In conclusion, both 2D and 3D S-A URANS and DES reasonably captured the main features of the subcritical flow (due to the use of the TLA) but only at the lower Reynolds numbers, whereas 2D k-ϵ failed to capture them at both lower and higher Reynolds numbers. As demonstrated here and also in several earlier studies reviewed in Section 1.4.5, it is a formidable task for today's CFD to correctly predict the flow past a circular cylinder at the Reynolds numbers close to the range between the subcritical and postcritical flow regimes. Hence in the next section, the lower Reynolds number of 0.4×10^5 is employed in order to discuss the capability of each simulation to predict the cessation of the von Kármán-type vortex shedding in ground effect, which is the main topic of the present study.

3.4 Main results and discussion

In this section, further results of computations are presented with a main focus on the issues relevant to the ground effect. Computational conditions are summarised in Table 3.8. Note that the Reynolds number is restricted to 0.4×10^5 in this section, following the discussion in the previous section. Also note that all the computations shown below were performed with the spatial and time rezolution used as 'Baseline' in Section 3.3.1.

Table 3.8: Summary of the conditions for the main computations.

Case	Type	Model	TLA*	h/d	Re
2D k-ϵ	2D, URANS	LS k-ϵ	No	0.1, 0.2, 0.3, 0.4, 0.5, 0.6, 1.0	0.4×10^5
2D S-A	2D, URANS	S-A	Yes	0.1, 0.2, 0.3, 0.4, 0.5, 0.6, 1.0	0.4×10^5
3D S-A	3D, URANS	S-A	Yes	0.1, 0.2, 0.3, 0.4, 0.5, 0.6, 1.0	0.4×10^5
DES	3D, DES	(Modified) S-A	Yes	0.1, 0.2, 0.3, 0.4, 0.5, 0.6, 1.0	0.4×10^5

*TLA: Trip-less approach (cf. Section 3.2.6)

3.4.1 Drag reduction and the cessation of Kármán vortex shedding

Figure 3.6 shows the time-averaged drag coefficient of the cylinder in ground effect. The results of the experiments in Chapter 2 (with end-plates at $y_e/d = 0$) are also presented in the figure for comparison. An important feature of the ground effect to be discussed here is the critical change in C_D due to the cessation of the large-scale von Kármán-type vortex shedding at $h/d < 0.35$. As can be seen from the figure, both 2D and 3D URANS predicted the critical change in C_D but at much smaller h/d of 0.2 to 0.1 (as they incorrectly predicted the large-scale vortex shedding at h/d of down to 0.2, as will be shown later). Meanwhile, the drag behaviour predicted by the DES agreed better with the experiments; the critical drag reduction was qualitatively correctly captured at h/d of 0.4 to 0.3.

Figure 3.7 shows the mean lift coefficient of the cylinder in ground effect. All simulations captured the rapid increase in C_L when the cylinder came close to the ground (see Figs. 2.8 and 2.9 for the experimental results). The 2D and 3D S-A URANS, however, predicted a local minimum C_L around $h/d = 0.3$ to 0.4. This is due to an (overly) asymmetric pressure distribution incorrectly predicted at these gap ratios, as shown later in Fig. 3.19.

Figure 3.8 shows the r.m.s. of the lift fluctuations of the cylinder in ground effect, and Figs. 3.9 to 3.11 show the time variation of the drag and lift coefficients. Note that the solid and dashed lines in Figs. 3.9 to 3.11 indicate the variations of C_D and C_L, respectively. It is obvious from these figures that the DES captured the cessation of the large-scale vortex shedding between two h/d of 0.4 and 0.3, consistent with the experiments in Chapter 2. On the other hand, both 2D and 3D URANS incorrectly predicted strong fluctuations even at $h/d = 0.2$ (note that at $h/d = 0.1$ the vortex shedding ceased and a steady solution was obtained in both 2D and 3D URANS, as indicated by $C'_L = 0$ in Fig. 3.8). Figure 3.12 shows the Strouhal number based on the lift fluctuations. The DES predicted St of about 0.21 to 0.22 for all h/d of greater than 0.3, which is comparable to the experiments for a circular cylinder placed near a fixed ground by Bearman and Zdravkovich (1978). Both 2D and 3D S-A URANS also predicted comparable St values at $h/d \geq 0.4$, even though they failed to capture the cessation of the vortex shedding at $h/d \leq 0.3$.

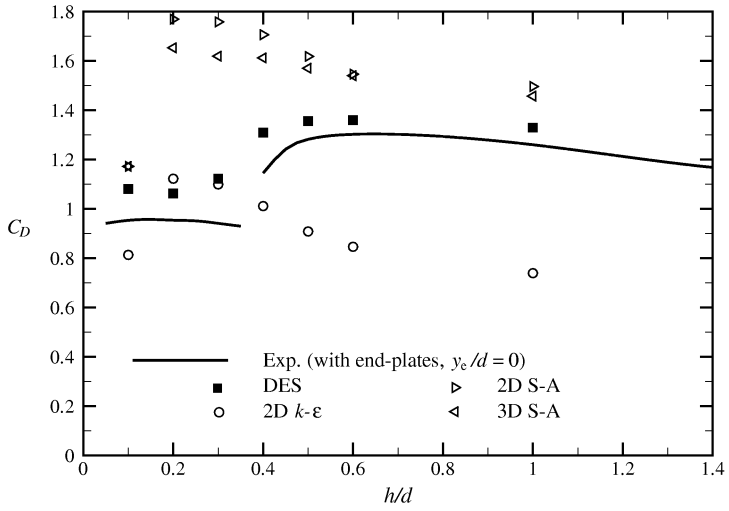

Figure 3.6: Mean drag coefficient of the cylinder in ground effect ($\mathrm{Re} = 0.4 \times 10^5$).

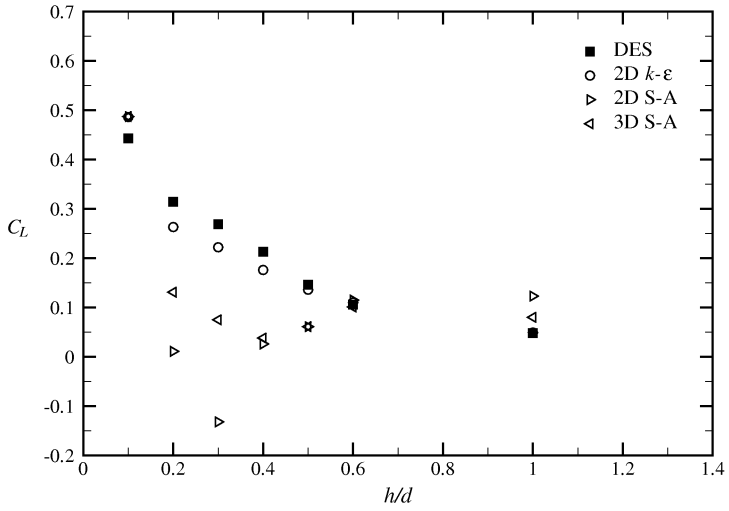

Figure 3.7: Mean lift coefficient of the cylinder in ground effect ($\mathrm{Re} = 0.4 \times 10^5$).

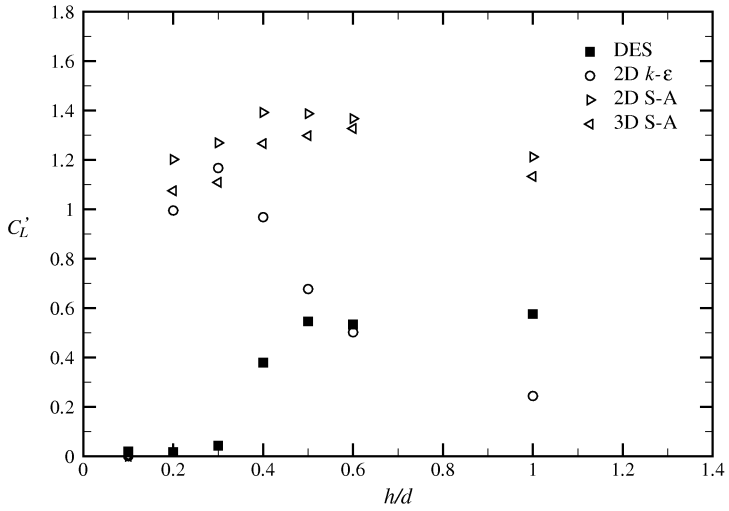

Figure 3.8: R.m.s. of C_L fluctuations of the cylinder in ground effect ($\mathrm{Re} = 0.4 \times 10^5$).

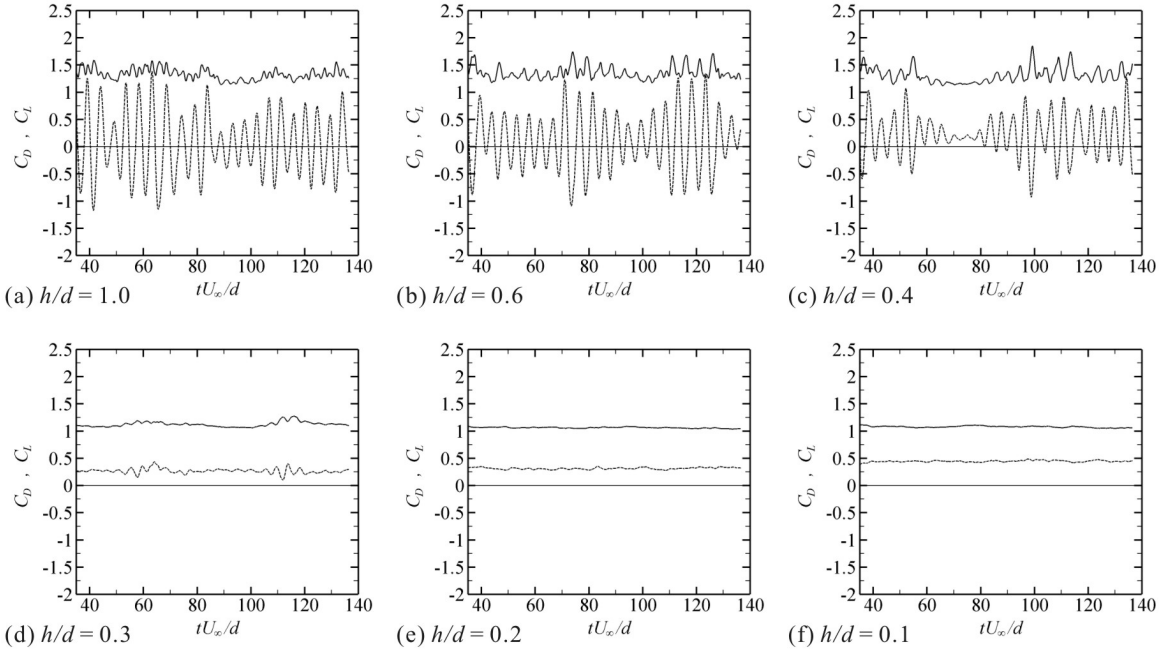

Figure 3.9: Time variation of drag and lift coefficients (DES, Re = 0.4×10^5); solid and dashed lines indicate C_D and C_L, respectively.

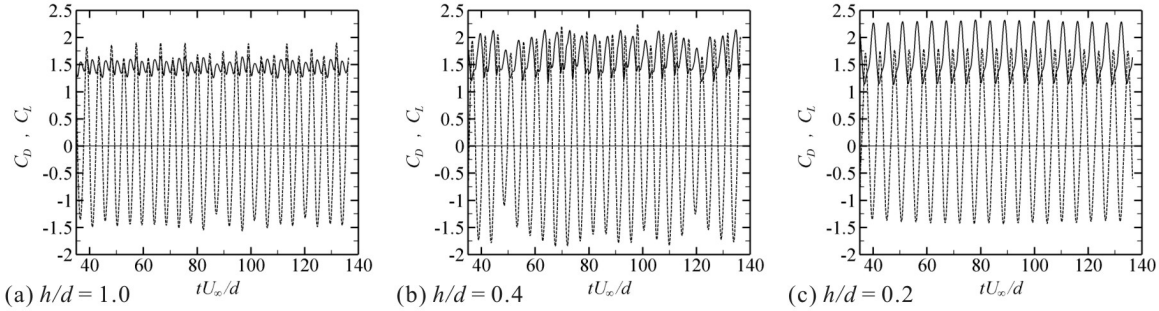

Figure 3.10: Time variation of drag and lift coefficients (3D S-A, Re = 0.4×10^5); solid and dashed lines indicate C_D and C_L, respectively.

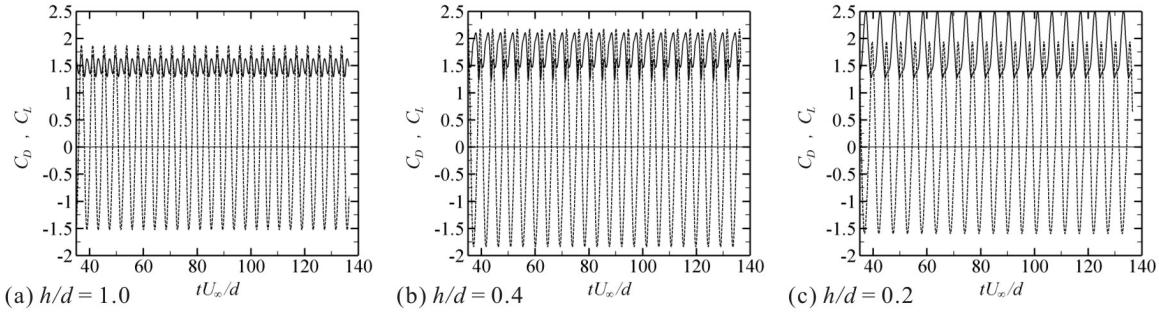

Figure 3.11: Time variation of drag and lift coefficients (2D S-A, Re = 0.4×10^5); solid and dashed lines indicate C_D and C_L, respectively.

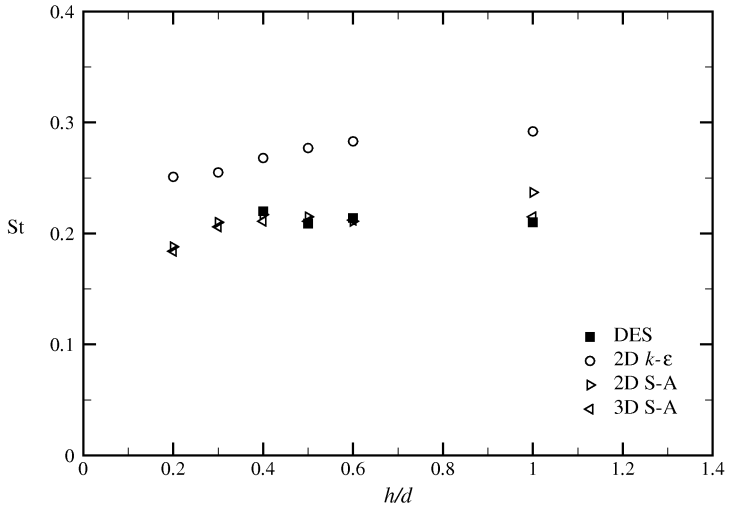

Figure 3.12: Strouhal number based on the lift fluctuations of the cylinder in ground effect ($\mathrm{Re} = 0.4 \times 10^5$).

3.4.2 Instantaneous flow characteristics

Figure 3.13 shows typical instantaneous wake structures of the cylinder at $h/d = 0.6$ and 0.2 predicted by the DES. A clear difference can be seen between the two cases: three-dimensional large-scale vortex shedding was predicted behind the cylinder at $h/d = 0.6$, whereas two nearly parallel shear layers (but still having embedded three-dimensional turbulent structures) were formed at $h/d = 0.2$. The mid-span sections of these two instantaneous flow fields are shown in Figs. 3.14(a) and (b), respectively, where the contours of non-dimensional spanwise vorticity are plotted. A comparison with the PIV results (cf. Fig. 2.16) suggests that the DES successfully captured the main features of the wake structure of the cylinder in both the large- and small-gap regimes.

Of further interest are the wake structures predicted at $h/d = 0.4$, which lies in the intermediate gap regime defined in Chapter 2. Figure 3.15 shows instantaneous spanwise vorticity fields behind the cylinder at $h/d = 0.4$ at two different time instants. It can be seen that at $tU_\infty/d = 75.6$ [Fig. 3.15(a)], around which time the fluctuations of the forces almost diminished to zero [cf. Fig. 3.9(c)], a small dead-fluid zone was temporarily generated behind the cylinder. At $tU_\infty/d = 136.5$ [Fig. 3.15(b)], however, large-scale vortices were formed just behind the cylinder, similar to those observed at $h/d = 0.6$ [cf. Fig. 3.14(a)]. This qualitatively agrees with the experimental observation in Chapter 2 that the von Kármán-type vortex shedding was intermittent in the intermediate gap regime.

Figure 3.16 shows typical instantaneous wake structures of the cylinder at $h/d = 0.6$ and 0.2 predicted by the 3D S-A URANS. Again it can be seen that the 3D S-A incorrectly predicted the large-scale vortex shedding at $h/d = 0.2$. Also of interest is that, at $h/d = 0.2$, the 3D S-A yielded an almost two-dimensional wake, whereas at $h/d = 0.6$ (and also at $h/d = 1.0$, cf. Fig. 3.4), it yielded a three-dimensional wake consisting of not only spanwise vortices but also streamwise 'rib' vortices. This can also be confirmed from the time variations of the force coefficients presented in Fig. 3.10, i.e., the 3D S-A showed some low-frequency

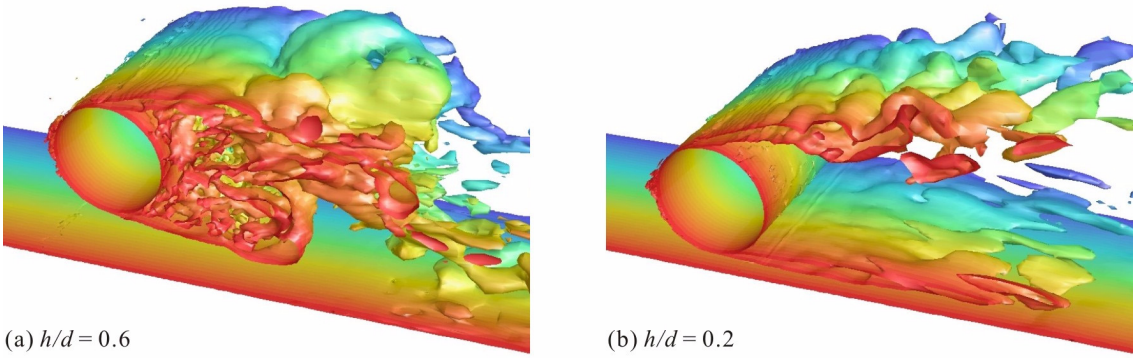

Figure 3.13: Typical instantaneous wake structures at $h/d = 0.6$ and 0.2 (isosurfaces of the magnitude of instantaneous vorticity, predicted by the DES, Re $= 0.4 \times 10^5$).

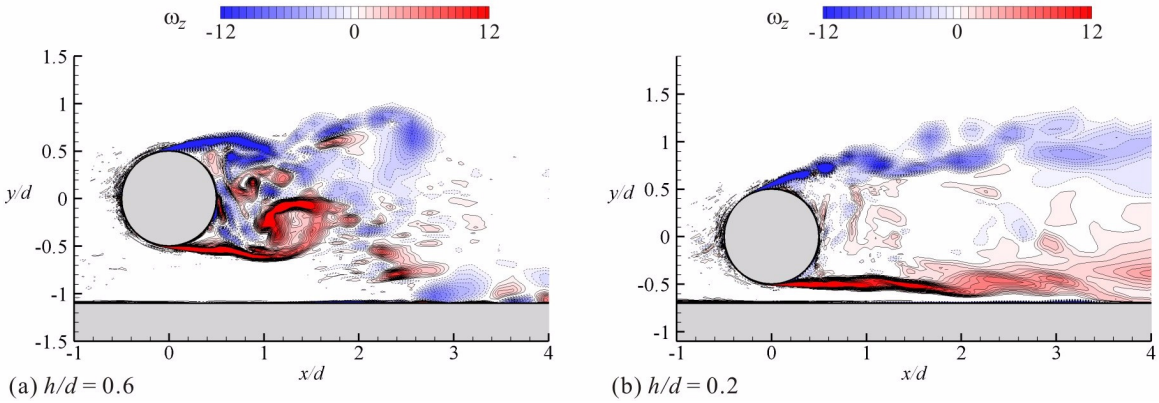

Figure 3.14: Typical instantaneous spanwise vorticity fields at $h/d = 0.6$ and 0.2 (DES, Re $= 0.4 \times 10^5$); the phases corresponding to those in Fig. 3.13.

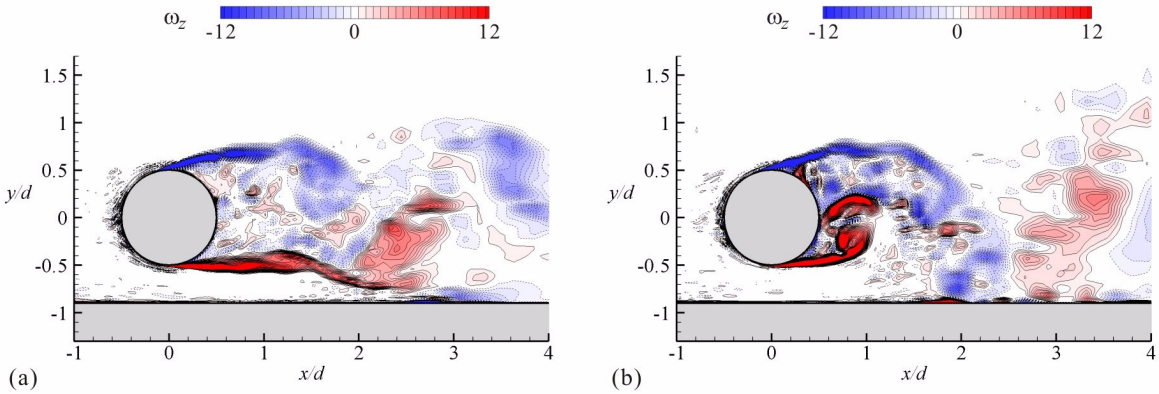

Figure 3.15: Instantaneous spanwise vorticity fields at $h/d = 0.4$ at two different phases: (a) $tU_\infty/d = 75.6$, (b) $tU_\infty/d = 136.5$ (DES, Re $= 0.4 \times 10^5$).

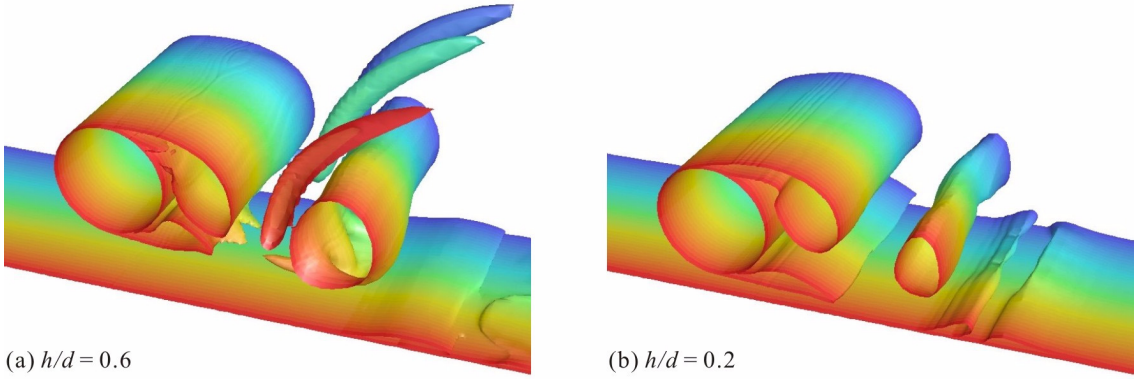

(a) $h/d = 0.6$ (b) $h/d = 0.2$

Figure 3.16: Typical instantaneous wake structures at $h/d = 0.6$ and 0.2 (isosurfaces of the magnitude of instantaneous vorticity, predicted by the 3D S-A URANS, $\mathrm{Re} = 0.4 \times 10^5$).

modulations at $h/d \geq 0.4$, but yielded almost totally periodic fluctuations at $h/d \leq 0.3$. In this connection, Shur *et al.* (2005) recently reported, for a circular cylinder in a free stream, that this type of low-frequency modulation and moderate three-dimensionality in 3D URANS may or may not be observed depending on the spanwise size of the domain and on the turbulence model employed. The present results are of interest in showing that it may also depend on a geometric parameter of the flow simulated, although the importance or relevance of this discussion to the real physics is still unclear. It is well known that these streamwise rib vortices are indeed experimentally observed in the laminar wake of a cylinder (Williamson 1996), and hence the suppression of the rib vortices predicted by the 3D S-A at $h/d \leq 0.3$ might be of some relevance to the physical mechanisms of the cessation of the von Kármán-type vortex shedding in ground effect. It must be remembered, however, that the structures of the turbulent wake of the cylinder investigated in this study are much more complicated, as predicted by the DES (cf. Fig. 3.13).

3.4.3 Time-averaged flow characteristics

Figure 3.17 compares the time-averaged separation angles on both upper (open) and bottom (gap) sides of the cylinder in ground effect. The separation angles estimated from the oil flow visualisation tests in Chapter 2 (at a higher Reynolds number of 1.0×10^5, with end-plates at $y_e/d = 0$) are also shown here for comparison (note that this Reynolds number for the oil flow tests is still within the subcritical regime and thus comparing the results is still reasonable). Also note that $|\theta_{\mathrm{sep}}|$ plotted in this figure indicates the magnitude of the angle from the front position ($x/d = -0.5$, $y/d = 0$) to the separation position (cf. Fig. 2.13). It can be seen that the DES agreed better with the experiments, whereas the URANS simulations predicted larger angles compared with the experiments.

Figures 3.18 and 3.19 show the mean pressure distributions on the cylinder predicted by the DES and 3D S-A URANS, respectively. The results of the DES describe the mechanisms of the drag and lift behaviours of the cylinder in ground effect; the rapid drag reduction at $h/d = 0.4$ to 0.3 occurs primarily due to an increase in the base pressure, whilst the lift

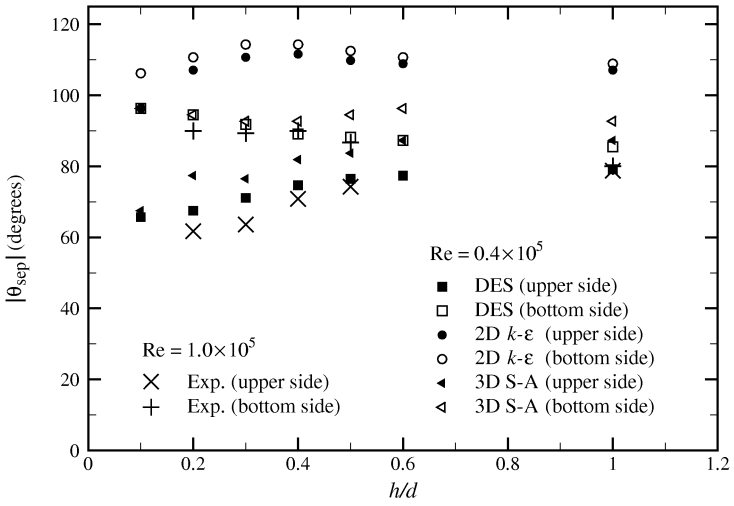

Figure 3.17: Time-averaged separation angle on a circular cylinder in ground effect.

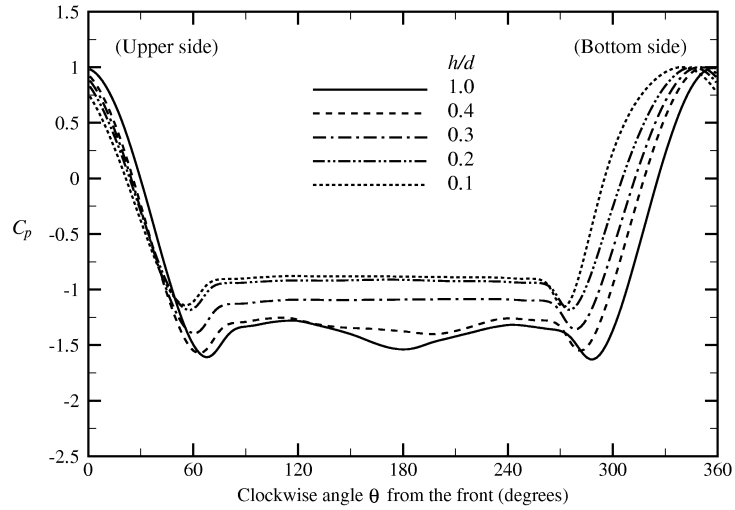

Figure 3.18: Mean pressure distributions around the cylinder (DES, Re $= 0.4 \times 10^5$).

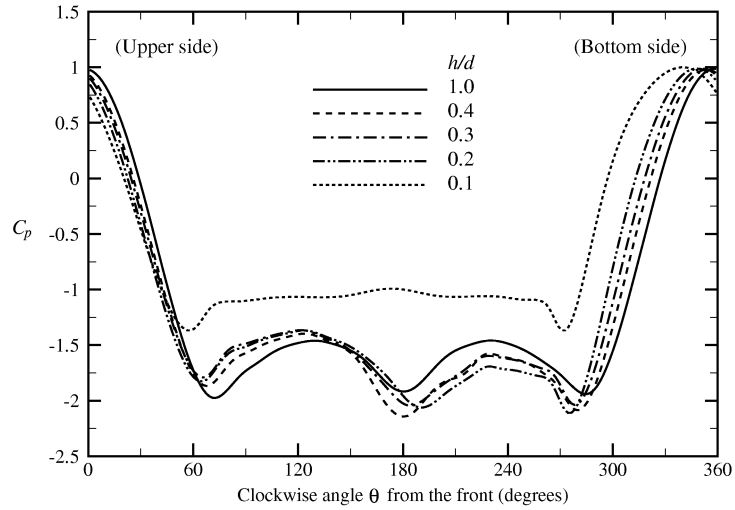

Figure 3.19: Mean pressure distributions around the cylinder (3D S-A, Re $= 0.4 \times 10^5$).

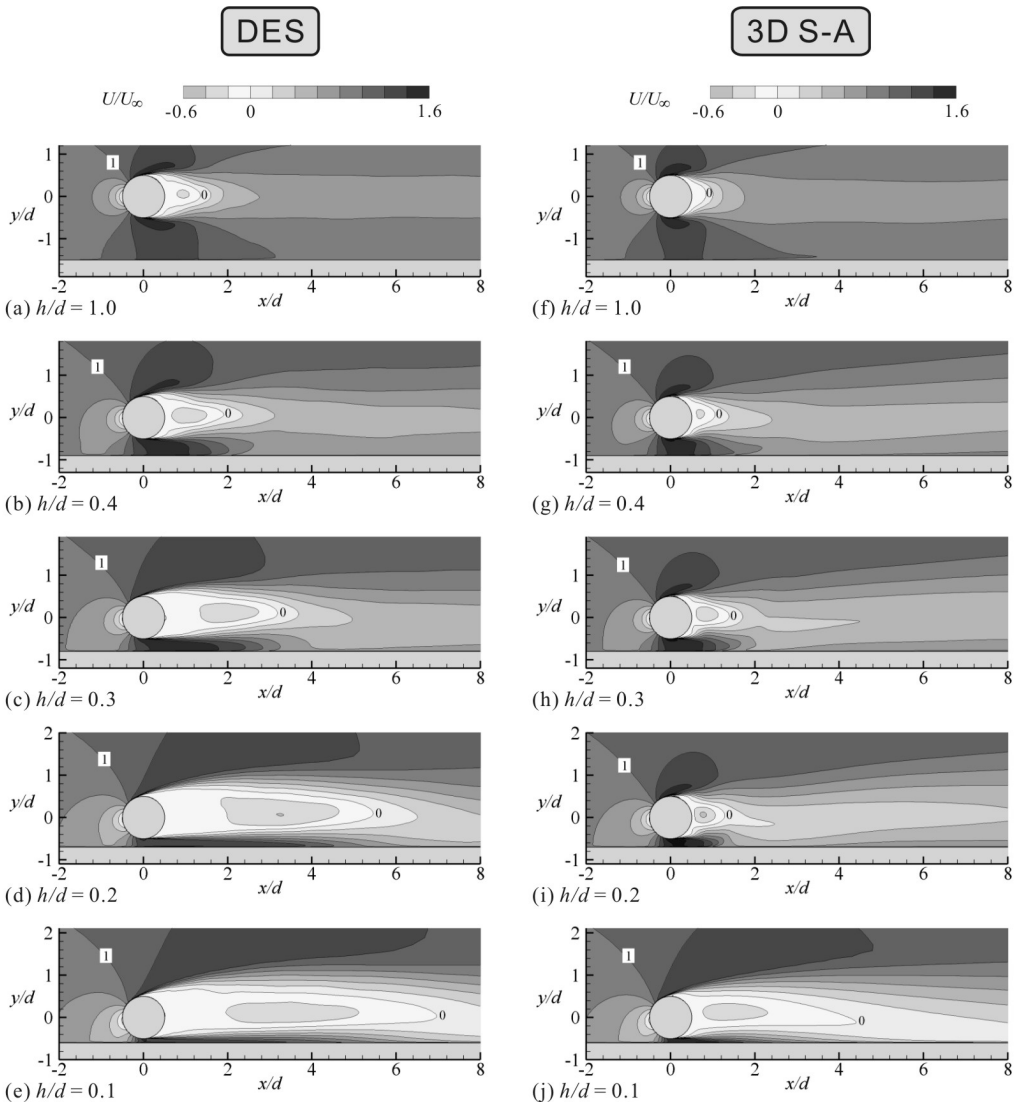

Figure 3.20: Contours of non-dimensional mean streamwise velocity: (a-e) DES, (f-j) 3D S-A ($\mathrm{Re} = 0.4 \times 10^5$).

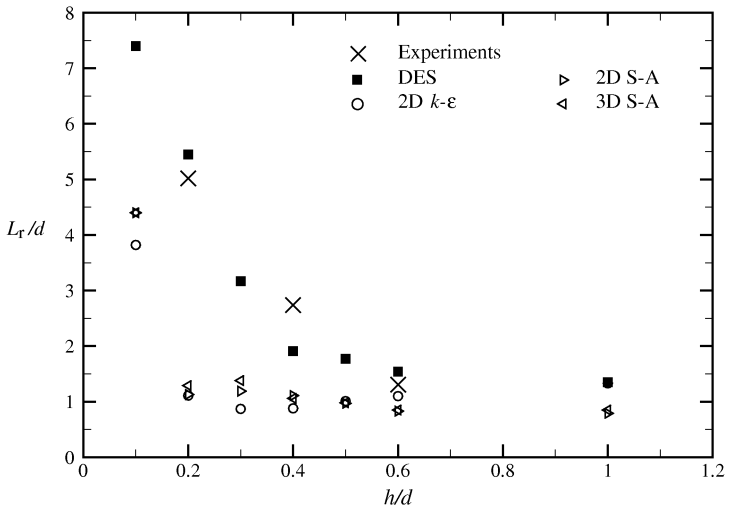

Figure 3.21: Recirculation length vs. gap ratio ($\mathrm{Re} = 0.4 \times 10^5$).

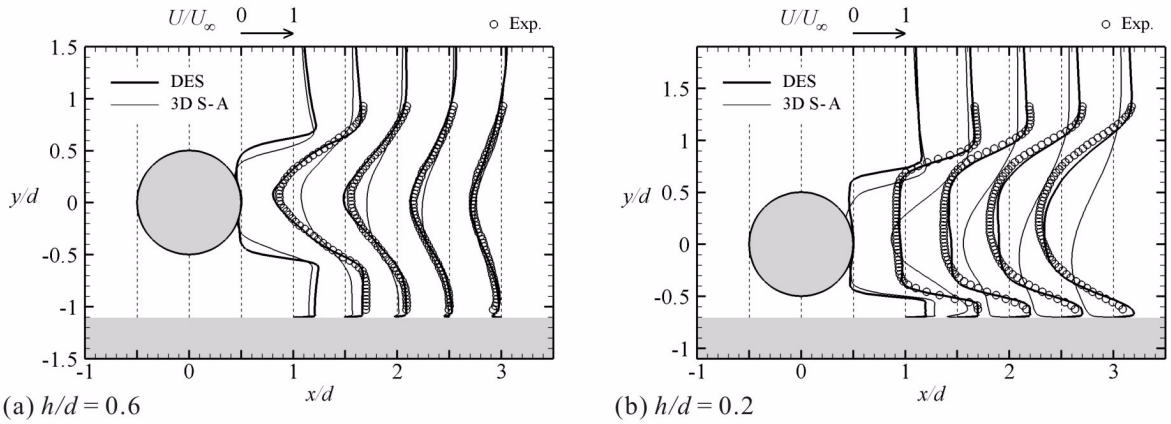

Figure 3.22: Comparison of mean streamwise velocity profiles ($\mathrm{Re} = 0.4 \times 10^5$).

gradually increases as the gap decreases mainly because the high pressure region around the front stagnation point shifts to the bottom side of the cylinder. Meanwhile, the results of the 3D S-A explain its incorrect predictions on the drag and lift behaviours. That is, the higher C_D values (except for $h/d = 0.1$, cf. Fig. 3.6) basically come from the lower base pressure predicted, whereas the local minimum C_L predicted around $h/d = 0.4$ (cf. Fig. 3.7) is due to the (overly) asymmetric base pressure, the effect of which cancels out the (physically correct) 'lifting' effect of the downward shift of the front stagnation point.

Figure 3.20 shows the mean streamwise velocity contours predicted by the DES and 3D S-A URANS. It can be seen that the DES predicted the recirculation region behind the cylinder to be significantly elongated as h/d decreased from 0.4 to 0.3 and below, due to the cessation of the von Kármán-type vortex shedding. This agrees with the results of the PIV measurements in Chapter 2, and is consistent with the increase in the base pressure described above in Fig. 3.18. In contrast, the recirculation region predicted by the 3D S-A remains small even at $h/d = 0.2$, primarily because the 3D S-A failed to capture the cessation of the vortex shedding as already shown in Figs. 3.10 and 3.16. This was also found to be the case with the 2D URANS simulations. Figure 3.21 compares the length of the recirculation region, L_r, predicted behind the cylinder. The results from the PIV measurements (at the same Reynolds number of 0.4×10^5, with end-plates at $y_\mathrm{e}/d = 0$) are also plotted here for the purpose of comparison. As is obvious from the figure, all URANS simulations in this study predicted smaller L_r compared with those by the DES and the experiments, especially at smaller gap ratios.

Figure 3.22 compares the mean streamwise velocity profiles behind the cylinder at $h/d = 0.6$ and 0.2. Note that the profiles at $x/d = 0.5$, 1.0, 1.5, 2.0, and 2.5 predicted by the DES and 3D S-A are shown in each figure, and those obtained by the PIV measurements (but only at $x/d = 1.0$, 1.5, 2.0, and 2.5) are also plotted for comparison. It can be seen that the DES successfully captured the mean wake profile of the cylinder at both larger and smaller gap ratios, i.e., the parabolic-like profiles because of the vortex shedding at $h/d = 0.6$ and the top-hat-like profiles due to the cessation of the vortex shedding at $h/d = 0.2$. In contrast, the 3D S-A showed some discrepancies in the near wake region at $h/d = 0.6$, but totally failed to

predict the correct profile at $h/d = 0.2$, again primarily because the 3D S-A failed to capture the cessation of the vortex shedding at this smaller gap ratio. This was also found to be the case with the 2D URANS simulations (not presented here).

3.4.4 Further discussion on the cessation of Kármán vortex shedding

After comparing the accuracy of the DES and URANS simulations in the preceding sections, the focus of the discussion is now back to the onset/cessation of the von Kármán-type vortex shedding. As demonstrated in this study, the capability of turbulence models/techniques to correctly predict the formation and cessation of large-scale vortex shedding is of crucial importance when they are applied to this type of bluff body flow. It is therefore worthwhile — not only from the physical but also from the computational point of view — to address the question: *"Why did the von Kármán-type vortices incorrectly 'survive' in the URANS simulations until the cylinder came much closer to the ground?"*

The first point to be mentioned here is that the incorrect vortex shedding observed in the URANS in this study seems to contradict a general view in CFD, i.e., vortex shedding should tend to be suppressed when the predicted flow is 'overly dissipative' (cf. Section 1.4.5) or the predicted eddy viscosity is excessively large. Figure 3.23 shows the contours of typical instantaneous eddy viscosity ratio predicted by the DES and 3D S-A URANS at $h/d = 0.6$, 0.2, and 0.1. It is obvious that the 3D S-A URANS yielded a much larger eddy viscosity than that by the DES in the region after the separation from the cylinder (note that in the region before the separation the eddy viscosity was kept almost zero in both DES and URANS due to the trip-less approach, cf. Section 3.2.6). This shows that the accuracy of the prediction of the onset/cessation of the vortex shedding cannot be simply or directly linked with the difference in the global level of eddy viscosity predicted.

A possible explanation for the 'delayed' cessation in the URANS, however, can be derived from the mean wake profiles predicted by the DES and URANS at the smallest gap ratio of 0.1, at which not only the DES but also the URANS captured the cessation of the vortex shedding due to the strong influence of the nearby ground. Figure 3.24 compares the mean streamwise velocity profiles at $x/d = 1.0$ and 1.5 predicted by the DES and 3D S-A URANS for $h/d = 0.1$. It can be seen that the DES predicted a wider top-hat-like wake profile with a smaller backflow velocity in this region, similar to that predicted for $h/d = 0.2$ [cf. 3.22(b)], whereas the 3D S-A still yielded a narrower parabolic-like wake profile with a larger backflow velocity despite having captured the cessation of the vortex shedding. This difference in the mean velocity profiles in the near wake region is of crucial importance when considering the stability characteristics of the wake.

As reviewed in Section 1.4.6, from the viewpoint of hydrodynamic stability of the wake, the key to the formation of von Kármán-type vortices is the existence of absolutely unstable regions in the near wake region, which allows local disturbances to propagate both upstream and downstream. Of interest here is that the near wake profiles predicted by the 3D S-A URANS seem to be more (inviscidly) absolutely-unstable than those predicted by the DES. As will be shown later in Chapter 4, a linear inviscid stability analysis of simplified wake profiles in ground effect indicates that the state of the wake tends to change from being absolutely

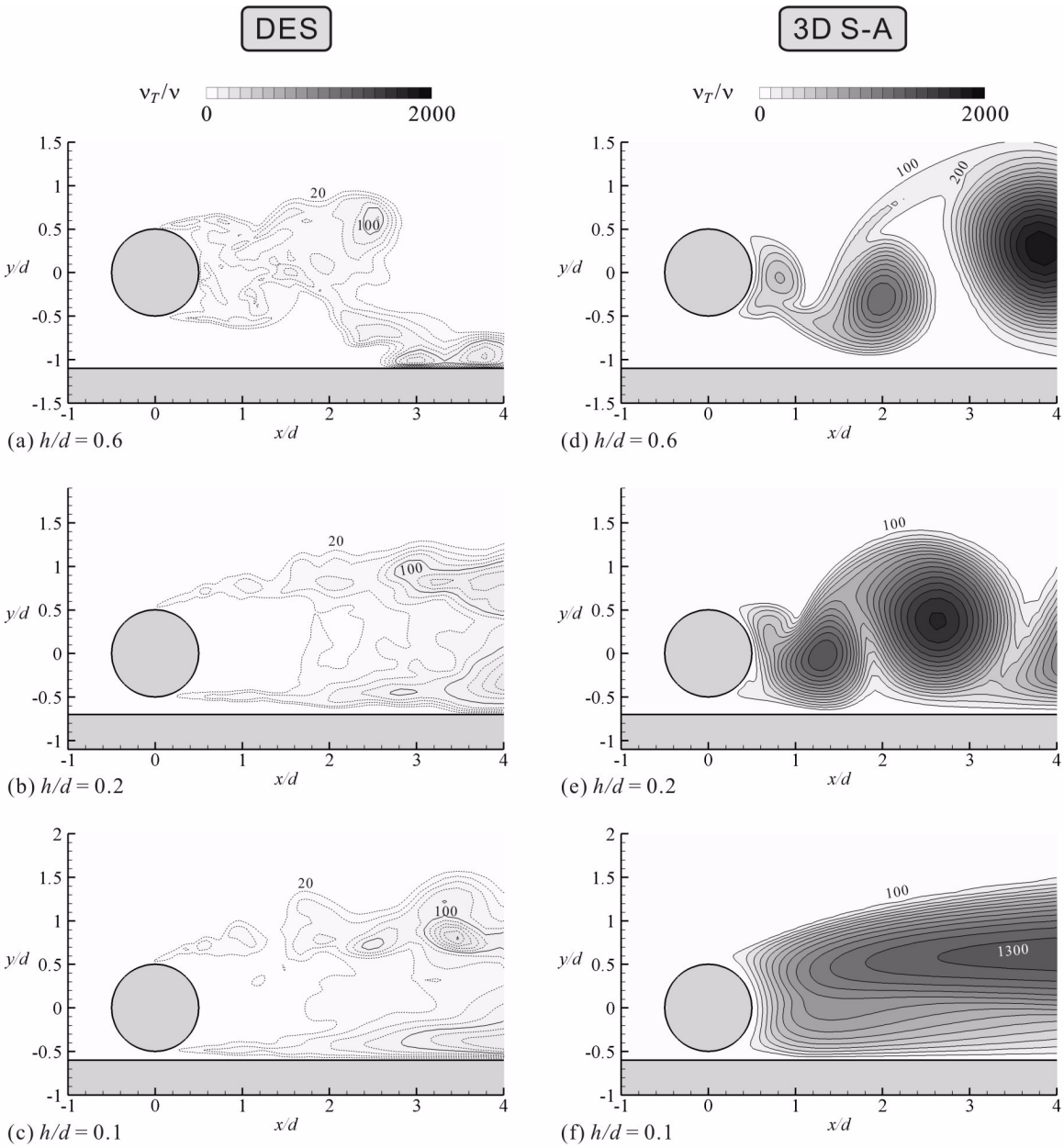

Figure 3.23: Instantaneous eddy viscosity ratio: (a-c) DES, (d-f) 3D S-A ($\mathrm{Re} = 0.4 \times 10^5$).

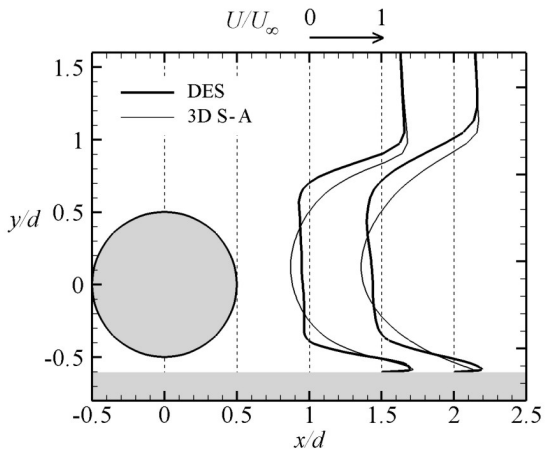

Figure 3.24: Comparison of mean streamwise velocity profiles ($h/d = 0.1$, $\mathrm{Re} = 0.4 \times 10^5$).

unstable to being convectively unstable as the relative ground distance (i.e., the distance from the wake centreline to the ground, H, divided by the wake width, B, see Chapter 4) is reduced, as well as when the reverse or backflow velocity of the wake is reduced. This might explain the main reason why the wakes in the URANS simulations were more susceptible to the formation of the von Kármán-type vortices in this study.

The above interpretation of the incorrect vortex shedding turns out to be more probable when the present results are compared with the 2D URANS simulations of flow past a square cylinder placed near a fixed ground by Bosch and Rodi (1996). In their study, the standard k-ϵ model predicted an 'earlier' cessation of the vortex shedding in ground effect (i.e., the shedding was predicted to cease at a higher gap ratio than that observed in experiments), in contrast to the URANS simulations in the present study. They showed that the prediction of the cessation could be improved by employing an *ad hoc* modification of the k-ϵ model proposed by Kato and Launder (1993) to prevent the excessive production of turbulence, and thus suggested that the 'earlier' cessation of the vortex shedding in ground effect predicted by the standard k-ϵ model was due to the excessive damping caused by the excessive eddy viscosity in the wake. However, these results may also be interpreted, from the hydrodynamic stability point of view, that the wider wake predicted by the standard k-ϵ model was less absolutely-unstable than the narrower wake predicted by the model with the Kato-Launder modification (note that the relative ground distance H/B decreases as the wake width B increases). That is to say, it is inferred that in the present study all URANS simulations predicted 'delayed' cessation of the vortex shedding behind the circular cylinder primarily because they predicted narrower wakes and therefore larger H/B in the near wake region, whereas in the study by Bosch and Rodi (1996) the standard k-ϵ model predicted 'earlier' cessation of the vortex shedding behind the square cylinder primarily because the standard k-ϵ model predicted wider wakes and therefore smaller H/B in the near wake region.

3.5 Conclusions

In this chapter, the results of URANS, LES, and DES were presented for a subcritical flow ($0.4 \times 10^5 \leq \mathrm{Re} \leq 1.0 \times 10^5$) around a circular cylinder placed near and parallel to a moving ground. The LES and DES were performed in a three-dimensional domain with periodicity imposed in the spanwise direction, whereas the URANS were conducted in both two- and three-dimensional domains.

The simulations were first performed with different spatial and time resolutions (for a representative case of $h/d = 1.0$, $\mathrm{Re} = 0.4 \times 10^5$). Good grid convergence was obtained in both 2D and 3D URANS simulations, whereas it was not obtained in the LES presumably because the grids used in this study were not fine enough for LES. The grid convergence in the DES was not perfect but clearly better than the LES performed on the same set of grids. Also the time resolution was found to be sufficient in both 2D/3D URANS and DES. The simulations were then performed with different Reynolds numbers (for a representative case of $h/d = 1.0$ with the standard spatial and time resolution). As was expected from the results of earlier studies by other researchers, all simulations in this study were also found to fail to

capture the correct 'subcritical' flow characteristics around the cylinder at higher Reynolds numbers. At the lower Reynolds number of 0.4×10^5, however, both 2D/3D URANS and DES were found to yield reasonable results.

As concerns the prediction of the ground effect, which was examined with the 'easiest' Reynolds number of 0.4×10^5, the DES successfully captured the main flow/force characteristics, whereas the URANS did not. The DES predicted the cessation of the large-scale von Kármán-type vortex shedding behind the cylinder between two h/d of 0.4 and 0.3, which was consistent with the earlier experiments, whereas both 2D and 3D URANS also predicted it but at a much smaller h/d of 0.2 to 0.1. The wake structures of the cylinder predicted by the DES were in good agreement with the experiments in both large- and small-gap regimes, and also in the intermediate-gap regime, where the DES captured the intermittence of the large-scale vortex shedding in the near wake region. The time-averaged drag coefficients, separation angles, and velocity profiles in the near wake region predicted by the DES were also in good agreement with the experiments. These results suggest the promise of DES to flows involving the problem of large-scale vortex shedding, and its control or suppression, often encountered in engineering applications.

Another interesting difference was also observed between the 2D and 3D S-A URANS solutions. That is, the former yielded fully periodic time variations in C_D and C_L at all h/d of greater than 0.1, whereas the latter showed some low-frequency modulations at $h/d \geq 0.4$, where moderately three-dimensional wake structures consisting of not only spanwise vortices but also streamwise 'rib' vortices were predicted. The vortical structures resolved in the 3D S-A URANS, however, were still much coarser than those by the DES despite the same grid employed and hence almost the same computational costs required. As far as the time-averaged properties of the flow were concerned, the difference between the 2D and 3D URANS seemed less significant than those between the 3D URANS and the DES.

Also examined was the reason of the 'delayed' cessation of the vortex shedding in the URANS simulations. The mean wake profiles predicted by the DES and 3D URANS were compared for $h/d = 0.1$, at which gap ratio even the URANS captured the cessation of the vortex shedding due to the strong influence of the nearby ground. It was inferred that the near wake profiles predicted by the URANS were more (inviscidly) absolutely-unstable than those predicted by the DES basically because the URANS predicted narrower wakes, which effectively increased the relative gap distance between the wake and the ground. Further discussions on this topic will be given in Chapter 4, where a linear inviscid stability analysis is applied to simplified model wake profiles in ground effect.

Chapter 4

Linear Stability Analysis of the Wake of Cylinders in Ground Effect

4.1 Introduction

As briefly discussed in the previous chapters, the mechanism of the formation of von Kármán-type vortices behind cylindrical bluff bodies can often be explained by the existence of *absolutely unstable* regions in the near wake region, which allows local disturbances to propagate both upstream and downstream. For example, a linear stability analysis by Monkewitz (1988) demonstrated the existence of an absolutely unstable region in the near wake of a circular cylinder at the critical Reynolds number of about 50 for the onset of the von Kármán-type vortex shedding. In analogy to this, the cessation of the vortex shedding at much higher Reynolds numbers behind a cylinder equipped with a backward splitter plate, which was first experimentally observed by Roshko (1955), may also be explained as the splitter plate prevents the hydrodynamic resonance in the near wake region (Oertel 1990).

The objective of the linear stability analysis presented in this chapter is to show that a similar explanation may also be applicable to the cessation of the von Kármán-type vortex shedding from cylindrical bluff bodies in ground effect. Although the near wake structures of two-dimensional bluff bodies are in general three-dimensional and highly complicated unless the Reynolds number of the flow is very low, this study employs a traditional *local* (i.e., parallel-assumed) *linear stability analysis* method — this type of analysis has been successful for many types of spatially developing flows as reviewed in Section 1.4.6. It is also assumed that the fluid is inviscid and incompressible. The analysis is first applied to a four-parameter family of velocity profiles, which is an extended version of a two-parameter symmetric near wake model by Monkewitz and Nguyen (1987) and Monkewitz (1988), in order to investigate the local absolute and local convective instabilities of the wake in ground effect. The analysis is then compared with the results of the experiments and numerical simulations in the previous chapters. Specifically, the streamwise variation of the local linear stability characteristics of the wake is examined to discuss the link between the local linear stability characteristics and the cessation of the von Kármán-type vortex shedding in ground effect. The discussion is based on the transition scenario of *steep global modes* by Pier and Huerre (2001), in which

the upstream edge of the region of local linear absolute instability acts as a *wavemaker* to generate nonlinear travelling waves in the downstream direction (cf. Section 4.4.3).

In the following, the details of the model wake profiles and the analysis procedure will be described in Sections 4.2 and 4.3, respectively, and the results of the analysis will be presented in Section 4.4. Finally a concluding summary will be given in Section 4.5.

4.2 Modelling of local wake profiles

The local velocity profile of the near wake of general two-dimensional bluff bodies placed near a ground may be approximated by the following analytical model equations:

$$U(y) = [1 - R_1 + 2R_1F_1(y)]\left(\frac{U_c + U_\infty}{2}\right) \qquad (\text{for } 0 \le y \le \infty)\,, \tag{4.1}$$

$$U(y) = [1 - R_2 + 2R_2F_2(y)]\left(\frac{U_c + U_g}{2}\right) \qquad (\text{for } -H \le y < 0)\,, \tag{4.2}$$

where

$$R_1 = \frac{U_c - U_\infty}{U_c + U_\infty}\,, \qquad F_1(y) = \left\{1 + \sinh^{2N_1}\left[y\sinh^{-1}(1)/b_1\right]\right\}^{-1}\,, \tag{4.3}$$

$$R_2 = \frac{U_c - U_g}{U_c + U_g}\,, \qquad F_2(y) = \left\{1 + \sinh^{2N_2}\left[y\sinh^{-1}(1)/b_2\right]\right\}^{-1}\,, \tag{4.4}$$

as described in Fig. 4.1. Here U_c and U_∞ are the velocities at $y = 0$ and ∞, respectively. U_g is a hypothetical velocity at $y = -\infty$, and H is the transverse distance between $y = 0$ and the ground. N_1 and N_2 determine the ratio of each mixing layer thickness to the width of the wake, and b_1 and b_2 are the so-called 'half-widths' of the wake, which are respectively the distances from $y = 0$ to the points where $U(y) = (U_c+U_\infty)/2$ for b_1 and $U(y) = (U_c+U_g)/2$ for b_2. It should be noted that this model is an extended asymmetric version of the symmetric near wake model by Monkewitz and Nguyen (1987) and Monkewitz (1988), which can be reproduced from the above equations with $U_g = U_\infty$, $N_1 = N_2$, $b_1 = b_2$, and $H = \infty$.

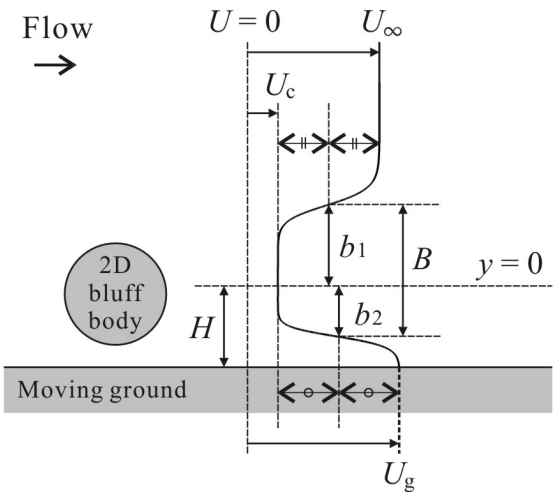

Figure 4.1: Near wake model of general two-dimensional bluff bodies in ground effect (note that $b_1 = b_2 = B/2$ in the present study).

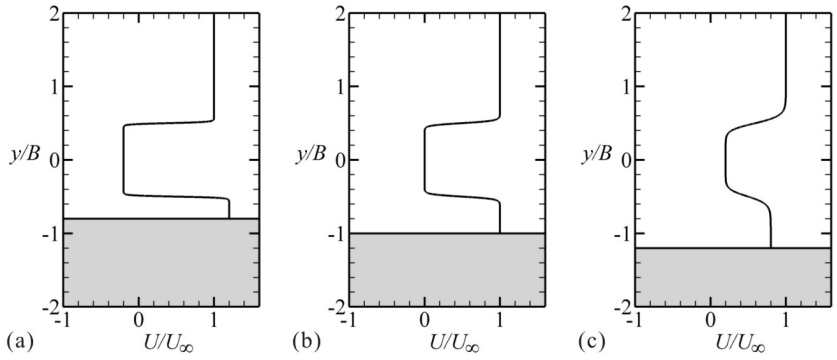

	(a)	(b)	(c)
N	25	12.5	4
U_g/U_∞	1.2	1	0.8
U_c/U_∞	-0.2	0	0.2
H/B	0.8	1	1.2

Figure 4.2: Examples of local wake profiles in ground effect.

Since the primary objective is to examine the fundamental influence of the nearby ground on the stability characteristics of the wake, $N_1 = N_2 = N$ and $b_1 = b_2 = B/2$ are also employed in this study for simplicity. It follows that U_∞ and B are the characteristic velocity and length of the flow (but note that B varies in the streamwise direction when the global instability of the wake is discussed later in Sections 4.4.3 and 4.4.4), and N, U_g, U_c, and H are the four parameters that are varied to determine the local velocity profiles in this study. Typical examples of the velocity profiles are shown in Fig. 4.2. Note that, as N increases, the thickness of each shear layer becomes thinner and hence the wake profile becomes closer to the so-called 'top-hat' profile. Also note that the ground distance H is varied in a certain range in this study such that the ground speed $U(-H)$ obtained from Eqs. (4.1) to (4.4) satisfies $U(-H) \geq 0.99U_g$ for a meaningful comparison with the experiments (and also the numerical simulations) using the moving ground in the previous chapters. More details of the comparison with the experiments will be discussed later in Section 4.4.3.

It should be noted that the wake profiles obtained from the above model are simplified or ideal ones; the real near wake profile of a bluff body depends on its cross-sectional geometry. The scope of the interest of this study is therefore limited to a qualitative description of the stability characteristics obtained. This, nonetheless, gives useful insights into the mechanisms of the cessation of von Kármán-type vortex shedding in ground effect.

4.3 Analysis procedure

The absolute and convective instabilities of the above wake profiles are investigated in this study by using a local linear stability analysis, basically following Monkewitz and Nguyen (1987). The flow analysed is assumed to be *quasi-laminar*, i.e., the turbulence is assumed to affect the instability waves only indirectly through the mean velocity profile, not directly through its stresses. It is further assumed that the fluid is inviscid, as the instabilities of interest here are those of inviscid or inflectional type, and it is also assumed that the flow is incompressible. It follows that the governing equations for the motion of small disturbances to be examined in this study can be derived from the Euler equations and the continuity equation as follows:

$$\left(\frac{\partial}{\partial t}+U\frac{\partial}{\partial x}\right)u'+\frac{\mathrm{d}U}{\mathrm{d}y}v'+\frac{\partial p'}{\partial x}=0\,, \tag{4.5}$$

$$\left(\frac{\partial}{\partial t}+U\frac{\partial}{\partial x}\right)v'+\frac{\partial p'}{\partial y}=0\,, \tag{4.6}$$

$$\frac{\partial u'}{\partial x}+\frac{\partial v'}{\partial y}=0\,, \tag{4.7}$$

where u' and v' are the perturbation velocities in the x (streamwise) and y (transverse) directions, respectively, and p' is the perturbation pressure. $U(y)$ is the mean streamwise velocity obtained from the near wake model of Eqs. (4.1) to (4.4).

The above perturbation equations can be re-written with the perturbation stream function ψ' (by which the perturbation velocities are given as $u'=\partial\psi'/\partial y$ and $v'=-\partial\psi'/\partial x$) as

$$\left(\frac{\partial}{\partial t}+U\frac{\partial}{\partial x}\right)\nabla^2\psi'-\frac{\mathrm{d}^2U}{\mathrm{d}y^2}\frac{\partial\psi'}{\partial x}=0\,, \tag{4.8}$$

where $\nabla^2=(\partial^2/\partial x^2+\partial^2/\partial y^2)$. Since the main concern here is to show general criteria for the absolute and convective instabilities of the flow, the so-called *normal-mode analysis* is employed in this study, i.e., ψ' is expressed in the form of complex normal modes as

$$\psi'(x,y,t)=\phi(y)\exp\left[ik(x-ct)\right]\,, \tag{4.9}$$

where $k=k_r+ik_i$ and $c=c_r+ic_i$ denote the complex wave number and wave velocity, respectively. The complex frequency, $\omega=\omega_r+i\omega_i$, is given by $\omega=kc=(k_rc_r-k_ic_i)+i(k_rc_i+k_ic_r)$. It should be noted that ω_i physically means the exponential growth rate of the disturbance wave in time. Substituting Eq. (4.9) into Eq. (4.8) finally leads to the well-known Rayleigh equation (see, e.g., Drazin and Reid 1981):

$$(U-c)\left(\frac{\mathrm{d}^2\phi}{\mathrm{d}y^2}-k^2\phi\right)-\frac{\mathrm{d}^2U}{\mathrm{d}y^2}\phi=0\,, \tag{4.10}$$

which, together with the boundary conditions

$$\phi=0\quad\text{at}\quad y=-H\quad\text{and}\quad+\infty\,, \tag{4.11}$$

defines the stability eigenvalue problem to be numerically solved in this study [the dispersion relation is described as $\mathcal{F}(k,c)=0$, or alternatively $\mathcal{F}(k,\omega)=0$, and the corresponding non-trivial solution $\phi(y)$ is the eigenfunction].

The determination of whether the local velocity profile $U(y)$ is absolutely or convectively unstable can be made by examining the *branch-point singularities* of the dispersion relation for k and ω based on the Briggs-Bers criterion (Briggs 1964; Bers 1983). Specifically, the flow is found to be absolutely unstable (i.e., there exist unstable modes travelling upstream) if at least one of the branch-point singularities that satisfy the so-called *pinching requirement* is in the upper half of the complex ω plane [i.e., $\omega_i^0>0$, where the superscript 0 indicates the zero group velocity; see, e.g., Huerre (2000) for a further description]. This can be confirmed by mapping the dispersion relation $\omega(k)$ for constant k_r and k_i on the complex ω plane, or equivalently $k(\omega)$ for constant ω_r and ω_i on the complex k plane, as will be shown later in Section 4.4.

As concerns numerical methods employed in this study, the standard fourth-order Runge-Kutta method was used to numerically integrate Eq. (4.10), and Muller's iterative method (see, e.g., Press *et al.* 1992) was used to find complex eigenvalues satisfying the boundary conditions of Eq. (4.11). The whole procedure was repeated a number of times in order to map the dispersion relation $k(\omega)$ for each set of parameters (N, U_g, U_c, and H) and thereby to obtain the boundaries between the absolute and convective instabilities. All computations were performed using MATLAB (The MathWorks, Inc. 2002).

4.4 Results and discussion

In this section, the results of the stability analysis are presented. Firstly, in Section 4.4.1, the analysis is applied to local wake profiles in a free stream to validate the analysis procedure. Secondly, in Section 4.4.2, the analysis is applied to local wake profiles in ground effect. Then, in Section 4.4.3, the analysis is compared with the experimental results to discuss the link between the local stability characteristics and the global onset/cessation of the von Kármán-type vortex shedding in ground effect. Finally, in Section 4.4.4, the analysis is compared with the CFD results to re-examine the possible explanation of the 'delayed' cessation of the vortex shedding in URANS simulations discussed in Chapter 3.

4.4.1 Local instability characteristics of wakes in a free stream

In order to validate the analysis procedure, it was first applied to local wake profiles in a free stream (i.e., $U_\mathrm{g}/U_\infty = 1$ and $H/B = \infty$), which were originally investigated by Monkewitz and Nguyen (1987). For these symmetric wake profiles, two types of modes exist, namely the sinuous (or Kármán) and varicose modes, where the eigenfunction $\phi(y)$ takes the forms of even and odd functions about the origin $y = 0$, respectively. It is known that only the sinuous mode shows a sign of absolute instability for a physically realistic range of the parameters N and U_c (Monkewitz and Nguyen 1987).

Figure 4.3 shows the dispersion relation $k(\omega)$ for the sinuous mode for the wake profile described by Eqs. (4.1) to (4.4) with $N = 1$, $U_\mathrm{g}/U_\infty = 1$, $U_\mathrm{c}/U_\infty = 0.051$, and $H/B = \infty$. Note that the profile with the condition $N = 1$ corresponds to a fully-developed wake profile, and the spatial stability of this particular profile was first investigated by Betchov and Criminale (1966). It can be seen from this figure that, for this particular wake profile, the branch point singularity exists at $\omega_i \approx 0$ [and this branch point satisfies the pinching requirement, i.e., one of the two 'hills' consists of k^+ branches and the other consists of k^- branches in the terminology of Huerre (2000)]. Further analysis reveals that this branch point singularity is found at $\omega_i > 0$ when $U_\mathrm{c}/U_\infty < 0.051$ and at $\omega_i < 0$ when $U_\mathrm{c}/U_\infty > 0.051$. This means that $U_\mathrm{c} = 0.051U_\infty$ is the critical centreline velocity of the wake, i.e., the flow is locally absolutely unstable when $U_\mathrm{c}/U_\infty < 0.051$ and is locally convectively unstable when $U_\mathrm{c}/U_\infty > 0.051$. This agrees with the results by Monkewitz and Nguyen (1987) and also the results by Betchov and Criminale (1966).

The analysis was also performed on the symmetric wake profiles with $N = 2$, 4, 12.5, and 25, and the critical U_c/U_∞ were found to be 0.089, 0.073, 0, and -0.032, respectively. This

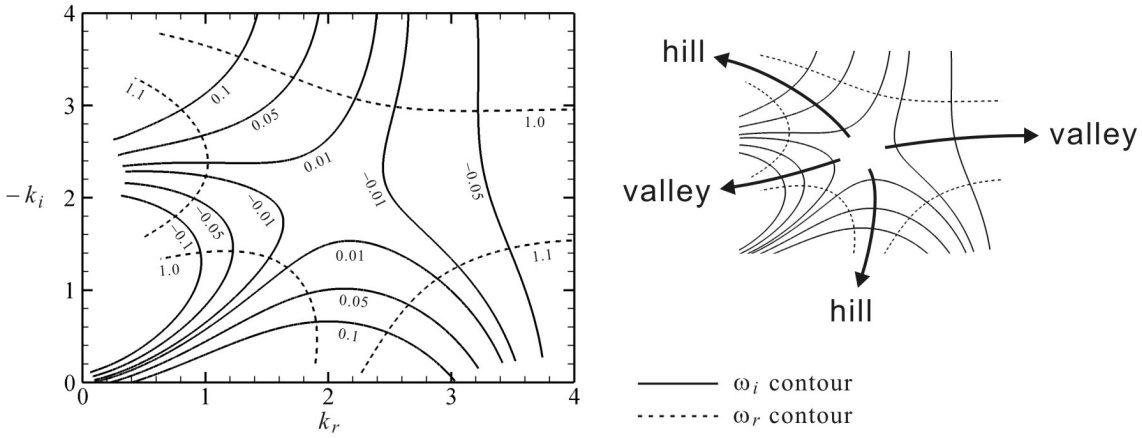

Figure 4.3: Dispersion relation for an unbounded wake profile (sinuous mode, $N = 1$, $U_g/U_\infty = 1$, $U_c/U_\infty = 0.051$, $H/B = \infty$).

also agrees with the results by Monkewitz and Nguyen (1987). It should be noted that the wake becomes more unstable as N increases from 1 to about 2.3 but it becomes less unstable as N further increases (Monkewitz and Nguyen 1987).

4.4.2 Local instability characteristics of wakes in ground effect

In the following, the analysis is applied to local wake profiles in ground effect (i.e., U_g and H are now variables as well as N and U_c). Although the wake profiles are no longer symmetric, there still exist two types of modes as the profile still possesses two inflection points: one of them (hereafter referred to as Mode I) shows the eigenfunction $\phi(y)$ of even functions and the other (hereafter referred to as Mode II) shows that of odd functions when H/B is sufficiently large. Since Mode I is physically relevant to the von Kármán-type vortex shedding (Criminale *et al.* 2003) and indeed shows a sign of absolute instability for a physically realistic range of the parameters, only the results for Mode I are discussed below.

Example of the change of dispersion relation in ground effect

Figure 4.4 shows an example of the influence of the relative ground distance H/B on the branch points of the dispersion relation (for the local wake profiles with $N = 12.5$, $U_g/U_\infty = 1$, and $U_c/U_\infty = 0$). Here the curves labelled 'Mode I-A' indicate the mode that corresponds to the sinuous mode for the unbounded wake (when H/B is sufficiently large). This can be confirmed from $\omega_i^0 \to 0$ as $H/B \to \infty$, which is consistent with the result by Monkewitz and Nguyen (1987) that $U_c/U_\infty = 0$ is the critical centreline velocity for the unbounded wake profile with $N = 12.5$, as noted in Section 4.4.1. As H/B decreases to less than about 1.6, however, another branch point with a larger $\omega_i^0 \to 0$ value (labelled 'Mode I-B' in the figure) appears on the dispersion relation. The key question here is whether this second branch point is relevant to the stability of the wake, or in other words, whether this branch point arises from the coalescence of upstream-propagating k^+ branches and downstream-propagating k^- branches.

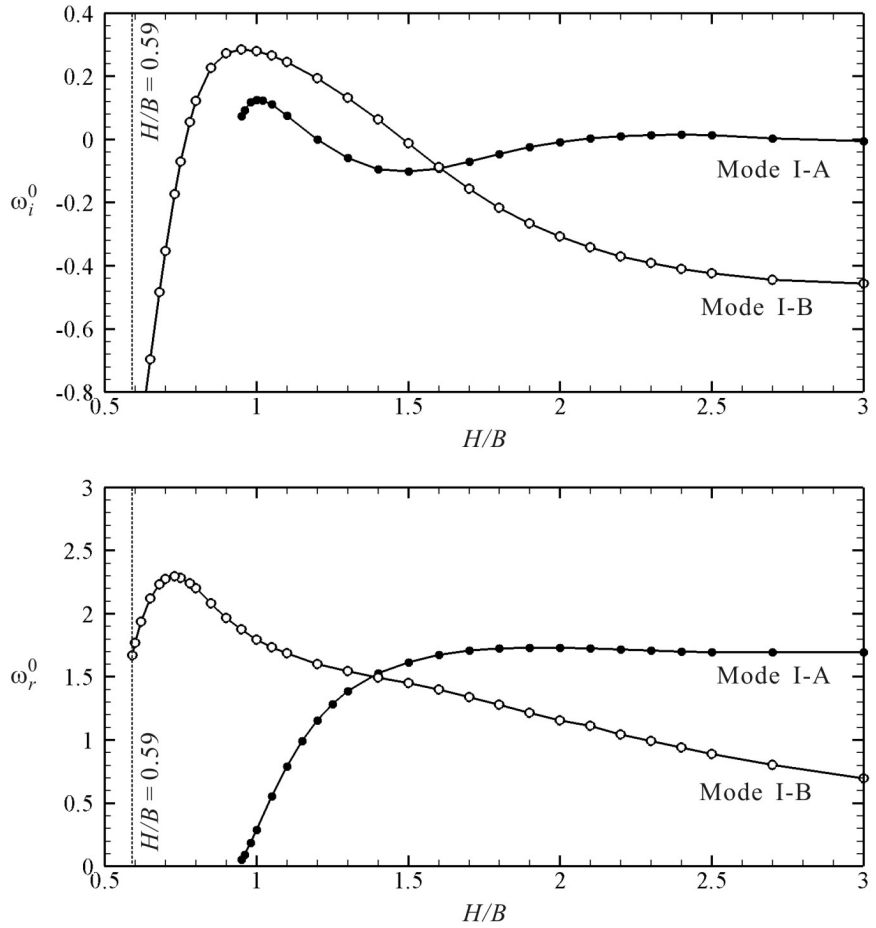

Figure 4.4: Influence of H/B on the imaginary and real parts of ω at the branch points ($N = 12.5$, $U_g/U_\infty = 1$, $U_c/U_\infty = 0$).

Figure 4.5 shows the maps of the dispersion relation for the cases with $H/B = 1.7$, 1.5, and 1.3. At $H/B = 1.7$ [Fig. 4.5(a)], both branch points are of the so-called k^+/k^- type, which can be verified from the fact that, for each branch point, one of the two hills originates in the $k_i > 0$ region and the other originates in the $k_i < 0$ region. Mode I-A still has a larger ω_i^0 value than Mode I-B (cf. Fig. 4.4), and hence has a dominant influence on the stability characteristics of the wake. At $H/B = 1.5$ [Fig. 4.5(b)], again both branch points are of the k^+/k^- type, but the ω_i^0 value of Mode I-A is now smaller than that of Mode I-B (cf. Fig. 4.4). This means that the more unstable mode is shifted from Mode I-A to Mode I-B as H/B is reduced from 1.7 to 1.5. Of interest is that, at $H/B = 1.3$ [Fig. 4.5(c)], the branch point for Mode I-A is no longer of the k^+/k^- type but of the k^-/k^- type, i.e., Mode I-A is not relevant to the stability characteristics of the wake when $H/B \leq 1.3$.

The value of ω_i^0 for Mode I-B becomes larger than zero as H/B decreases to less than 1.5 (cf. Fig. 4.4), which physically means that the wake becomes absolutely unstable in this H/B range. As H/B further decreases to less than about 0.95, however, ω_i^0 for Mode I-B rapidly decreases, and finally the state of the wake changes back to being convectively unstable for $H/B < 0.77$. It should be noted that the analysis for this example was performed for

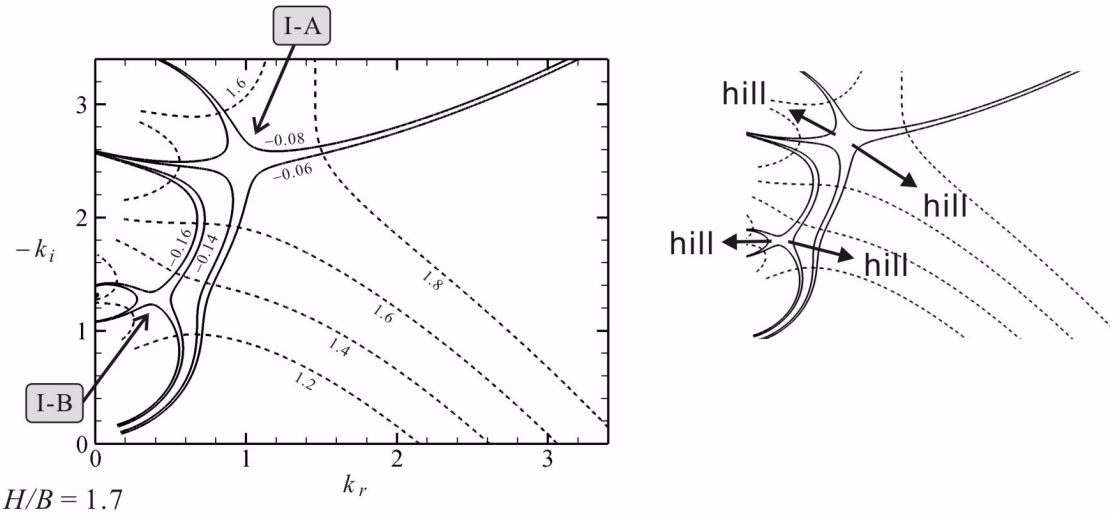

(a) $H/B = 1.7$

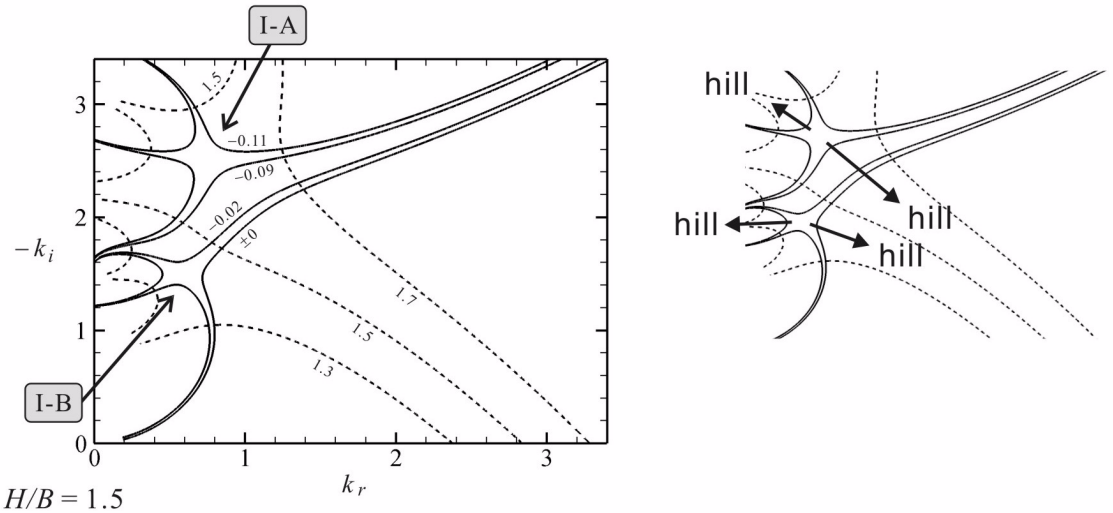

(b) $H/B = 1.5$

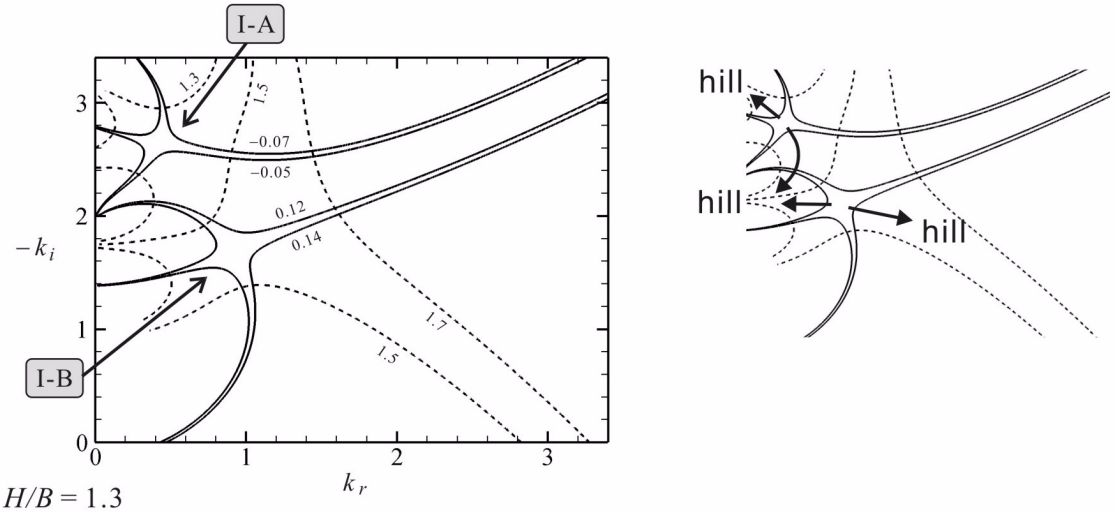

(c) $H/B = 1.3$

Figure 4.5: Dispersion relation for local wake profiles ($N = 12.5$, $U_g/U_\infty = 1$, $U_c/U_\infty = 0$) with three different H/B; solid and dashed lines indicate the contours of ω_i and ω_r, respectively.

$H/B \geq 0.59$, in which range the condition of $U(-H) \geq 0.99U_\infty$ was maintained for the wake profile with $N = 12.5$, and the ω_i^0 value at $H/B = 0.59$ was found to be -1.09. This suggests a strong 'stabilizing' effect of the nearby ground on the wake.

Absolute versus convective instability boundaries in ground effect

The main focus of the discussion is now on the transition between the absolute and convective instabilities especially in the smaller H/B region, which was observed around $H/B = 0.77$ in the above example with $N = 12.5$, $U_g/U_\infty = 1$, and $U_c/U_\infty = 0$. Figures 4.6(a) and (b) show the absolute instability boundaries in the $(U_c/U_\infty) - (H/B)$ plane for different N and for different U_g/U_∞, respectively. Note that the kink of each curve around $H/B = 1.5$ corresponds to the turnover of the more unstable mode between Mode I-A and Mode I-B described in the above example in Figs. 4.4 and 4.5. Also note that the range $N \geq 4$ shown here corresponds to the 'top-hat-like' near-wake profiles that are of interest in this study (cf. Fig. 4.2), whereas the range $0.8 \leq U_g/U_\infty \leq 1.2$ covers almost completely the corresponding (hypothetical) velocity-ratio range experimentally observed in the near wake region of the cylinder in Chapter 2, as shown later in Fig. 4.9(c). For all the cases shown in Fig. 4.6, it can

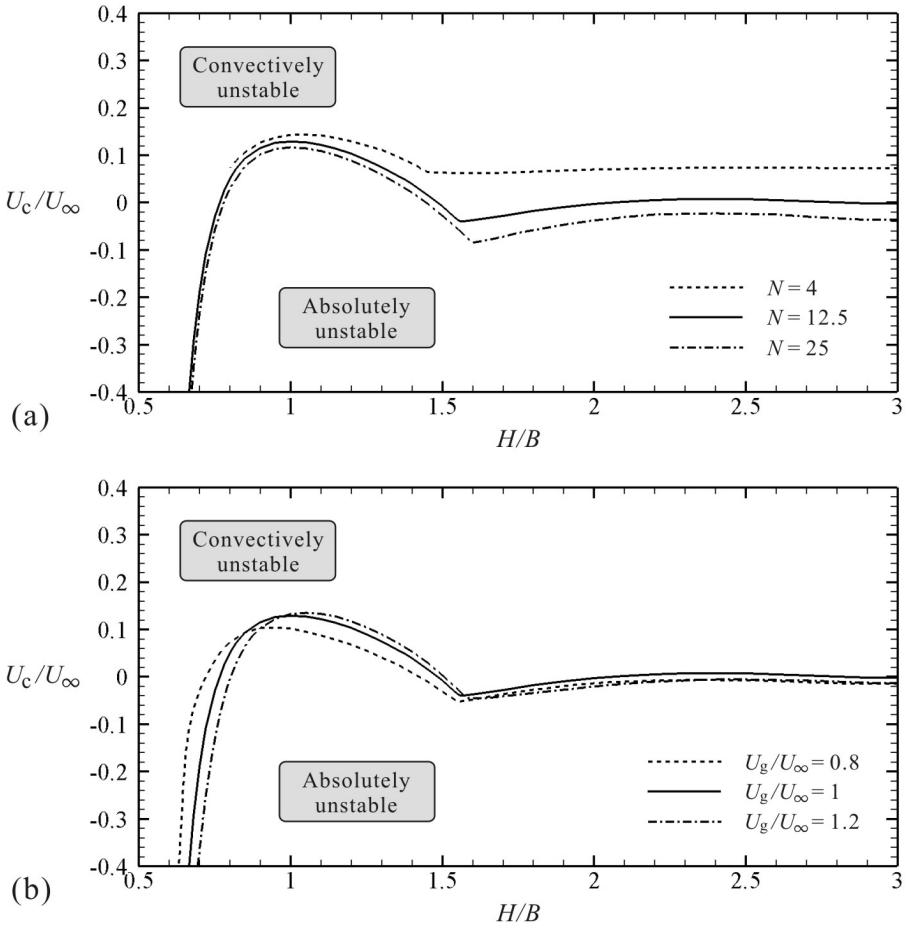

Figure 4.6: Absolute instability boundaries in the $(U_c/U_\infty) - (H/B)$ plane: (a) for different N with $U_g/U_\infty = 1$; (b) for different U_g/U_∞ with $N = 12.5$.

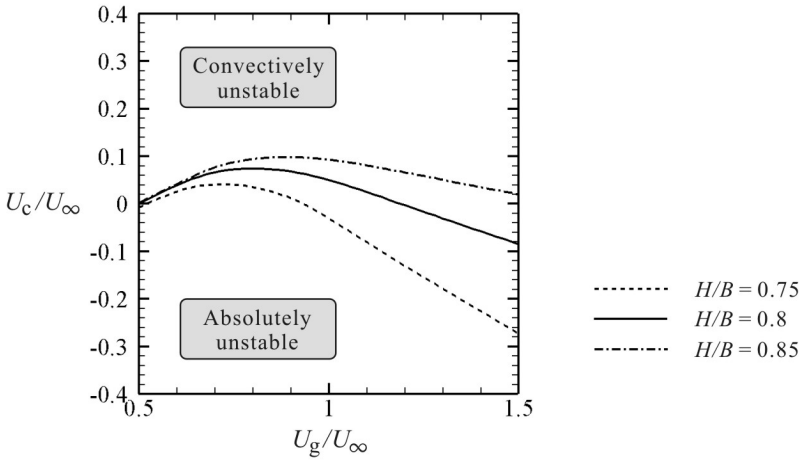

Figure 4.7: Absolute instability boundaries in the $(U_c/U_\infty) - (U_g/U_\infty)$ plane for different H/B (with $N = 12.5$).

be seen that the critical centreline velocity rapidly decreases as H/B decreases to less than about 0.9. This again shows the strong stabilizing effect of the nearby ground on the wake; at $H/B = 0.6$, for example, the wake with $N = 12.5$, $U_g/U_\infty = 1$, and $U_c/U_\infty - 0.4$ is still within the region of convectively unstable rather than absolutely unstable, despite its strong backflow.

Of further interest is the influence of the wake parameters N and U_g/U_∞ on the results. As concerns the influence of N, it can be seen from Fig. 4.6(a) that the profiles with smaller N (i.e., with thicker mixing layers, cf. Fig. 4.2) are more absolutely unstable than the profiles with larger N (i.e., with thinner mixing layers) for the range of $N \geq 4$ examined here. This tendency has already been reported by Monkewitz and Nguyen (1987) for the unbounded wake profiles with $U_g/U_\infty = 1$ and $H/B = \infty$, as discussed in Section 4.4.1. For $H/B \leq 0.9$, however, there seems to be little influence of N on the stability characteristics of the wake, even though the analysis for $N = 4$ was performed only for $H/B \geq 0.8$ so as to maintain the condition of $U(-H) \geq 0.99U_\infty$ in this study.

As for the influence of U_g/U_∞, only small differences can be seen in the results at $H/B \geq 1.6$ [cf. Fig. 4.6(b)]. At $H/B \leq 0.85$, however, the figure shows an interesting trend that the wake becomes more absolutely unstable as U_g/U_∞ decreases. Figure 4.7 shows the absolute instability boundaries in the $(U_c/U_\infty) - (U_g/U_\infty)$ plane for $H/B = 0.75$, 0.8, and 0.85. It can be seen that the most unstable U_g/U_∞ range shifts towards $U_g/U_\infty < 1$ as H/B decreases. In other words, the wake becomes more unstable as the velocity on the 'near-ground' side is slightly decreased compared with that on the 'far-ground' side. This interesting influence of U_g/U_∞ on the local linear stability characteristics of the wake might be related to a counter-intuitive experimental observation by Lei *et al.* (1999) for a circular cylinder placed near a fixed ground. As reviewed in Section 1.4.3, they observed that the critical gap ratio for the onset/cessation of the von Kármán-type vortex shedding slightly decreased from 0.3 to 0.2 as the boundary layer thickness on the ground *increased* from 0.14 to 0.48 — this will be discussed later in the next subsection.

4.4.3 Global instability and Kármán vortex shedding in ground effect

In the previous subsection, the linear stability characteristics of local wake profiles in ground effect were investigated. In summary the results showed that, when the relative ground distance H/B is small, the local linear stability characteristics of the wake are largely affected by the parameters H/B, U_c/U_∞, and U_g/U_∞, but not by N. In this subsection, further investigations are performed to discuss the link between the local linear stability characteristics and the cessation of the von Kármán-type vortex shedding in ground effect. Specifically, the local linear stability analysis performed in the previous subsection is now applied to velocity profiles varying in the streamwise direction so as to examine the streamwise variation of the local stability characteristics of the wake in ground effect.

As briefly reviewed in Section 1.4.6, this type of analysis has been successful for many types of spatially developing flows (e.g., Chen and Jirka 1997; Hammond and Redekopp 1998; Alam and Sandham 2000; Castro 2005) since several researchers suggested in the mid-1980s a close link between the local linear stability characteristics and the global mode selection of the flows (Pierrehumbert 1984; Koch 1985; Monkewitz and Nguyen 1987). Among them, Monkewitz and Nguyen (1987) proposed the *initial resonance criterion* for the wakes of two-dimensional bluff bodies; that is, the global mode (i.e., the overall frequency and associated spatial structures) of the wake is determined by the local resonance at the first streamwise station of local absolute instability. This scenario was recently found to be the case not only in the framework of linear stability theory but also in the theory of *steep nonlinear global modes*, which was first identified in a model problem using the one-dimensional complex Ginzburg-Landau equation by Pier *et al.* (1998) and was then confirmed in the context of real wake flows governed by the Navier-Stokes equations by Pier and Huerre (2001). According to these authors, the upstream edge or front of the region of local linear absolute instability acts as a wavemaker to generate nonlinear waves travelling downstream and imposes its local frequency on the global oscillation of the downstream flow. Hence the results of the linear stability analysis presented here would still give some useful insights into the physics of the cessation of the real (nonlinear) von Kármán-type vortex shedding in ground effect.

Approximation of experimental wake profiles by the analytical model

The streamwise variation of the wake profile to be investigated here is determined based on the results of the earlier experiments in Chapter 2 on the circular cylinder placed near the moving ground (at the upper-subcritical Reynolds number of 0.4×10^5 based on the cylinder diameter d). Specifically, the local wake parameters corresponding to H/B, U_c/U_∞, and U_g/U_∞ are extracted from the experimental mean velocity profiles at several streamwise positions behind the cylinder. The influence of the parameter N is assumed to be negligible, according to the results in Section 4.4.2 (note that only the small gap range of $H/B < 0.9$ is of interest here). An example of the comparison between the experimental data and the model wake profile is shown in Fig. 4.8.

Since the real (experimental) near wake profiles have velocity overshoots on both sides of the wake, here the parameters U_∞ and U_g for the model wake profiles are determined by

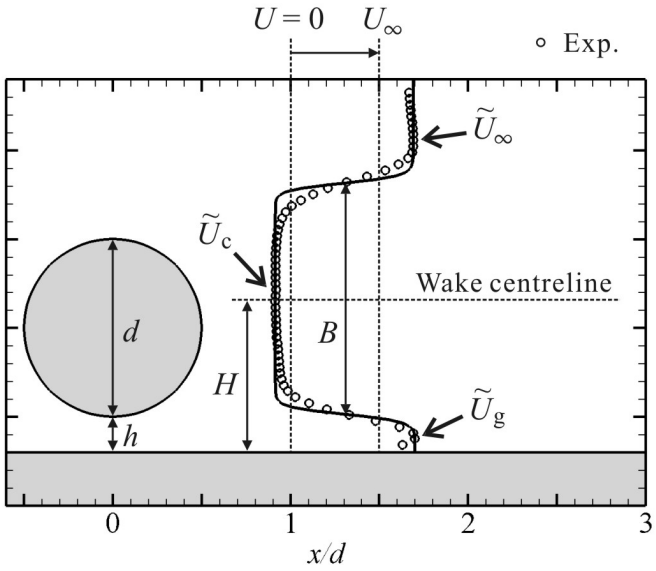

Figure 4.8: Example of a comparison of local wake profiles; open circles show the experimental results in Chapter 2 (with end-plates at $y_e/d = 0$, $h/d = 0.2$, $x/d = 1$) and the solid line shows the model profile ($\widetilde{U}_\infty = 1.381U_\infty$, $\widetilde{U}_g = 1.400U_\infty$, $\widetilde{U}_c = -0.172U_\infty$, $H = 0.866d$, $B = 1.299d$, $N = 12.5$).

the two local maximum velocities on each side of the wake (hereafter referred to as $\widetilde{U}_\infty$ and $\widetilde{U}_g$), respectively. The parameter U_c, meanwhile, is determined by the minimum velocity of the wake (hereafter referred to as $\widetilde{U}_c$) rather than by the centreline velocity of the wake. The wake width B is determined by the transverse distance between the two points where the streamwise velocity reaches $(\widetilde{U}_c + \widetilde{U}_\infty)/2$ and $(\widetilde{U}_c + \widetilde{U}_g)/2$, respectively. The ground distance H is determined by the distance from the ground surface to the centreline of the two transverse positions that define the wake width B. In addition to these extracted parameters, a constant N of 12.5 is retained for the following analysis.

Streamwise variation of local stability characteristics in ground effect

Figures 4.9(a-c) show the streamwise variation of the local wake parameters H/B, $\widetilde{U}_c/\widetilde{U}_\infty$, and $\widetilde{U}_g/\widetilde{U}_\infty$ extracted from the experimental mean velocity profiles behind the cylinder at two different gap ratios of 0.2 and 0.3. Note that, in the experiments, the von Kármán-type vortex shedding was found to be suppressed (at least in the near wake region of $x/d \leq 2.75$) at these two gap ratios (cf. Chapter 2). Also note that the figures show the variation of the wake parameters at $1 \leq x/d \leq 2.75$, in which region the experimental local velocity profiles showed common characteristics (i.e., having a local maximum on each side of the wake and also a local minimum near the centreline of the wake) and were therefore able to be approximated by the model wake profiles in the manner described above.

It can be seen that, for both h/d cases, H/B gradually increases in the downstream direction [Fig. 4.9(a)] since the flow is slightly deflected upward in this region. It is also obvious that, at each streamwise position, H/B decreases as h/d decreases. Meanwhile, $\widetilde{U}_c/\widetilde{U}_\infty$ becomes increasingly negative in the downstream direction [Fig. 4.9(b)] since this

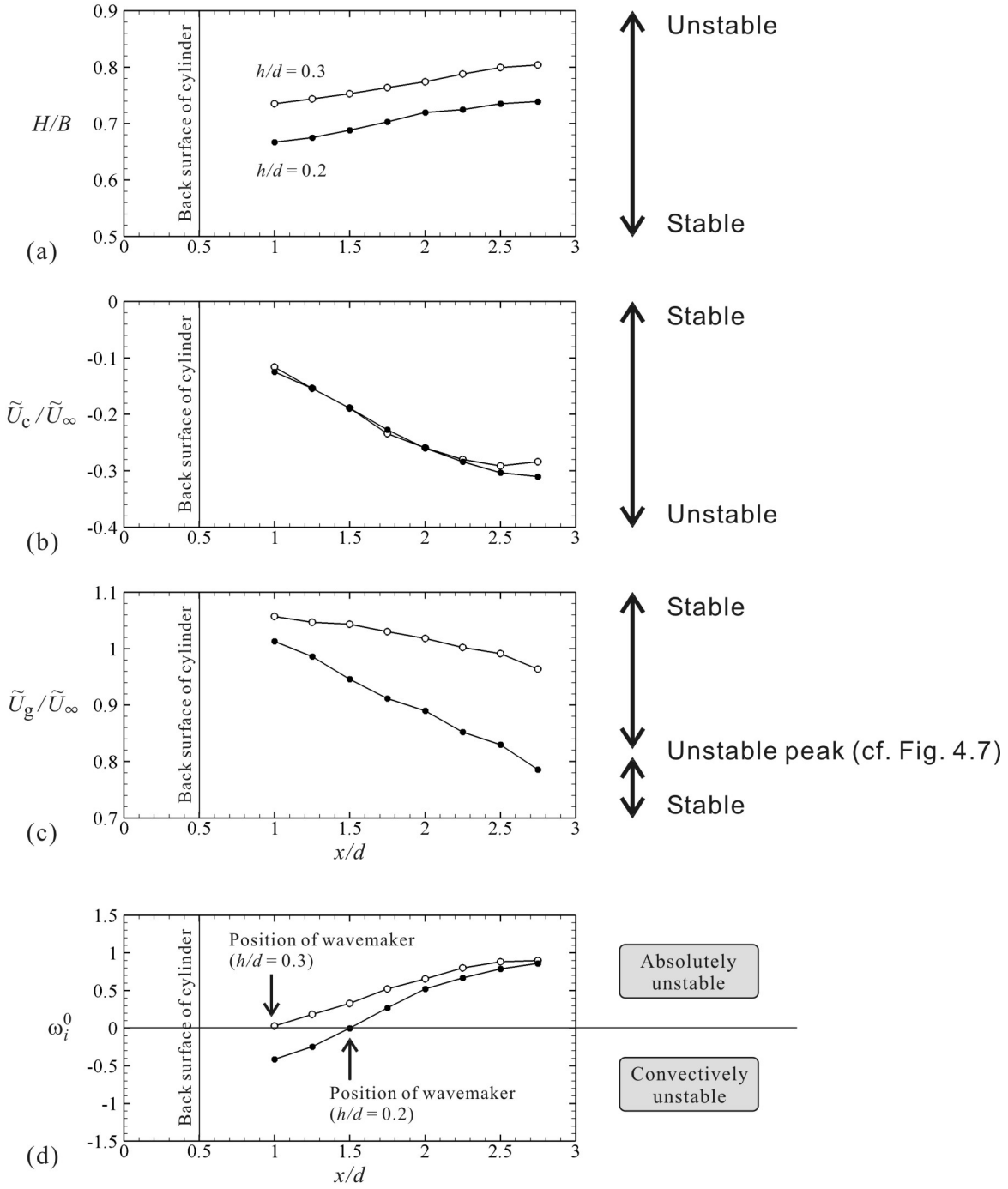

Figure 4.9: Streamwise variation of the local stability characteristics of circular cylinder wakes in ground effect: (a-c) local wake parameters extracted from the experimental data, and (d) local stability characteristics calculated based on the extracted parameters.

region corresponds to the upstream part of the large recirculation region behind the cylinder (cf. Fig. 2.15). However, the difference in the variation of $\widetilde{U}_c/\widetilde{U}_\infty$ between the two h/d cases appears to be very small. The velocity ratio $\widetilde{U}_g/\widetilde{U}_\infty$ also decreases as the wake develops downstream [Fig. 4.9(c)]. This is because, on the far-ground side of the wake the ambient fluid is entrained (i.e., momentum is supplied) as the shear layer spreads, whereas on the near-ground side of the wake no supply of the ambient fluid is available and thus the velocity overshoot diminishes faster than that on the far-ground side. This also explains the reason why $\widetilde{U}_g/\widetilde{U}_\infty$ decreases faster at $h/d = 0.2$ than at $h/d = 0.3$.

Figure 4.9(d) shows the streamwise variation of ω_i^0 calculated based on the extracted local wake parameters shown in Fig. 4.9(a-c). Note that $\omega_i^0 > 0$ physically means that the wake is locally absolutely unstable, as discussed in the previous sections. It can be seen that the state of the (very) near wake region changes from being absolutely unstable to being convectively unstable as the gap ratio h/d decreases. This local stabilisation in the (very) near wake region is mainly explained by the decrease in the relative gap distance H/B shown in Fig. 4.9(a). In the region further downstream, however, there still exists an absolutely unstable region, the front of which is located around $x/d = 1$ for $h/d = 0.3$, and at $x/d = 1.5$ for $h/d = 0.2$. This is largely due to the strong backflow in this region, as shown in Fig. 4.9(b).

According to Pier and Huerre (2001), this front should act as a wavemaker to generate nonlinear travelling waves and a self-sustained global oscillation should develop downstream of the front — this is not quantitatively consistent with the experimental observation in Chapter 2 that the von Kármán-type vortex shedding was suppressed at these gap ratios, at least in the region of $x/d \leq 2.75$. In addition, the local frequency ω_r^0 at the front of the locally absolutely unstable region was found in the stability analysis to be 2.52 [rad/s] (for $h/d = 0.3$) and 2.31 [rad/s] (for $h/d = 0.2$), which correspond to the Strouhal number (based on the cylinder diameter d rather than on the local wake width B) of 0.31 and 0.27, respectively. Although the corresponding experimental data (for a cylinder near a moving ground) were not measured in this study, Bearman and Zdravkovich (1978) have reported (for a cylinder near a fixed ground) that the frequency of the von Kármán-type vortex shedding in the near wake region was almost constant at about 0.21 for $h/d \geq 0.3$ — again some quantitative differences exist between the experiments and the stability analysis.

These quantitative differences might be explained by the fact that the experiments in Chapter 2 in this study [and also those by Bearman and Zdravkovich (1978)] were carried out in the upper-subcritical Reynolds number regime, i.e., the near wake of the cylinder was fully turbulent regardless of whether or not the von Kármán-type vortex shedding was suppressed by the ground effect. In the stability analysis, on the other hand, the flow was assumed to be quasi-laminar, i.e., the turbulence was assumed to affect the (organised) instability waves only indirectly through the mean velocity profile. This assumption, however, generally leads to only qualitatively correct results when applied to fully turbulent shear flows (Reynolds and Hussain, 1972). Another possible cause of the differences might be the simple representation of the velocity profile near the ground used in the stability analysis. It should be noted that, in the experiments in Chapter 2, even though the ground was moving at the same speed as the free stream, a very thin boundary layer still existed on the moving ground. Although the

scale of this thin boundary layer is much smaller than that of the wake, its influence on the stability characteristics of the wake is still unclear. Nevertheless, it may be concluded that the present stability analysis has qualitatively indicated some fundamental mechanisms of the cessation of the von Kármán-type vortex shedding in the near wake region of the cylinder in ground effect.

Further comments on the stability of wakes in ground effect

Some additional comments are made below on the influence of the velocity ratio $\widetilde{U}_{\rm g}/\widetilde{U}_{\infty}$ on the onset and cessation of the von Kármán-type vortex shedding in ground effect. It was shown in Section 4.4.2 that the local model wake profile becomes more absolutely unstable as the velocity on the near-ground side ($U_{\rm g}$) is slightly decreased compared with that on the far-ground side (U_{∞}) when the relative gap distance H/B is small (cf. Fig. 4.7). Here, if we (boldly) assume that the near wake profile behind a cylinder placed near a fixed ground (on which a boundary layer of a certain thickness exists) may also be approximated by the model wake profile used in this study, the trend of the influence of $U_{\rm g}/U_{\infty}$ (and thus of $\widetilde{U}_{\rm g}/\widetilde{U}_{\infty}$) qualitatively agrees with the counter-intuitive experimental observation by Lei *et al.* (1999) that the critical gap ratio for the onset/cessation of the von Kármán-type vortex shedding decreased as the boundary layer thickness on the ground increased. This might be explained from the viewpoint of the stability of the wake because the flow through the gap between the cylinder and the ground decreases (which might be considered to correspond to a slight decrease in $\widetilde{U}_{\rm g}/\widetilde{U}_{\infty}$ and to make the wake more unstable) when the boundary layer thickness increases. In other words, as the boundary layer thickness on the ground increases the so-called 'effective' gap ratio might be considered to decrease, but in a way such that $\widetilde{U}_{\rm g}/\widetilde{U}_{\infty}$ decreases [like that described in Fig. 4.9(c)] and not such that H/B decreases [like that described in Fig. 4.9(a)].

4.4.4 Re-examination of the instability of wakes in CFD

Before concluding this chapter, the discussion on the 'delayed' cessation of the von Kármán-type vortex shedding in the URANS simulations in Chapter 3 is re-examined. Specifically, the series of investigation on the stability of wakes performed above is now applied to the wake profiles predicted by the DES and 3D S-A URANS simulations.

Figures 4.10(a-c) show the streamwise variation of the wake parameters H/B, $\widetilde{U}_{\rm c}/\widetilde{U}_{\infty}$ and $\widetilde{U}_{\rm g}/\widetilde{U}_{\infty}$ extracted from the mean wake profiles predicted by the DES and 3D S-A URANS at $h/d = 0.1$ ($\mathrm{Re} = 0.4 \times 10^5$). Note that, at this smallest gap ratio, not only the DES but also the URANS captured the cessation of the vortex shedding due to the strong influence of the nearby ground (cf. Chapter 3). As briefly discussed in Chapter 3, clear differences of the mean wake profiles can be seen between the DES and URANS simulations. The URANS yielded larger H/B in the near wake region compared to the DES [Fig. 4.10(a)] basically because the URANS predicted a narrower wake compared to the DES (cf. Fig. 3.20). Also the backflow predicted in the URANS is stronger than that predicted in the DES in the (very) near wake region of $x/d \leq 1.8$ [Fig. 4.10(b)], although this trend is reversed at $x/d \geq 1.9$ as the recirculation region predicted by the URANS is shorter than that predicted by the DES

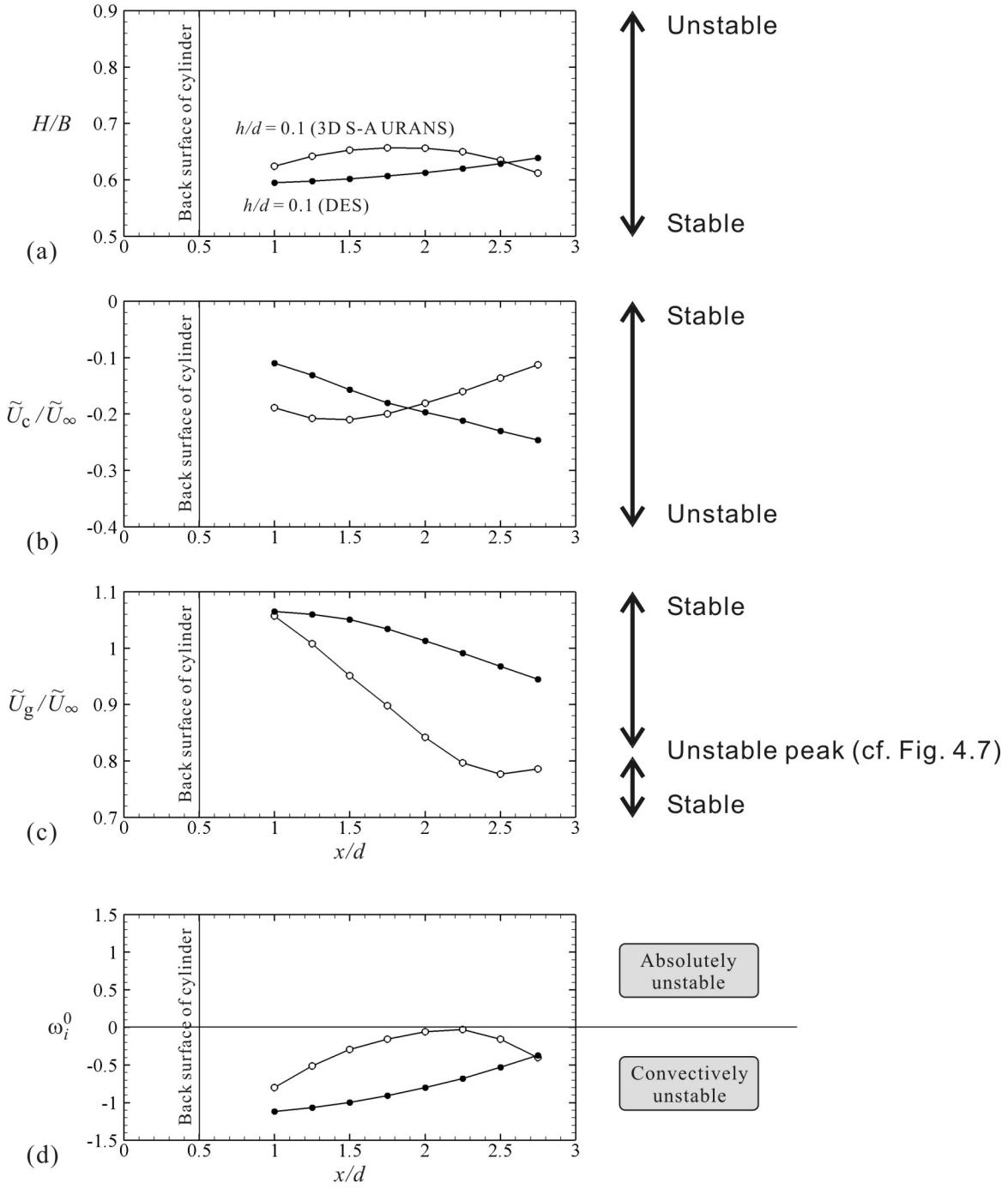

Figure 4.10: Streamwise variation of the local stability characteristics of circular cylinder wakes in the DES and 3D S-A URANS simulations: (a-c) local wake parameters extracted from the simulation data, and (d) local stability characteristics calculated based on the extracted parameters.

(cf. Fig. 3.20). Another remarkable difference can also be seen in the velocity ratio $\widetilde{U}_g/\widetilde{U}_\infty$ [Fig. 4.10(c)], which also contributes to the difference of the stability of the wakes predicted by the DES and URANS simulations.

Figure 4.10(d) shows the streamwise variation of ω_i^0 calculated based on the extracted local wake parameters shown in Figs. 4.10(a-c). The results clearly show that the near wake of the cylinder predicted by the URANS is more (inviscidly) unstable than that predicted by the DES, as was predicted from the visual comparison of the velocity profiles in Chapter 3. Also the results indicate that the wakes predicted by both DES and URANS are still convectively unstable rather than absolutely unstable in the near wake region, which qualitatively agrees with the cessation of the von Kármán-type vortex shedding predicted at this smallest gap ratio. Although the analysis using the CFD results was performed only for this gap ratio [because this is the only gap ratio at which both DES and URANS predicted the cessation of the von Kármán-type vortex shedding; note that this type of stability analysis should be applied to basis flow profiles that have *not* been altered by the instability to be investigated (Hannemann and Oertel 1989)], the results shown here qualitatively support the discussion in Chapter 3, i.e., the 'delayed' cessation of the von Kármán-type vortex shedding in the URANS simulations is due to the excessively unstable wake profiles predicted.

4.5 Conclusions

In this chapter, the local and global stability characteristics of the wakes of general two-dimensional bluff bodies placed near and parallel to a ground were investigated by using an inviscid, linear, normal-mode stability analysis.

The analysis was first applied to the four-parameter (i.e., N, U_c/U_∞, U_g/U_∞, and H/B) family of local velocity profiles, which was proposed in this study as an extended version of the two-parameter symmetric near wake model by Monkewitz and Nguyen (1987) and Monkewitz (1988), to investigate the fundamental local linear stability characteristics of the wakes in ground effect. For $H/B < 0.9$ (roughly corresponding to $h/d < 0.4$, in which range the onset/cessation of the von Kármán-type vortex shedding was found to take place for the case of a circular cylinder), the local wake profiles were found to become more unstable when the relative centreline velocity (U_c/U_∞) decreases, and also when the relative ground distance (H/B) increases. In addition, the wake was found to become more unstable when the velocity on the near-ground side (U_g) is slightly smaller than that on the far-ground side (U_∞) [cf. Fig. 4.7]. The influence of the shape factor (N) of the wake, however, was found to be very small in this H/B range.

The analysis was then compared with the experiments on a circular cylinder in ground effect in Chapter 2 to discuss the global instability of the wake in ground effect. Specifically, the analysis was applied to the model wake profiles with the parameters corresponding to H/B, U_c/U_∞, and U_g/U_∞ extracted from the experimental mean velocity data at several streamwise positions behind the cylinder. The streamwise variation of the local linear stability characteristics of the wake was then examined based on the transition scenario of 'steep global modes' by Pier and Huerre (2001). The results indicated that the very near wake of

the cylinder changes from being absolutely unstable to being convectively unstable when the cylinder comes close to the ground. This seems qualitatively consistent with the transition scenario of the global mode for general wake-type flows, i.e., the cessation of the von Kármán-type vortex shedding in the near wake region of the cylinder in ground effect may also be explained by the change of the near wake from being absolutely unstable to being convectively unstable, in analogy with the case for a cylinder equipped with a backward splitter plate. The quantitative agreement between the experiments and the stability analysis, however, was not good: the upstream edge of the absolutely unstable region was found in the stability analysis to be around $x/d = 1$ when $h/d = 0.3$ and $x/d = 1.5$ when $h/d = 0.2$, whereas in the experiments in Chapter 2 the von Kármán-type vortex shedding was found to be suppressed at least in the region of $x/d \leq 2.75$ at these gap ratios.

The analysis was also compared with the CFD results on a circular cylinder in ground effect in Chapter 3 to re-examine the discussion on the 'delayed' cessation of the von Kármán-type vortex shedding in the URANS simulations. The results indicated that the near wake profiles predicted by the URANS were more (inviscidly) unstable than those predicted by the DES, supporting the earlier discussion in Chapter 3 that the 'delayed' cessation of the vortex shedding in the URANS was due to the excessively unstable wake profiles predicted.

Finally, the following point should be mentioned once again. In the stability analysis in this study, the flow was assumed to be inviscid and quasi-laminar. This means that, when the analysis is applied to the mean velocity profiles of turbulent flows, the turbulence is assumed to affect the organised instability waves only indirectly through the mean velocity profiles. This assumption, unfortunately, resulted in the quantitative disagreement between the analysis and the experiments. Nevertheless, the qualitative agreement obtained between them suggests that, even when the flow is fully turbulent, the organized instability waves of inviscid or inflectional type indeed play key role in the onset/cessation of the von Kármán-type vortex shedding in ground effect. What should be noted here is that this interpretation is also consistent with the 'delayed' cessation of the vortex shedding in the 'overly dissipative' URANS simulations, i.e., the excessively large eddy viscosity yielded by the URANS does not necessarily promote the cessation of the vortex shedding. It may therefore be concluded that the cessation of the vortex shedding in ground effect is triggered mainly by the change in the stability characteristics of inviscid type in the near wake region rather than that of viscous type, even though the turbulence still significantly affects the inviscid stability characteristics through the mean velocity profiles of the wake.

Chapter 5

POD Analysis of the Wake of a Circular Cyinder in Ground Effect

5.1 Introduction

The proper orthogonal decomposition (POD) method has attracted the attention of many researchers during the last two decades in the context of active feedback flow control (Moin and Bewley 1994). One of the biggest challenges in the development of feedback flow control systems is to reduce the huge amount of information about the flow to be controlled, and the POD can be used for this purpose, i.e., to extract only the (energetically) dominant flow structures as spatial basis functions, or *modes*, and to build a 'low-dimensional' or 'reduced-order' model of the flow to be controlled (Holmes *et al.* 1996).

In this chapter, the POD is applied to the near-wake field data of a circular cylinder in ground effect obtained by the PIV measurements in Chapter 2 and also those obtained by the numerical simulations in Chapter 3. As mentioned in Section 1.4.7, the vortical wake of a cylinder is a typical example of unsteady flows to which the POD-based low-dimensional feedback control may be applied (Gillies 1998; Cohen *et al.* 2003; Bergmann *et al.* 2005), but the effectiveness of such low-dimensional control of the wake has been confirmed only in the laminar flow regime so far. It has been reported that the turbulent wake of a cylinder (in a free stream) may also be well-represented by a small number of POD modes (Ma *et al.* 2000; van Oudheusden *et al.* 2005), but it is still unclear whether this is still the case *when the turbulent vortex shedding is being controlled or suppressed.* Of interest here is that the wake of a cylinder in ground effect gives a good example of the turbulent vortex shedding that is being suppressed. That is to say, the POD of the cylinder wake in ground effect, especially in the intermediate gap regime where the vortex shedding becomes intermittent, might provide an illustration of the capability of the low-dimensional POD basis to capture the onset and cessation of turbulent vortex shedding. The results presented in this chapter may therefore be useful for the possible future application of the POD-based low-dimensional techniques to the control of turbulent vortex shedding, even though the development of practical control systems is outside the scope of the present study.

In the following, the details of the POD analysis are described in Section 5.2, and the

results of the analysis are presented in Section 5.3. The results are presented for four different gap ratios (h/d) of 0.6, 0.4, 0.3 and 0.2, and a single Reynolds number of 0.4×10^5. Finally, a concluding summary is given in Section 5.4.

5.2 Snapshot POD method

The proper orthogonal decomposition (POD), also known as Karhunen-Loève transform, is a procedure that decomposes multi-dimensional data into a linear combination of a finite number of orthogonal functions. In the context of fluid flow fields (and also other spatio-temporal fields), the POD is usually used to decompose the field into the so-called spatial basis functions (or POD modes) and time-dependent modal coefficients. For example, a time-dependent velocity field $\vec{u}(\vec{x},t)$ is decomposed as

$$\vec{u}(\vec{x},t) = \vec{U}(\vec{x}) + \vec{u'}(\vec{x},t) = \vec{U}(\vec{x}) + \sum_{i=1}^{M} a_i(t)\vec{\phi}_i(\vec{x}) \,, \tag{5.1}$$

where $\vec{U}(\vec{x})$ and $\vec{u'}(\vec{x},t)$ are the mean and fluctuating parts of the velocity, respectively, $a_i(t)$ are the time-dependent modal coefficients, and $\vec{\phi}_i(\vec{x})$ are the spatial basis functions. The basis functions obtained by the POD are 'optimal' (compared to other linear representations such as a Fourier series) in the sense that the averaged projection of the original field onto the basis functions is maximised. It is due to this optimality that the POD is a logical and efficient way to build a low-dimensional basis that captures the energetically dominant flow features [see e.g., Holmes *et al.* (1996) for further description].

The present study employs the *snapshot POD* method, which was proposed by Sirovich (1987) in order to reduce the huge computational costs required to calculate the basis functions $\vec{\phi}_i(\vec{x})$ and the modal coefficients $a_i(t)$ by the original (or classical) POD procedure. In the snapshot POD method the modal coefficients $a_i(t)$ are calculated, in a discrete form of a_i^k with k indicating a time instant $t = t_k$, as the elements of the eigenvectors of the following eigenvalue problem:

$$Ca_i^k = \lambda_i a_i^k \,, \tag{5.2}$$

where C is the two-time covariance matrix (of the size $N \times N$) with its elements C_{pq} computed from N sets of snapshots of the flow (i.e., instantaneous velocity field data) as

$$C_{pq} = \frac{1}{N}\int_{\Omega} \vec{u'}(\vec{x},t_p)\cdot\vec{u'}(\vec{x},t_q)\,\mathrm{d}\vec{x} \,, \tag{5.3}$$

and then $\vec{\phi}_i(\vec{x})$ can be obtained from the modal coefficients a_i^k and the instantaneous velocity field data as

$$\vec{\phi}_i(\vec{x}) = \sum_{k=1}^{N} a_i^k \vec{u'}(\vec{x},t_k) \,. \tag{5.4}$$

Note that the eigenvalues λ_i calculated from Eq. (5.2) are in proportion to the average kinetic (or fluctuating) energy of each mode; thus, sorting $\vec{\phi}_i(\vec{x})$ in order of decreasing the corresponding eigenvalues (i.e., $\lambda_i \geq \lambda_{i+1}$ for $i = 1$ to $N-1$) reveals the energetically dominant modes. The value of $\lambda_n / \sum_{i=1}^{N} \lambda_i$ then represents the proportion of the kinetic

energy contained in the n-th dominant mode relative to the total kinetic energy of the flow. Hence the original instantaneous velocity field at a certain time instant $t = t_k$ may be approximately reproduced from only the first n sets of $\vec{\phi}_i(\vec{x})$ coupled with the corresponding modal coefficients a_i^k, by using Eq. (5.1) with $M = n$, if the majority of the kinetic energy of the flow is contained in the first n modes.

5.3 Results and discussion

In this study, the snapshot POD method described above was first applied to 400 samples (i.e., $N = 400$) of the earlier PIV data in Chapter 2 for each h/d case of 0.6, 0.4, 0.3 and 0.2 (with end-plates at $y_e/d = 0$, $\mathrm{Re} = 0.4 \times 10^5$). The near-wake region in which the snapshot POD was applied to the PIV data is illustrated in Fig. 5.1 for the case of $h/d = 0.6$. As described in Chapter 2, the 400 samples were continuously recorded for each h/d case but with a much lower sampling rate of 2 Hz compared to the frequency of the large-scale vortex shedding of about 30 to 40 Hz. These samples can therefore be considered as independent instantaneous data.

Then the snapshot POD was also performed on 100 instantaneous data (i.e., $N = 100$) obtained from the DES and 2D S-A URANS simulations in Chapter 3 ($\mathrm{Re} = 0.4 \times 10^5$). For the DES, only two-dimensional velocity data at the mid-span of the computational domain were used here for the purpose of comparison with the PIV results. For both DES and URANS, however, the snapshot POD was performed on a larger area compared to that for the PIV (cf. Fig. 5.1). The 100 instantaneous data from the DES were sampled over about five vortex-shedding cycles, whereas those from the 2D S-A URANS were sampled within one vortex-shedding cycle since the shedding motion predicted by the 2D S-A URANS was fully periodic in time, as discussed in Chapter 3.

The snapshot POD procedure in this study, including the eigenvalue/eigenvector computation defined by Eq. (5.2), was performed using MATLAB (The MathWorks, Inc. 2002). All velocity data were non-dimensionalised by the free-stream velocity U_∞ before the POD procedure.

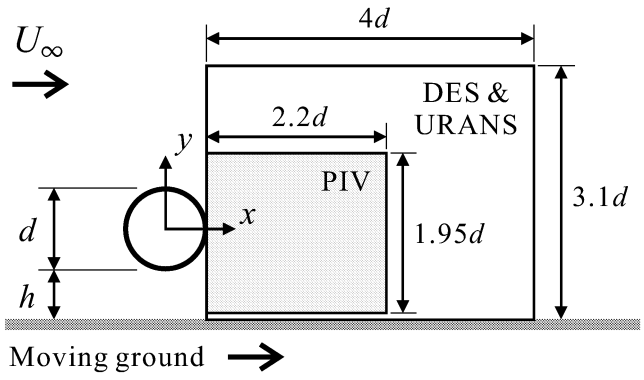

Figure 5.1: Near wake region to which the snapshot POD was applied ($h/d = 0.6$).

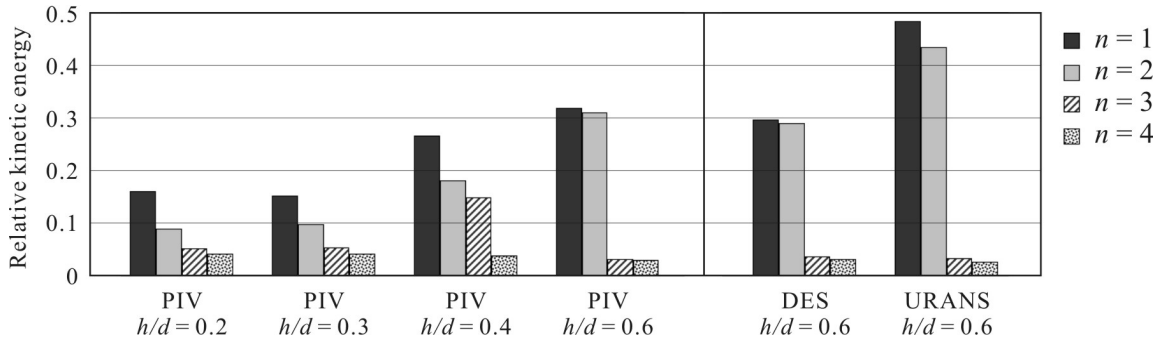

Figure 5.2: Relative kinetic energy ($\lambda_n / \sum_{i=1}^{N} \lambda_i$) for the first four POD modes.

5.3.1 Relative kinetic energy distribution

Figure 5.2 shows the relative kinetic energy values ($\lambda_n / \sum_{i=1}^{N} \lambda_i$) for the first four dominant modes calculated from the PIV results ($h/d = 0.2$ to 0.6). Those calculated from the DES and URANS results are also shown here for the purpose of comparison ($h/d = 0.6$). Note that the 400 PIV samples used here are sufficient (in the statistical sense) to obtain reliable information on at least these dominant modes; the influence of the number of PIV samples on the relative kinetic energy values for these four modes is shown in Fig. 5.3 for each gap ratio case. The convergence of the results is not perfect but reasonably acceptable. Also the cumulative kinetic energy values ($\sum_{i=1}^{n} \lambda_i / \sum_{i=1}^{N} \lambda_i$) for the first n modes are summarised in Table 5.1 for reference.

For the results from the PIV data, a clear difference of the relative kinetic energy distribution can be seen between the large-gap ($h/d = 0.6$, where the large-scale von Kármán-type vortex shedding was continuously observed behind the cylinder) and the small-gap ($h/d = 0.3$ and 0.2, where the vortex shedding was suppressed) cases. At $h/d = 0.6$, the first two modes are energetically dominant; in the time-averaged sense, more than 60% of the total kinetic energy of the wake is contained within these two modes. This tendency is similar to that for the

Table 5.1: Cumulative kinetic energy ($\sum_{i=1}^{n} \lambda_i / \sum_{i=1}^{N} \lambda_i$) for the first n modes.

	PIV $h/d = 0.2$	PIV $h/d = 0.3$	PIV $h/d = 0.4$	PIV $h/d = 0.6$	DES $h/d = 0.6$	2D S-A $h/d = 0.6$
$n = 1$	0.1599	0.1511	0.2659	0.3185	0.2961	0.4824
2	0.2486	0.2488	0.4464	0.6274	0.5855	0.9158
3	0.2993	0.3016	0.5943	0.6584	0.6217	0.9482
4	0.3397	0.3416	0.6314	0.6866	0.6516	0.9746
5	0.3768	0.3774	0.6589	0.7117	0.6781	0.9855
6	0.4090	0.4094	0.6811	0.7319	0.7029	0.9952
10	0.5020	0.5052	0.7409	0.7899	0.7695	0.9993
20	0.6312	0.6364	0.8186	0.8590	0.8599	1.0000
30	0.7034	0.7087	0.8581	0.8942	0.9068	1.0000
40	0.7543	0.7572	0.8846	0.9154	0.9374	1.0000
50	0.7919	0.7932	0.9039	0.9299	0.9582	1.0000
100	0.8924	0.8925	0.9530	0.9668	1.0000	1.0000

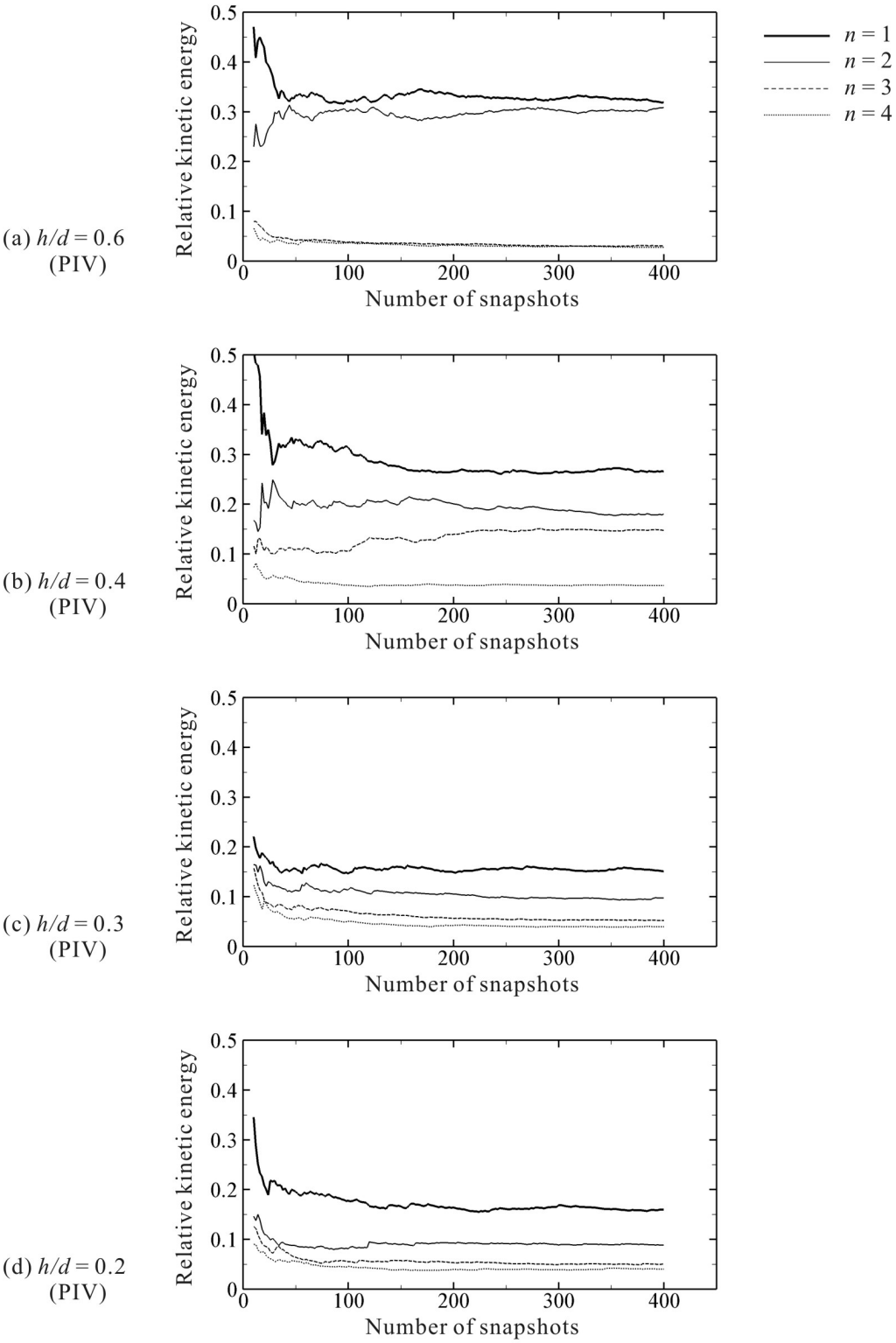

Figure 5.3: Convergence of the relative kinetic energy ($\lambda_n / \sum_{i=1}^{N} \lambda_i$) calculated from N samples of the PIV data for the first four POD modes.

turbulent wake of a circular cylinder in a free stream (Ma *et al.* 2000). At $h/d = 0.3$ and 0.2, however, only 25% of the total kinetic energy is contained within the first two modes as the dominant large-scale vortex shedding motion is suppressed in the near wake region. Of interest here is that, another type of energy distribution can be observed in the intermediate-gap case ($h/d = 0.4$, where the large-scale vortex shedding was intermittent behind the cylinder). In this case, the first three modes are energetically dominant; about 60% of the total kinetic energy is contained within these three modes.

Another interesting trend can be seen in the results obtained from the DES and URANS data at $h/d = 0.6$, where both simulations predicted the von Kármán-type vortex shedding behind the cylinder. As can be seen from Fig. 5.2 and also from Table 5.1, the energy distribution calculated from the DES results is quite similar to that from the PIV data described above — about 60% of the total kinetic energy is contained within the first two modes — despite the different number and area size of the samples analysed. Meanwhile, the energy distribution calculated from the URANS results is rather different from that from the PIV and DES results. More than 90% of the kinetic energy was found to be in the first two modes, since the URANS simulations are 'overly dissipative' and cannot capture small-scale turbulent structures, as discussed in Chapter 3. In fact, this high occupancy rate incorrectly predicted by the URANS is close to that for the laminar wake of a circular cylinder in a free stream (Deane *et al.* 1991), where more than 97% of the kinetic energy was found to be within the first two modes.

5.3.2 Spatial basis functions

In the following, the characteristics of the POD modes/coefficients calculated from the PIV results are examined in more detail. Figure 5.4 shows the contours of the streamwise velocity component of the spatial basis functions ($\phi_{x,n}$) for the first three modes for each gap ratio case. At $h/d = 0.6$, the spatial patterns for the first two modes appear similar to those for the turbulent wake of a circular cylinder in a free stream (Ma *et al.* 2003). The patterns are clear and almost symmetric, indicating that the influence of the existence of the ground is not significant and the von Kármán-type vortex shedding is still dominant at this gap ratio. As first reported by Deane *et al.* (1991) for the laminar wake of a cylinder in a free stream, the von Kármán-type, alternating vortex shedding motion can mostly be reproduced from the combination of these two dominant modes.

Such an almost symmetric pattern corresponding to the von Kármán-type vortex shedding can also be seen at $h/d = 0.4$, but only in the second mode [Fig. 5.4(b)]. The patterns for the first and third modes are also relatively clear, but are less symmetric and somewhat elongated in the streamwise direction. As will be demonstrated later, both shedding and non-shedding states intermittently observed at this intermediate gap ratio can roughly be reproduced by the combination of these three dominant modes. Meanwhile, no such dominant patterns can be seen in the first three modes at $h/d = 0.3$ and 0.2 [Figs. 5.4(c) and (d)] as the large-scale vortex shedding is suppressed at these gap ratios. It should also be noted that the spatial patterns for the first three modes are quite similar between $h/d = 0.3$ and 0.2.

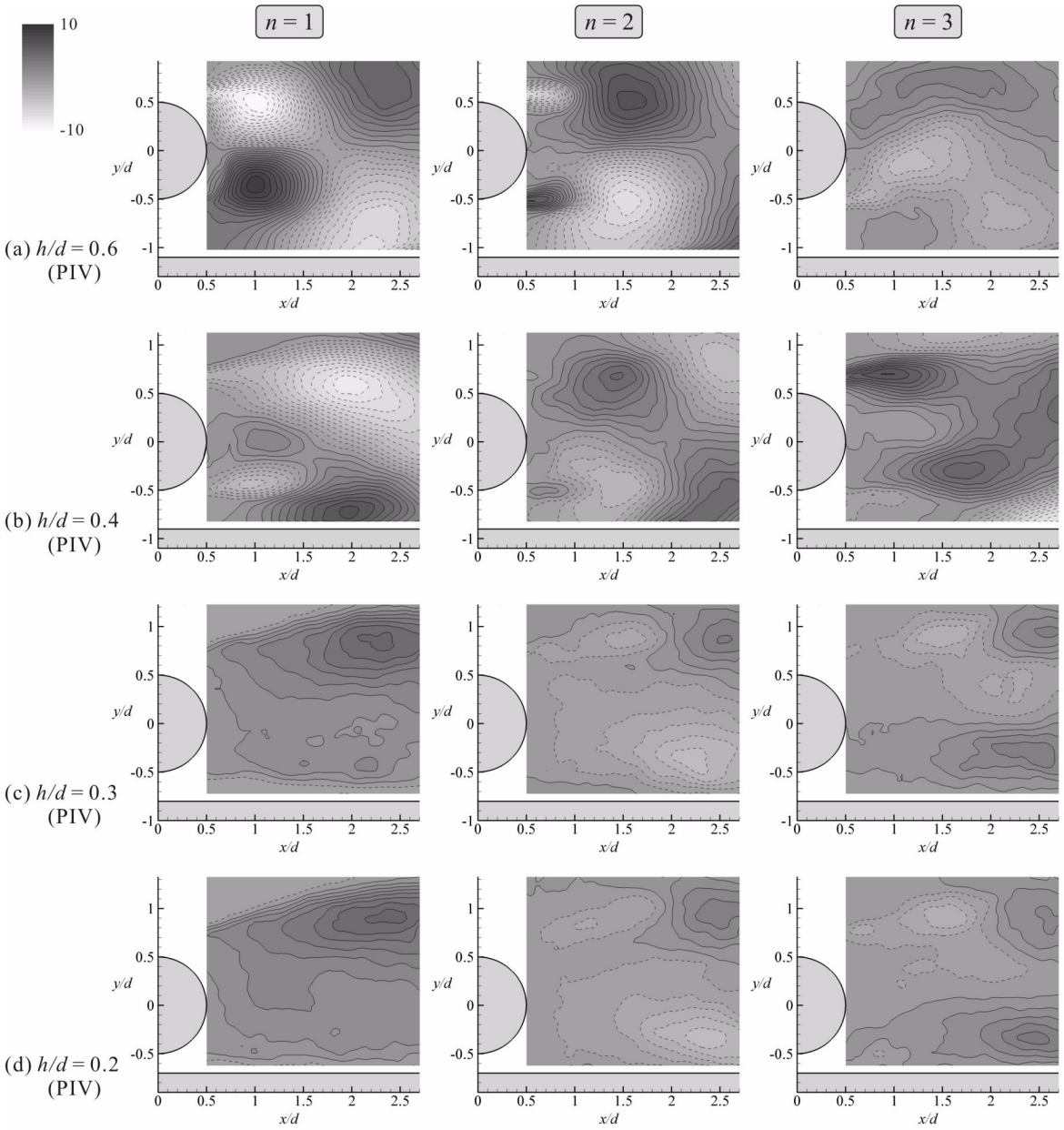

Figure 5.4: Contours of the streamwise velocity component ($\phi_{x,n}$) for the first three POD modes.

5.3.3 Time-dependent modal coefficients

Figure 5.5 shows the plots of the time-dependent modal coefficients for the first three modes for each gap ratio case. Specifically, the 400 pairs of the modal coefficients (a_i^k, a_j^k), where $k = 1$ to 400, are plotted for $(i, j) = (1, 2)$, $(1, 3)$ and $(2, 3)$ in each subfigure.

At $h/d = 0.6$, a certain relation can be seen between the first two modes, i.e., the plots roughly show a circular orbit with the centre at $(a_1, a_2) = (0, 0)$. It should be noted that, for the laminar von Kármán-type vortex shedding in a free stream, the values of $(a_1)^2 + (a_2)^2$ are constant as a_1 and a_2 fluctuate with the same amplitude, the same frequency, and a phase difference of 90 degrees (Deane *et al.* 1991). Hence the relation between the first two modes

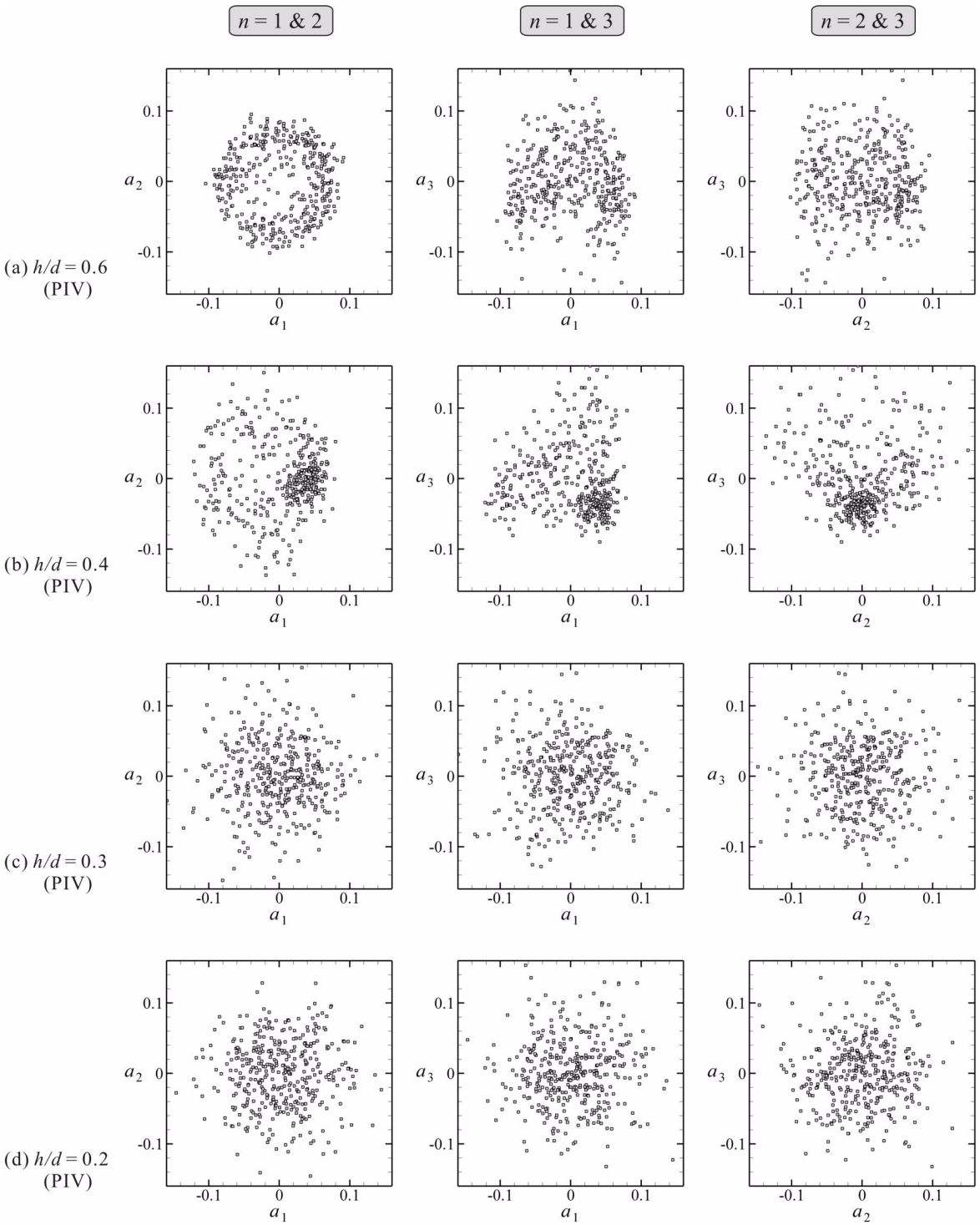

Figure 5.5: Correlation of the modal coefficients (a_n) for the first three POD modes.

observed above again shows that the turbulent vortex shedding at $h/d = 0.6$ is indeed of the von Kármán-type. The relations for $(i, j) = (1, 3)$ and $(2, 3)$, however, are not clear since the third mode is 'noisy' due to the background turbulence motions.

Of interest is that, at $h/d = 0.4$, a different type of relation can be seen between the first three modes [Fig. 5.5(b)]. It can be seen that a_1 and a_3 show a clear correlation when a_2 is close to zero, and also that the relation between a_1 and a_2 looks quite similar to that between a_3 and a_2. As will be presented in the next section, the relation between these three dominant modes is closely related to the intermittency of the large-scale vortex shedding; the shedding states can roughly be reproduced by the combination of these three modes, whereas the non-shedding states can roughly be reproduced by the combination of only the first and third modes, i.e., with $a_2 \approx 0$.

At $h/d = 0.3$ and 0.2 [Figs. 5.5(c) and (d)], no correlation can be seen between the first three modes, as the large-scale periodic vortex shedding is suppressed at these gap ratios.

5.3.4 Reproduction of instantaneous flow fields

It was shown in Section 5.3.1 that, in the time-averaged sense, about 60% of the total kinetic energy of the wake was contained only in the first two or three modes when the large-scale von Kármán-type vortices were continuously ($h/d = 0.6$) or intermittently ($h/d = 0.4$) generated behind the cylinder. The crucial question here, however, is whether these limited numbers of POD modes are indeed sufficient to describe the major dynamic features of the wake, which would be the minimum requirement for the possible future application of POD to the low-dimensional control of turbulent vortex shedding. To examine this, in the following some instantaneous flow fields behind the cylinder are reproduced from the combination of limited numbers of POD modes [using Eq. (5.1) with the calculated modal coefficients a_i^k] and then compared with the original PIV data.

Figure 5.6 shows comparisons between the original instantaneous PIV data and the corresponding instantaneous velocity data reproduced from the first three and fifty POD modes (i.e., $M = 3$ and 50) at $h/d = 0.6$. Note that Figs. 5.6(a) and (b) show an example of the comparison, and Figs. 5.6(c) and (d) show another example of the comparison. Also note that Figs. 5.6(a) and (c) compare the velocity vector plots behind the cylinder, whereas Figs. 5.6(b) and (d) compare the instantaneous streamwise velocity contours behind the cylinder. It can be seen from these figures that the first three POD modes roughly capture the main feature of the large-scale vortex shedding, although the details of the vortex structures are more precisely reproduced by increasing the number of the modes from 3 to 50. The time-dependent modal coefficients for the first three modes are $(a_1, a_2, a_3) = (0.038, 0.057, -0.064)$ at the moment of Figs. 5.6(a) and (b), and $(a_1, a_2, a_3) = (-0.069, -0.023, -0.010)$ at the moment of Figs. 5.6(c) and (d), respectively.

Of further interest are the results at $h/d = 0.4$, at which the large-scale vortex shedding becomes intermittent in the near wake region. Figure 5.7 shows the comparisons between the original PIV data and the corresponding data reproduced by the POD modes at $h/d = 0.4$. Note that Figs. 5.7(a) and (b) show an example for the (temporarily) shedding states, and Figs. 5.7(c) and (d) show another example for the (temporarily) non-shedding states. It can

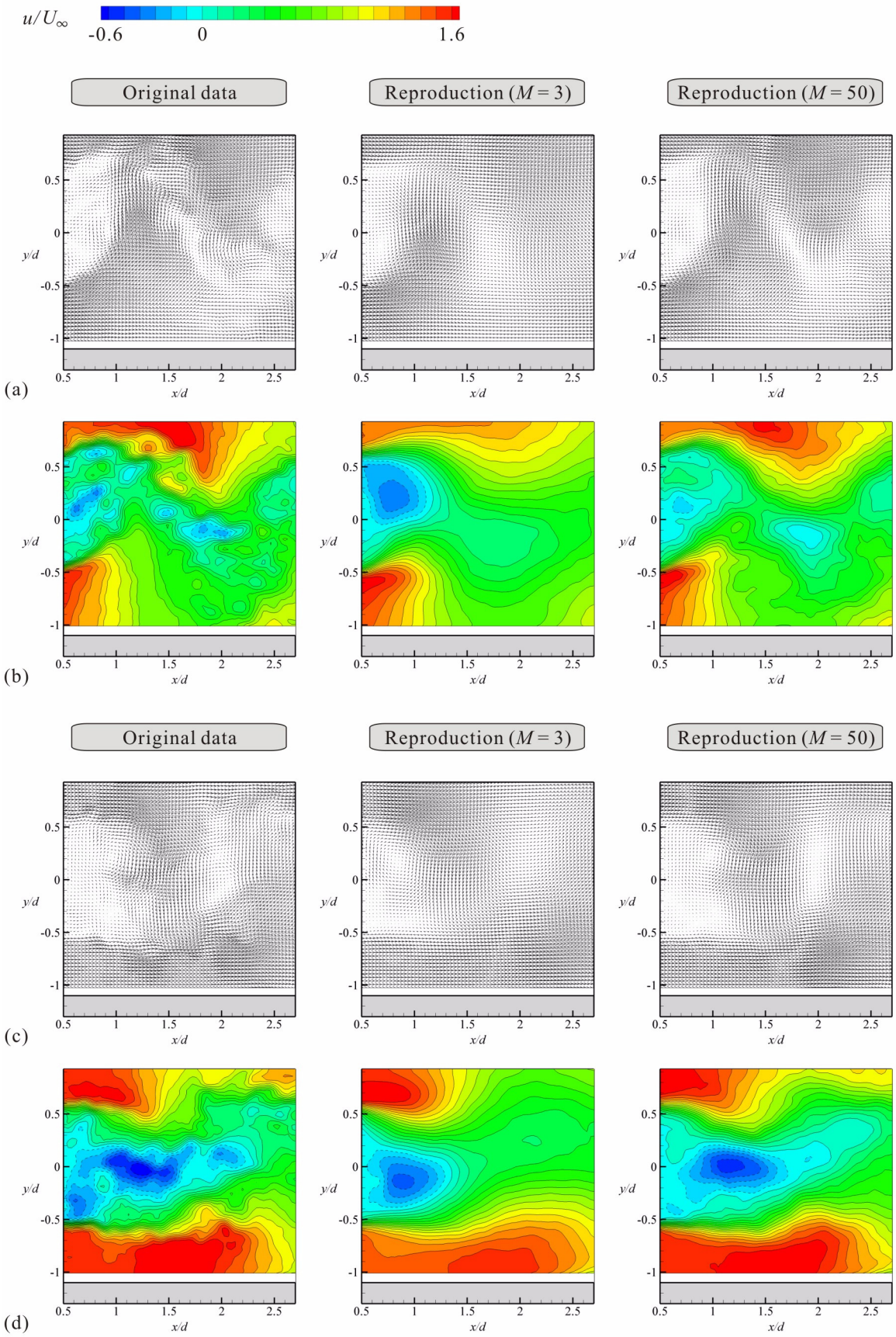

Figure 5.6: Reproduction of instantaneous flow fields based on the first three and fifty POD modes (PIV, $h/d = 0.6$); (a, b) an example at $t = t_0$, (c, d) another example at $t = t_0 + 0.5$ second.

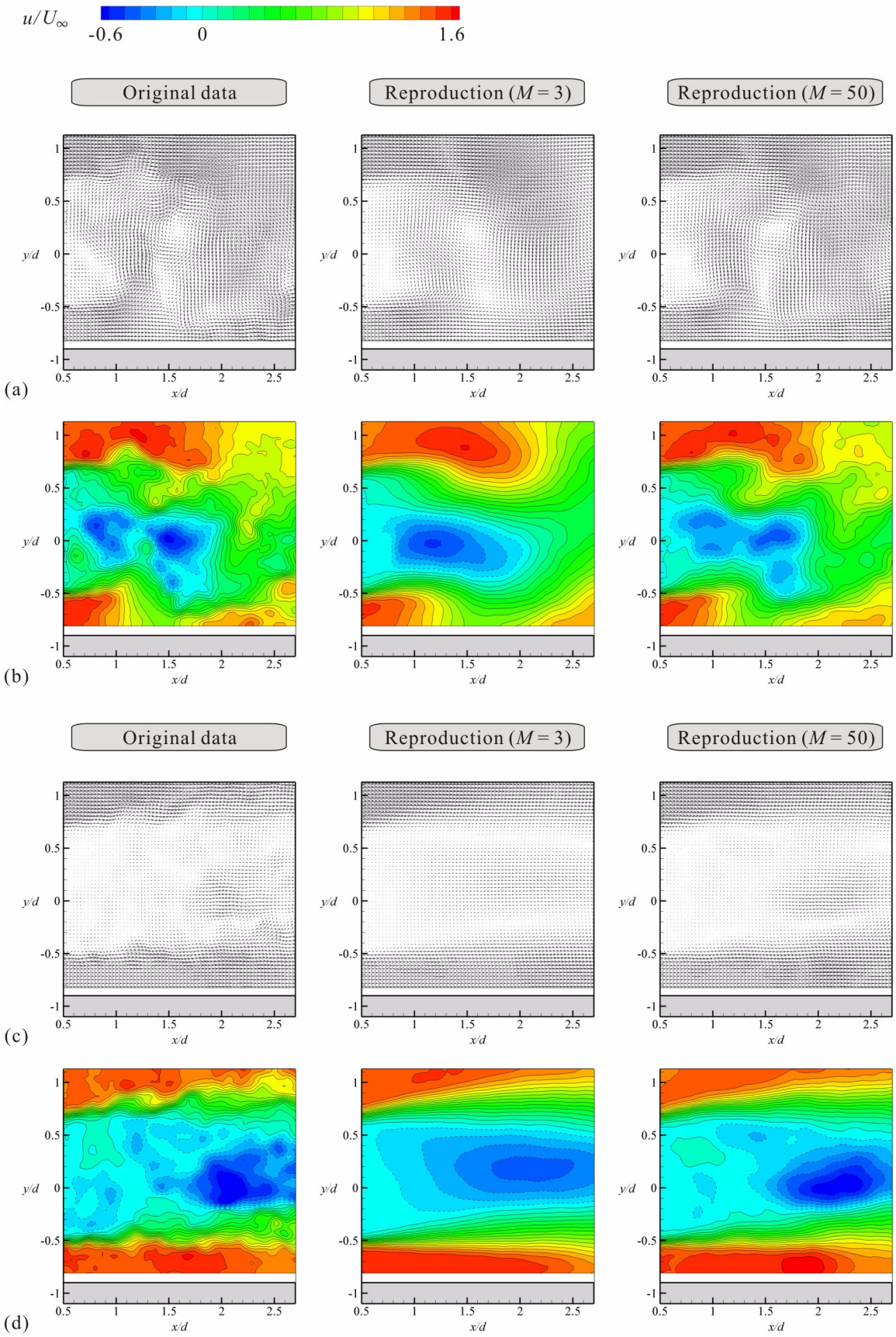

Figure 5.7: Reproduction of the intermittency of the large-scale vortex shedding based on the first three and fifty POD modes (PIV, $h/d = 0.4$); (a, b) shedding state, (c, d) non-shedding state.

be seen that the first three POD modes roughly capture the intermittency of the large-scale vortex shedding at this intermediate gap ratio. The time-dependent modal coefficients for the first three modes are $(a_1, a_2, a_3) = (-0.097, 0.072, -0.043)$ at the moment of Figs. 5.7(a) and (b), and $(a_1, a_2, a_3) = (0.039, -0.004, -0.032)$ at the moment of Figs. 5.7(c) and (d), respectively.

As concerns the non-shedding states [Figs. 5.7(c) and (d)], however, the details of the small-scale vortices due to the shear layer instability cannot be captured even by the fifty modes, since these small-scale vortices are less energetic than the large-scale vortices and are therefore captured only by the modes of much lower levels. This difficulty comes primarily from the fact that the information of two different types of flow states (i.e., shedding and non-shedding) is contained in a single set of POD modes at this intermediate gap ratio. This problem is closely related to the discussion on the robustness of the POD basis for real flow control problems (Bergmann *et al.* 2005), which is outside the scope of the present study. Nevertheless, the capability of the single set of POD modes (of only the first three levels) to capture the main features of both shedding and non-shedding states demonstrated here is promising for the possible future application of the POD-based low-dimensional techniques to the control of turbulent vortex shedding.

5.4 Conclusions

In this chapter, the snapshot POD analysis was performed on the experimental and computational data described in Chapters 2 and 3 for the turbulent near wake of the circular cylinder in ground effect. The POD eigenvalues calculated from the PIV data showed that, in the near wake region, about 60% of the total kinetic energy was contained only in the first two modes when $h/d = 0.6$, and in the first three modes even when $h/d = 0.4$ (at which the large-scale shedding was intermittent). The eigenvalues calculated from the DES data showed a good agreement with those from the PIV data, but the results from the 2D S-A URANS showed a large discrepancy from the PIV and DES results.

The spatial basis functions and time-dependent modal coefficients calculated from the PIV data were then examined in detail. In particular, an interesting correlation was found between the first three dominant modes at $h/d = 0.4$. It was also demonstrated that, at this intermediate gap ratio, the main features of both vortex shedding and non-shedding states in the near wake region could be successfully reproduced from the combination of these three POD modes. Although the details of the small-scale vortices were not clearly captured even by the first fifty POD modes, the results obtained in this study are promising for the possible future application of the POD-based low-dimensional techniques to the control of turbulent vortex shedding, for which the first requirement is to properly capture the large-scale motion rather than the small-scale motion.

For the realization of such low-dimensional flow control systems, however, there are still several issues to be resolved. One of the most significant would be the (real-time) estimation of the modal coefficients a_i for the flow field to be controlled. In this study the original flow field was 'reproduced' from the spatial basis functions $\vec{\phi}_i(\vec{x})$ and also the time-dependent

modal coefficients $a_i(t)$, both of which were obtained from the existing samples of the flow field. In the case of feedback flow control, however, the time-dependent modal coefficients need to be 'estimated' from the (rather limited) real-time data of the flow field. A possible solution to this issue is to use the linear stochastic estimation (LSE); Bonnet *et al.* (1994) reported, for an axisymmetric turbulent jet and also a two-dimensional turbulent mixing layer, that the POD modal coefficients were successfully estimated from the LSE with limited instantaneous velocity data measured on coarse hot-wire grids. More recently, Pinier *et al.* (2007) demonstrated that turbulent flow separation from the upper surface of an inclined airfoil could be effectively controlled with the POD modal coefficients estimated only from limited instantaneous pressure data on the airfoil surface by using a modified version of the LSE. Similar techniques might therefore be applicable to the control of the turbulent wake of general bluff bodies; further investigations are needed on this issue.

Chapter 6

Conclusions

In this chapter, a concluding summary of the study is presented. The achievements of the study are summarised in Section 6.1, followed by some recommendations for future research in Section 6.2. The objective of this chapter is to review the most important parts of the study in the context of past (and also possible future) studies in this research field, rather than to reiterate the whole results summarised in the concluding part of each chapter.

6.1 Summary of achievements

In this study, a combined experimental, computational and theoretical investigation was performed on flow past a circular cylinder placed near and parallel to a moving ground — one of the most fundamental flow configurations that accompany an important fluid-dynamic problem of (turbulent) vortex shedding and its suppression behind bluff bodies. The basic philosophy of the study was to obtain systematic knowledge about this fundamental but still unresolved flow system, and thus to contribute to a better understanding of the physics of general bluff body flows as well as to the development of a variety of engineering applications. To make a meaningful contribution, an extensive literature survey was conducted in advance, which was summarised as a part of the introduction of the thesis in Chapter 1.

In Chapter 2, the flow was experimentally investigated. One of the most crucial points of this experimental study was the use of the moving ground facility in the wind tunnel, which provided an ideal condition for observing the fundamental physics or essence of the ground effect, i.e., the effect of the nearby ground itself with (practically) no influence of the boundary layer on the ground. The outcome was more striking than expected; the drag coefficient of the cylinder (with end-plates) decreased as the gap ratio h/d decreased to less than 0.5 but became constant for h/d of less than 0.35, unlike the gradual drag reduction observed in the earlier experiments for a cylinder near a fixed ground (cf. Fig. 2.6). The subsequent PIV measurements showed that the critical drag reduction of the cylinder was directly related to the cessation of von Kármán-type vortex shedding in the near wake region. Also revealed by the PIV measurements was that the von Kármán-type vortex shedding could indeed be suppressed even when the ground was moving and hence the flow through the gap between the cylinder and the ground was *not* blocked at all. This clearly demonstrated that the direct interference between the cylinder and the boundary layer on the ground, which was observed

by many researchers in the earlier studies using a fixed ground, was not the only reason for the cessation of von Kármán-type vortex shedding in ground effect — this finding triggered the further discussion based on the linear stability analysis in Chapter 4.

In Chapter 3, the flow was numerically investigated using LES, DES, and URANS simulations. The main objective of the numerical study in this chapter, however, was to critically examine whether these state-of-the-art numerical simulations can indeed be used to predict this type of bluff body flow, rather than to study the physics of the flow simulated. One of the important conclusions was that a good/reasonable level of grid-convergence was achieved in the URANS/DES, the computational costs of which were acceptable, whereas no satisfactory grid-convergence was achieved in the LES performed on the same set of grids. Further investigation showed that the DES correctly predicted the cessation of the von Kármán-type vortex shedding (and the attendant drag reduction of the cylinder) in ground effect, suggesting the promise of DES for this type of bluff body flow. Meanwhile, the URANS showed some discrepancies with the experiments and the DES, but in such a way that the cessation of the vortex shedding was *delayed* (i.e., the vortices incorrectly *survived* until the cylinder came much closer to the ground), contrary to the general view in today's CFD that vortices should tend to be suppressed when the predicted flow is overly dissipative. The comparison between the DES and URANS results clearly demonstrated that the accuracy of prediction of the onset/cessation of large-scale vortex shedding cannot be simply or directly linked with differences in the global level of eddy viscosity predicted, and this finding also triggered the discussion based on the linear stability analysis in Chapter 4.

In Chapter 4, the mechanisms of the cessation of the von Kármán-type vortex shedding in ground effect were further investigated by using a linear, normal-mode stability analysis. The flow investigated in this chapter, however, was slightly different from that studied in the previous two chapters in the sense that it was assumed to be inviscid and quasi-laminar. Also, in contrast to the previous two chapters, this chapter focused on the wake of not only a circular cylinder but general two-dimensional bluff bodies in ground effect. The analysis was first applied to an analytical, four-parameter family of local velocity profiles, which was proposed in this study as an extended version of the two-parameter symmetric wake model by Monkewitz and Nguyen (1987). The results revealed the influence of the parameters of the local wake profiles on their absolute versus convective instability characteristics, which provided new fundamental knowledge, or a basis, for the study of two-dimensional wakes in ground effect. The local linear analysis was then compared with the experiments and numerical simulations in the previous two chapters, in line with the transition scenario of 'steep nonlinear global modes' by Pier and Huerre (2001). Although the quantitative agreement was not obtained due to the several assumptions applied in the analysis, the comparison indicated that the cessation of the von Kármán-type vortex shedding in ground effect may also be largely explained by the change of inviscid instability characteristics of the near wake from being absolutely unstable to being convectively unstable. This also explained the possible reason for the delayed cessation of the vortex shedding in the URANS solutions in Chapter 3, i.e., the wakes predicted by the URANS were more (inviscidly) unstable than those predicted by the DES.

In Chapter 5, the near wake structure of the cylinder in ground effect was further investigated by applying the snapshot POD method to the PIV data in Chapter 2 (and also to the CFD data in Chapter 3 for comparison). The purpose of this additional investigation, however, was not just to analyse the near wake structure in more detail but also to demonstrate the capability of the low-dimensional POD basis to capture the onset/cessation of the turbulent vortex shedding in ground effect. At $h/d = 0.6$, about 60 % of the total kinetic energy in the near wake region (in the time-averaged sense) was found to be contained only in the first two POD modes. The spatial functions for these two POD modes were similar to those for the wake of a cylinder in a free stream, indicating that the influence of the ground was not significant and the von Kármán-type vortex shedding was still energetically dominant at this gap ratio. Of particular interest were the results at $h/d = 0.4$, at which the von Kármán-type vortex shedding was found to become intermittent in the experiments. Even at this gap ratio, about 60 % of the total kinetic energy was contained only in the first three POD modes, although the spatial functions were rather different from those at $h/d = 0.6$. Further investigation showed that both shedding and non-shedding states at $h/d = 0.4$ could be roughly reproduced from the combination of the first three POD modes — promising for the possible future application of the POD-based low-dimensional techniques to the control of turbulent vortex shedding.

6.2 Recommendations for future research

Although many useful results were obtained in the present study, there are still a number of important issues to be investigated in this research field. Some recommendations for possible future research are described below.

As concerns the experimental study, further insight into the physics of two-dimensional wakes in ground effect might be obtained by testing a circular cylinder in different Reynolds number regimes, or a cylinder with different cross-sectional shapes. Of particular interest would be a circular cylinder in the postcritical regime, which is hard to be naturally obtained in laboratory experiments due to the high Reynolds number required but can be artificially created using a tripping wire or a roughened surface (cf. Section 1.4.2). Buresti and Lanciotti (1979) have reported that, for a circular cylinder with a fixed ground, the critical gap ratio was slightly decreased (i.e., the cessation of the vortex shedding was *delayed*) when the flow was changed from subcritical to postcritical. If this is found to be the case also for a circular cylinder with a moving ground, the importance of the relative ground distance H/B on the cessation of the von Kármán-type vortex shedding discussed in Chapter 4 would be further supported (note that the wake width B in the postcritical regime is narrower than that in the subcritical regime).

As for the numerical study, it would be interesting to apply some other recent turbulence models/techniques, such as the scale-adaptive simulation (SAS) model (Menter *et al.* 2003), to the present flow problem. As discussed in Chapter 3, a reasonable level of grid-convergence was achieved in the DES in this study, but a more grid-independent method would certainly be desirable. The SAS model resolves the problem of explicit grid-dependency in the original

DES and has already shown good results for a circular cylinder in a free stream (Menter *et al.* 2003); hence the SAS of the flow past a circular cylinder in ground effect would provide a further illustration of the usefulness of this type of turbulence model.

Although turbulent wakes are of more importance (than laminar wakes) in many engineering applications and were therefore focused on in the experimental and computational studies, this resulted in some difficulties in the comparison of the results between the experiments/simulations and the stability analysis. The agreement between them was found to be only qualitative presumably because the stability analysis was based on the quasi-laminar assumption. Hence a possible future direction here would be to take into account the direct influence of turbulence on the motion of organised instability waves in the stability analysis. The governing equation of such organised instability waves in turbulent flows (so-called turbulent Orr-Sommerfeld equation) has been derived by Reynolds and Hussain (1972) using the triple decomposition of time-dependent variables, similar to that used for the URANS formulation in Section 3.2. This equation, however, contains unknown terms representing 'wave-induced' Reynolds stress, the modelling of which is not straightforward. Therefore, from the viewpoint of the comparison between the experiments/simulations and the stability analysis, it might be sensible to perform similar experiments/simulations but in the laminar regime and to compare them with the current stability analysis, even though laminar wakes are of less importance in many engineering applications.

It would also be possible and desirable to perform further study in relation to the POD analysis in Chapter 5. One of the main goals here is to use the POD-based low-dimensional techniques for the control of turbulent vortex shedding, and the next step towards this goal would be the development of a practical sensor-controller-actuator system. As mentioned in the concluding part of Chapter 5, the key to the POD-based low-dimensional control is the real-time estimation of the POD modal coefficients, and this needs to be performed using only the flow data that are measurable in real time, probably on a wall surface. Pinier *et al.* (2007) recently reported that turbulent flow separation from the upper surface of an inclined airfoil could be effectively controlled with a limited number of sensors measuring pressure on the airfoil surface, from which the POD modal coefficients were estimated in the controller, and with *synthetic jet* (or zero-net-mass-flux jet) actuators placed upstream of the pressure sensors. Similar techniques might therefore be applicable to the control of turbulent vortex shedding from general bluff bodies, which would bring great benefit to various engineering applications in the future.

Bibliography

[1] Achenbach, E. (1968). Distribution of local pressure and skin friction around a circular cylinder in cross-flow up to Re $= 5 \times 10^6$. *Journal of Fluid Mechanics* **34**, 625-639.

[2] Achenbach, E. (1971). Influence of surface roughness on the cross-flow around a circular cylinder. *Journal of Fluid Mechanics* **46**, 321-335.

[3] Adrian, J., Christensen, K.T., and Liu, Z.-C. (2000). Analysis and interpretation of instantaneous turbulent velocity fields. *Experiments in Fluids* **29**, 275-290.

[4] Alam, M. and Sandham, N.D. (2000). Direct numerical simulation of 'short' laminar separation bubbles with turbulent reattachment. *Journal of Fluid Mechanics* **410**, 1-28.

[5] Angrilli, F., Bergamaschi, S., and Cossalter, V. (1982). Investigation of wall induced modifications to vortex shedding from a circular cylinder. *Transactions of the ASME: Journal of Fluids Engineering* **104**, 518-522.

[6] Baker, C.J. (1979). The laminar horseshoe vortex. *Journal of Fluid Mechanics* **95**, 347-367.

[7] Baker, C.J. (1980). The turbulent horseshoe vortex. *Journal of Wind Engineering and Industrial Aerodynamics* **6**, 9-23.

[8] Bearman, P.W. (1965). Investigation of the flow behind a two-dimensional model with a blunt trailing edge and fitted with splitter plates. *Journal of Fluid Mechanics* **21**, 241-255.

[9] Bearman, P.W. (1968). Some effects of turbulence on the flow around bluff bodies. In: *Proceedings of the Symposium on Wind Effects on Buildings and Structures*, National Physical Laboratory, The Royal Aeronautical Society, NPL Aero Report 1264.

[10] Bearman, P.W. (1969). On the vortex shedding from a circular cylinder in the critical Reynolds number regime. *Journal of Fluid Mechanics* **37**, 577-585.

[11] Bearman, P.W. (1980). Review − Bluff body flows applicable to vehicle aerodynamics. *Transactions of the ASME: Journal of Fluids Engineering* **102**, 265-274.

[12] Bearman, P.W. and Morel, T. (1983). Effect of free stream turbulence on the flow around bluff bodies. *Progress in Aerospace Sciences* **20**, 97-123.

[13] Bearman, P.W. and Trueman, D.M. (1972). An investigation of the flow around rectangular cylinders. *Aeronautical Quarterly* **23**, 229-237.

[14] Bearman, P.W. and Zdravkovich, M.M. (1978). Flow around a circular cylinder near a plane boundary. *Journal of Fluid Mechanics* **89**, 33-47.

[15] Bergmann, M., Cordier, L., and Brancher, J.-P. (2005). Optimal rotary control of the cylinder wake using proper orthogonal decomposition reduced-order model. *Physics of Fluids* **17**, 097101.

[16] Berkooz, G., Holmes, P., and Lumley, J.L. (1993). The proper orthogonal decomposition in the analysis of turbulent flows. *Annual Review of Fluid Mechanics* **25**, 539-575.

[17] Bers, A. (1983). Space-time evolution of plasma instabilities — absolute and convective. In: *Handbook of plasma physics*, edited by M.N. Rosenbluth and R.Z. Sagdeev, North-Holland, Amsterdam, pp. 451-517.

[18] Betchov, R. and Criminale, W.O. (1966). Spatial instability of the inviscid jet and wake. *Physics of Fluids* **9**, 359-362.

[19] Bloor, M.S. (1964). The transition to turbulence in the wake of a circular cylinder. *Journal of Fluid Mechanics* **19**, 290-304.

[20] Bonnet, J.P., Cole, D.R., Delville, J., Glauser, M.N., and Ukeiley, L.S. (1994). Stochastic estimation and proper orthogonal decomposition: Complementary techniques for identifying structure. *Experiments in Fluids* **17**, 307-314.

[21] Bosch, G., Kappler, M., and Rodi, W. (1996). Experiments on the flow past a square cylinder placed near a wall. *Experimental Thermal and Fluid Science* **13**, 292-305.

[22] Bosch, G. and Rodi, W. (1996). Simulation of vortex shedding past a square cylinder near a wall. *International Journal of Heat and Fluid Flow* **17**, 267-275.

[23] Braza, M., Perrin, R., and Hoarau, Y. (2006). Turbulence properties in the cylinder wake at high Reynolds numbers. *Journal of Fluids and Structures* **22**, 757-771.

[24] Breuer, M. (1998). Numerical and modeling influences on large eddy simulations for the flow past a circular cylinder. *International Journal of Heat and Fluid Flow* **19**, 512-521.

[25] Breuer, M. (2000). A challenging test case for large eddy simulation: High Reynolds number circular cylinder flow. *International Journal of Heat and Fluid Flow* **21**, 648-654.

[26] Briggs, R. (1964). *Electron-Stream Interaction with Plasmas*, M.I.T.Press, MA, USA.

[27] Buresti, G. (1981). The effect of surface roughness on the flow regime around circular cylinders. *Journal of Wind Engineering and Industrial Aerodynamics* **8**, 115-122.

[28] Buresti, G. and Lanciotti, A. (1979). Vortex shedding from smooth and roughened cylinders in cross-flow near a plane surface. *Aeronautical Quarterly* **30**, 305-321.

[29] Buresti, G. and Lanciotti, A. (1992). Mean and fluctuating forces on a circular cylinder in cross-flow near a plane surface. *Journal of Wind Engineering and Industrial Aerodynamics* **41**, 639-650.

[30] Burgin, K., Adey, P.C., and Beatham, J.P. (1986). Wind tunnel tests on road vehicle models using a moving belt simulation of ground effect. *Journal of Wind Engineering and Industrial Aerodynamics* **22**, 227-236.

[31] Cantwell, B. and Coles, D. (1983). An experimental study of entrainment and transport in the turbulent near wake of a circular cylinder. *Journal of Fluid Mechanics* **136**, 321-374.

[32] Castro, I.P. (2005). The stability of laminar symmetric separated wakes. *Journal of Fluid Mechanics* **532**, 389-411.

[33] Catalano, P., Wang, M., Iaccarino, G., and Moin, P. (2003). Numerical simulation of the flow around a circular cylinder at high Reynolds numbers. *International Journal of Heat and Fluid Flow* **24**, 463-469.

[34] Celik, I. and Shaffer, F.D. (1995). Long time-averaged solutions of turbulent flow past a circular cylinder. *Journal of Wind Engineering and Industrial Aerodynamics* **56**, 185-212.

[35] Chen, D. and Jirka, G.H. (1997). Absolute and convective instabilities of plane turbulent wakes in a shallow water layer. *Journal of Fluid Mechanics* **338**, 157-172.

[36] Chyu, C. and Rockwell, D. (1996). Evolution of patterns of streamwise vorticity in the turbulent near wake of a circular cylinder. *Journal of Fluid Mechanics* **320**, 117-137.

[37] Cohen, K., Siegel, S., McLaughlin, T., and Gillies, E. (2003). Feedback control of a cylinder wake low-dimensional model. *AIAA Journal* **41**, 1389-1391.

[38] Criminale, W.O., Jackson, T.L., and Joslin, R.D. (2003). *Theory and Computation of Hydrodynamic Stability.* Cambridge University Press, Cambridge, UK.

[39] Deane, A.E., Kevrekidis, I.G., Karniadakis, G.E., and Orszag, S.A. (1991). Low-dimensional models for complex geometry flows: Application to grooved channels and circular cylinders. *Physics of Fluids A* **3**, 2337-2354.

[40] Djeridi, H., Braza, M., Perrin, R., Harran, G., Cid, E., and Cazin, S. (2003). Near-wake turbulence properties around a circular cylinder at high Reynolds number. *Flow, Turbulence and Combustion* **71**, 19-34.

[41] Drazin, P.G. and Reid, W.H. (1981). *Hydrodynamic Stability.* Cambridge University Press, Cambridge, UK.

[42] Durao, D.F.G., Gouveia, P.S.T., and Pereira, J.C.F. (1991). Velocity characteristics of the flow around a square cross section cylinder placed near a channel wall. *Experiments in Fluids* **11**, 341-350.

[43] Durbin, P.A. (1995). Separated flow computations with the k-ϵ-v^2 model. *AIAA Journal* **33**, 659-664.

[44] Dwyer, H. and McCroskey, W.J. (1973). Oscillating flow over a cylinder at large Reynolds number. *Journal of Fluid Mechanics* **61**, 753-767.

[45] Everitt, K.W. (1982). A normal flat plate close to a large plane surface. *Aeronautical Quarterly* **33**, 90-104.

[46] Ferziger, J.H. (1996). Large eddy simulation. In: *Simulation and Modeling of Turbulent Flows*, edited by T. Gatski, M.Y. Hussaini, and J.L. Lumley, Oxford University Press, Oxford, UK, Chapter III.

[47] Ferziger, J.H. and Peric, M. (2002). *Computational Methods for Fluid Dynamics: 3rd Edition.* Springer Verlag, Berlin, Chapter 9.

[48] Fluent Inc. (2005). *Fluent 6.2 User's Guide.* Fluent Inc., Lebanon, NH, USA.

[49] Fox, T.A., Apelt, C.J., and West, G.S. (1993). The aerodynamic disturbance caused by the free-ends of a circular cylinder immersed in a uniform flow. *Journal of Wind Engineering and Industrial Aerodynamics* **49**, 389-400.

[50] Franke, R. and Rodi, W. (1991). Calculation of vortex shedding past a square cylinder with various turbulence models. In: *Proceedings of the 8th Symposium on Turbulent Shear Flows*, 9-11 September, Munich, Germany, pp. 20-1-1-20-1-6.

[51] Galletti, B., Bruneau, C.H., Zannetti, L., and Iollo, A. (2004). Low-order modelling of laminar flow regimes past a confined square cylinder. *Journal of Fluid Mechanics* **503**, 161-170.

[52] Germano, M., Piomelli, U., Moin, P., and Cabot, W.H. (1991). A dynamic subgrid-scale eddy viscosity model. *Physics of Fluids A* **3**, 1760-1765.

[53] Gerrard, J.H. (1965). A disturbance sensitive Reynolds number range of the flow past a circular cylinder. *Journal of Fluid Mechanics* **22**, 187-196.

[54] Gillies, E.A. (1998). Low-dimensional control of the circular cylinder wake. *Journal of Fluid Mechanics* **371**, 157-178.

[55] Goldstein, S. (1965). *Modern Developments in Fluid Dynamics.* Dover Publications Inc., New York.

[56] Grass, A.J., Raven, P.W.J., Stuart, R.J., and Bray, J.A. (1984). Influence of boundary layer velocity gradients and bed proximity on vortex shedding from free spanning pipelines. *Transactions of the ASME: Journal of Energy Resources Technology* **106**, 70-78.

[57] Griffin, O.M. and Votaw, C.W. (1972). The vortex street in the wake of a vibrating cylinder. *Journal of Fluid Mechanics* **55**, 31-48.

[58] Guven, O., Farell, C., and Patel, V.C. (1980). Surface roughness effects on the mean flow past circular cylinders. *Journal of Fluid Mechanics* **98**, 673-701.

[59] Hammond, D.A. and Redekopp, L.G. (1997). Global dynamics of symmetric and asymmetric wakes. *Journal of Fluid Mechanics* **331**, 231-260.

[60] Hammond, D.A. and Redekopp, L.G. (1998). Local and global instability properties of separation bubbles. *European Journal of Mechanics B/Fluids* **17**, 145-164.

[61] Hannemann, K. and Oertel, H. (1989). Numerical simulation of the absolutely and convectively unstable wake. *Journal of Fluid Mechanics* **199**, 55-88.

[62] Hiwada, M., Mabuchi, I., Kumada, M., and Iwakoshi, H. (1986). Effect of the turbulent boundary layer thickness on the flow characteristics around a circular cylinder near a plane surface. *Transactions of the Japan Society of Mechanical Engineers B* **52**, 2566-2574 [in Japanese].

[63] Holloway, D.S., Walters, D.K., and Leylek, J.H. (2004). Prediction of unsteady, separated boundary layer over a blunt body for laminar, turbulent, and transitional flow. *International Journal for Numerical Methods in Fluids* **45**, 1291-1315.

[64] Holmes, P., Lumley, J.L., and Berkooz, G. (1996). *Turbulence, Coherent Structures, Dynamical Systems and Symmetry.* Cambridge University Press, Cambridge, UK.

[65] Huerre, P. (2000). Open shear flow instabilities. In: *Perspectives in Fluid Dynamics: A Collective Introduction to Current Research*, edited by G.K. Batchelor, H.K. Moffat, and M.G. Worster, Cambridge University Press, Cambridge, UK, pp. 159-229.

[66] Huerre, P. and Monkewitz, P.A. (1990). Local and global instabilities in spatially developing flows. *Annual Review of Fluid Mechanics* **22**, 473-537.

[67] Humphreys, J.S. (1960). On a circular cylinder in a steady wind at transition Reynolds numbers. *Journal of Fluid Mechanics* **9**, 603-612.

[68] Hussain, A.K.M.F. and Reynolds, W.C. (1970). The mechanics of an organized wave in turbulent shear flow. *Journal of Fluid Mechanics* **41**, 241-258.

[69] Iaccarino, G., Ooi, A., Durbin, P.A., and Behnia, M. (2003). Reynolds averaged simulation of unsteady separated flow. *International Journal of Heat and Fluid Flow* **24**, 147-156.

[70] Jensen, K.D. (2004). Flow measurements. *Journal of the Brazilian Society of Mechanical Sciences and Engineering* **26**, 400-419.

[71] Kamemoto, K., Oda, Y., and Aizawa, M. (1984). Characteristics of the flow around a bluff body near a plane surface. *Bulletin of the Japan Society of Mechanical Engineers* **27**, 1637-1643.

[72] Kato, M. and Launder, B.E. (1993). The modeling of turbulent flow around stationary and vibrating square cylinders. In: *Proceedings of the 9th Symposium on Turbulent Shear Flows*, 16-18 August, Kyoto, Japan, pp. 10-4-1-10-4-6.

[73] Koch, W. (1985). Local instability characteristics and frequency determination of self-excited wake flows. *Journal of Sound and Vibration* **99**, 53-83.

[74] Kourta, A., Boisson, H.C., Chassaing, P., and Ha Minh, H. (1987). Nonlinear interaction and the transition to turbulence in the wake of a circular cylinder. *Journal of Fluid Mechanics* **181**, 141-161.

[75] Kumarasamy, S. and Barlow, J.B. (1995), Interference of plane wall on periodic shedding behind a half cylinder. In: *Proceedings of the 26th AIAA Fluid Dynamics Conference*, 19-22 June, San Diego, CA, AIAA Paper 95-2285.

[76] Langtry, R.B., Menter, F.R., Likki, S.R., Suzen, Y.B., and Huang, P.G. (2004). A correlation-based transition model using local variables, Part II - Test cases and industrial applications. In: *Proceedings of the ASME Turbo Expo 2004*, 14-17 June, Vienna, Austria, Vol. 4, pp. 69-79.

[77] Launder, B.E., Reece, G.J., and Rodi, W. (1975). Progress in the development of a reynolds-stress turbulence closure. *Journal of Fluid Mechanics* **68**, 537-566.

[78] Launder, B.E. and Sharma, B.I. (1974). Application of the energy-dissipation model of turbulence to the calculation of flow near a spinning disc. *Letters in Heat and Mass Transfer* **1**, 131-137.

[79] Launder, B.E. and Spalding, D.B. (1974). Numerical computation of turbulent flows. *Computer Methods in Applied Mechanics and Engineering* **3**, 269-289.

[80] Lee, B.E. (1975). The effect of turbulence on the surface pressure field of a square prism. *Journal of Fluid Mechanics* **69**, 263-282.

[81] Leonard, A. (1974). Energy cascade in large-eddy simulations of turbulent fluid flows. *Advances in geophysics* **18-A**, 237-248.

[82] Lei, C., Cheng, L., and Kavanagh, K. (1999). Re-examination of the effect of a plane boundary on force and vortex shedding of a circular cylinder. *Journal of Wind Engineering and Industrial Aerodynamics* **80**, 263-286.

[83] Lilly, D.K. (1992). Proposed modification of the Germano subgrid-scale closure method. *Physics of Fluids A* **4**, 633-635.

[84] Lin, C., Lin, W-J., and Lin, S-S. (2005). Flow characteristics around a circular cylinder near a plane boundary. In: *Proceedings of the Sixteenth International Symposium on Transport Phenomena (ISTP-16)*, Prague, Czech Republic (CD-ROM).

[85] Lumley, J.L. (1967). The structure of inhomogeneous turbulence. In: *Atmospheric turbulence and radio wave propagation*, edited by A.M. Yaglom and V.L. Tatarski, Nauka, Moscow, pp. 166-178.

[86] Ma, X., Karamanos, G.-S., and Karniadakis, G.E. (2000). Dynamics and low-dimensionality of a turbulent near wake. *Journal of Fluid Mechanics* **410**, 29-65.

[87] Ma, X., Karniadakis, G.E., Park. H., and Gharib, M. (2003). DPIV-driven flow simulation: a new computational paradigm. *Proceedings of the Royal Society A* **459**, 547-565.

[88] Martinuzzi, R.J., Bailey, S.C.C., and Kopp, G.A. (2003). Influence of wall proximity on vortex shedding from a square cylinder. *Experiments in Fluids* **34**, 585-596.

[89] Menter, F.R. (1994). Two-equation eddy-viscosity turbulence models for engineering applications. *AIAA Journal* **32**, 1598-1605.

[90] Menter, F.R., Kuntz, M., and Bender, R. (2003). A scale-adaptive simulation model for turbulent flow predictions. In: *Proceedings of the 41st AIAA Aerospace Sciences Meeting and Exhibit*, Reno, Nevada, AIAA Paper 2003-0767.

[91] Moin, P. and Bewley, T.. (1994). Feedback control of turbulence. *Applied Mechanics Reviews* **47(6-2)**, S3-S13.

[92] Moffat, R.J. (1982). Contributions to the theory of single-sample uncertainty analysis. *Transactions of the ASME: Journal of Fluids Engineering* **104**, 250-260.

[93] Monkewitz, P.A. (1988). The absolute and convective nature of instability in two-dimensional wakes at low Reynolds numbers. *Physics of Fluids* **31**, 999-1006.

[94] Monkewitz, P.A. and Nguyen, L.N. (1987). Absolute instability in the near-wake of two-dimensional bluff bodies. *Journal of Fluids and Structures* **1**, 165-184.

[95] Obasaju, E.D. (1983). Investigation of the effects of incidence on the flow around a square section cylinder. *Aeronautical Quarterly* **34**, 243-259.

[96] Oertel, H. (1990). Wakes behind blunt bodies. *Annual Review of Fluid Mechanics* **22**, 539-564.

[97] Patankar, S.V. (1980). *Numerical Heat Transfer and Fluid Flow.* Hemisphere Publishing Corporation, Washington.

[98] Pier, B. and Huerre, P. (2001). Nonlinear self-sustained structures and fronts in spatially developing wake flows. *Journal of Fluid Mechanics* **435**, 145-174.

[99] Pier, B., Huerre, P., Chomaz, J.-M., and Couairon, A. (1998). Steep nonlinear global modes in spatially developing media. *Physics of Fluids* **10**, 2433-2435.

[100] Pierrehumbert, R.T. (1984). Local and global baroclinic instability of zonally varying flow. *Journal of Atmospheric Sciences* **41**, 2141-2162.

[101] Pinier, J.T., Ausseur, J.M., Glauser, M.N., and Higuchi, H. (2007). Proportional closed-loop feedback control of flow separation. *AIAA Journal* **45**, 181-190.

[102] Pope, S.B. (2000). *Turbulent Flows.* Cambridge University Press, Cambridge, UK.

[103] Press, W.H., Teukolsky, S.A., Vetterling, W.T., and Flannery, B.P. (1992). *Numerical recipes in FORTRAN: Second edition.* Cambridge University Press, Cambridge, UK, p. 364.

[104] Price, S.J., Sumner, D., Smith, J.G., Leong, K., and Paidoussis, M.P. (2002). Flow visualization around a circular cylinder near to a plane wall. *Journal of Fluids and Structures* **16**, 175-191.

[105] Raffel, M., Willert, C., and Kompenhans, J. (1998). *Particle Image Velocimetry: A Practical Guide.* Springer-Verlag, Berlin.

[106] Reynolds, W.C. and Hussain, A.K.M.F. (1972). The mechanics of an organized wave in turbulent shear flow. Part 3. Theoretical models and comparisons with experiments. *Journal of Fluid Mechanics* **54**, 263-288.

[107] Rhie, C.M. and Chow, W.L. (1983). Numerical study of the turbulent flow past an airfoil with trailing edge separation. *AIAA Journal* **21**, 1525-1532.

[108] Rodi, W., Ferziger, J.H., Breuer, M., and Pourquie, M. (1997). Status of large eddy simulation: Results of a workshop. *Transactions of the ASME: Journal of Fluids Engineering* **119**, 248-262.

[109] Roshko, A. (1955). On the wake and drag of bluff bodies. *Journal of the Aeronautical Sciences* **22**, 124-132.

[110] Roshko, A. (1961). Experiments on the flow past a circular cylinder at very high Reynolds number. *Journal of Fluid Mechanics* **10**, 345-356.

[111] Roshko, A. (1993). Perspectives on bluff body aerodynamics. *Journal of Wind Engineering and Industrial Aerodynamics* **49**, 79-100.

[112] Roshko, A., Steinolfson, A., and Chattoorgoon, V. (1975). Flow forces on a cylinder near a wall or near another cylinder. In: *Proceedings of the 2nd U.S. National Conference on Wind Engineering Research*, Colorado State University, Fort Collins, Paper IV-15.

[113] Saghafian, M., Stansby, P.K., Saidi, M.S., and Apsley, D.D. (2003). Simulation of turbulent flows around a circular cylinder using nonlinear eddy-viscosity modelling: Steady and oscillatory ambient flows. *Journal of Fluids and Structures* **17**, 1213-1236.

[114] Schlichting, H. (1979). *Boundary Layer Theory (7th Edition).* McGraw-Hill, New York.

[115] Shimizu, K. and Kawamura, M. (1972). Spanwise correlation measurement behind a circular cylinder in subcritical Reynolds number region. *Journal of the Physical Society of Japan* **32**, 1454.

[116] Shur, M., Spalart, P., Strelets, M., and Travin, A. (1996). Navier-Stokes simulation of shedding turbulent flow past a circular cylinder and a cylinder with backward splitter plate. In: *Proceedings of the 3rd ECCOMAS Computational Fluid Dynamics Conference*, 9-13 September, Paris, France, pp. 676-682.

[117] Shur, M., Spalart, P.R., Strelets, M., and Travin, A. (1999). Detached-eddy simulation of an airfoil at high angle of attack. In: *Engineering Turbulence Modelling and Experiments 4*, edited by W. Rodi and D. Laurence, Elsevier, Oxford, UK, pp. 669-678.

[118] Shur, M., Spalart, P.R., Squires, K.D., Strelets, M., and Travin, A. (2005). Three dimensionality in Reynolds-averaged Navier-Stokes solutions around two-dimensional geometries. *AIAA Journal* **43**, 1230-1242.

[119] Sirovich, L. (1987). Turbulence and the dynamics of coherent structures, Part I: Coherent structures. *Quarterly of Applied Mathematics* **45**, 561-571.

[120] Smagorinsky, J. (1963). General circulation experiments with the primitive equations: I. The basic experiment. *Monthly Weather Review* **91**, 99-165.

[121] Spalart, P.R. (2000). Strategies for turbulence modelling and simulations. *International Journal of Heat and Fluid Flow* **21**, 252-263.

[122] Spalart, P.R. (2001). Young-person's guide to detached-eddy simulation grids. Technical Report NASA/CR-2001-211032, Langley Research Center, National Aeronautics and Space Administration (NASA), Virginia.

[123] Spalart, P.R. and Allmaras, S.R. (1992). A one-equation turbulence model for aerodynamic flows. In: *Proceedings of the 30th AIAA Aerospace Sciences Meeting and Exhibit*, Reno, Nevada, AIAA Paper 92-0439.

[124] Spalart, P.R., Jou, W.H., Strelets, M., and Allmaras, S.R. (1997). Comments on the feasibility of LES for wings, and on a hybrid RANS/LES approach. In: *Proceedings of the First AFOSR International Conference on DNS/LES*, Ruston, Louisiana.

[125] Stansby, P.K. (1974). The effects of end plates on the base pressure coefficient of a circular cylinder. *Aeronautical Journal* **78**, 36-37.

[126] Surry, D. (1972) Some effects of intense turbulence on the aerodynamics of a circular cylinder at subcritical Reynolds number. *Journal of Fluid Mechanics* **52**, 543-563.

[127] Szepessy, S. and Bearman, P.W. (1992). Aspect ratio and end plate effects on vortex shedding from a circular cylinder. *Journal of Fluid Mechanics* **234**, 191-217.

[128] Taneda, S. (1965). Experimental investigation of vortex streets. *Journal of the Physical Society of Japan* **20**, 1714-1721.

[129] Taniguchi, S. and Miyakoshi, K. (1990). Fluctuating fluid forces acting on a circular cylinder and interference with a plane wall. *Experiments in Fluids* **9**, 197-204.

[130] Taylor, J.R. (1982). *An Introduction to Error Analysis.* University Science Books, Sausalito, CA.

[131] The MathWorks, Inc. (2002). *Using MATLAB.* The MathWorks, Inc., Natick, MA, USA.

[132] Toebes, G.H. (1969). The unsteady flow and wake near an oscillating cylinder. *Transactions of the ASME: Journal of Basic Engineering* **91**, 493-505.

[133] Travin, A., Shur, M., Strelets, M., and Spalart, P. (2000). Detached-eddy simulations past a circular cylinder. *Flow, Turbulence and Combustion* **63**, 293-313.

[134] van Oudheusden, B.W., Scarano, F., van Hinsberg, N.P., and Watt, D.W. (2005). Phase-resolved characterization of vortex shedding in the near wake of a square-section cylinder at incidence. *Experiments in Fluids* **39**, 86-98.

[135] Vickery, B.J. (1966). Fluctuating lift and drag on a long cylinder of square cross-section in a smooth and in a turbulent stream. *Journal of Fluid Mechanics* **25**, 481-494.

[136] von Kármán, T. (1954). *Aerodynamics.* Cornell University Press, Ithaca, New York.

[137] Wilcox, D.C. (1998). *Turbulent Modelling for CFD (2nd Edition).* DCW Industries, CA.

[138] Williamson, C.H.K. (1996). Vortex dynamics in the cylinder wake. *Annual Review of Fluid Mechanics* **28**, 477-539.

[139] Williamson, C.H.K. and Govardhan, R. (2004). Vortex-induced vibrations. *Annual Review of Fluid Mechanics* **36**, 413-455.

[140] Wu, J., Sheridan, J., Welsh, M.C., and Hourigan, K. (1996). Three-dimensional vortex structures in a cylinder wake. *Journal of Fluid Mechanics* **312**, 201-222.

[141] Zdravkovich, M.M. (1985a). Observation of vortex shedding behind a towed circular cylinder near a wall. In: *Flow Visualization III: Proceedings of the Third International Symposium on Flow Visualization*, edited by W.J. Yang, Hemisphere, Washington D.C., pp. 423-427.

[142] Zdravkovich, M.M. (1985b). Forces on a circular cylinder near a plane wall. *Applied Ocean Research* **7**, 197-201.

[143] Zdravkovich, M.M. (1997). *Flow Around Circular Cylinders: Vol 1: Fundamentals.* Oxford University Press, Oxford, UK.

[144] Zdravkovich, M.M. (2003). *Flow Around Circular Cylinders: Vol 2: Applications.* Oxford University Press, Oxford, UK.

[145] Zdravkovich, M.M., Brand, V.P., Mathew, G., and Weston, A. (1989). Flow past short circular cylinders with two free ends. *Journal of Fluid Mechanics* **203**, 557-575.

[146] Zhang, X., Mahon, S., Van Den-Berg, M., and Williams, C. (2005). Aerodynamics of a half-cylinder in ground effect. In: *Engineering Turbulence Modelling and Experiments 6 (Proceedings of the ERCOFTAC International Symposium on Engineering Turbulence Modelling and Measurements - ETMM6)*, edited by W. Rodi and M. Mulas, Elsevier, Amsterdam, pp. 461-470.

[147] Zhang, X., Toet, W., and Zerihan, J. (2006). Ground effect aerodynamics of race cars. *ASME Applied Mechanics Reviews* **59**, 33-49.

Vita

The author, Takafumi Nishino, was born in Aichi, Japan, in May 1979. He graduated from Asahigaoka High School in Aichi in 1998, and obtained his bachelor's and master's degrees in mechanical engineering at Kyoto University in 2002 and 2004, respectively. In this period, he developed his interest in academic research under the supervision of the late Professor Kenjiro Suzuki, and he was given a chance to present his work at an international conference held in the United States in April 2003, at the age of 23. After completing his studies at Kyoto University, he decided to pursue a doctoral degree in aerodynamics at the University of Southampton in the United Kingdom. During his three-year doctoral study in Southampton, he wrote four journal papers and two conference papers. As of August 2007, he is planning to continue his academic career in the field of flow control after his doctoral degree.

List of publications (refereed articles)

- Nishino, T., Komori, H., Iwai, H., Suzuki, K. (2003). Development of a comprehensive numerical model for analyzing a tubular-type indirect internal reforming SOFC. In: *Proceedings of the First International Conference on Fuel Cell Science, Engineering and Technology*, 21-23 April, Rochester, NY, USA, pp. 521-528.

- Nishino, T., Iwai, H., Suzuki, K. (2004). Numerical investigation on the strategies for reducing the cell temperature gradient of an indirect internal reforming tubular SOFC. In: *Proceedings of the Second International Conference on Fuel Cell Science, Engineering and Technology*, 14-16 June, Rochester, NY, USA, pp. 353-360.

- Nishino, T., Iwai, H., Suzuki, K. (2005). Comprehensive numerical simulation of an indirect internal reforming tubular SOFC. *Transactions of the Japan Society of Mechanical Engineers B* **71**, 2800-2807 [in Japanese].

- Suzuki, K., Iwai, H., Nishino, T. (2005). Electrochemical and thermo-fluid modeling of a tubular solid oxide fuel cell with accompanying indirect internal fuel reforming. In: *Transport Phenomena in Fuel Cells*, edited by B. Sunden and M. Faghri, WIT Press, Southampton, UK, Chapter 3, pp. 83-131.

- Nishino, T., Iwai, H., Suzuki, K. (2006). Comprehensive numerical modeling and analysis of a cell-based indirect internal reforming tubular SOFC. *Transactions of the ASME: Journal of Fuel Cell Science and Technology* **3**, 33-44.

- Nishino, T., Roberts, G.T., Zhang, X. (2006). An experimental study of flow around a circular cylinder with and without end plates in ground effect. In: *Proceedings of the 36th AIAA Fluid Dynamics Conference and Exhibit*, 5-8 June, San Francisco, CA, USA, AIAA Paper 2006-3551, CD-ROM, 15pp.

- Nishino, T., Roberts, G.T., Zhang, X. (2006). Detached-eddy simulation of flow around a circular cylinder in ground effect. In: *Proceedings of the 17th International Symposium on Transport Phenomena*, 4-8 September, Toyama, Japan, CD-ROM, 6pp.

- Nishino, T., Roberts, G.T., Zhang, X. (2007). Vortex shedding from a circular cylinder near a moving ground. *Physics of Fluids* **19**, 025103, 12pp.

- Nishino, T., Roberts, G.T., Zhang, X. (2007). Unsteady RANS and detached-eddy simulations of flow around a circular cylinder in ground effect. *Journal of Fluids and Structures* (to be published).

- Nishino, T., Roberts, G.T. (2007). Absolute and convective instabilities of two-dimensional bluff body wakes in ground effect. *European Journal of Mechanics B/Fluids* (under review).

- Nishino, T., Zhang, X., Roberts, G.T. (2007). Low-dimensional description of the turbulent near wake of a circular cylinder in ground effect. *Journal of Fluids and Structures* (under review).